



SAPIENZA  
UNIVERSITÀ DI ROMA

## Search for SUSY events with off-time photons

Scuola di Dottorato in Scienze Astronomiche,  
Chimiche, Fisiche e Matematiche "Vito Volterra"  
Dottorato di Ricerca in Fisica – XXIII Ciclo

Candidate

Daniele Franci  
ID number 697313

Thesis Advisors

Prof. Egidio Longo  
Dott. Daniele del Re  
Prof. Shahram Rahatlou

A thesis submitted in partial fulfillment of the requirements  
for the degree of Doctor of Philosophy in Physics

October 2010

Thesis not yet defended

Daniele Franci. *Search for SUSY events with off-time photons.*

Ph.D. thesis. Sapienza – University of Rome

© October 2010

VERSION: 14 November 2010

EMAIL ADDRESS: [daniele.franci@roma1.infn.it](mailto:daniele.franci@roma1.infn.it)

# Contents

<b>1</b>	<b>Non-standard long-lived particles</b>	<b>9</b>
1.1	The Standard Model . . . . .	9
1.2	Problems with the Standard Model . . . . .	12
1.3	Models with long-lived particles . . . . .	15
1.3.1	Charged particles . . . . .	15
1.3.2	Colored particles . . . . .	16
1.3.3	Neutral particles . . . . .	16
<b>2</b>	<b>General description of Supersymmetry</b>	<b>17</b>
2.1	Basic concepts . . . . .	17
2.2	Motivation for Supersymmetry . . . . .	18
2.3	The Minimal Supersymmetric Standard Model . . . . .	19
2.4	Supersymmetry breaking in the MSSM . . . . .	22
<b>3</b>	<b>The GMSB model</b>	<b>25</b>
3.1	Basics of gauge-mediated breaking mechanism . . . . .	25
3.2	Soft symmetry breaking in the observable sector . . . . .	26
3.3	GMSB model parameters . . . . .	27
3.4	Phenomenology of long-lived neutralino decay . . . . .	30
<b>4</b>	<b>The CMS experiment at the LHC</b>	<b>33</b>
4.1	The Large Hadron Collider . . . . .	33
4.2	The Compact Muon Solenoid detector . . . . .	36
4.2.1	Magnet . . . . .	39
4.2.2	Tracker . . . . .	40
4.2.3	Electromagnetic calorimeter . . . . .	42
4.2.4	Hadron calorimeter . . . . .	42
4.2.5	The muon system . . . . .	43
4.2.6	The trigger system . . . . .	44
4.2.7	CMS software components . . . . .	45
4.3	The electromagnetic calorimeter . . . . .	47
4.3.1	Lead tungstate crystals . . . . .	47
4.3.2	Mechanical design . . . . .	49
4.3.3	Photodetectors . . . . .	50
4.3.4	Electronics chain . . . . .	53
4.3.5	Amplitude and time reconstruction . . . . .	54
4.3.6	Energy resolution . . . . .	55

4.4	Photon reconstruction . . . . .	56
4.4.1	Hybrid algorithm . . . . .	56
4.4.2	Energy corrections . . . . .	57
4.4.3	Position measurement . . . . .	58
<b>5</b>	<b>Determination of long-lived particle lifetime</b>	<b>61</b>
5.1	Event samples . . . . .	61
5.2	Selection criteria for off-pointing photons . . . . .	63
5.2.1	ECAL timing . . . . .	63
5.2.2	Cluster shape . . . . .	67
5.3	Rejection of photon conversions . . . . .	75
5.4	Algorithm for lifetime reconstruction . . . . .	81
5.4.1	Reconstruction of photon momentum vector . . . . .	81
5.4.2	Flight path calculation . . . . .	84
<b>6</b>	<b>Identification of SUSY events with photons</b>	<b>93</b>
6.1	Signature of new physics with photons . . . . .	93
6.2	Sources of background . . . . .	95
6.2.1	In-time backgrounds . . . . .	95
6.2.2	Off-time backgrounds . . . . .	98
6.3	GMSB event selection . . . . .	98
6.3.1	Photon identification . . . . .	100
6.3.2	MET reconstruction . . . . .	103
6.3.3	Jet reconstruction . . . . .	112
6.3.4	Measured time in the ECAL . . . . .	112
<b>7</b>	<b>Analysis results</b>	<b>119</b>
7.1	Event selection . . . . .	119
7.1.1	Unbinned maximum likelihood fit . . . . .	120
7.1.2	Optimization of selection criteria . . . . .	121
7.2	Exclusion limits . . . . .	123
7.3	Systematic uncertainties . . . . .	123
7.3.1	Missing transverse energy . . . . .	127
7.3.2	ECAL time measurement . . . . .	128
7.3.3	Luminosity uncertainties . . . . .	128
7.3.4	Theoretical uncertainties . . . . .	129
<b>8</b>	<b>Conclusions</b>	<b>131</b>
<b>A</b>	<b>Identification of photons and <math>\pi^0</math> in the ECAL</b>	<b>133</b>
A.1	Datasets and analysis procedure . . . . .	133
A.1.1	Distance between the decay photons . . . . .	134
A.2	Moments of the ECAL cluster . . . . .	137
A.3	Improved discrimination . . . . .	139
A.3.1	Lateral moment . . . . .	142
A.3.2	Pseudo-Zernike moments . . . . .	142
A.3.3	Combination of different discriminants . . . . .	143

<b>B Improvements on <math>\pi^0</math> reconstruction</b>	<b>149</b>
B.1 Dataset and photon reconstruction . . . . .	149
B.2 Variation of the lateral containment . . . . .	150
B.3 Improved $\pi^0$ reconstruction algorithm . . . . .	153
B.3.1 Parametrization of photon shower shape . . . . .	155
B.3.2 Improved $\pi^0$ reconstruction . . . . .	158
<b>Bibliography</b>	<b>163</b>



# Introduction

The Standard Model (SM) of elementary particles and their fundamental interactions provides a very elegant theoretical framework and it has been verified with high accuracy by several experiments, showing an excellent agreement between theoretical expectations and experimental results. Today, the SM is a well established theory applicable over a wide range of conditions.

Despite the striking experimental success of the SM, this theory still have some drawbacks and unsolved problems, that range from the origin of particle masses to the nature of the Dark Matter in the Universe and represent a strong conceptual indication for physics in the TeV energy domain.

Recent theoretical and experimental advances have brought a new focus on theoretical proposals for physics beyond the SM with massive and long-lived particles, which are common in several Supersymmetry (SUSY) models and also in more exotic scenarios. From an experimental point of view, models with long-lived particles decaying into an energetic photon are very accredited for early discoveries of new physics from the experiments at the Large Hadron Collider (LHC), the proton-proton collider at the CERN laboratories of Geneva. The LHC provide collisions at a center of mass energies in the range of 7-14 TeV, and it will allow to explore the realm of the new physics that many theories place in the TeV range.

Although a model-independent approach is followed, this thesis is focused on SUSY theories with Gauge Mediated Supersymmetry Breaking since they have a relatively high production cross section and have a very distinctive experimental signature. According to the choice of the parameters, GMSB model foresees the existence of a long-lived, massive, neutral particle (the *neutralino*  $\tilde{\chi}_1^0$ ) which decays into a high energy photon and a *gravitino*  $\tilde{G}$ . Since the gravitino is stable and weakly interacting it usually escapes from detection. Therefore it can be considered as a massive neutrino.

The general-purpose detector of the Compact Muon Solenoid (CMS) experiment is used to identify events with long-lived particles decaying into photons. The excellent performance of the electromagnetic calorimeter (ECAL) allows for the identification of off-pointing and off-time photons from the decay of long-lived particles, thanks respectively to its fine lateral segmentation and the optimal resolution on time measurement. In this thesis, an algorithm to extract the lifetime of long-lived particles decaying into photons is presented.

In addition, a study of the  $\tilde{\chi}_1^0 \rightarrow \tilde{G} + \gamma$  decay within the GMSB model, with a full simulation of the CMS detector, is also illustrated. The presence of high energy photons, large missing transverse energy due to gravitinos and high multiplicity of hadronic jets in the final state, makes the experimental signature of such events very clear.

The dissertation is organized as follows:

- a theoretical outline of the SM, its unsolved problems and the importance of new physics theories with long-lived particles are discussed in Chapter 1;
- a general description of SUSY is provided in Chapter 2;
- the GMSB mechanism and its experimental implications at collider experiments are illustrated in Chapter 3;
- a brief overview of the most important features of the LHC and the CMS experiment is presented in Chapter 4;
- the algorithm to obtain the lifetime of long-lived particles decaying into photons is discussed in Chapter 5;
- the phenomenology of SUSY events with photons, large missing transverse energy and high jet multiplicity is described in Chapter 6;
- the method to establish exclusion limits for  $\tilde{\chi}_1^0 \rightarrow \tilde{G} + \gamma$  with early CMS data is presented in Chapter 7;
- the conclusion are discussed in Chapter 8.

In addition, a  $\pi^0 - \gamma$  discrimination algorithm based on the analysis of the shape of the energy deposits in the electromagnetic calorimeter is presented in Appendix A. Finally, an optimized reconstruction technique for high energy  $\pi^0$ s is discussed in Appendix B.

# Chapter 1

## Non-standard long-lived particles

This chapter describes the importance of the theoretical proposals of physics beyond the Standard Model which foresee the existence of massive and long-lived particles. The chapter begins with a general overview of the basic concepts of the Standard Model. Then, the unsolved theoretical problems and drawbacks of the Standard Model are discussed. Finally, some examples of new physics models involving massive and long-lived particles are presented.

### 1.1 The Standard Model

All known particle physics phenomena are extremely well described within the Standard Model (SM) of elementary particles and their fundamental interactions[1][2]. The SM provides a very elegant theoretical framework and it has been verified with high accuracy by several experiments in the last decades, showing an excellent agreement between the theoretical expectations and the experimental results. Because of its high predictive power, the SM is considered to be the triumph of particle physics of the 1970's. Today, the SM is a well established theory applicable over a wide range of conditions.

The SM provides a description of the strong, weak and electromagnetic interactions in terms of "gauge theories", i.e. theories which possess invariance under a set of space-time dependent transformations (called "local transformations"). According to the gauge principle, all the fundamental forces (with the exception of gravity) are mediated by the exchange of the gauge fields, corresponding to a specific symmetry group. The symmetry group which stands at the basis of the SM is

$$SU(3)_C \otimes SU(2)_L \otimes U(1)_Y \tag{1.1}$$

obtained as direct product of the symmetry group of strong interactions,  $SU(3)_C$ , and the symmetry group of the electroweak interactions,  $SU(2)_L \otimes U(1)_Y$ . The symmetry group of the electromagnetic interactions,  $U(1)_{EM}$ , appears in the SM as a subgroup of  $SU(2)_L \otimes U(1)_Y$  and it is in this sense that the weak and electromagnetic interactions are said to be unified.

The gauge sector of SM is composed of 12 spin-1 gauge bosons: 8 bosons (gluons) for  $SU(3)_C$ , 3 bosons ( $W_i$ ) for  $SU(2)_L$  and 1 boson ( $B$ ) for  $U(1)_Y$ . The  $W^\pm$  bosons

are obtained as a linear combination of  $W_1$  and  $W_2$ , while the  $Z$  boson and the photon  $\gamma$  can be seen as a linear combination of  $W_3$  and  $B$ . The gluons are massless, electrically neutral and carry color quantum number. The consequence of gluons being colorful is that they can interact with themselves. The weak bosons  $W^\pm$  and  $Z$  are massive particles and also self-interacting. The photon  $\gamma$  is massless, chargeless and non-selfinteracting.

Matter fields are represented by spin- $\frac{1}{2}$  leptons and quarks, organized in three families with identical properties, except for mass. The particle content in each family is summarized in Table 1.1 and 1.2, respectively for leptons and quarks.

	Left-Handed	Right-Handed
1 <sup>st</sup> family	$\begin{pmatrix} \nu_e \\ e^- \end{pmatrix}_L$	$e_R^-$
2 <sup>nd</sup> family	$\begin{pmatrix} \nu_\mu \\ \mu^- \end{pmatrix}_L$	$\mu_R^-$
3 <sup>rd</sup> family	$\begin{pmatrix} \nu_\tau \\ \tau^- \end{pmatrix}_L$	$\tau_R^-$

**Table 1.1.** Particle content of the three lepton families.

	Left-Handed	Right-Handed
1 <sup>st</sup> family	$\begin{pmatrix} u \\ d \end{pmatrix}_L$	$u_R, d_R$
2 <sup>nd</sup> family	$\begin{pmatrix} c \\ s \end{pmatrix}_L$	$c_R, s_R$
3 <sup>rd</sup> family	$\begin{pmatrix} t \\ b \end{pmatrix}_L$	$t_R, b_R$

**Table 1.2.** Particle content of the three quark families.

The scalar sector of SM is not experimentally confirmed yet. The fact that the weak gauge bosons have a mass different from zero indicates that the electroweak group is not a symmetry of the vacuum. Also the fermion masses can not be included without violating gauge symmetry. Mass terms can be introduced exploiting the Spontaneous Symmetry Breaking mechanism, first proposed by Higgs [3], which produces the following pattern in the SM:

$$SU(3)_C \otimes SU(2)_L \otimes U(1)_Y \rightarrow SU(3)_C \otimes U(1)_{em} \quad (1.2)$$

with the purpose to give mass to the weak bosons and fermions and, at the same time, keep the photon massless. The above pattern is implemented by means of

the so-called Higgs Mechanism, which predicts the existence of a new scalar and electrically neutral particle: the Higgs boson.

Although this particle has not been seen in the experiment so far, some constraints on its mass can be extracted by a global fit to the precision electroweak data. The most recent results (updated to July 2010) are shown in the Figure 1.1 [4], where the precision electroweak measurements performed at LEP, SLD, CDF and D0 are combined to obtain a  $\Delta\chi^2$  curve as a function of the Higgs mass. The

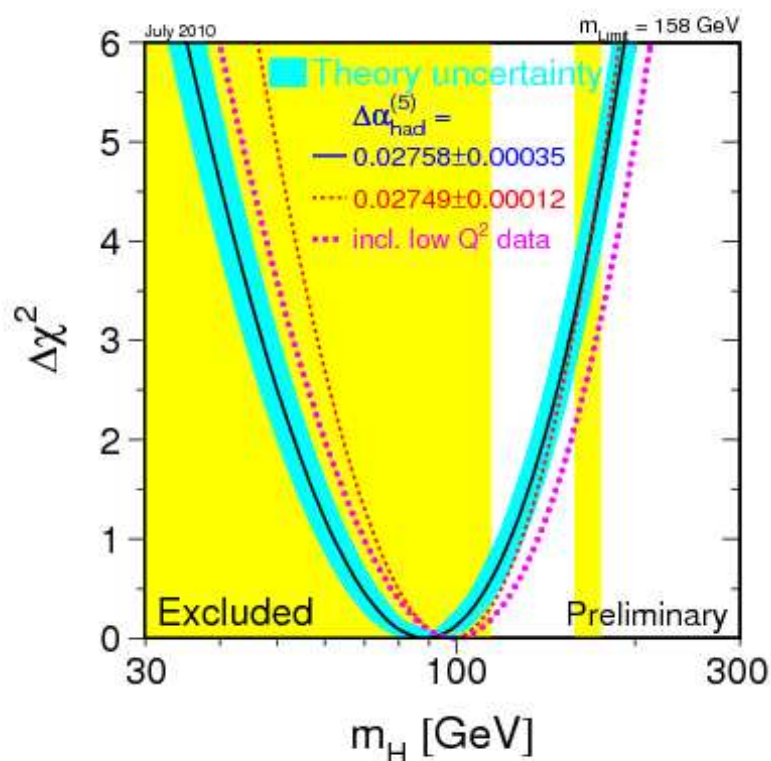


**Figure 1.1.**  $\Delta\chi^2$  curve derived from electroweak precision observables measured at LEP, SLD, CDF and D0 as a function of the Higgs mass, assuming the SM to be the correct theory of nature.

preferred value for Higgs mass (89 GeV, corresponding to the minimum of the curve) is excluded by the LEP-2 direct search limit of 114 GeV. Also the mass range of 158 to 175 GeV is excluded by direct search performed by the Tevatron experiments CDF and D0 [5]. The precision electroweak measurement suggests the existence of a SM Higgs boson with a mass lower than 158 GeV.

Because of the fundamental role played within the SM, the hunting for the Higgs boson represents one of the most exciting challenge for the current high-energy physics experiments.

## 1.2 Problems with the Standard Model

Despite the striking experimental success of the SM, physics community is still not fully satisfied with that theory. The main reason is that there are strong conceptual indications for physics beyond the SM, which is expected to be manifest at energies in the TeV domain. In the following, some of the open issues of the SM will be discussed.

### 1. Gravitational force

As already stated, the SM describes in a unified way three of the four fundamental forces: weak, strong and electromagnetic force. At the present, gravity is not included in the SM pattern: the standard procedure for quantizing fields has failed to work for gravity, in spite of a half-century of effort. However, the idea of Grand Unified Theories [6] (GUTs) which unify all the fundamental forces into a single gauge principle, is now in very much vogue via the Superstring theory [7].

### 2. Unification of coupling constant

In addition to a quantum mechanic description of gravity, the existence of GUTs implies that, at high energy scales, all the gauge interactions of the SM are merged into one unique interaction characterized by a larger gauge symmetry. Therefore, at the unification scale, electromagnetic, weak and strong interactions have to be described by one unified coupling constant rather than three independent ones. In the SM the coupling constants evolve, according with the normalization group equation, as a function of the energy scale  $Q$  [8]

$$\alpha_i^{-1}(Q) = \alpha_i^{-1}(M_Z) + \frac{b_i}{2\pi} \log \frac{Q}{M_Z} \quad (1.3)$$

where  $\alpha_i(M_Z)$  is the coupling constant calculated at the Z boson mass  $M_Z$  scale and  $b_i$  is a coefficient characteristic of each coupling. As demonstrated in Figure 1.2, which shows the evolution of the coupling constants as a function of the energy scale  $Q$ , the constants do not come to a common value at any scale. The failure in providing a unification of the fundamental interactions suggests the presence of new physics phenomena beyond the SM, occurring at a higher energy scale.

### 3. The hierarchy problem

The hierarchy problem arises when radiative corrections to the Higgs mass are considered. When the SM is assumed to be a low-energy effective theory, a cut-off  $\Lambda$  should be imposed, corresponding to the scale of the new physics. The fields describing all the known particles benefit from the protection of symmetry principles which ensure that the radiative corrections to the tree-level masses are only logarithmically divergent with  $\Lambda$

$$\delta m^2 \simeq m^2 \log \Lambda \quad (1.4)$$

However, Higgs boson evades this rule. Figure 1.3 shows a correction to the Higgs mass  $M_h^2$  from a loop containing Dirac fermion  $f$  with mass  $m_f$ . Considering the coupling of Higgs boson to  $f$

$$- \lambda_f H \bar{f} f \quad (1.5)$$

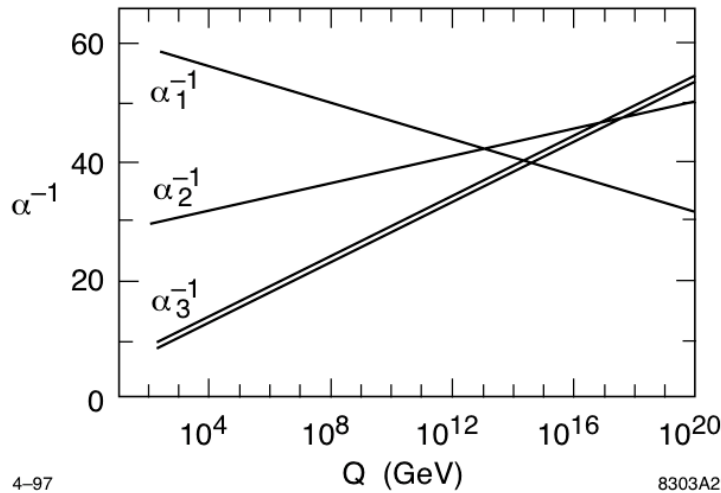


**Figure 1.2.** Evolution of the gauge couplings to high energy scales. The double line for  $\alpha_3$  indicates the experimental error.

the Feynman diagram in Figure 1.3 yields a correction

$$\left(\Delta M_h^2\right)_f \sim \frac{\lambda_f^2}{4\pi^2} \left(\Lambda^2 + m_f^2\right) + \dots \quad (1.6)$$

which diverges quadratically with the cut-off value  $\Lambda$ .

If one assumes that the SM is valid up to the Planck scale  $M_P \simeq 10^{19}$  GeV, radiative corrections are some 30 orders of magnitude larger than the expected value for the SM Higgs mass, which is around 100 GeV: this means that a very unnatural cancellation between tree-level Higgs mass and radiative corrections is required to preserve SM prediction. To keep the mass shift under control avoiding any unnatural fine-tuning, new physics is required at an energy scale below 1 TeV.

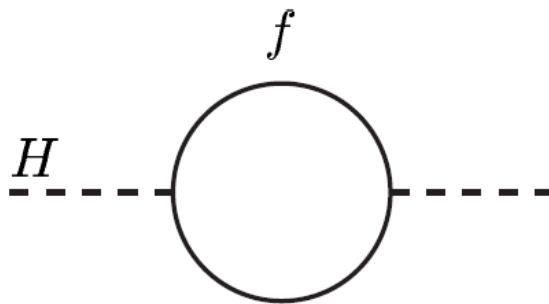


**Figure 1.3.** One-loop fermion correction to the Higgs mass.

#### 4. Neutrino mass

The simplest form of the Higgs mechanism for Spontaneous Symmetry Break-

ing provides masses for all the elementary fermions except the neutrino. However, on the strength of the recent report of atmospheric neutrino oscillations [9], as well as previous other indications of solar [10] and accelerator [11], neutrino masses are now considered to be almost established experimentally.

### 5. Barion asymmetry

The SM does not provide any obvious explanation for the observed imbalance in baryonic and anti-baryonic matter in the Universe. The Big Bang should have produced equal amounts of matter and anti-matter, ensuring a total cancellation of both. Since this is not the case, some physical laws must have acted differently for matter and anti-matter.

### 6. Origin of the Dark Matter

The shining matter is not the only one in the Universe. Considerable amount consists of the so-called Dark Matter, which is non relativistic, non baryonic, non luminous, neutral and weakly interacting. The direct evidence for the presence of the Dark Matter are the rotation curves of galaxies [12]. Figure 1.4 shows the rotation speed of the planets of the solar system (left) and the stars in some typical spiral galaxy (right), as a function of the distance from the sun/center of galaxy. In the solar system all the planets perfectly fit the

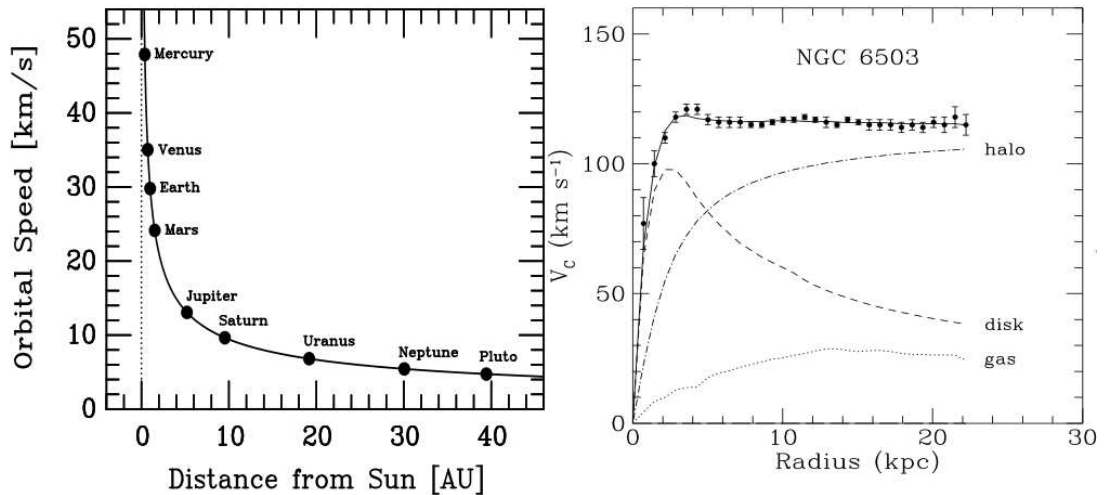


Figure 1.4. Rotation curves for the solar system and galaxy.

curve obtained from Newton mechanics. At the same time, the galaxy has a completely different behavior. To explain these curves, the existence of a galactic halo made of non shining matter which takes part in gravitational interaction is needed. Several cosmological measurement confirms that around 25% of the energy density of the Universe is represented by the Dark Matter, as confirmed by the composition of the universe shown in Figure 1.5.

The problem related to the Dark Matter is that the SM has no possible candidates for such kind of matter.

According to the above arguments, the existence of new physics phenomena at the TeV scale is necessary to address all the SM problems. For what concerns this thesis, only those theoretical models which predict long-lived particles will be considered.



Figure 1.5. Composition of the Universe.

### 1.3 Models with long-lived particles

Recent theoretical and experimental advances have brought a new focus on models beyond the SM with massive, long-lived particles. Such particles are common in several Supersymmetry scenarios [13][14] and also in models with hidden sectors and a mass gap (the so-called “hidden valleys” [15]). They are also predicted in other exotic scenarios like Universal Extra Dimensions [16] and lepto-quark theories [17]. Because of this, both discovery and non discovery is important in excluding different exotic models. From an experimental point of view, the major advantage of many of these models consists in non negligible cross sections and relatively small SM background. On the other hand, a very deep knowledge and control of the detectors used to perform this kind of searches is required, in order to keep the instrumental backgrounds as low as possible. In this section, a brief review of the most accredited models are presented. According to the characteristics of the long-lived particle, three main categories has been identified.

#### 1.3.1 Charged particles

In many Supersymmetric models, charged particles with large lifetime, due to small decay phase space, are expected to exist. They mimic the case of very high momentum muons, crossing the detector with velocity significantly lower than the speed of light. This unique signature makes the search for it a model-independent search, based on measurement of both the time of flight and the energy loss by ionization. In this context, only those models with a *gravitino*  $\tilde{G}$  in the final state are considered. According to the nature of the long-lived particle, two different categories can be distinguished:

1. Lepton-like particles like *s-leptons*  $\tilde{l}_i$ , decaying into the correspondent SM leptonic partner (electron, muon or tau) via

$$\tilde{l}_i \rightarrow l_i + \tilde{G} \quad (1.7)$$

2. Hadron-like particles like *s-top*  $\tilde{t}$ , decaying into the SM top quark via

$$\tilde{t} \rightarrow t + \tilde{G} \quad (1.8)$$

For an exhaustive review of these models, see [18] [19].

### 1.3.2 Colored particles

A long-lived, colored *gluino*  $\tilde{g}$  is a generic prediction of several models of physics beyond the SM, such as Split-Supersymmetry [20]. In this scenarios,  $\tilde{g}$  decays into scalar particles are forbidden and gluinos acquire a macroscopic lifetime. During this time, they can hadronize into the so-called “R-hadrons”, bound states of the gluino and quarks or gluons. R-hadrons live long inside the detector and, in case they are electrically charged, can lose all their momentum via ionization and come at rest.

These particles, commonly referred as “stopped gluinos” can decay after a long time via

$$\tilde{g} \rightarrow g + \tilde{\chi}_1^0 \quad (1.9)$$

where  $\tilde{\chi}_1^0$  is a massive and weak interacting exotic particle (*neutralino*) and  $g$  is a gluon which hadronizes into a jet. Stopped gluinos provide a striking experimental signature, established by a large amount of delayed hadronic activity without anything else.

### 1.3.3 Neutral particles

The primary motivation to look for massive neutral particles with large lifetime is provided by the Gauge-Mediate Supersymmetry Breaking model (GMSB) [21], although they can also be present in other models, such as “hidden valley” scenarios. For what concern this thesis, the attention will be focused on GMSB model with long-lived neutralino decaying into a gravitino plus a high-energy photon

$$\tilde{\chi}_1^0 \rightarrow \tilde{G} + \gamma \quad (1.10)$$

The combination of displaced decay photons and significant energy imbalance in the transverse plane (due to gravitino which escapes from detection), generally leads to extremely clean, nearly background-free analysis. The theoretical foundations of the GMSB model will be described in details in Chapter 3.

## Chapter 2

# General description of Supersymmetry

This chapter is devoted to a general overview of the Supersymmetry, the most plausible and theoretically motivated framework for extending the SM.

The first part of the chapter describes the basic concepts that stand at the basis of the theory. Then, the motivations for Supersymmetry are presented, with a particular focus on the solutions to many of the SM problems provided by supersymmetric proposals.

Later, the minimal extension to the SM that realizes Supersymmetry is introduced: the Minimal Supersymmetric Standard Model. Finally, a brief overview of the most accredited mechanism of soft breaking of Supersymmetry are presented.

### 2.1 Basic concepts

Theoretical proposals based on Supersymmetry (SUSY)[22] assumes that the Nature has to obey to a new symmetry law that relates elementary particles of spin-1 to other particles that differ by half a unit of spin. In other terms, the existence of SUSY implies that for every type of boson, a corresponding type of fermion should exist, and vice versa. A SUSY transformation can be described by an operator  $Q$  that turns a bosonic (fermionic) state into a fermionic (bosonic) one

$$\begin{aligned} Q |Boson\rangle &= |Fermion\rangle \\ Q |Fermion\rangle &= |Boson\rangle \end{aligned} \tag{2.1}$$

The possible forms for  $Q$  operator in an interacting quantum field theory are highly restricted by the Coleman-Mandula theorem [23], which implies that  $Q$  must satisfy an algebra of anticommutation and commutation relations with the schematic form

$$\begin{aligned} \{Q, Q^\dagger\} &= P^\mu \\ \{Q, Q\} &= \{Q^\dagger, Q^\dagger\} = 0 \\ [P^\mu, Q] &= [P^\mu, Q^\dagger] = 0 \end{aligned} \tag{2.2}$$

where  $P^\mu$  is the four-momentum generator of spacetime translation.

The basic idea of Supersymmetry models is that the theory is invariant under Q transformations. This requirement can be satisfied including additional supersymmetric fields which play the role of the supersymmetric partners of the SM particles. As a result, the number of elementary particles is at least doubled.

## 2.2 Motivation for Supersymmetry

The main reason of the large success of SUSY theory is that it is able to provide a plausible and elegant solution to many of the unsolved problems of the SM described in Section 1.2.

A very much appreciated feature of SUSY models is the cancellation of quadratic divergences produced by one-loop fermionic Higgs mass correction (Eq. 1.6). The existence of scalar super-partner  $\tilde{f}$  leads to a new one-loop correction, shown in Figure 2.1, described by the Lagrangian term

$$-\lambda_{\tilde{f}}|H|^2|\tilde{f}|^2 \quad (2.3)$$

Then the Feynman diagram in Figure 2.1 gives a correction

$$\left(\Delta M_h^2\right)_{\tilde{f}} \sim -\frac{\lambda_{\tilde{f}}^2}{4\pi^2} \left(\Lambda^2 + m_{\tilde{f}}^2\right) + \dots \quad (2.4)$$

Thus, the total one-loop correction to Higgs mass corresponds to the sum of Eq.

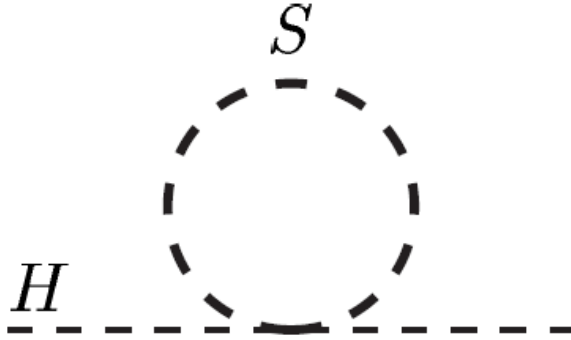


**Figure 2.1.** One-loop scalar correction to the Higgs mass.

1.6 and 2.4

$$\Delta M_h^2 = \left(\Delta M_h^2\right)_f + \left(\Delta M_h^2\right)_{\tilde{f}} \sim \left(N_f \lambda_f^2 - N_{\tilde{f}} \lambda_{\tilde{f}}^2\right) \cdot \Lambda^2 + \sum \left(m_f^2\right)_i - \sum \left(m_{\tilde{f}}^2\right)_i \quad (2.5)$$

Since SUSY predicts

$$\begin{aligned} N_f &= N_{\tilde{f}} \\ \lambda_f^2 &= \lambda_{\tilde{f}}^2 \end{aligned} \quad (2.6)$$

quadratic divergences cancel. Note that if SUSY were an exact symmetry of Nature, corrections would completely vanish since  $m_f = m_{\tilde{f}}$ .

In addition to this, SUSY also provides the unification of gauge coupling constant at a GUT energy scale which is well below the Plank scale. It has been shown [24] that, assuming a SUSY mass scale  $M_{SUSY}$  around 1 TeV, the introduction of the super-partners of gauge bosons (commonly referred as *gauginos*) sensibly modifies the structure of the coefficients  $b_i$  that enter in the normalization group equation (Eq. 1.3). These modifications lead to the unification of the coupling constants at the  $M_{GUT} = 10^{16}$  GeV energy scale. The convergence of the three coupling constants is shown in Figure 2.2.

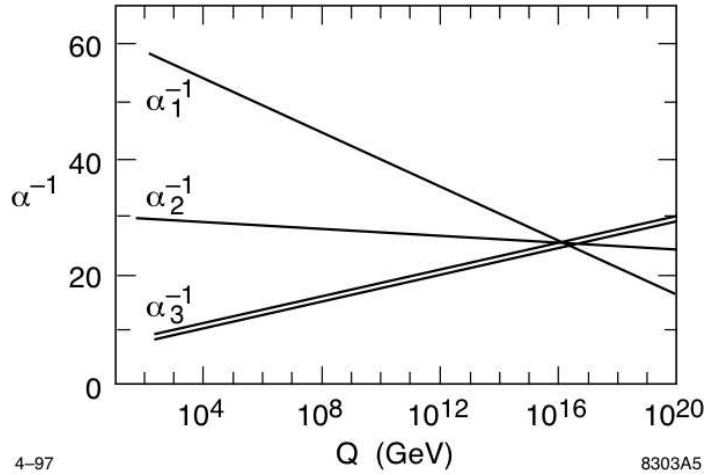


**Figure 2.2.** Evolution of the gauge couplings to high energy scales, using the renormalization group equation of the supersymmetric generalization of the SM. The double line for  $\alpha_3$  indicates the experimental error.

Moreover, SUSY offers a very definite solution to the problem of the origin of dark matter. Many SUSY models predict the existence of a massive, neutral, stable and weakly-interacting particle. If this particle were produced in the early universe, some density of this type of matter should still be present. Possible dark matter candidates include the lightest neutralino, the lightest sneutrino  $\tilde{\nu}$  (neutrino super-partner) and the gravitino. A discussion of the other candidates can be found in [25].

Finally, some SUSY extensions provide a quantum mechanical description of gravity [26], thus linking together all the fundamental interactions.

## 2.3 The Minimal Supersymmetric Standard Model

As implied by the name, the Minimal Supersymmetric Standard Model [26] (MSSM) is essentially a straightforward supersymmetrization of the SM. In particular, "minimal" means that the number of super-fields and interactions introduced by the new symmetry law, is kept as low as possible. Several non-minimal extensions of MSSM exist [27][28], but they will be not discussed in this thesis.

In the minimal version of SUSY, the number of particles is doubled, with the addition of another Higgs doublet with its super-partner. The particle content of MSSM is shown in Figure 2.3. The names for the spin-0 partners of the quarks and leptons are modified by the addition of the "s-" (for *scalar*) prefix: they are gener-

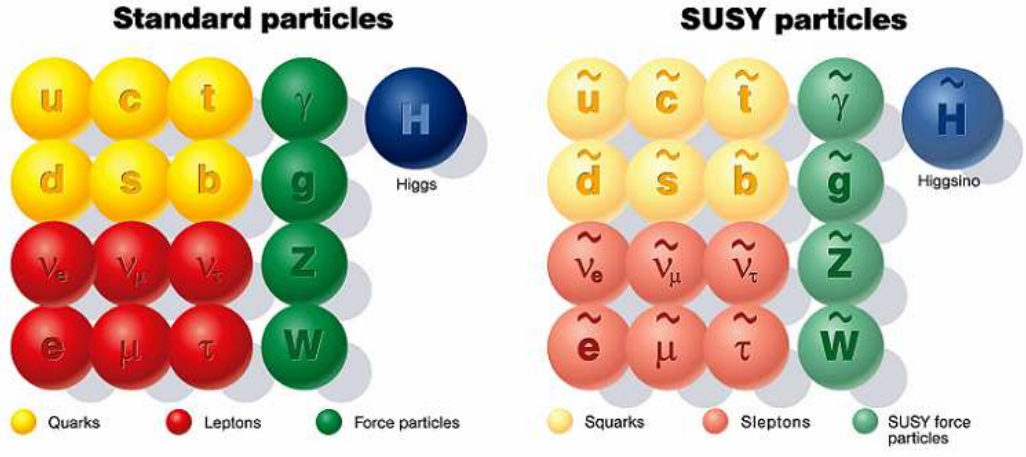


Figure 2.3. Particle content of MSSM.

ically called *squarks* and *sleptons*, or sometimes *sfermions*. Instead, the fermionic partner of the SM gauge bosons get an “-ino” suffix, and they are called *gauginos*. The symbols used to identify sfermions and gauginos are the same already used for the corresponding fermions and gauge bosons, with the addition of a tilde ( $\sim$ ) used to denote the super-partner of a SM particle. Two complex Higgs doublets are predicted by the MSSM

$$H_u = (H_u^+, H_u^0)$$

$$H_d = (H_d^0, H_d^-)$$
(2.7)

where the subscripts  $u$  and  $d$  indicate the coupling respectively to charge  $+2/3$  up-type quarks (up, charm and top) and to charge  $-1/3$  down-type quarks (down, strange and bottom). There is also the gravitino  $\tilde{G}$ , which is postulated to be the SUSY partner of the yet undiscovered spin-2 graviton (the carrier of gravitational interaction).

If SUSY were a perfect symmetry of the Nature, super-partners would have the same mass of their SM counterparts and would have been already discovered. The absence of them at modern energies is believed to be explained by the fact that their masses are very heavy, that means that SUSY should be broken. Figure 2.4 shows a graphical description of SUSY broken symmetry. The Lagrangian of the MSSM can be written as

$$L_{MSSM} = L_{SUSY} + L_{BREAK}. \quad (2.8)$$

The first part of the Lagrangian almost exactly repeats that of the SM, except that the fields are now the super-fields rather than the ordinary fields of the SM. The only difference is the presence of an additional part which describes the Higgs mixing. It is absent in the SM since there is only one Higgs field there. The second part of the Lagrangian represents the SUSY breaking, as mentioned above.

Due to SUSY breaking mechanism, MSSM states can mix to form physical mass eigenstate. The gauge super-multiplets containing  $W^0$  and  $B^0$  mix to give mass eigenstate  $Z^0$  and  $\gamma$ , and the corresponding mixtures of  $\tilde{W}^0$  and  $\tilde{B}^0$  are called *zino*

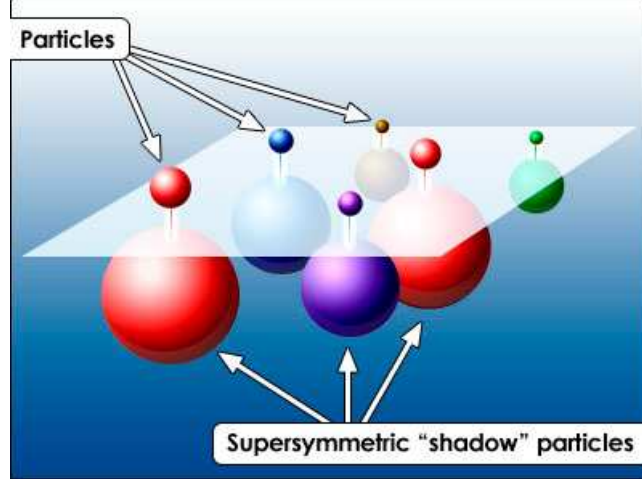


**Figure 2.4.** Schematic view of SM particles with the SUSY counterparts.

( $\tilde{Z}^0$ ) and *photino* ( $\tilde{\gamma}$ ) respectively. The higgsino and electroweak gauginos mix with each other because of the effects of the electroweak symmetry breaking. The neutral higgsinos ( $\tilde{H}_u^0, \tilde{H}_d^0$ ) and the neutral gauginos ( $\tilde{B}, \tilde{W}^0$ ) combine to form four neutral mass eigenstates. The charged higgsinos ( $\tilde{H}_u^\pm, \tilde{H}_d^\pm$ ) and winos ( $\tilde{W}^+, \tilde{W}^-$ ) mix to form four charged mass eigenstates. These are denoted as the neutralino ( $\tilde{\chi}_1^0, \tilde{\chi}_2^0, \tilde{\chi}_3^0, \tilde{\chi}_4^0$ ) and chargino ( $\tilde{\chi}_1^\pm, \tilde{\chi}_2^\pm$ ) mass eigenstates. By convention, these states are ordered by increasing mass, so that

$$M_{\tilde{\chi}_1^0} < M_{\tilde{\chi}_2^0} < M_{\tilde{\chi}_3^0} < M_{\tilde{\chi}_4^0} \quad (2.9)$$

and

$$M_{\tilde{\chi}_1^\pm} < M_{\tilde{\chi}_2^\pm} \quad (2.10)$$

Gauge and mass eigenstates in MSSM are listed in Table 2.1.

The general super-potential of the MSSM contains terms where the baryon and lepton numbers are violated. Since both baryon and lepton number conservation have been tested to a high degree of precision, a new symmetry law, R-parity [29], has been introduced to avoid this problem. The conserved quantum number R is defined as

$$R = (-1)^{3(B-L)+2s} \quad (2.11)$$

where B, L and s represent respectively the baryonic number, leptonic number and spin of the particle. This quantity is designed to be  $R = +1$  for SM particles (including the Higgs bosons) and  $R = -1$  for SUSY counterparts. Since R-parity is conserved, no mixing between SM and SUSY particles can occur. The R-parity conservation has extremely important phenomenological consequences. They include:

1. any initial state created in laboratories has  $R = +1$ : this implies that SUSY particles must be created in pairs;
2. any SUSY particle (except the LSP) must decay into a state that contains an odd number of SUSY particles;

Names	Spin	Gauge Eigenstates	Mass Eigenstates
squarks	0	$\tilde{u}_L \tilde{u}_R \tilde{d}_L \tilde{d}_R$	(same)
		$\tilde{s}_L \tilde{s}_R \tilde{c}_L \tilde{c}_R$	(same)
		$\tilde{t}_L \tilde{t}_R \tilde{b}_L \tilde{b}_R$	$\tilde{t}_1 \tilde{t}_2 \tilde{b}_1 \tilde{b}_2$
sleptons	0	$\tilde{e}_L \tilde{e}_R \tilde{\nu}_e$	(same)
		$\tilde{\mu}_L \tilde{\mu}_R \tilde{\nu}_\mu$	(same)
		$\tilde{\tau}_L \tilde{\tau}_R \tilde{\nu}_\tau$	$\tilde{\tau}_1 \tilde{\tau}_1 \tilde{\nu}_\tau$
neutralinos	1/2	$\tilde{B}^0 \tilde{W}^0 \tilde{H}_u^0 \tilde{H}_d^0$	$\tilde{\chi}_1^0 \tilde{\chi}_2^0 \tilde{\chi}_3^0 \tilde{\chi}_4^0$
charginos	1/2	$\tilde{W}^+ \tilde{W}^- \tilde{H}_u^+ \tilde{H}_d^-$	$\tilde{\chi}_1^+ \tilde{\chi}_1^- \tilde{\chi}_2^+ \tilde{\chi}_2^-$
gluino	1/2	$\tilde{g}$	(same)
gravitino	3/2	$\tilde{G}$	(same)

**Table 2.1.** The gauge and mass eigenstate particles in the MSSM, with sfermion mixing for the first two families assumed to be negligible.

- due to energy and R-parity conservation laws, the lightest supersymmetric particle (LSP) must be stable. If the LSP is electrically neutral, it can only interact via weak forces with the ordinary matter. Therefore the LSP represents a very attractive dark matter candidate for the observed missing mass of the universe;
- a light stable LSP is neutral and weakly interacting to have escaped detection.

These features imply that, when a pair of SUSY particles are produced, two distinct decay chains start. In each vertex involving a sparticle, the production of a SM plus a SUSY particle is expected. Finally, each chain ends with the LSP. A typical decay chain is shown in Figure 2.5.

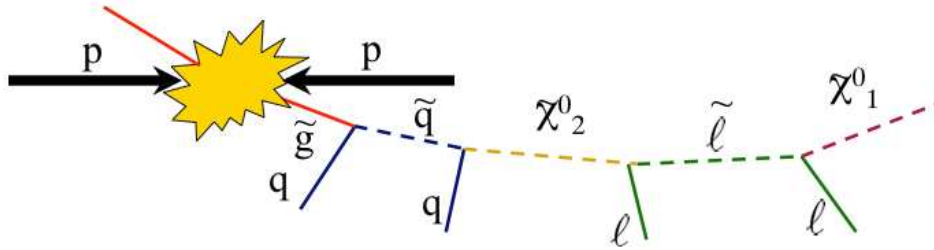


**Figure 2.5.** A typical SUSY decay chain.

## 2.4 Supersymmetry breaking in the MSSM

As previously noted, none of the super-partners have been yet discovered. If SUSY were a perfect symmetry then the sparticles would be easily detected long time

ago. Clearly, therefore, SUSY is a broken symmetry. Since none of the fields of the MSSM can develop non-zero vacuum expectation value (vev) to break SUSY without spoiling the gauge invariance, it is supposed that spontaneous supersymmetry breaking takes place via some other fields. The most common scenario for producing low-energy supersymmetry breaking is called the *hidden sector* one [30], which is a collection of yet-unobserved quantum fields and particles at a much higher mass scale that do not directly interact with the leptons, quarks or gauge bosons. In this way, SUSY breaking relies on two sectors: the usual matter belongs to the “visible” one, while the second, “hidden”, sector contains all the new fields which lead to breaking of SUSY. These two sectors interact with each other by exchange of some field called *messengers*, which mediate SUSY breaking from the hidden to the visible sector. A schematic view of SUSY breaking mechanism is shown in Figure 2.6. This mechanism, referred to as “soft” SUSY breaking, is very appealing since

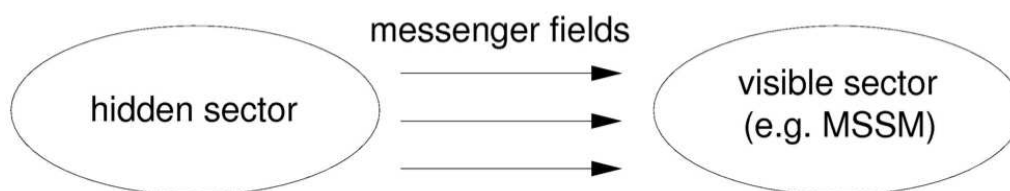


**Figure 2.6.** Schematic view of SUSY breaking mechanism.

SUSY is spontaneously broken in the hidden sector which has no direct coupling to SM particles. This means that all the attractive features of SUSY models (such as the cancellation of quadratic divergences) are maintained.

There are two main competing proposals for what the mediating interaction might be. The first (and historically the more popular) is the presence of a gravity mediation sector (SUGRA) [31]. A second possibility is that the interactions for SUSY breaking are gauge-mediated via the ordinary SM gauge interactions. This model is commonly known as Gauge Mediated Supersymmetry Breaking (GMSB) [32][33][34].

GMSB theories provide an important alternative to SUGRA scenario. These models predict a natural suppression of flavor violations in the SUSY sector and have very distinctive phenomenological features, such as high-energy photons in the final state due to  $\tilde{\chi}_1^0 \rightarrow \gamma \tilde{G}$ . Due to the central role played within this thesis, GMSB model will be described in the next chapter.

Other alternative scenarios, such as the Anomaly-Mediated Supersymmetry Breaking (AMSB) models [35] or the Gaugino-Mediated Supersymmetry Breaking [36], exist but they will be not discussed in this thesis.



# Chapter 3

## The GMSB model

This chapter is devoted to a general description of the Gauge-Mediated Supersymmetry Breaking (GMSB) [21][37] model. Theoretical foundations of the gauge mediated breaking mechanism are discussed in Section 3.1. Section 3.2 describes the effects of soft breaking in the observable sector. Then, the minimal version of GMSB model and the most important regions of the parameter phase space are introduced in Section 3.3. Finally, Section 3.4 describes the phenomenology of GMSB models with long-lived neutralinos.

### 3.1 Basics of gauge-mediated breaking mechanism

As already stated, the key ingredients of low-energy supersymmetry breaking scenarios are:

- an observable sector, which contains the usual quarks, leptons and two Higgs doublets, together with their supersymmetric partners;
- a hidden sector, responsible for supersymmetry breaking. It contains a collection of yet-unobserved quantum superfields and the corresponding hypothetical particles. This sector contains the *goldstino* field, which is the close analog of the Goldstone boson [21] controlling the spontaneous electroweak symmetry breaking. The goldstino field is represented by a chiral superfield  $X$ , which acquires a non-zero vev along the scalar and auxiliary components

$$\langle X \rangle = \langle M_m \rangle + \theta^2 \langle F \rangle \quad (3.1)$$

- a messenger sector, formed by some new superfields  $\Phi$  and  $\bar{\Phi}$  that transform under the  $SU(3)_C \otimes SU(2)_L \otimes U(1)_Y$  gauge group as a real non-trivial representation and couple at tree level with the goldstino superfield  $X$ , via some Yukawa interaction.

The parameters  $M_m$  and  $\sqrt{F}$  in Eq. 3.1 represent the fundamental mass scales in the theory and can vary from several tens of TeV to almost the GUT scale.

In the GMSB model the interaction between the messenger superfields  $\Phi$ ,  $\bar{\Phi}$  and the goldstino superfield  $X$  is given by the superpotential term

$$W = \lambda_{ij} \bar{\Phi}_i X \Phi_j \quad (3.2)$$

According to the  $X$  vev of Eq. 3.1, the coupling between  $\Phi$  and  $X$  generates masses for the messenger fields expressed by

$$(M_{\pm})^2 = (M_m)^2 \pm F \quad (3.3)$$

where the coupling constant of Eq. 3.2 can be absorbed in the definition of  $M_m$  and  $\sqrt{F}$ , which represent the mass scale for the messenger fields and the mass splitting between the component of the messenger multiplets respectively.

The positivity of the messenger squared masses requires  $F < (M_m)^2$ .

### 3.2 Soft symmetry breaking in the observable sector

The mass scale  $\sqrt{F}$  can be considered as the measure of SUSY breaking in the messenger sector. However, what is most interesting is the amount of SUSY breaking in the observable sector. At the tree level, ordinary particle supermultiplets are degenerate in mass, since they do not directly couple to the goldstino superfield  $X$ . Mass splitting arises because of gauge interactions between observable and messenger fields.

In this context, the masses of SM particles (vector bosons and matter fermions) are protected by gauge invariances while SUSY particles (gauginos, squarks and sleptons) can acquire masses consistently with the gauge symmetry, once SUSY is broken. Gaugino masses are generated at one loop (Figure 3.1a), but squark and slepton masses can only arise at two loops (Figure 3.1b), since the exchange of both gauge and messenger particles is necessary. Gaugino and scalar masses which arise

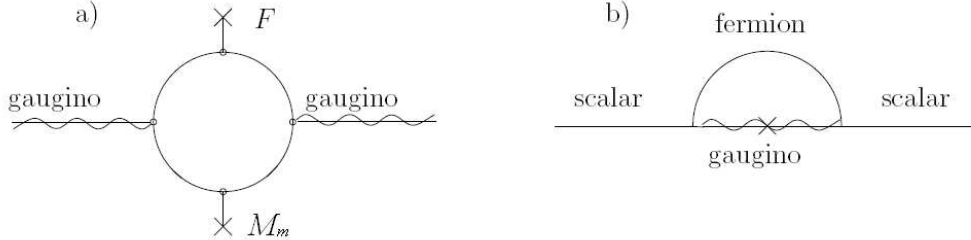


**Figure 3.1.** One-loop diagram of messenger fields responsible for gaugino masses a) and a typical diagram contributing to soft masses of MSSM scalars b). The cross denotes the insertion of the loop shown in a).

through the loops in Figure 3.1 can be parametrized as follows

$$\begin{aligned} M_{\lambda_i} &\sim c_i \frac{\alpha_i}{4\pi} \Lambda \propto N_m \Lambda \\ \tilde{m} &\sim 2\Lambda^2 \sum C_i c_i \left(\frac{\alpha_i}{4\pi}\right)^2 \propto N_m \Lambda^2 \end{aligned} \quad (3.4)$$

where  $\alpha_1 = \alpha / \cos^2 \theta_W$  and  $\alpha_2, \alpha_3$  are the coupling constant of weak and strong interaction;  $c_i$  is the sum of Dynkin indices of messenger fields running in the loop,  $c_1 = 5/3$ ,  $c_2 = c_3 = 1$ ;  $C_i$  are the eigenvalues of the quadratic operator for squark, slepton or Higgs representation.

All soft masses are therefore determined by a two parameters additional to the SM: the number of messenger generations  $N_m$  and the effective SUSY breaking scale

in the visible sector

$$\Lambda = \frac{F}{M_m} \quad (3.5)$$

The final mass spectrum of MSSM particles is then obtained by the evolution of sparticle masses from  $M_m$  scale down to the MSSM scale (TeV), via renormalization group equations.

Eq. 3.3 also implies that soft masses of sparticles are proportional to their coupling constants. This means that squarks are the heaviest sparticles (around 1 TeV at  $\Lambda \sim 100$  TeV) and spin-3/2 gravitino  $\tilde{G}$  is the LSP. This kind of LSP is a characteristic feature of models with gauge mediation. Gravitino arises when the globally supersymmetric theory is coupled to gravity and promoted to a locally supersymmetric theory. As a result of the super-Higgs mechanism, the gravitino acquires a supersymmetry-breaking mass which is given by [38][39]

$$m_{\tilde{G}} = \frac{F_0}{\sqrt{3}M_P} \quad (3.6)$$

where  $F_0$  can be interpreted as the fundamental scale of SUSY breaking. This scale can be very different from  $F$ , which is the scale of SUSY breaking felt by the messenger particles, i.e. the mass splitting inside their multiplets. The mechanism by which SUSY breaking is communicated to the messengers can be described by the ratio

$$C_{grav} = \frac{F_0}{F} \quad (3.7)$$

Gravitino mass can be thus rewritten as

$$m_{\tilde{G}} = C_{grav} \left( \frac{\sqrt{F}}{100 \text{ TeV}} \right)^2 2.4 \text{ eV} \quad (3.8)$$

where the model-dependent coefficient  $C_{grav}$  is such that  $C_{grav} > 1$ , and possibly  $C_{grav} \gg 1$ .

In gauge-mediated models, the gravitino is the LSP for any relevant value of  $F$ .

### 3.3 GMSB model parameters

The sparticle masses and couplings of the observable sector are fully determined by six free parameters [40]. In the following, a list of the GMSB parameters with a short description of their physical meaning is provided.

- **$\Lambda$** : this parameter sets the mass scale for the SUSY breaking in the observable sector. Superpartner masses scale linearly with this parameter, as implied by Eq. 3.4. To obtain superpartners with masses at the electroweak scale ( $\sim 1$  TeV),  $\Lambda \sim 100$  TeV is required
- **$N_m$** : the number of messenger generations. Gaugino masses scale with  $N_m$ , while squark and slepton masses scale with  $\sqrt{N_m}$ , as implied by Eq. 3.4. For  $\Lambda \sim \mathcal{O}(100 \text{ TeV})$ , the typical value for the number of messenger generations is between 1 and 5, in order to have sparticle masses in the TeV region. The  $N_m$  parameter is also important to set which is the Next-To Lightest SUSY Particle (NLSP) of the theory. In general, for low values of  $N_m$ , the lightest neutralino  $\tilde{\chi}_1^0$  is the NLSP, while for large values the stau  $\tilde{\tau}$  is the NLSP.

- $\mathbf{M}_m$ : the messenger scale that defines the mass scale at which MSSM sparticles obtain their masses via gauge interactions with the massive messenger fields. The electroweak scale and all the sparticle masses depend on the logarithm of  $M_m$ . In this thesis, only models with  $M_m > \Lambda$  will be considered, as they avoid flavor breaking in the messenger sector. Another constraint on  $M_m$  comes from the necessity of SUSY to be broken at low energy to solve the hierarchy problem. This implies that  $M_m < 10^{16}$  GeV.
- $\mathbf{\tan\beta}$ : the ratio between the two MSSM Higgs vev. Reasonable values for this parameter are in the range  $1.5 < \tan\beta < 60$ . Very low values of  $\tan\beta$  are forbidden due to the limits on light CP-even Higgs scalars, which are excluded by the LEP experiment [41]. On the other hand, large values of  $\tan\beta$  yield a  $\tilde{\tau}$  which is significantly lighter than the other sleptons.
- $\mathbf{\text{sign}(\mu)}$ : the sign of Higgs and Higgsino SUSY mass parameter  $\mu$ . The absolute value of  $\mu$  is determined by the electroweak-breaking condition. The case  $\mu < 0$  gives a larger mixing between the sparticles than the  $\mu > 0$  case.
- $\mathbf{C_{grav}}$ : the ratio between the fundamental scale of SUSY breaking and the scale of SUSY breaking felt by the messenger particles ( $C_{grav} = F_0/F$ ). This parameter controls both the gravitino mass and the NLSP lifetime.

The parametrization adopted in the GMSB model considerably simplifies the MSSM, where a detailed scanning over a huge parameter space (more than one hundred) would be necessary to cover all the phenomenological scenarios. However, even a sampling of the six-dimensional parameter space provided by the GMSB model is beyond the present capabilities for phenomenological studies. For this reason, specific benchmark scenarios are commonly considered (the so-called “*model lines*”).

In this study, the Snowmass Points and Slopes [42] (SPS) proposals will be considered. The SPS consist of model lines (“*slopes*”), i.e. continuous sets of parameters depending on one dimensionful parameter ( $\Lambda$  for GMSB). There are two distinct proposals for GMSB, which lead to different phenomenological consequences:

- **SPS 7**: in this scenario, the lightest stau is the NLSP, which decays via

$$\tilde{\tau} \rightarrow \tilde{G} + \tau \quad (3.9)$$

The parameter slope for SPS 7 is defined in Table 3.1

$\Lambda$	$\mathbf{M}_m$	$\mathbf{N}_m$	$\mathbf{\tan\beta}$	$\mathbf{\text{sign}(\mu)}$	$\mathbf{C_{grav}}$
free	$2\Lambda$	3	15	+	free

**Table 3.1.** SPS 7 parameter slope.

- **SPS 8**: in this scenario, the lightest neutralino is the NLSP, which decays via

$$\tilde{\chi}_1^0 \rightarrow \tilde{G} + \gamma \left( Z^0 \right) \quad (3.10)$$

The parameter slope for SPS 8 is defined in Table 3.2

$\Lambda$	$M_m$	$N_m$	$\tan\beta$	$\text{sign}(\mu)$	$C_{\text{grav}}$
free	$2\Lambda$	1	15	+	free

Table 3.2. SPS 8 parameter slope.

The phenomenology of the GMSB model is very sensitive to  $C_{\text{grav}}$ . Besides ruling the gravitino mass according to Eq. 3.8,  $C_{\text{grav}}$  also sets the lifetime of the NLSP. In particular, NLSP lifetime scales with  $C_{\text{grav}}^2$  as

$$c\tau \simeq C_{\text{grav}}^2 \left( \frac{100 \text{ GeV}}{M_{\text{NLSP}}} \right) \left( \frac{M_m}{\Lambda} \right)^2 \cdot 10^{-5} \text{ m} \quad (3.11)$$

Figure 3.2 shows the experimental signatures for both the SPS proposals and different values of NLSP lifetime. This thesis will be focused on SPS 8 proposal (neutralino as NLSP) and “medium” NLSP lifetime. The particle spectra for SPS 8 proposal assuming  $\Lambda = 100 \text{ TeV}$  is shown in Figure 3.3.

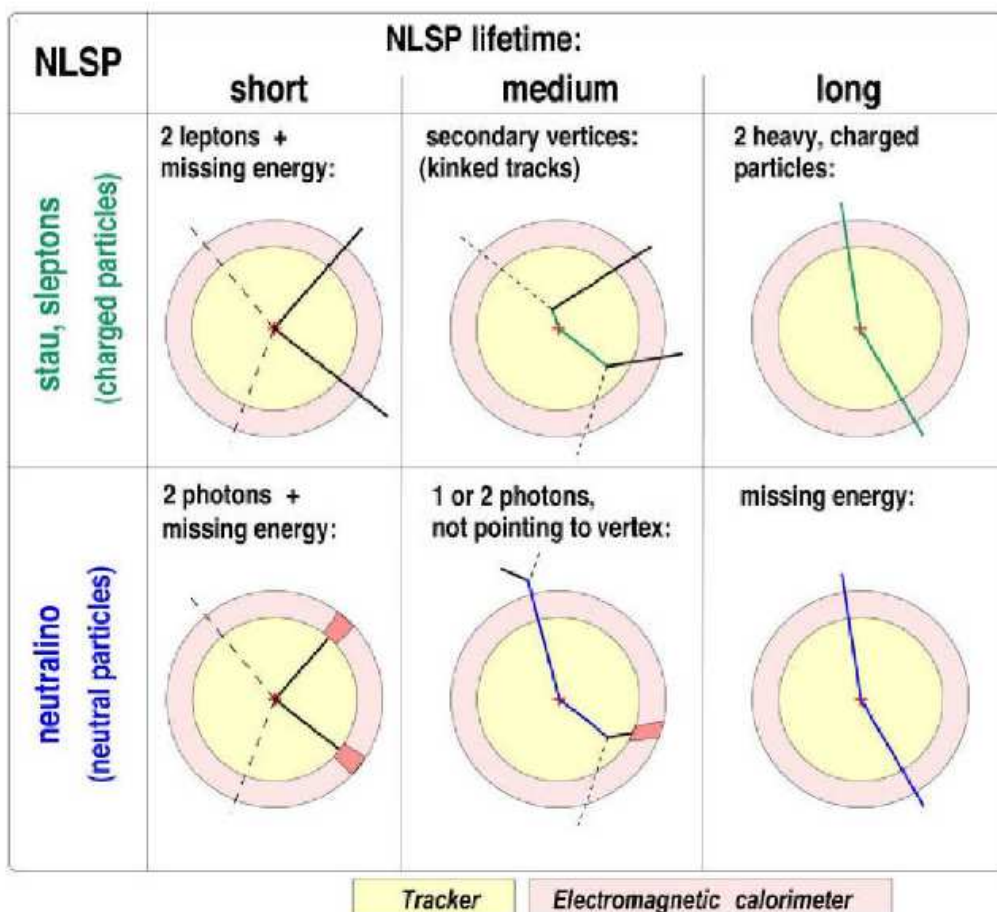
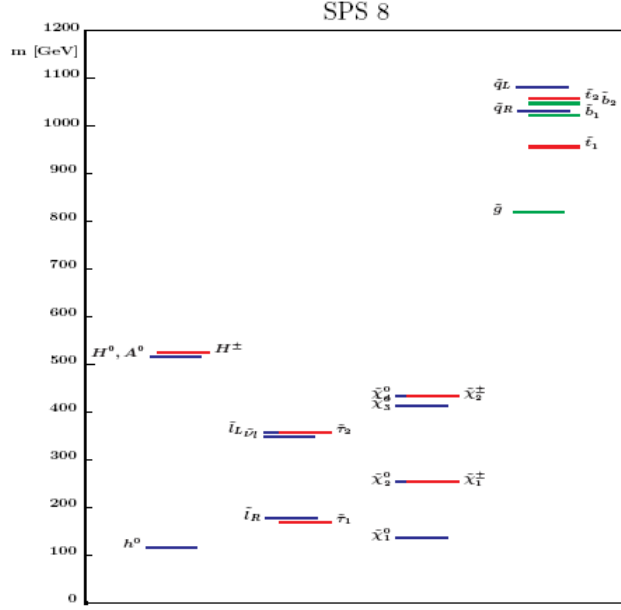


Figure 3.2. Experimental signatures for SPS 7 (up) and SPS 8 (down) scenario. Different values of NLSP lifetime are considered.



**Figure 3.3.** The SUSY particle spectrum for the benchmark point corresponding to SPS8 [42].

### 3.4 Phenomenology of long-lived neutralino decay

The SPS 8 proposal represents a benchmark scenario for SUSY discovering. Although different  $\tilde{\chi}_1^0$  decay channels are allowed, this work is focused on  $\tilde{G} + \gamma$  channel, which is dominant in a wide range of  $\Lambda$ . Assuming, for example,  $\Lambda = 100$  TeV, the branching ratio of neutralino decay into gravitino plus photon is around 95%.

The process of interest will be therefore:

$$p + p \rightarrow \tilde{s}_1 \tilde{s}_2 + X \rightarrow \cdots \rightarrow 2\tilde{\chi}_1^0 + X' \rightarrow 2\tilde{G} + 2\gamma + X'' \quad (3.12)$$

where  $\tilde{s}_1, \tilde{s}_2$  are generic sparticles and  $X, X', X''$  are SM particles produced in the event. A schematic picture of this process is shown in Figure 3.4.

The presence of two high-momentum photons, energy imbalance in the transverse plane (gravitinos which leave the detector without interacting) and large amount of hadronic activity due to many SM quarks produced in the decay chain, provides a striking experimental signature affected by a very low-level background.

Even more interesting, from an experimental point of view, is the case of long-lived neutralinos, i.e.  $C_{grav} > 1$ . If the lifetime is not too large, the most part of  $\tilde{\chi}_1^0$  travels through the detector and finally decays at a certain place which is displaced from the interaction point (IP). In addition to this, a photon from a long-lived  $\tilde{\chi}_1^0$  is typically out-of-time with respect to a photon from a promptly decay. These features can be summarized saying that long-lived neutralinos produce displaced and delayed photons (Figure 3.5). In the following they will be referred as *off-pointing* (OP) photons.

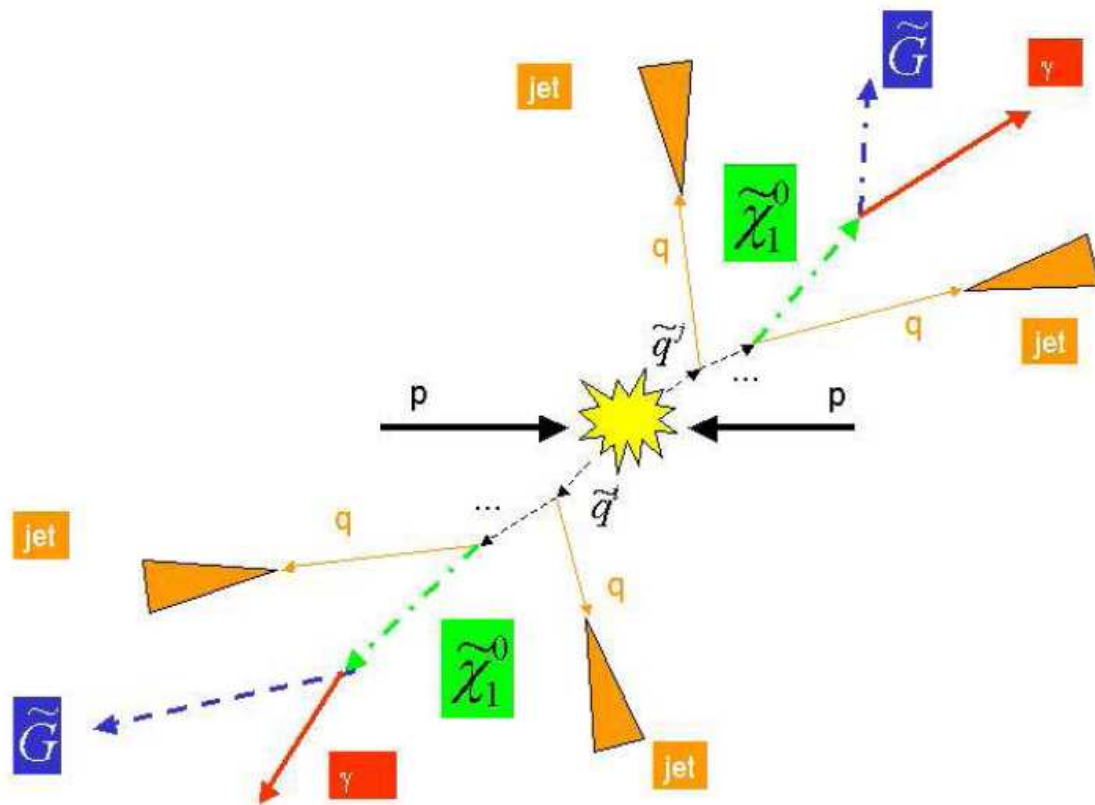


Figure 3.4. Schematic view of a GMSB decay chain with two neutralinos in the final state.

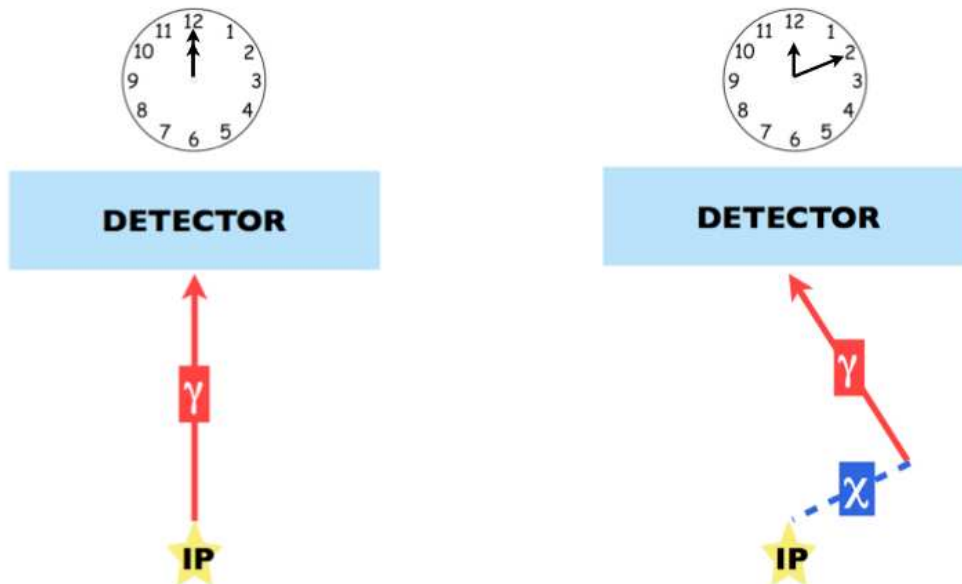


Figure 3.5. Comparison between the detection of a prompt photon (left) and an OP photon (right).

Detection of OP photons can be considered as a very exciting experimental challenge for the current generation of particle physics experiment. In particular, a detector that meets the following requirements is necessary:

1. optimal energy resolution;
2. very fine lateral segmentation, for a very precise determination of photon direction;
3. excellent time resolution, to distinguish between in-time and out-of-time photons.

The detector of the Compact Muon Solenoid (CMS) experiment provides an unique tools to investigate GMSB with long-lived  $\tilde{\chi}_1^0$ : it will be widely described in the next chapter.

## Chapter 4

# The CMS experiment at the LHC

An overall description of the Large Hadron Collider and the Compact Muon Solenoid experiment is provided in this chapter. The main characteristics of the Large Hadron Collider are presented in Section 4.1. Section 4.2 and 4.3 are respectively devoted to a general introduction of the Compact Muon Solenoid detector and a detailed description of the electromagnetic calorimeter. Finally, the technique used for photon reconstruction is illustrated in Section 4.4.

### 4.1 The Large Hadron Collider

The Large Hadron Collider [43] (LHC) at CERN is the world's largest and highest-energy particle accelerator. It is installed into the existing 27 km long tunnel previously occupied by LEP, as much as 175 meters beneath the Franco-Swiss border near Geneva, Switzerland. The LHC will provide proton-proton collisions at a center of mass energy  $\sqrt{s} = 14$  TeV, with a design luminosity of  $10^{34}$  cm<sup>-2</sup>s<sup>-1</sup>.

On 10 September 2008, the protons beams were successfully circulated in the main ring of the LHC for the first time, but nine days later operations were halted due to a serious fault between two superconducting bending magnets. After one year in repairs, the first proton-proton collision was recorded on 23 November 2009 at the injection energy of 450 GeV per beam. On 30 March 2010, the first planned collisions at  $\sqrt{s} = 7$  TeV took place. Collisions at  $\sqrt{s} = 14$  TeV are planned for the beginning of 2013.

Proton beams are delivered to LHC by a series of pre-accelerators that bring the protons to the injection energy of 450 GeV in three steps (Figure 4.1): the LINAC brings them to 50 MeV, the PS further accelerates them up to 1.4 GeV and the SPS injects them into the LHC ring at 450 GeV.

Since the collisions occur between particle of the same electrical charge, two separate acceleration cavities and two different magnetic field configurations are required. The LHC is equipped with 1232 superconducting 14.2m long Ni-Ti dipole magnets, cooled down to 1.9 K by means of super-fluid Helium, that create a bending magnetic field of about 8.4 T; they are placed in the eight curved sections which connect the straight sections of the LHC ring. Boosts are given by 400 MHz radiofrequency cavities with a voltage between 8 and 16 MV. The channels for the

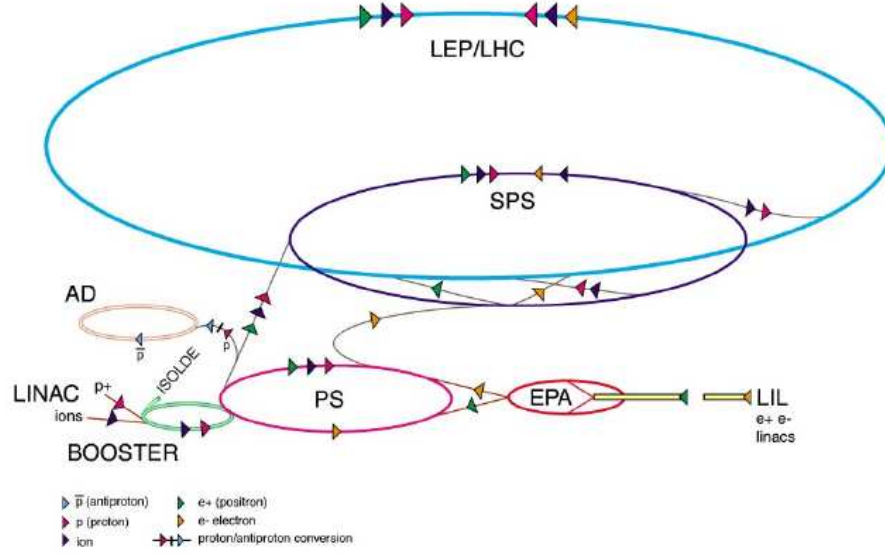


Figure 4.1. The LHC injection chain.

two proton beams acceleration are inserted in a single cryostat.

The high luminosity of the LHC is obtained by a high frequency bunch crossing and a high number of protons per bunch: two beams of protons with an energy of 7 TeV (3.5 TeV in the initial physics runs), circulating in two different vacuum chambers, contain each 2808 bunches. The bunches, with a nominal number of  $10^{11}$  protons each, have a very small transverse spread ( $\sigma_x \approx \sigma_y \approx 15 \mu\text{m}$ ) and are 7.5 cm long in the beam directions at the interaction points. The bunches cross at the rate of 40 MHz, i.e. one collision each 25 ns.

The LHC is also able to accelerate and collide beams of heavy ions, such as Pb, at 2.76 TeV to study the deconfined state of matter: the quark-gluon plasma. A summary of the main technical parameters of LHC is given in Table 4.1. There are four interaction points: the two at high luminosity are devoted to the multi-purpose CMS and ATLAS experiments. The other two, at lower luminosity, are used by ALICE and LHCb, optimized respectively for heavy-ion physics and the  $b$  quark physics. Figure 4.2 shows the underground tunnel LHC with the position of the four experiments.

The LHC luminosity can be calculated as

$$\mathcal{L} = f \frac{n_1 n_2}{4\pi\sigma_x\sigma_y} \quad (4.1)$$

where  $n_1$  and  $n_2$  are the number of protons in each bunch,  $f$  is the collision frequency and  $\sigma_x$ ,  $\sigma_y$  represent the Gaussian beam profile in the transverse plane.

The operating condition at the LHC are extremely challenging for the experiments. The total  $p-p$  cross section at the LHC is estimated to be about 100 mb [44] which implies about 20 proton interaction per bunch crossing, i.e  $10^9$  interactions per second. A strong online event selection is therefore required in order to reduce the event rate at around 100 Hz, corresponding to the maximum data storage rate sustainable by the existing device technology. The detectors must also have a fast

Parameter	Value
Circumference [km]	27
Number of magnet dipoles	1232
Dipolar magnetic field [T]	8.33
Radiofrequency [MHz]	400
Number of bunches	2808
Magnet temperature [K]	1.9
Nominal beam energy [TeV]	7
Nominal luminosity [ $\text{cm}^{-2}\text{s}^{-1}$ ]	$10^{34}$
Initial beam energy [TeV]	3.5
Protons per bunch	$1.05 \cdot 10^{11}$
Bunch spacing [m]	7.48
Bunch time separation [ns]	25
RMS bunch length [cm]	7.5
Crossing angle [rad]	$2 \cdot 10^{-4}$
Beam lifetime [h]	7
Luminosity lifetime [h]	10

**Table 4.1.** Main LHC technical parameters.

response time (around 25 ns) and a fine granularity in order to minimize the effect of simultaneous events. In addition to this, the high flux of particles coming from  $p - p$  interactions implies that each component of the detector has to be radiation resistant. Finally, to fully understand the physical processes occurring at the LHC, multi-purpose detectors are required to satisfy the following requirements:

- full hermeticity to provide accurate measures of missing transverse energy and momentum. This feature is crucial especially for analysis involving stable and weakly interacting particles, which escape from detection (like the gravitino in the GMSB model, as discussed in Section 3.4);
- excellent reconstruction of high momentum photons (and leptons)
- precise determination of charged particles momentum and impact point via an efficient tracking system;
- Accurate reconstruction of hadronic activity from QCD processes and heavy particle decays.

The detector of the Compact Muon Solenoid experiment meets all these stringent requirements. A detailed description of mechanical characteristics and performances of the CMS detector will be provided in the next section.

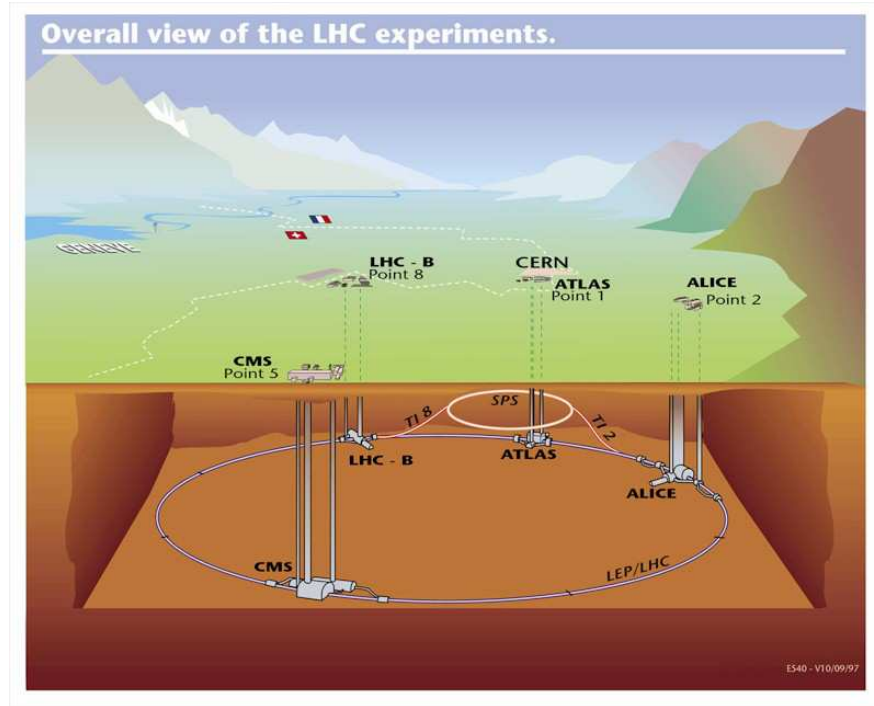


Figure 4.2. Overall view of the LHC.

## 4.2 The Compact Muon Solenoid detector

The Compact Muon Solenoid (CMS)[45] is one of the two general-purpose experiments that take data at the LHC. The main feature of CMS detector is a very strong magnetic field of 3.8 T generated by a superconducting solenoid, allowing for a very compact design. The philosophy adopted for the detector design has been:

1. a redundant efficient muon detection system;
2. an excellent electromagnetic calorimeter;
3. a high quality tracking system;
4. a  $4\pi$  hadron calorimetry.

The apparatus exhibits a cylindrical symmetry around the beam direction and it follows the typical structure of collider-based physics experiment: a cylindrical central section made of several layers coaxial with the beam axis (referred as *barrel* layers), closed at its ends by two hermetic disks orthogonal to the beam pipe (referred as *endcaps*). Some technical parameters of the CMS detector are listed in Table 4.2.

An overall view of the CMS detector is given in Figure 4.3. Longitudinal and cross-sectional views of the CMS detector are shown in Figure 4.4.

The natural coordinate frame used to describe the detector geometry is a cartesian system with:

- x axis pointing to the centre of the LHC ring;
- z axis coincident with the CMS cylinder axis;

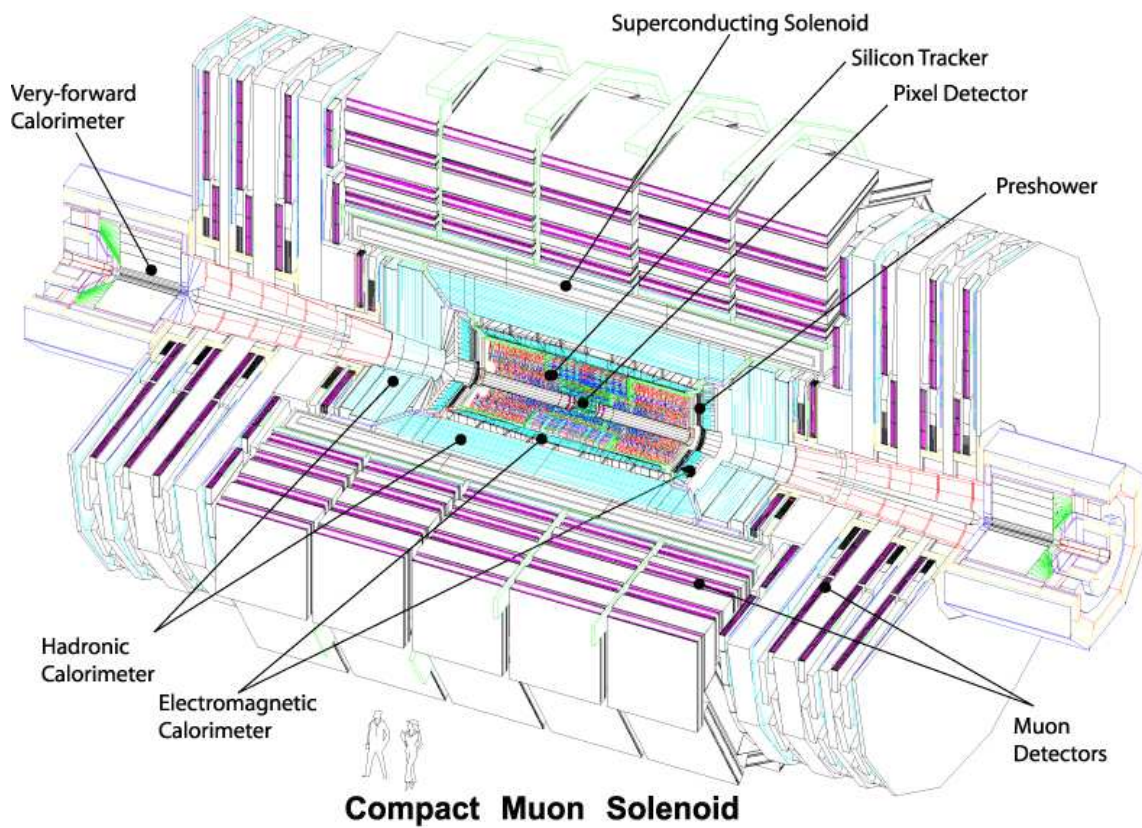


Figure 4.3. The complete CMS detector.

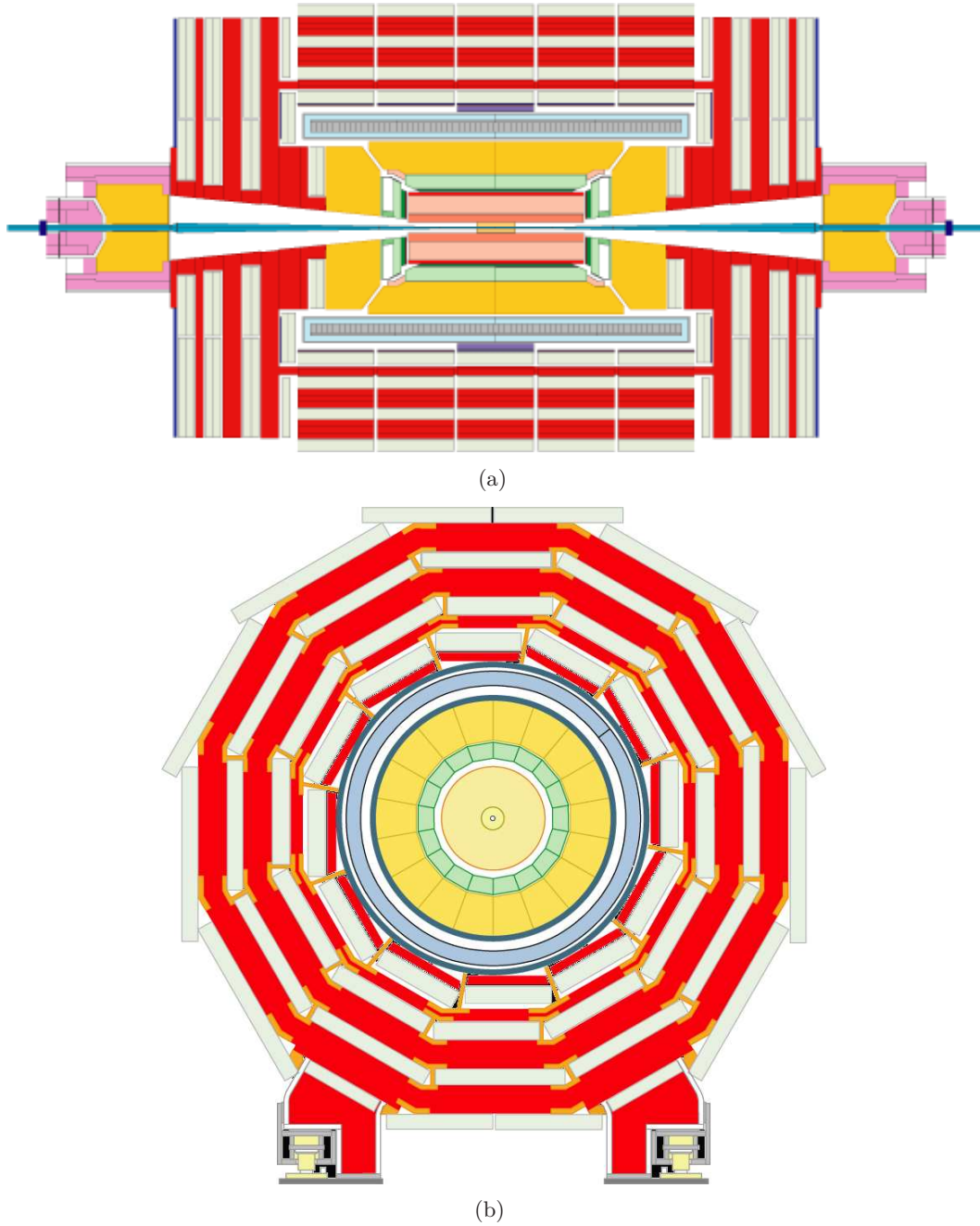


Figure 4.4. Longitudinal and cross-sectional view of the CMS detector.

Parameter	Value
Full length [m]	21.6
Diameter [m]	15
Total weight [t]	12500
Average density [g/cm <sup>3</sup> ]	3.3
Magnetic field [T]	3.8

**Table 4.2.** Technical parameters of the CMS detector.

- y axis directed upwards along the vertical.

Cylindrical symmetry of CMS design drives the use of a pseudo-angular reference frame, given by the triplet  $(r, \phi, \eta)$ , where  $r$  is the distance from the  $z$  axis,  $\phi$  is the azimuthal coordinate with respect to the  $x$  axis and  $\eta$ , commonly referred as *pseudorapidity*, is defined as

$$\eta = -\ln \left[ \tan \left( \frac{\theta}{2} \right) \right] \quad (4.2)$$

where  $\theta$  is the angle with respect to the  $z$  axis. The use of pseudorapidity instead of the polar angle is motivated by the fact that  $\eta$  is Lorentz invariant under longitudinal boosts.

The CMS design is driven by the choice of its magnet, a 13 m long superconducting solenoid with a diameter of 5.9 m. Cooled with liquid helium, it generate a magnetic field of 3.8 T which is kept uniform by a massive iron return yoke. The detector is constituted by different sub-detectors according to different tasks. Starting from the beam line they are: the inner tracking system; the electromagnetic calorimeter (ECAL); the hadron calorimeter (HCAL) and the muon chambers, hosted by the iron yoke.

In the following sections, a brief description of the different detector components will be provided. The trigger system, used for the online event selection, and the software tools will be also discussed. Particular attention will be focused on the ECAL description because of the great importance of this sub-detector for studies involving long-lived particles decaying into high energy photons.

### 4.2.1 Magnet

The choice of a compact design for the CMS detector imposes a strong solenoidal magnetic field in order to achieve an optimal resolution on the muon momentum measurement.

The magnet system [46] provides a uniform magnetic field of 3.8 T using a 13 m long superconducting coil with a diameter of 5.9 m. The magnetic flux is returned via a 1.8 m thick saturated iron yoke. The solenoid is composed by the winding (divided in four parts) with its mechanical support, the thermal radiation shield and the vacuum tank. The conductor is formed by three concentric sections: the flat Nb-Ti superconducting cable with high purity aluminium stabilizer and two external aluminium-alloy reinforcing slabs.

The cooling system aims at protecting against sudden power failure. In fact, a complete re-cooling from a non-superconducting state needs about twelve days.

Being the largest element of the CMS detector, the magnet must also provide the principal support structure for all the barrel detector components (tracking system and calorimetres inside the coil, muon stations outside).

The magnet system also includes the cryogenic system, power supply, quench protection vacuum pumping and control system.

### 4.2.2 Tracker

The tracker [47] is the sub-detector closest to the beam pipe. It is devoted to the determination of the interaction point, the reconstruction of charged tracks and the identification of secondary vertexes. The tracking system must be able to operate without degrading its performances in the hard radiation environment of LHC and it has to comply with severe material budget (as shown in Figure 4.5) constraints, in order not to degrade the excellent energy resolution for the whole tracker. By considering the charged particle flux at various radii at high luminosity,

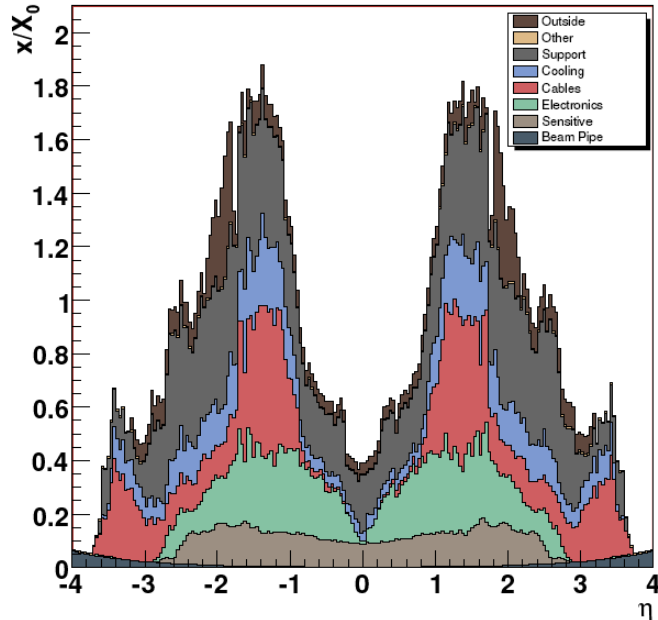


**Figure 4.5.** Material budget as a function of  $\eta$ . The thickness is expressed in terms of radiation length ( $X_0$ ). The peak around  $|\eta| = 1.5$  corresponds to the cables and services of the tracker.

three different regions can be deliniated:

- closest to the interaction vertex where the particle flux is the highest ( $\approx 10^7/s$  at  $r \approx 10$  cm), pixel detectors are placed. The size of a pixel is about  $100 \times 150 \mu\text{m}^2$ , giving an occupancy of about  $10^{-4}$  per pixel per LHC crossing;
- the intermediate region ( $20 < r < 55$  cm), where the particle flux is low enough to enable use of silicon microstrip detectors with a minimum cell size of  $10 \text{ cm} \times 80 \mu\text{m}$ , leading to an occupancy of  $\approx 2 - 3\%/LHC$  crossing;

- the outermost region ( $r > 55$  cm) of the inner tracker, where the particle flux has dropped sufficiently to allow use of larger-pitch silicon microstrips with a maximum cell size of  $25 \text{ cm} \times 180 \mu\text{m}$ , whilst keeping occupancy around 1%.

Even in heavy-ion (Pb-Pb) running, the occupancy is at the level of 1% in the pixel detectors and less than 20% in the outer silicon strip detectors, permitting track reconstruction in the high density environment.

The pixel detector consists of three barrel layers and two endcap disks at each side, as shown in Figure 4.6. The barrel layers are located at 4.4 cm, 7.3 cm and 10.2 cm and are 53 cm long. The two end disks, extending from 6 to 15 cm in radius, are placed on each side at  $|z| = 34.5$  cm and 46.5 cm. This design allows to obtain at least two points per track in the  $|\eta| < 2.2$  region for tracks originating within  $2\sigma_z$  from the central interaction point. The total number of channels is about 44 millions, organized in about 16000 modules of 52 columns and 80 rows. The active area is close to  $0.92 \text{ m}^2$ . The presence of high magnetic field causes a noticeable drift of the electrons (and a smaller drift for the holes) from the ionizing point along the track with a Lorentz angle of about 32 degrees. This leads to a charge sharing between pixels which, using an analog readout, can be exploited to considerably improve the resolution down to about  $10 \mu\text{m}$ . In the endcap the modules of the detector are arranged in a turbine-like shape with a tilt of 20 degrees, again in order to enhance charge sharing.

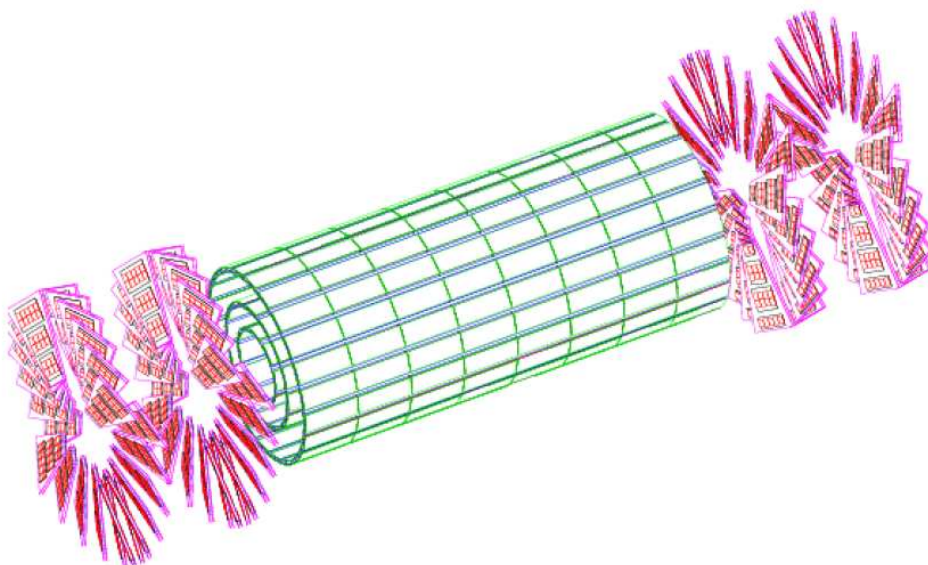


**Figure 4.6.** Three dimensional view of the silicon pixel detector of the CMS tracker.

The inner and outer tracker detector is shown in Figure 4.7. They are based on silicon  $p^+$  strips on a  $n$ -type bulk whose thickness is close to 300 and  $500 \mu\text{m}$  respectively in the inner and the outer tracker. In the barrel the strips are parallel to the beam axis while for the endcaps they follow a radial orientation. The inner tracker is made of four barrel layers, the two innermost are double sided and the endcaps count three disks each. The outer tracker consists of six layers in the barrel (the two innermost are double sided) while the endcaps are made of nine layers (the

first, the second and the fifth are double sided). On the whole, the silicon tracker is made of about 10 millions of channels for an active area close to 198 m<sup>2</sup>.

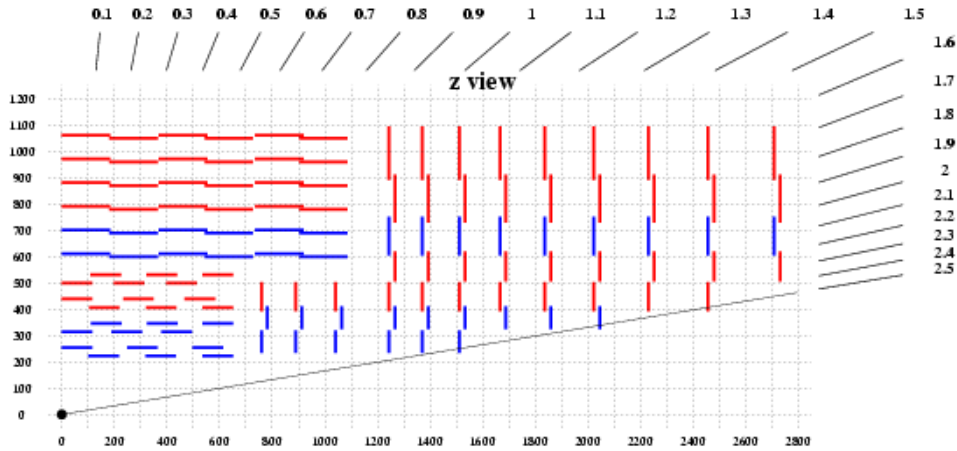


**Figure 4.7.** Schematic longitudinal view of a quarter of the tracker layout. Red lines represent single modules, blue lines double modules.

### 4.2.3 Electromagnetic calorimeter

A high performance electromagnetic calorimeter (ECAL) is a fundamental requirement for any general purpose LHC experiment, in order to have precise measurements of electrons and photons. The CMS collaboration has chosen a homogeneous calorimeter composed by segmented crystals of lead tungstate (PbWO<sub>4</sub>), which is a radiation resistant and chemically inert scintillator suited to work in the LHC high dose environment. A detailed description of the electromagnetic calorimeter will follow in Section 4.3.

### 4.2.4 Hadron calorimeter

The hadron calorimeter (HCAL) is used together with the electromagnetic one to measure the energy and direction of hadronic *jets* (coming from the fragmentation of quarks and gluons), the transverse energy and the imbalance of transverse energy. High hermeticity is required together with a material thickness which is sufficient to contain the whole hadron shower.

The CMS HCAL [48] is a sampling calorimeter made of 3.7 mm thick active layers of plastic scintillators alternated with 5 cm thick brass plate absorbers. The signal is readout with wavelength-shift fibres. The barrel granularity  $\Delta\eta \times \Delta\phi = 0.087 \times 0.087$ , matching a  $5 \times 5$  crystals ECAL tower, is fine enough to allow an efficient di-jet separation. The longitudinal view of HCAL is shown in Figure 4.8: the barrel ( $|\eta| < 1.4$ ) and the endcap ( $1.4 < |\eta| < 3.0$ ) with an overall thickness from 8.9 to 10 interaction lengths  $\lambda_0$  respectively. Since the barrel part of the calorimeter is not sufficiently thick to entirely contain the very high energy showers, an additional tail-catcher, composed of scintillators tiles, is placed outside the magnet.

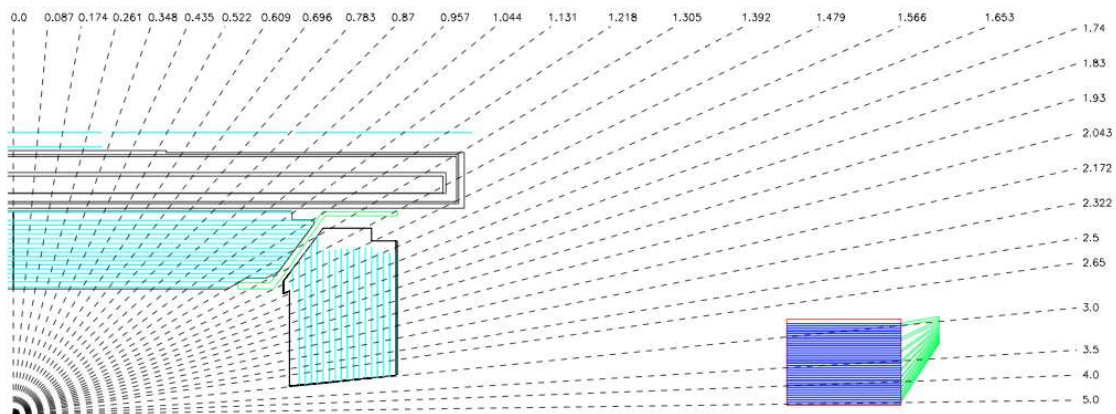


**Figure 4.8.** Longitudinal view of a quarter of CMS hadron calorimeter, divided into barrel and endcap HCAL. It is placed inside the magnetic coil, the outer barrel tail-catcher and the very forward calorimeter HF.

To improve the hermeticity, a very forward calorimeter (HF) is placed outside the magnet yoke,  $\pm 11$  m away along the beam direction from the nominal interaction point, covering from  $|\eta| = 3$  up to  $|\eta| = 5$ . Quartz fibers are used as active elements. They are placed in parallel to the beam pipe, interleaved into steel plate absorbers which constitute the passive material. With this configuration, the HCAL has an overall depth of more than  $11 \lambda_0$  over the entire coverage. The designed hadronic energy resolution combined with ECAL measurements is

$$\frac{\sigma(E)}{E} = \frac{100\%}{\sqrt{E [\text{GeV}]}} \oplus 4.5\% \quad (4.3)$$

The performances of the HF are:

$$\frac{\sigma(E)}{E} = \frac{182\%}{\sqrt{E [\text{GeV}]}} \oplus 9\%, \text{ for hadrons} \quad (4.4)$$

$$\frac{\sigma(E)}{E} = \frac{138\%}{\sqrt{E [\text{GeV}]}} \oplus 5\%, \text{ for electrons.} \quad (4.5)$$

#### 4.2.5 The muon system

The muon system [49] has three functions: muon identification, momentum measurement and triggering. Good muon momentum resolution and trigger capability are enabled by the high-field solenoidal magnet and its flux-return yoke. The latter also serves as a hadron absorber for the identification of muons. In the CMS experiment, the muon detectors are placed beyond the calorimeters and solenoid. Since the muon system consists of about  $25000 \text{ m}^2$  of detection planes, the muon chambers have to be inexpensive, reliable and robust.

A sketch of the muon system is shown in Figure 4.9. The barrel drift tube (DT) chambers cover the pseudorapidity region  $|\eta| < 1.2$  and are organized into four stations interspersed with the layers of the flux return plates. The number of chambers in each station and their orientation were chosen to provide good efficiency for linking together muon hits from different stations into a single muon track and

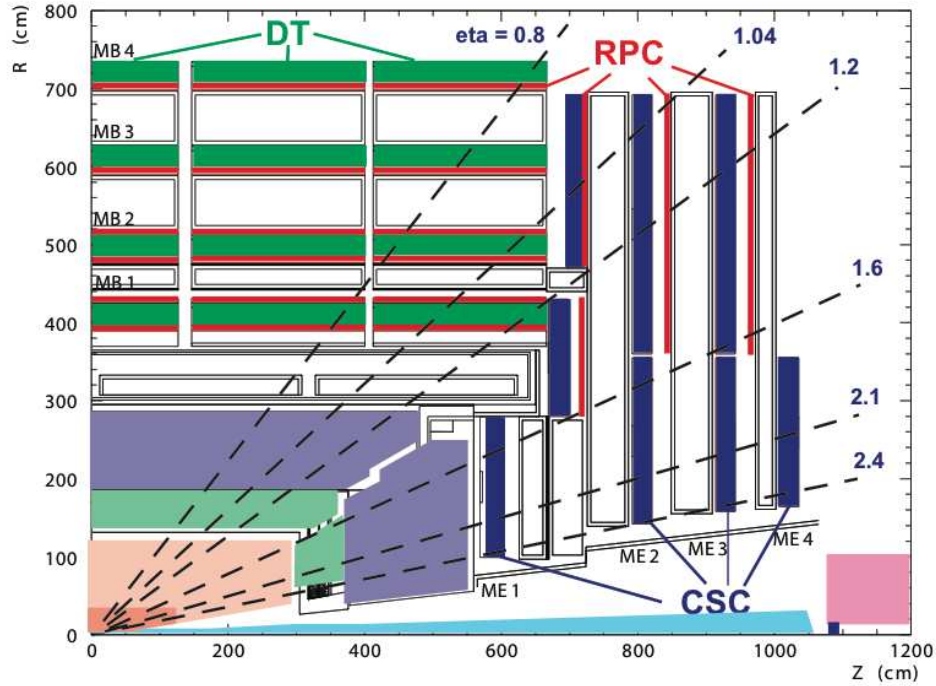


Figure 4.9. Layout of one quarter of the CMS muon system.

for rejecting background hits. In the two endcap regions of CMS, where muon rates and background levels are high and the magnetic field is large and non-uniform, the muon system uses cathode strip chambers (CSC). The CSCs identify muons between  $0.9 < |\eta| < 2.4$ . There are four stations of CSCs in each endcap, with chambers positioned perpendicular to the beam line and interspersed between the flux return plates. A crucial characteristic of the DT and CSC sub-systems is that they can each trigger on the transverse momentum of muons with good efficiency and high background rejection, independent of the rest of the detector.

Because of the uncertainty in the ability of the muon system to measure the correct beam-crossing time when the LHC reaches full luminosity, a complementary, dedicated trigger system consisting of resistive plate chambers (RPC) was added in both the barrel and endcap regions. The RPCs provide a fast, independent and highly-segmented trigger with a sharp threshold on transverse momentum over a large portion of the pseudorapidity range ( $|\eta| < 1.6$  for the first period of data taking) of the muon system. The RPCs are double-gap chambers, operated in avalanche mode to ensure good operation at high rates.

#### 4.2.6 The trigger system

At the nominal LHC luminosity the expected event rate is about  $10^9$  Hz; given the typical size of a raw event (about 1 MB) it is not possible to record all the information for all the events. Indeed, the event rate is largely dominated by soft  $p-p$  interactions with particles of low transverse momentum. The triggering system must have a large reduction factor and maintain at the same time a high efficiency on the potentially interesting events, reducing the rate down to about 100 Hz, which

is the maximum sustainable rate for storing events.

The trigger system consists of two main steps: a Level-1 Trigger (L1) and a High Level Trigger (HLT). The L1 consists of custom-designed, largely-programmable electronics, whereas the HLT is a software system implemented in a filter farm of about one thousand commercial processors. The rate reduction capability is designed to be a factor of  $10^7$  for the combined L1 and HLT.

### The Level-1 trigger

The Level-1 trigger [50] reduces the rate of selected events down to 50 (100) kHz for the low (high) luminosity running. The full data are stored in pipelines of processing elements, while waiting for the trigger decision. The L1 decision is about taking or discarding data from a particular bunch crossing has to be taken in  $3.2 \mu\text{s}$ ; if the L1 accepts the event, the data are moved to be processed by the HLT. To deal with the high bunch crossing rate, the L1 trigger has to take a decision in a time too short to read data from the whole detector, therefore it employs the calorimetric and muons information only, since the tracker algorithm are too slow for this purpose. The L1 trigger is organized into a Calorimeter Trigger and a Muon Trigger, whose informations are transferred to the Global Trigger which takes the accept-reject decision.

The Calorimeter Trigger is based on trigger towers,  $5 \times 5$  matrices of ECAL crystals, which match the granularity of the HCAL towers. The trigger towers are grouped in calorimetric regions of  $4 \times 4$  trigger towers. The Calorimeter Trigger identifies, from the calorimetric region information, the best four candidates of each of the following classes: electrons and photons, central jets, forward jets and  $\tau$ -jets identified from the shape of the deposited energy. The information of these objects is passed to the Global Trigger, together with the measured missing transverse energy. The Muon Trigger is performed separately for each muon detector. The information is then merged and the best four muon candidates are transferred to the Global Trigger.

The Global Trigger takes the accept-reject decision exploiting both the characteristic of the single objects and of combination of them.

### The High Level Trigger

The HLT [51] reduces the output rate down to around 100 Hz. The idea of the HLT trigger software is the regional reconstruction on demand, that is only those objects in the useful regions are reconstructed and the uninteresting events are rejected as soon as possible. This leads to the development of three “virtual trigger” levels: at the first level only the full information of the muon system and of the calorimetry is used, in the second level the information of the tracker pixels is added and in the third and final level the full event information is available.

#### 4.2.7 CMS software components

The goals of the CMS software are to process end select events inside the HLT farm, to deliver the processed results to the experimenters within the CMS collaboration and to provide tools them to analyze the processed information in order to produce physics results. The overall collection of software, now referred as CMSSW [52], is

built around a *Framework, an Event Data Model, Services* needed by the simulation, calibration and alignment and reconstruction models that process event data so that physicists can perform analysis. The physics and utility modules are written by detector groups. The modules can be plugged into the application framework at run time, independently of the computing environment. The software should be developed keeping in mind not only performance but also modularity, flexibility, maintainability, quality assurance and documentation. CMS has adopted an object-oriented development methodology, based primarily on the C++ programming language.

The primary goal of the CMS Framework and Event Data Model (EDM) is to facilitate the development and deployment of reconstruction and analysis software. The EDM is centered around the Event. It holds all data that was taken during a triggered physics event as well as all data derived from the data taking (e.g. calibration and alignment constants).

The detailed CMS detector and physics simulation is currently based on GEANT 4 [53] simulation toolkit and the CMS object-oriented framework and event model. The simulation is implemented for all CMS detectors in both the central and forward region, including the field map from the 3.8 T solenoid. In addition, several test-beam prototypes and layouts have been simulated. The full simulation program implements the sensitive detector behavior, track selection mechanism, hit collection and digitization (i.e. detector response). The detailed simulation workflow is as follows:

- a physics group configures an appropriate Monte Carlo event generator (several are used) to produce the data samples of interest;
- the production team/system runs the generator software to produce generator event data files;
- the physics group validates the generator data samples and selects a configuration for the GEANT 4-based simulation of CMS, with generator events as input, to produce (using the standard CMS framework) persistent hits in the detectors;
- the physics group validates these hit data which are then used as input to the subsequent digitization step, allowing for pile-up to be included. This step converts hits into digitizations (also known as *digis*) which correspond to the output of the CMS electronics.

As mentioned above, the full simulation relies on the GEANT 4 toolkit. GEANT 4 provides a rich set of physics processes describing electromagnetic and hadronic interactions in detail. It also provides tools for modeling the full CMS detector and geometry and the interfaces required for retrieving information from particle tracking through these detectors and the magnetic field. The validation of GEANT 4 in the context of CMS is described in detail in [54]. The CMS GEANT 4-based simulation program uses the standard CMS software framework and utilities, as used by the reconstruction programs.

The digitization step, following the hit creation step, constitutes the simulation of the electronic readout used to acquire data by the detector. It starts from the hit positions and simulated energy losses in the detectors and produces an output

that needs to be as close as possible to real data coming from CMS. Information from the generation stage (e.g. particle type and momentum) is preserved in the digitization step.

### 4.3 The electromagnetic calorimeter

The CMS ECAL [55] is the sub-detector devoted to a very precise reconstruction of high momentum photons and electrons. The benchmark which has been used to set the design and the performance of the ECAL is the search of the Higgs boson in the di-photon decay channel  $H \rightarrow \gamma\gamma$ . Moreover, the ECAL plays a fundamental role also in the searches for physics beyond the SM, where it is very usual to find final states with photons or electrons.

ECAL design aims at achieving an excellent di-photon mass resolution, expressed as

$$\frac{\sigma_m}{m} = \frac{1}{2} \left( \frac{\sigma_{E_1}}{E_1} \oplus \frac{\sigma_{E_2}}{E_2} \oplus \frac{\sigma_\theta}{\tan(\theta/2)} \right) \quad (4.6)$$

where  $E_{1,2}$  are the energies of the two photons and  $\theta$  represents the angular separation between the two photons. In order to maximize the reconstruction performance, excellent energy and angular resolution are required.

A fine segmented, homogeneous crystal calorimeter guarantees an optimal resolution on energy measurement and a precise determination of the decay angle. The CMS collaboration opted for a hermetic, homogeneous electromagnetic calorimeter built out of 75848 lead tungstate ( $\text{PbWO}_4$ ) crystals. In this section a detailed description of the CMS ECAL will be provided.

#### 4.3.1 Lead tungstate crystals

The main properties of  $\text{PbWO}_4$  are listed in Table 4.3 The choice of  $\text{PbWO}_4$  is

Parameter	Value
Density [ $\text{g}/\text{cm}^3$ ]	8.28
Radiation Length [cm]	0.89
Molière Radius [cm]	2.2
Emission peak [nm]	420
$1/\text{LY} \times d(\text{LY})/dT$ at $T=20^\circ\text{C}$ [%/°C]	-2
LY relative to NaI(Tl) [%]	1.3
Scintillation light decay time [ns]	5-15

**Table 4.3.** Main properties of  $\text{PbWO}_4$ .

motivated by its short radiation length  $X_0$  (0.89 cm) and its small Molière radius (2.19 cm). This allows the calorimeter to be sufficiently compact to be inserted inside the magnet coil and very fine-grained to have a good  $\pi^0 - \gamma$  separation, to reduce the effect of multiple collisions and to obtain an excellent angular resolution.

Another important characteristic of  $\text{PbWO}_4$  is that it is a radiation resistant and chemically inert scintillator, suited to work in the LHC high dose environment

(from 0.18 Gy/h at  $|\eta| = 0$  to 6.5 Gy/h at  $|\eta| = 2.6$  at high luminosity). It also has a short scintillation decay time (around 10 nanoseconds) that allows to collect 85% of the light in the 25 ns interval between consecutive  $p - p$  collisions.

The main disadvantage of the  $\text{PbWO}_4$  is the very low light yield, about two orders of magnitude less than the other scintillators commonly used in particle physics experiments (such as NaI). In fact, the scintillation mechanism of  $\text{PbWO}_4$  is strongly limited by the thermal quenching. Also the short decay time and the strong light yield dependence on the temperature ( $-2\%/^{\circ}\text{C}$  at room temperature) can be explained with the thermal quenching. To overcome this difficulties, a new photodetector has been developed: the Avalanche Photo Diode (APD). In addition to this, a very complex cooling system has been designed in order to stabilize the system temperature. These devices will be described later in the text.

Figure 4.10 shows the emission spectrum and transmission of  $\text{PbWO}_4$  [56]. As already stated, an emission peak is found in the region around 420 nm. The improvement on  $\text{PbWO}_4$  crystal radiation resistance (one of the most critical issues at the LHC) has required a strong effort. The environment for the CMS ECAL is very hostile,

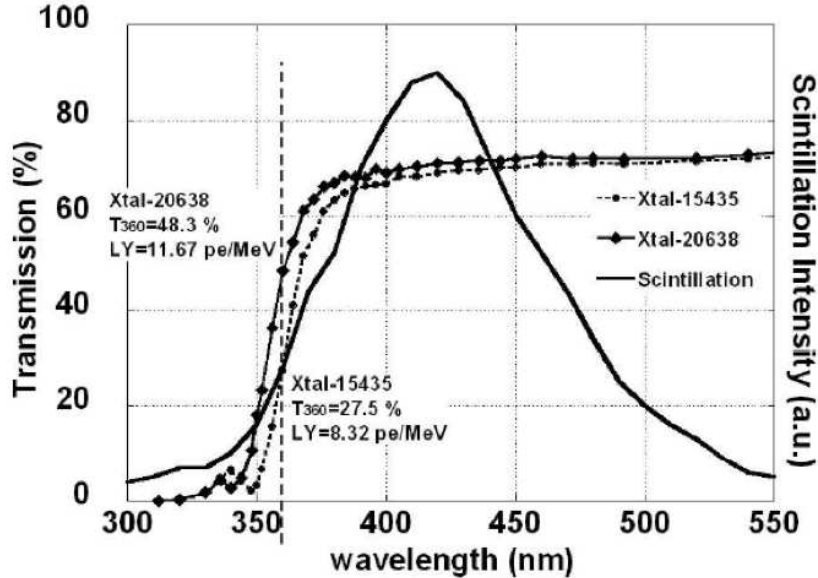


Figure 4.10. Emission spectrum and transmission of  $\text{PbWO}_4$  crystals.

since the maximum expected doses rate for the electromagnetic radiation at high luminosity are:

- around 0.25 Gy/h in the ECAL barrel region;
- around 0.30 Gy/h in the junctions between barrel and endcap;
- around 15 Gy/h  $|\eta| = 3.0$ .

The neutron flux in the ECAL barrel is expected to reach  $2 \times 10^{13}$  neutrons/cm<sup>2</sup> (around  $10^{15}$  in the ECAL endcaps) in 10 years of running at LHC. However, no damage by neutron irradiation has been seen so far. Moreover, it has been shown that the scintillation mechanism is not damaged, nor the scintillation emission spectrum changed.

On the other hand, the crystal transparency is largely affected by ionizing radiation. The decrease in light output is caused by radiation-induced absorption, i.e. by the formation of color centers which reduce the crystal transparency. Stoichiometric fine tuning, doping and optimized growth conditions have improved the radiation hardness and the light transmission of the crystals. The ECAL  $\text{PbWO}_4$  crystals show a light yield loss which is, at saturation, on average less than 3% if irradiated with photons at 0.15 Gy/h. The transmission loss due to irradiation can be monitored using a light injection system which allows to apply corrections for this effect.

Detailed studies on  $\text{PbWO}_4$  properties have also succeeded in reducing light collection non-uniformity (by depolishing and shading) below the limit of 0.35%/ $X_0$ .

### 4.3.2 Mechanical design

The CMS ECAL consists of a central part (barrel) and two caps (endcaps) to ensure hermeticity. A three dimensional representation of ECAL is shown in Figure 4.11. The principal design requirements are driven by the necessity of accurate measurement of electrons, photons and missing energy. The engineering design aims in particular at minimizing the amount of material in front of the calorimeter, optimizing the interface with the tracking system, ensuring an accurate hermeticity by minimizing the gaps between adjacent crystal or in the barrel-endcap transition regions and stabilizing the crystal temperature within a tenth of a degree.

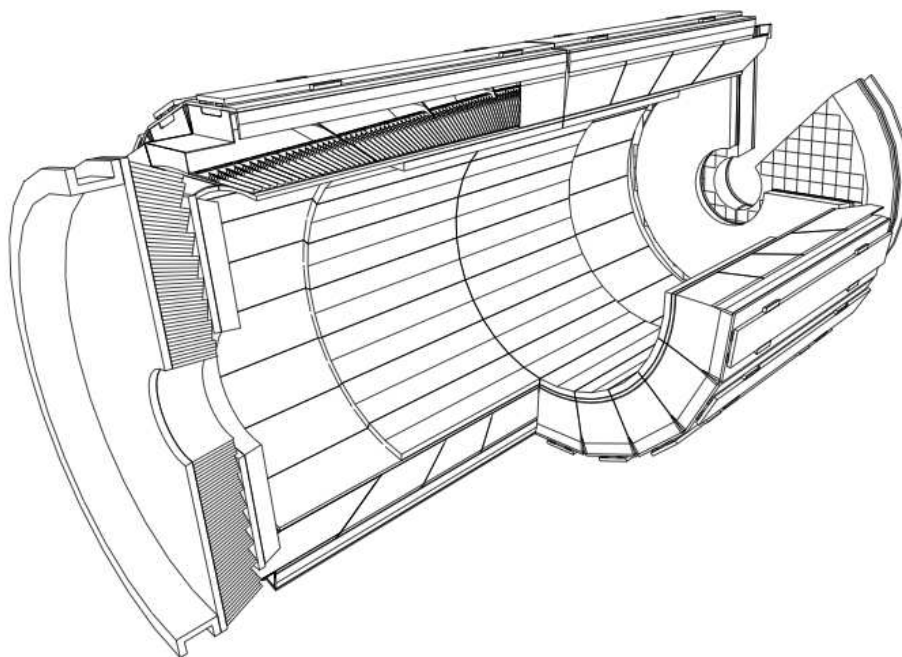


**Figure 4.11.** A three dimensional view of ECAL.

Figure 4.12 shows the longitudinal section of a quarter of the CMS ECAL. The barrel region covers a pseudorapidity range up to  $|\eta| < 1.479$ . It consists of  $2 \times 18$  supermodules each of which contains 20 crystals in  $\phi$  and 85 crystals in  $\eta$ . In both detector halves in  $\eta$ , each supermodule is divided into four support structures called

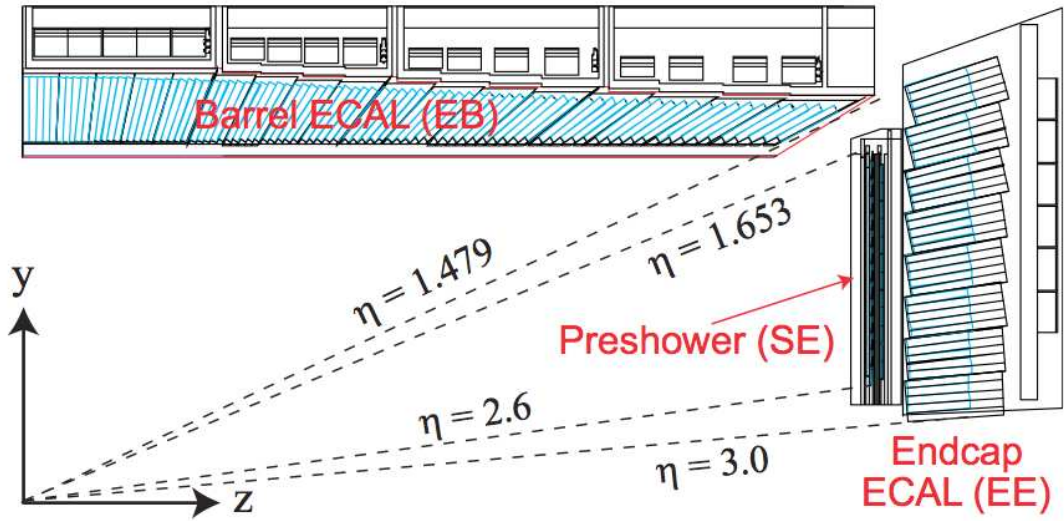


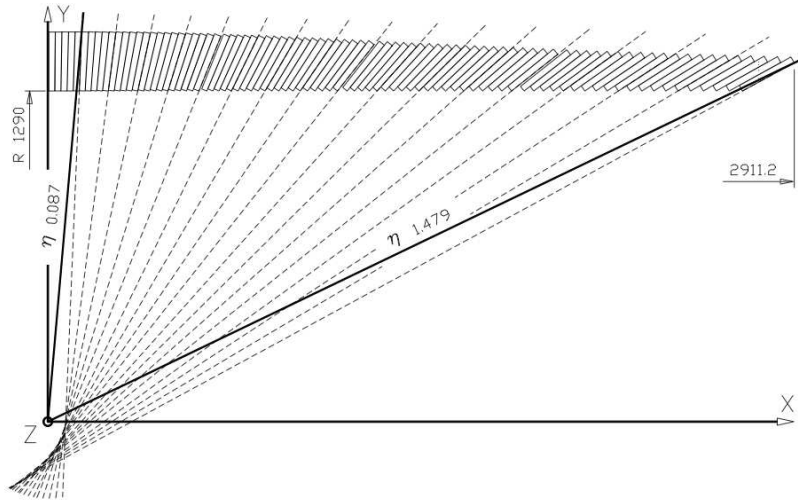
Figure 4.12. Longitudinal view of a quarter of ECAL.

modules. There are 17 different crystal types in the barrel: each crystal has a length of 230 mm, corresponding to 25.8 radiation lengths, and a front face area close to  $22 \times 22 \text{ mm}^2$ . The resulting granularity of ECAL is of  $\Delta\eta \times \Delta\phi = 0.0175 \times 0.0175$ . The crystals are tapered and their longitudinal axes have a constant off-point angle of  $3\text{a}$  with respect to the nominal vertex position in both  $\eta$  and  $\phi$  (Figure 4.13). This particular configuration increases the hermeticity of the structure since it avoids gaps that are pointing to the interaction region. The resulting ECAL geometry is referred as *quasi-projective*.

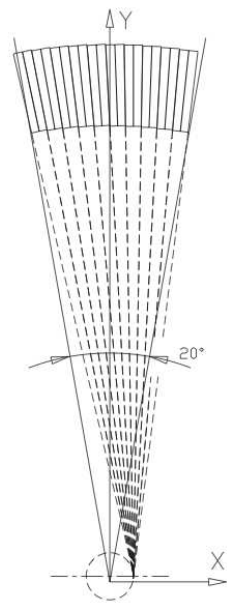
The ECAL endcaps provides accurate energy measurement in the pseudorapidity range from  $|\eta| > 1.48$  up to  $|\eta| < 2.6$ . In order to further increase ECAL hermeticity, crystals are installed up to  $|\eta| < 3$ . Endcap crystals are grouped in  $5 \times 5$  matrices of crystals with the same shape and dimension ( $2.6 \times 2.6 \times 22 \text{ cm}^3$ ). These matrices are called *super-crystals*. Endcap crystals are shorter than the barrel ones due to the presence of a  $3X_0$  thick preshower detector placed in front of the calorimeter.

### 4.3.3 Photodetectors

Because of the relatively low light yield of  $\text{PbWO}_4$ , photodetectors with intrinsic amplification are needed. In addition, they have to be fast, resistant to radiation and able to operate in a strong magnetic field. In the barrel region, these requirements are satisfied by avalanche photodiodes (APDs). In the endcaps the radiation levels are expected to be much higher than in the barrel. In particular, the expected neutron flux is too large for APDs. For this reason, the CMS collaboration has chosen to use vacuum phototriodes (VPTs) in the endcap regions, profiting from the favorable orientation of the magnetic field with respect to the photodetector axis ( $8.5\text{a} < \theta < 25.5\text{a}$ ). A brief description of these photodetectors will follow in the next sections.



(a)



(b)

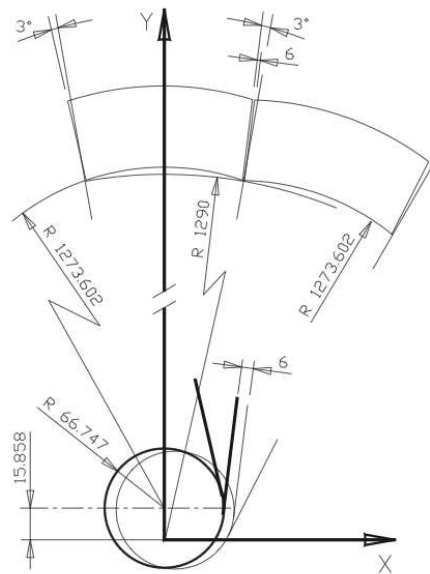


**Figure 4.13.** Crystal tilt in a)  $\eta$  and b)  $\phi$ .

### Avalanche photodiodes

The principle of operation of the APD is shown in Figure 4.14. The primary photon generates a photoelectron which is accelerated in an electric field, thus producing an avalanche of secondary electrons. Two APDs are integrated and connected in parallel within a capsule, which provides an active area per crystal of  $2 \times 25 \text{ mm}^2$ .

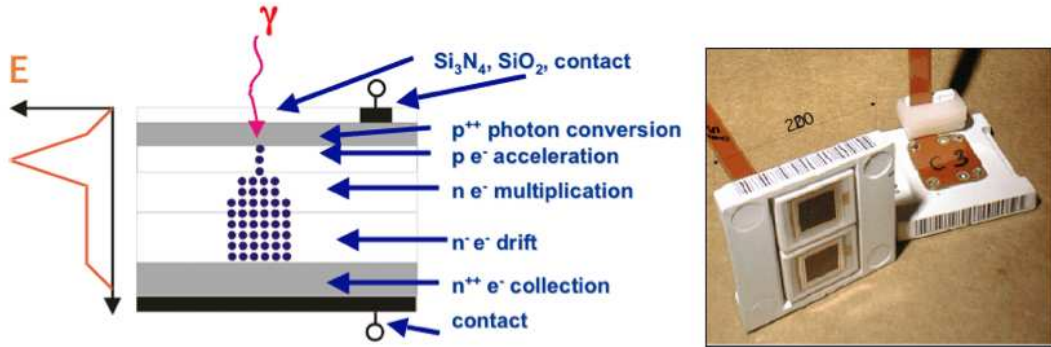


**Figure 4.14.** Principle of operation of an APD (left) and two APDs per capsule (right).

The photo-detection devices has a large impact on the calorimeter performances, since they contribute to the terms of the energy resolution. The poissonian nature of the multiplication process, the sensitivity of the gain on voltage and temperature and the leakage currents flowing through the device affect the ECAL performances on energy resolution. Damages caused by radiation can increase the leakage currents. The main damage comes from the neutrons which create defects in the silicon lattice. Gain seems to be not affected up to absorbed fluxes of  $10^{13} \text{ n/cm}^2$ , while the leakage current increases linearly with the flux up to values of  $\sim 10 \mu\text{A}$ , for the maximum dose expected.

Another issue is the sensitivity to traversing radiation. In the APDs, this effect is minimized by the amplification that occurs just behind the photo-conversion layer. This means that only the energy deposited in this  $5 \mu\text{m}$  thin layer is amplified while signal from ionizing particle traversing the bulk of the silicon is not amplified.

More detailed description of the APDs can be found in [57].

### Vacuum phototriodes

A VPT is a device that is able to work in an axial or quasi-axial magnetic field. A typical VPT is shown in Figure 4.15

Photoelectrons are generated on the photocathode and part of them passes through the anode mesh and impacts on the dynode where the secondary electron cascade arises. The secondary electrons are attracted back to the anode mesh which captures a large fraction of them. The quantum efficiency of these devices for the  $\text{PbWO}_4$  peak wavelength is about 15% and their sensitive area is of  $300 \text{ mm}^2$ . Thus the total light collection efficiency is of the same order of the APDs. This device is less sensitive to the temperature than the APD ( $< 0.1\%/^{\circ}\text{C}$ ) and it is very insensitive to the variations of bias voltage ( $< 0.1\%/V$ ). In addition, VPTs have a low capacitance (few pF) and a leakage current  $< 2 \text{ nA}$ .

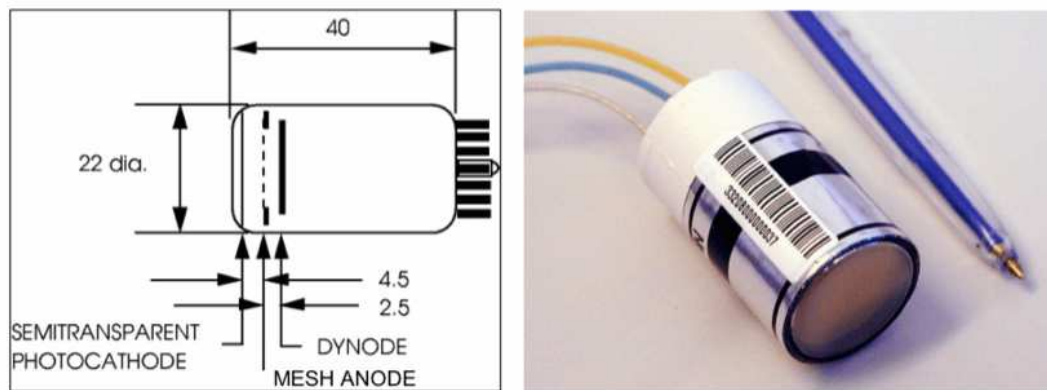


Figure 4.15. Schematics and view of a VPT.

Particular attention was posed in order to obtain photodetectors with a uniform response for different radiation rates and conditions: it is shown that the anode response is independent on the radiation dose and the neutron flux [58].

#### 4.3.4 Electronics chain

The objectives for the front-end electronics are extremely challenging. The electronics must be extremely fast in order to match the 25 ns LHC crossing rate and it must provide a very precise energy measurement on a dynamic range as large as  $\sim 95$  dB (50 MeV - 1.5 TeV). The noise has to be kept below 50 MeV per crystal in the barrel region. In addition, since it is placed on the detector, the front-end electronics must be radiation-hard and reliable.

A sketch of the electronic scheme is presented in Figure 4.16 [59]. The crystals

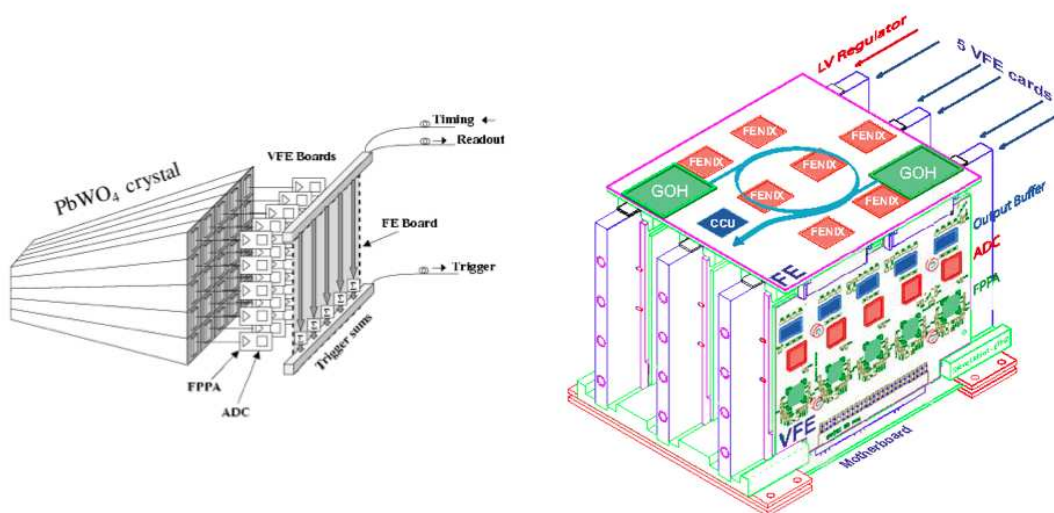


Figure 4.16. Schematic view of the ECAL readout electronics for  $5 \times 5$  crystals (left) and the arrangement of the front-end electronics into VFE and FE boards (right).

are organized in  $5 \times 5$  matrices of crystals, forming a so-called trigger tower. The

small electrical signals coming from each photodetector are sent to a motherboard, housing five Very Front End (VFE) cards and a Low Voltage Regulator (LVR) card [60], which distributes regulated voltages to the VFE cards. The motherboard is also used to filter and distribute high voltage to the photodetectors. The output of the five VFE cards is feed into the Front End (FE) card which processes the digitized data of one trigger tower.

Each VFE card houses five identical electronics channels. A channel consists of three different Application Specific Integrated Circuits (ASICs), a multi gain pre amplifier (MGPA), an ADC and a buffer, all designed in radiation tolerant  $0.25 \mu\text{m}$  technology. In addition, a Detector Control Unit (DCU), measuring the APD leakage currents and the crystal temperature, is implemented in each VFE card. The FE board stores and processes the digitized data from VFE cards during the L1 trigger latency. The trigger data are then transmitted to the off-detector electronics through a serial digital data link operating at 800 Mb/s, which is sufficient to complete the transfer of trigger data every 25 ns. For every L1 accept, ten time-slices of data are transmitted off the detector in  $7.5 \mu\text{s}$ . This system uses a digital optical link system, controlled b the off-detector front-end control boards.

### 4.3.5 Amplitude and time reconstruction

The raw data for a single channel consists of a series of consecutive digitization of the signal making up a time frame. The number of samples is adjustable ( $2+4n$ ) with a default of 10. The digitizations are made at the bunch crossing frequency of 40 MHz, i.e. one sample each 25 ns. In addition, the timing of the signal is adjusted in LHC running so that the signal pulse maximum corresponds to one of the samplings. Figure 4.17 shows an example of the time sampling for a signal pulse as a function of the time difference ( $T - T_{max}$ ), where  $T$  and  $T_{max}$  indicate the time of the generic ADC sample and the time corresponding to the maximum of the pulse shape respectively.

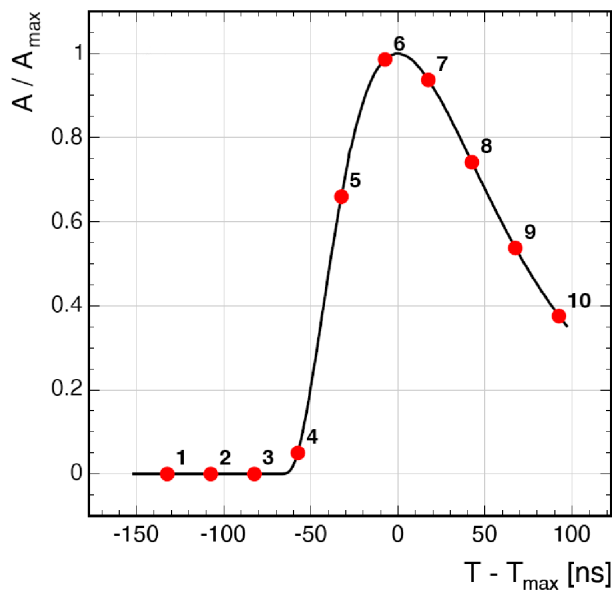


**Figure 4.17.** Pulse shape measured in the ECAL as a function of  $(T - T_{max})$ .

The simplest method of reconstructing the amplitude of the channel is to take the sampling on the maximum as the measurement of the signal. However, a larger number of samples is preferred since it allows more sophisticated digital processing of the signal to reduce noise contribution. The other reason is to enable the identification of pile-up events from other bunch crossing.

The signal amplitude is computed as a linear combination of discrete time samples:

$$\mathcal{A} = \sum_{i=0}^N w_i \times S_i \quad (4.7)$$

where  $w_i$  are the weights,  $S_i$  the time sample values in ADC counts and  $N$  is the number of samples used in the filtering. The weights are determined to minimize the noise contribution.

Amplitude and time measurement are strongly correlated. After a signal has been amplified and shaped by the front-end electronics, the channel timing reconstruction consists in a precise measurement of the time the pulse reaches its maximum values  $A_{max}$ . Looking at Figure 4.17, the reconstructed time of a channel corresponds to the value of  $T_{max}$ . The algorithm used to determine the time of the ECAL channels will be described in Section 5.2.1.

### 4.3.6 Energy resolution

The energy resolution of a homogeneous calorimeter can be expressed as a sum in quadrature of three different terms

$$\frac{\sigma_E}{E} = \frac{a}{\sqrt{E}} \oplus \frac{b}{E} \oplus c \quad (4.8)$$

where  $E$  is the energy expressed in GeV and  $a$ ,  $b$  and  $c$  represent the *stochastic*, *noise* and *constant* term respectively. Different effects contribute to the different terms in Equation 4.8:

- the stochastic term  $a$  is a direct consequence of the poissonian statistics associated with the development of the electromagnetic shower in the calorimeter and the successive recollection of the scintillation light. This term represents the intrinsic resolution of an ideal calorimeter with infinite size and no response deterioration due to instrumental effects. The original energy  $E_0$  of a particle detected by a calorimeter is linearly related to the total track length  $T_0$ , defined as the sum of all the ionization tracks produced by all the charged particles in the electromagnetic shower. Since  $T_0$  is proportional to the number of track segments in the shower and the shower development is a stochastic process, the intrinsic resolution from purely statistical arguments is given by

$$\frac{\sigma_E}{E} \propto \frac{\sqrt{T_0}}{T_0} \propto \frac{1}{\sqrt{E_0}} \quad (4.9)$$

For a real calorimeter, this term also absorbs the effects related to the shower containment and the statistical fluctuations in the scintillation light recollection;

- the noise term accounts for all the effects that can alter the measurements of the energy deposit independently of the energy itself. It includes the electronic noise and the physical noise due to energy released by particles coming from multiple collision events. Electronic noise is mainly caused by the photodetectors, that contribute basically via two components: one is proportional to its capacitance, the other is connected to the fluctuations of the leakage current;
- the constant term dominates at high energy. Many different effects contribute to this term: the stability of the operating conditions such as the temperature and the high voltage of the photodetectors; the electromagnetic shower containment and the presence of the dead material; the light collection uniformity along the crystal axis; the radiation damage of  $\text{PbWO}_4$  crystals; the intercalibration between the different channels.

The design goal for the CMS ECAL are about 2.7% for  $a$ , (0.12) 0.20 GeV when adding the signal of  $(3 \times 3)$   $5 \times 5$  crystals for  $b$  and 0.5% for  $c$ . Measurements conducted on the ECAL barrel with electron test beam at CERN [61][62][63] show that ECAL perform consistently with the design goals of the experiment.

Using the first  $\sim 100 \text{ nb}^{-1}$  collected with the CMS detector in 2010 at a center of mass energy of 7 TeV, studies of the CMS ECAL calibration methods and procedures are carried out. The achieved calibration precision in the central barrel ( $|\eta| < 0.8$ ) with the sample size available is 1.15% [64], in good agreement with the expectation from Monte Carlo studies.

## 4.4 Photon reconstruction

The last part of the chapter is devoted to the description of the photon reconstruction technique. Photon showers deposit their energy in several crystals in the ECAL. A collection of adjacent ECAL crystals which is used to reconstruct the energy and the direction of a particle is commonly referred as *cluster*. Approximately 94% of the incident energy of a single photon is contained in  $3 \times 3$  cluster and 97% in  $5 \times 5$  cluster. Summing the energy measured in such fixed arrays gives the best reconstruction performance for unconverted photons.

However, the presence of material in front of the calorimeter results in bremsstrahlung and photon conversions. Furthermore, because of the strong magnetic field, the energy reaching the calorimeter is spread in  $\phi$ . Due to these effects, dynamic cluster algorithms are necessary in order to recover the entire energy of the incoming photon. Although different cluster algorithms [65] are used in the CMSSW framework, only the Hybrid algorithm will be discussed in this context.

### 4.4.1 Hybrid algorithm

The Hybrid algorithm attempts to use the  $\eta - \phi$  geometry of the barrel crystals to exploit the knowledge of the lateral shower shape in the  $\eta$  direction, while searching dynamically for separate energy in the  $\phi$  direction. The basic principles of Hybrid algorithm are shown in Figure 4.18. Starting from a crystal with transverse energy  $E_T > E_T^{hyb}$ ,  $1_\phi \times 3_\eta$  crystal dominoes are made, each with the central crystal aligned in  $\eta$  with the seed crystal. If the energy of the central crystal of a domino exceeds a

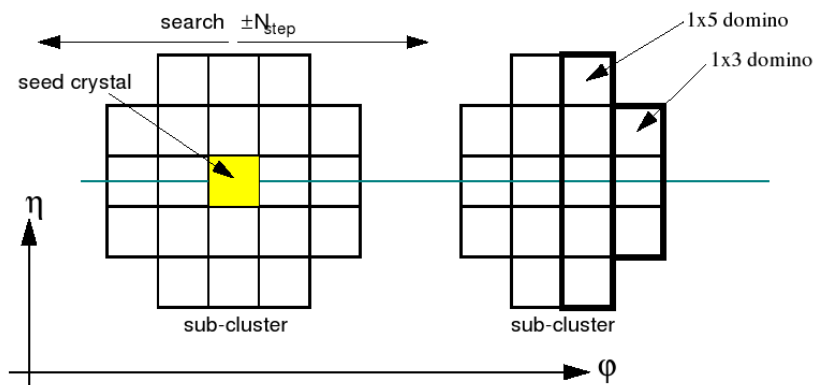


Figure 4.18. Basic principles of Hybrid algorithm.

certain threshold  $E_{wing}$ ,  $1 \times 5$  domino (instead of  $1 \times 3$ ) is used. The same procedure is repeated  $N_{step}$  times, in both the  $\phi$  directions from the original seed. Once  $\eta - \phi$  scan is finished, dominoes with  $E < E_{th}$  are removed and the cluster is completed. To distinguish a new, disconnected subcluster, a central domino with  $E > E_{seed}$  is required. The parameter values used in the standard reconstruction procedure are listed in Table 4.4 When all the clusters in the event have been reconstructed, they

$E_T^{hyb}$	1 GeV
$N_{step}$	10
$E_{wing}$	1 GeV
$E_{th}$	0.1 GeV
$E_{seed}$	0.35 GeV

Table 4.4. Parameter values used in the standard reconstruction procedure.

are grouped, according to specific rules, to form a so-called *supercluster*. The most energetic cluster is identified and all the other clusters inside a fixed  $\eta - \phi$  region are associated with it. The search region is much larger along  $\phi$  because it is the direction along which all the charged particles inside the electromagnetic shower are bent, due to the effect of the magnetic field. A schematic view of supercluster reconstruction algorithm is shown in Figure 4.19.

#### 4.4.2 Energy corrections

The simplest way to reconstruct the total energy of a photon is to sum up the contributes from all the crystals that form a (super)cluster. There are some sources of variation in the clustered energy for which corrections can be made:

- the fraction of energy in a fixed array varies as a function of the shower position with respect to the cluster boundary. This effect is known as a variation of “local containment”;
- large losses due to rear leakage can be encountered for shower close to the barrel inter-module and inter-supermodule borders. At these borders there

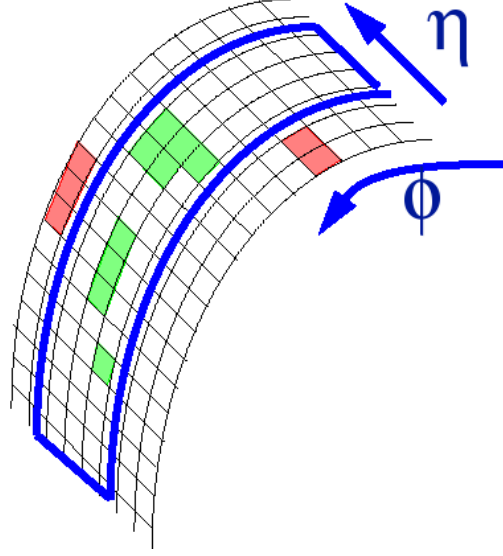


**Figure 4.19.** Schematic view of supercluster reconstruction algorithm.

are cracks containing negligible material that cause a considerable reduction of the effective depth of the ECAL;

- the spread of energy due to showering in the tracker material and the behavior of the supercluster algorithms;
- for photons,  $e^+ - e^-$  conversions.

The overall impact of these effects on the reconstructed energy can be estimated with high accuracy and simple corrections can be applied during the reconstruction step.

#### 4.4.3 Position measurement

The measurement of the shower position [65] can be obtained by calculating the energy weighted mean position of the crystals in the cluster. Because of the ECAL quasi-projective geometry, the lateral position of the crystal axis depends on the depth, which can be parametrized as  $A[B + \log(E)]$ , where  $E$  represents the energy and  $A$ ,  $B$  are two parameters that depend on the nature of the incoming particle. The dependence of the lateral position of the crystal axis on depth is illustrated in Figure 4.20.

Since the energy density decreases almost exponentially with the lateral distance from the shower core, an unbiased estimate of cluster position can be obtained by taking a weighted mean calculated using the logarithm of the crystal energy [66]:

$$x = \frac{\sum x_i \cdot W_i}{\sum W_i} \quad (4.10)$$

where  $x_i$  is the position of  $i$ -th crystal and  $W_i$  is the logarithmic weight defined as

$$W_i = \max \left[ W_0 + \log \left( \frac{E_i}{\sum E_j} \right); 0 \right] \quad (4.11)$$

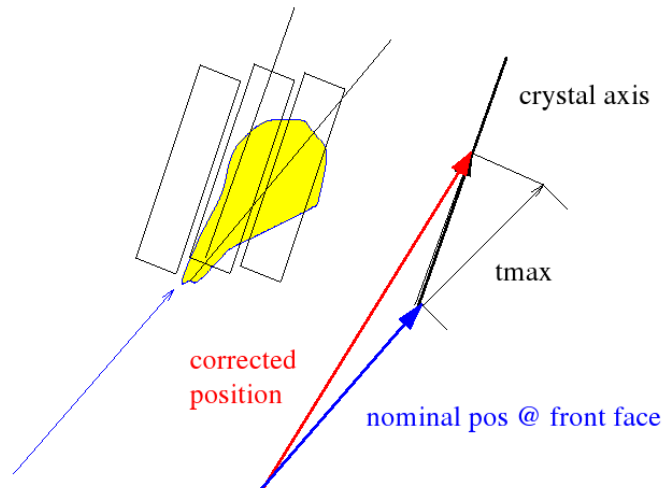


**Figure 4.20.** Dependence of the lateral position of the crystal axis on the depth.

The parameter  $W_0$  controls the smallest fractional energy that a crystal can have to contribute to the position measurement. Its default value, obtained after optimization studies, is 4.2 which means that crystals containing more than 1.5% of the cluster energy contribute to position measurement.

The position of a supercluster is calculated by making the energy-weighted mean of positions of its component clusters.



## Chapter 5

# Determination of long-lived particle lifetime

There are many physics scenarios beyond the SM which predict the existence of massive long-lived particles. This study will be focused on long-lived and electrically neutral particles decaying into photons. The main phenomenological feature of these models is that the photons will not originate from the interaction point and are hence referred to as “off-pointing” (OP). For this reason, OP photons provide a clear signature for long-lived decays and give a strong indication of new physics scenarios. The information from the CMS ECAL, namely the reconstructed photon time measurement and the shape of the energy deposit, will be used in this study in order to select OP photons. In fact, the ECAL provides an excellent resolution for time measurement and also offers a very fine lateral granularity allowing for detailed studies on the geometry of the energy deposits, which will be used for OP photon selection. Once OP photons are identified, an algorithm to extract the lifetime of long-lived particles decaying into photons is presented.

This thesis will focus on the GMSB model, where the neutralino  $\tilde{\chi}_1^0$  plays the role of NLSP and decays into a gravitino plus a high energy photon ( $\tilde{\chi}_1^0 \rightarrow \tilde{G}\gamma$ ). In this model the neutralino lifetime is free to be non-zero, producing OP photons.

The chapter is organized as follows:

- Section 5.1 introduces the event samples used in this study;
- Section 5.2 is devoted to the description of the selection criteria for OP photons based on ECAL time measurement and the shape of the energy deposits;
- Section 5.3 details a cluster shape-based algorithm to reject photon conversion;
- Section 5.4 describes the algorithm used to reconstruct the flight path of the long-lived particles.

### 5.1 Event samples

The generation of the GMSB event samples is performed in two different steps. In the first step, the software ISAJET (version 7.80) [67] is used to generate the “SUSY Les Houches Accord” (SLHA) spectrum [68] containing supersymmetric model parameters, masses of SUSY particles, couplings and branching ratio. After this step,

SLHA spectra are used as input to PYTHIA [69], which calculates cross sections and perform quark showering and hadronization.

The GMSB datasets used for this study follows SPS 8 model line, whose parameters are listed in Table 3.2. The SUSY breaking scaling parameter  $\Lambda$ , which is left free in the SPS 8 line, is set to  $\Lambda = 100$  TeV. This choice set the neutralino mass to be  $M_{\tilde{\chi}_1^0} = 139.3$  GeV. The value of  $\Lambda$  chosen for this study corresponds to the benchmark scenario for GMSB model, agreeded at the 2001 ‘‘Snowmass Workshop on the Future of Particle Physics’’.

As stated in Section 3.3, the choice of GMSB SPS 8 line ensures that the lightest neutralino  $\tilde{\chi}_1^0$  plays the role of NLSP. In addition, the branching ratio for the decay channel  $\tilde{\chi}_1^0 \rightarrow \tilde{G}\gamma$  is very close to 100%. The process studied at the LHC is:

$$p + p \rightarrow 2 \text{ decay chains} \rightarrow 2\tilde{\chi}_1^0 + X \rightarrow 2\tilde{G} + 2\gamma + X \quad (5.1)$$

Figure 5.1 shows the distribution of the number of photons from neutralino decays in each event, at the generator level. As expected, there are two photons in the largest fraction of the events (around 90%).

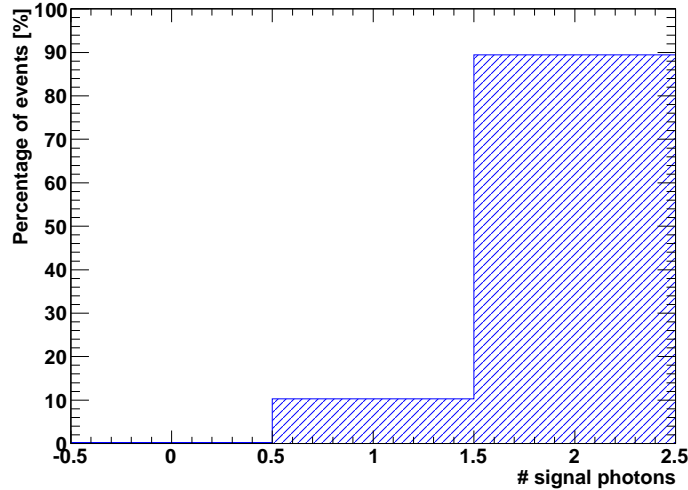


**Figure 5.1.** Number of photons from neutralino decays at the generator level.

In order to investigate scenarios with different values of neutralino lifetime, four signal datasets of around 50K events each have been generated assuming different values of the  $C_{grav}$  parameter. This parameter sets both the neutralino lifetime and the gravitino mass:

- $C_{grav} = 46.7$  for  $c\tau \simeq 250$  mm and  $m_{\tilde{G}} \simeq 0.224$  keV;
- $C_{grav} = 66.1$  for  $c\tau \simeq 500$  mm and  $m_{\tilde{G}} \simeq 0.317$  keV;
- $C_{grav} = 93.5$  for  $c\tau \simeq 1000$  mm, and  $m_{\tilde{G}} \simeq 0.448$  keV;
- $C_{grav} = 132.2$  for  $c\tau \simeq 2000$  mm and  $m_{\tilde{G}} \simeq 0.634$  keV.

In the following, these four samples will be identified according to their value of  $c\tau$ . The distribution of the neutralino flight length at the generator level for the four

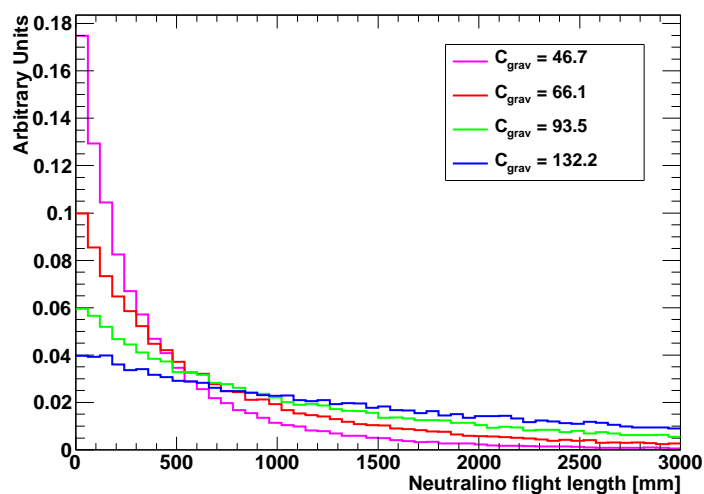


**Figure 5.2.** Distribution of the neutralino flight length at the generation level for different values of  $C_{grav}$ .

samples is shown in Figure 5.2. Signal datasets are generated and reconstructed using the software version CMSSW\_3\_5\_6, including the full simulation of the CMS detector with GEANT4 [70] at center of mass energy  $\sqrt{s} = 7$  TeV.

In addition, a sample of 2000 single pointing photons has been used for comparison. These photons point to the CMS interaction vertex, have energies uniformly distributed from 10 GeV up to 100 GeV and are in the barrel region, i.e.  $|\eta| < 1.479$ . Finally, to study the effect of the magnetic field on the shape of the ECAL energy deposits, the same photons have been reconstructed after switching off the 3.8 T CMS magnetic field.

## 5.2 Selection criteria for off-pointing photons

Photons from the decay of the long-lived particle have a very distinctive experimental signature. Looking at Figure 5.3, which presents a schematic view of the long-lived neutralino decay  $\tilde{\chi}_1^0 \rightarrow \tilde{G}\gamma$ , two main characteristics of photons from neutralino decay can be identified. Firstly, they reach the calorimeter after the other particles produced at the interaction point and traveling at the speed of the light: the excellent precision in time measurement obtained from the CMS ECAL makes it possible to identify them by calculating the arrival delay. Secondly, photon direction forms a non-zero angle with the axis of the ECAL crystals, resulting in a skewed cluster. The characteristic shape of clusters from OP photons can be therefore exploited to identify them.

### 5.2.1 ECAL timing

The combination of the scintillation timescale for the  $\text{PbWO}_4$  crystals in the ECAL, the electronic pulse shaping and the sampling rate allow for an excellent time resolution. As discussed in Section 4.3.5 the ECAL time reconstruction consists in a

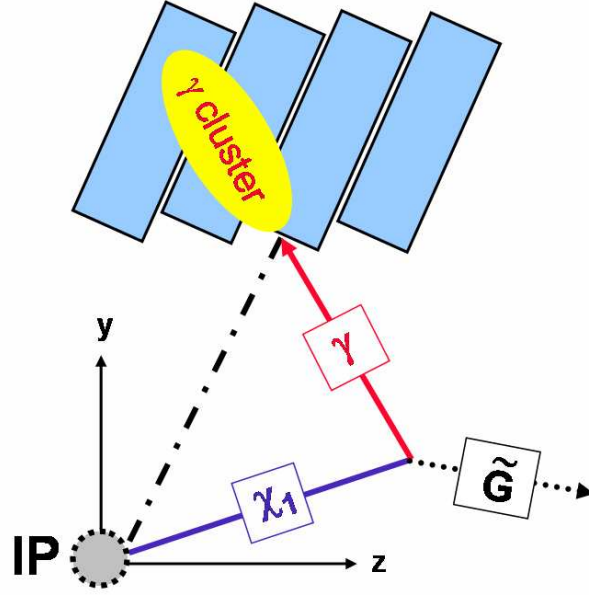


**Figure 5.3.** Schematic diagram of the long-lived neutralino decay  $\tilde{\chi}_1^0 \rightarrow \tilde{G}\gamma$ .

precise measurement of  $T_{max}$ , i.e. the time corresponding to the maximum of the signal pulse shape (Figure 4.17).

The algorithm used to extract  $T_{max}$  [73] relies on an alternative representation of the pulse shape, provided by a variable defined as the ratio between the amplitudes of two consecutive samples

$$R(T) = \frac{A(T)}{A(T + 25 \text{ ns})} \quad (5.2)$$

where  $A(T)$  represents the pulse amplitude at time  $T$ .

Figure 5.4 illustrates the two representations for the pulse shape. On the left, the common amplitude vs time representation is shown. On the right, the same pulse shape has been parametrized by using the time difference  $(T - T_{max})$  as a function of  $R(T)$ . In view of the universal character of the pulse shape, this representation is independent on the maximum amplitude  $A_{max}$  and can be described well with a simple polynomial parametrization.

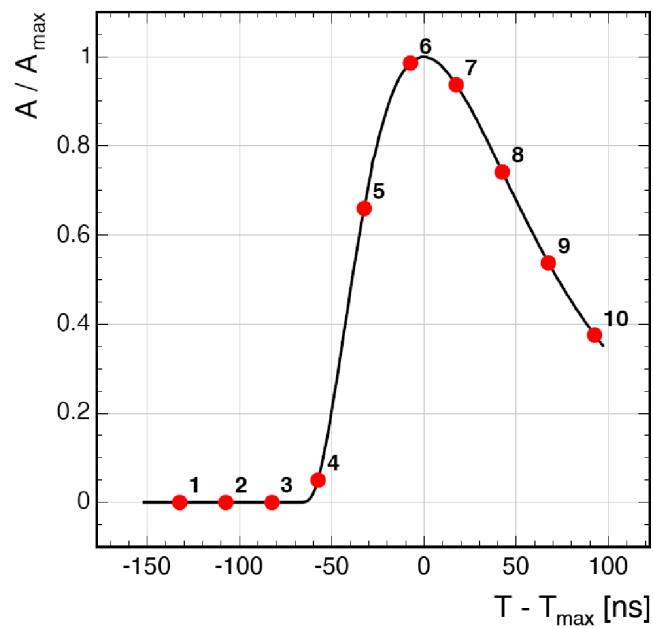
Each pair of consecutive samples gives a measurement of the ratio

$$R_i = \frac{A(T + i \cdot 25 \text{ ns})}{A(T + [i + 1] \cdot 25 \text{ ns})}. \quad (5.3)$$

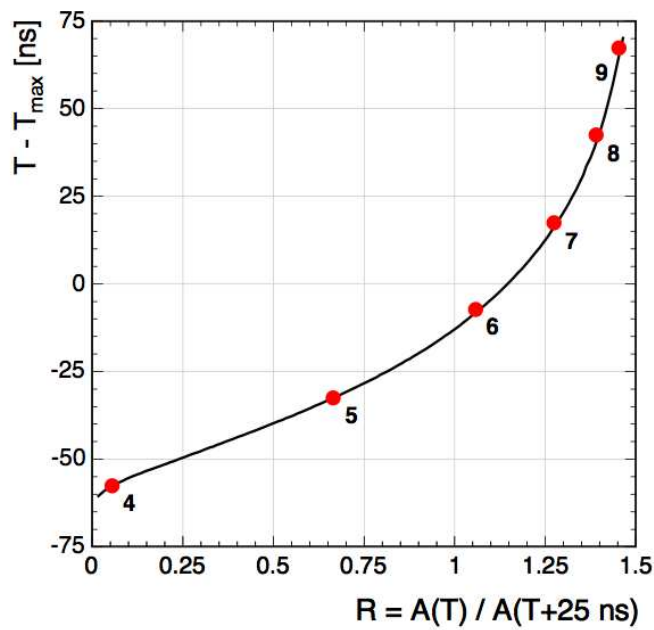
An estimate  $T_{max,i}$  of the maximum time can be obtained from each  $R_i$  ratio as  $T_{max,i} = T_i - T(R_i)$ . A more precise determination of the maximum time and its uncertainty is then obtained from the weighted average of the estimated  $T_{max,i}$ :

$$T_{max} = \frac{\sum_i \frac{T_{max,i}}{\sigma_i^2}}{\sum_i \frac{1}{\sigma_i^2}} \quad (5.4)$$

$$\frac{1}{\sigma_T^2} = \sum_i \frac{1}{\sigma_i^2} \quad (5.5)$$



(a)



(b)

**Figure 5.4.** Two different representation for pulse shape: a) pulse amplitude as a function of the time difference ( $T - T_{\max}$ ) and b) time difference ( $T - T_{\max}$ ) as a function of the ratio of the amplitudes  $R(T)$ .

The typical number of available ratios  $R_i$  is five or six.

To determine the intrinsic time resolution of the ECAL, electrons from a test beam with energy between 15 and 300 GeV are used. The time resolution is extracted from the distribution of the time difference between adjacent crystals that share the same electromagnetic shower and measure similar energies. The distribution of the time difference is well described by a Gaussian function, whose width can be parametrized as [73]

$$\sigma^2(t_1 - t_2) = \left( \frac{N\sigma_n}{A_{eff}} \right)^2 + 2C^2 \quad (5.6)$$

where  $A_{eff} = E_1 E_2 / \sqrt{E_1^2 + E_2^2}$ , with  $t_{1,2}$  and  $E_{1,2}$  corresponding to the times and energies measured in the two crystals,  $\sigma_n$  is a parameter related to the noise level,  $N$  and  $C$  represent the noise and constant term coefficients of time resolution. The extracted width is presented in Figure 5.5 as a function of the variable  $A_{eff}/\sigma_n$ . The energy scales for barrel and endcap are superimposed in the plot.

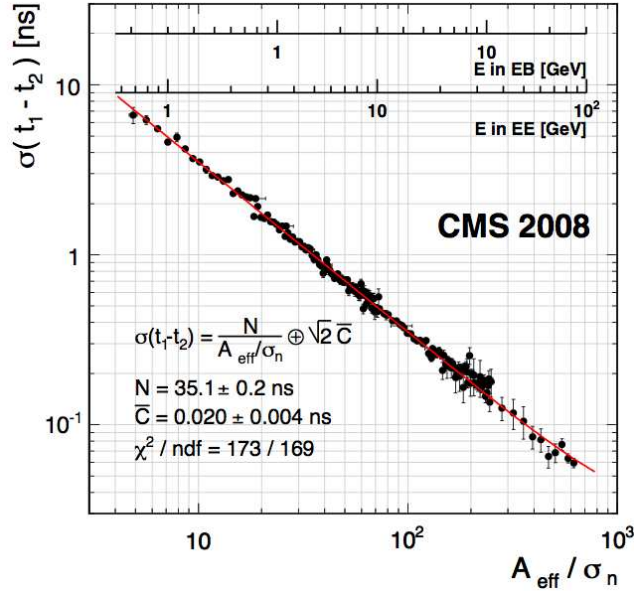


**Figure 5.5.** Gaussian width of the time difference between two neighboring crystals as a function of the variable  $A_{eff}/\sigma_n$ , for test beam electrons between 15 and 300 GeV. The equivalent single-crystal energy scales for barrel and endcaps are overlaid on the plot.

For energies around 10 GeV, the time resolution in the barrel region is  $\sim 0.2$  ns. This value can be compared with the typical time needed by a photon to reach the ECAL surface. Assuming a 10 GeV photon directed towards the centre of the barrel, the measured ECAL time would be

$$T \sim \frac{1.24 \text{ m}}{0.3 \text{ m/ns}} = 4 \text{ ns} \quad (5.7)$$

where 1.24 m represents the radius of the ECAL barrel. The resulting time resolution for 10 GeV photon is therefore around 5%.

The excellent precision in the ECAL time measurement allows for a feasible identification of long-lived particles decaying into photons. Figure 5.6 shows a comparison between the distributions of the measured time  $T_{REC}$  of the most energetic ECAL crystal for single photons (in blue), and photons from GMSB neutralino decay (in red) with  $c\tau = 500$  mm. Both distributions have been normalized to unity. The plot clearly demonstrates that the measured time in ECAL is a very powerful variable in identifying OP photons. In fact, almost all the in-time photons are rejected by requiring an ECAL time measurement larger than 0.8 ns.

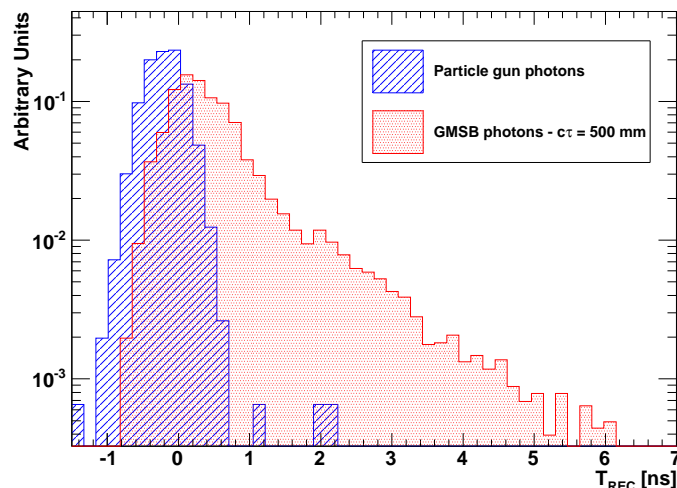


**Figure 5.6.** ECAL time distributions for pointing photons (in blue) and from GMSB neutralino decay with  $c\tau = 500$  mm (in red).

The measured time  $T_{REC}$  can be compared with the total time of flight  $T_{TRUE}$ , extracted by Monte Carlo informations and defined as:

$$T_{TRUE} = T_{\tilde{\chi}_1^0} + T_{\gamma} \quad (5.8)$$

where  $T_{\tilde{\chi}_1^0}$  is the neutralino decay time and  $T_{\gamma}$  is the time required by the photon to reach the ECAL surface. The scatter plot of  $T_{REC}$  as a function of  $T_{TRUE}$  is shown in Figure 5.7, exhibiting a striking linear correlation. The scatter plot is fitted with a linear function to obtain the following expression:

$$T_{TRUE} = 0.145 + 1.03 \times T_{REC} \text{ [ns]} \quad (5.9)$$

Figure 5.8 shows the uncertainty in the determination of the total time of flight using Equation 5.9. It can be noticed that the ECAL time measurement provides a very precise determination of the total time of flight, where the uncertainty stays at a constant value of around 0.2 ns as a function of  $T_{TRUE}$ .

## 5.2.2 Cluster shape

Another distinctive feature of an OP photon is the shape of the energy deposit in the ECAL. Due to the quasi-projective geometry of the calorimeter, the direction

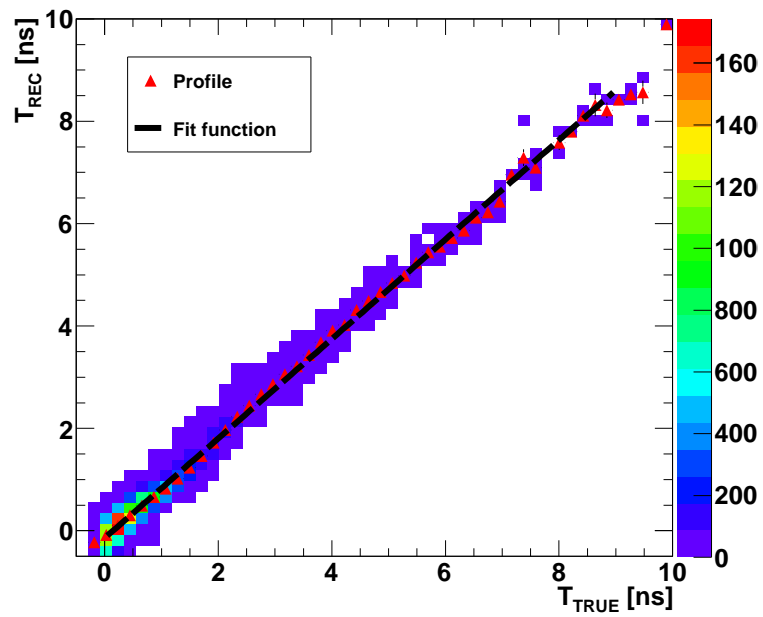


**Figure 5.7.** Scatter plot  $T_{REC}$  as a function  $T_{TRUE}$ . Histogram profile is superimposed and fitted with a linear function.

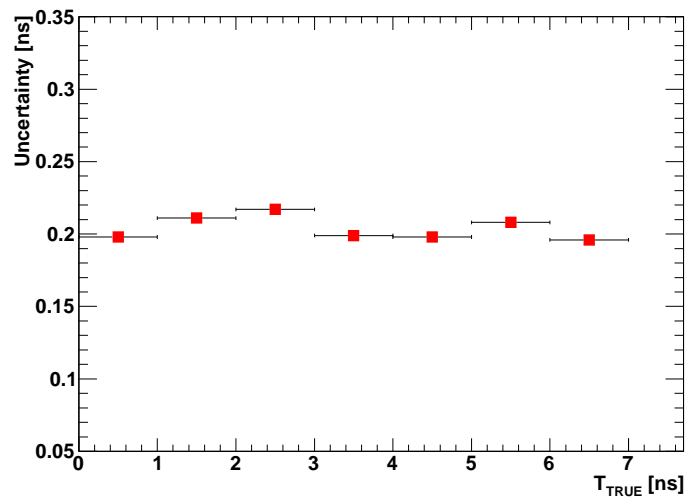


**Figure 5.8.** Uncertainty in the determination of the total time of flight as a function of  $T_{TRUE}$ .

of a photon which does not point to the CMS interaction vertex will form a non-zero angle  $\delta$  with the axis of the ECAL crystal, which is illustrated in Figure 5.9. As a consequence, a large fraction of the energy of OP photons escapes from the

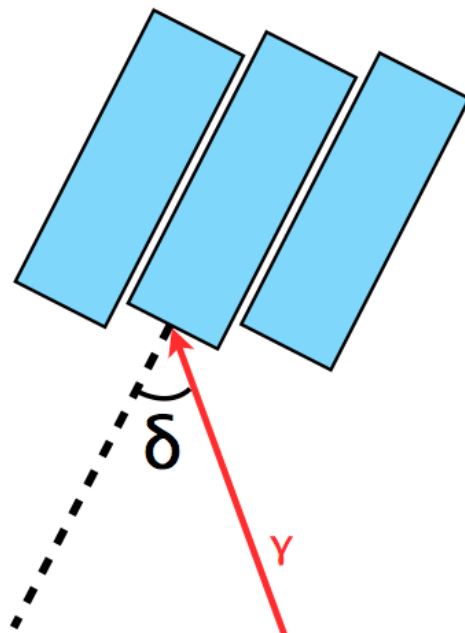


**Figure 5.9.** The angle of incidence,  $\delta$ , between the axis of the ECAL crystal and the direction of the OP photon.

central crystal and the resulting energy deposit has a distinctive elliptical shape. The differences in cluster shape for pointing and off-pointing photons are shown in Figure 5.10. In case of pointing photons (Figure 5.10a), the most part of the incoming energy is deposited in the central crystal, giving a round, symmetric shape to the cluster. On the other hand, the energy of an OP photon (Figure 5.10b) is spread over a larger number of crystals. The shape of the cluster is elliptical whose major axis orientation is related to the original direction of the OP photon.

The characteristic shape of an OP photon cluster can be exploited to identify the decay products of a long-lived particle. The geometrical properties of an energy deposit in the ECAL can be described by the following covariance matrix:

$$\text{COV}_{\eta\phi} = \begin{pmatrix} \sigma_{\eta\eta} & \sigma_{\eta\phi} \\ \sigma_{\phi\eta} & \sigma_{\phi\phi} \end{pmatrix} \quad (5.10)$$

with,

$$\sigma_{\mu\nu} = \sum_{i=1}^N w_i (\mu_i - \langle\mu\rangle) (\nu_i - \langle\nu\rangle) \quad (5.11)$$

where  $N$  is number of crystals in the cluster,  $\mu_i$  and  $\nu_i$  are respectively the  $\eta$ ,  $\phi$  indexes that identify the  $i$ -th crystal of the cluster and  $\langle\mu\rangle = \frac{\sum_i w_i \mu_i}{\sum_i w_i}$ . The logarithmic weight  $w_i$ , defined as:

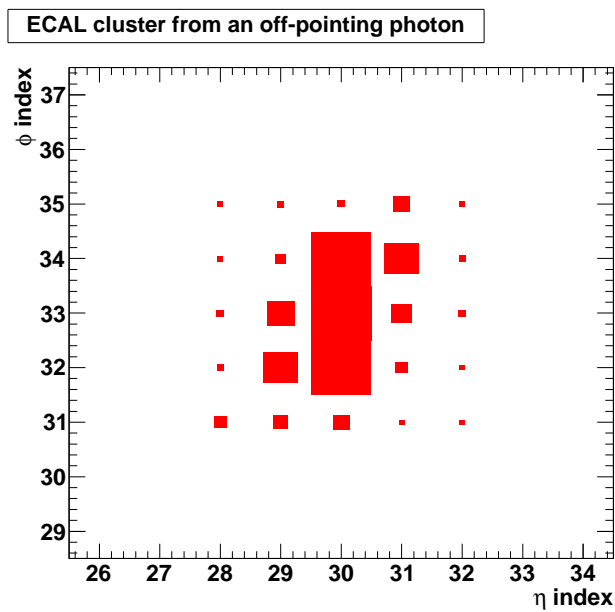
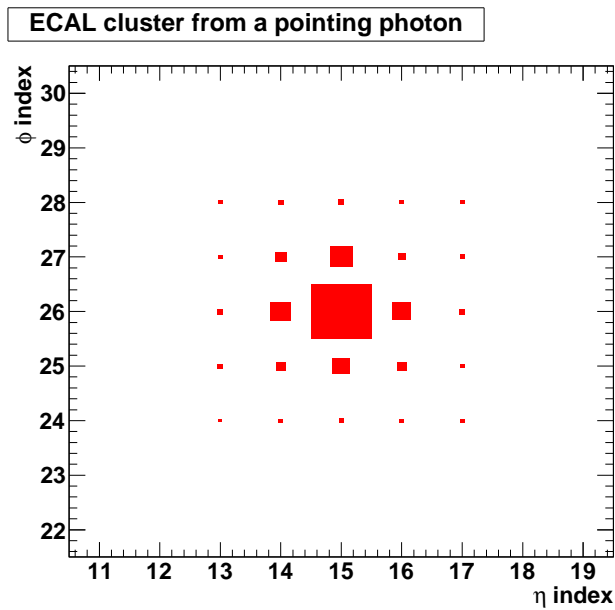


**Figure 5.10.** Energy deposits in the ECAL for: a) a pointing photon; b) an off-pointing photon.

$$w_i = \max \left[ K + \log \left( \frac{E_i}{E_{CLUSTER}} \right); 0 \right] \quad (5.12)$$

is the same used to calculate the cluster position (Equation 4.11) and  $E_i$  is the energy of the  $i$ -th crystal in the cluster.

The covariance matrix can be diagonalized in order to find the major and minor axes of the ellipse from the energy deposit. So

$$\text{COV}_{\eta\phi} = \begin{pmatrix} S_{major} & 0 \\ 0 & S_{minor} \end{pmatrix} \quad (5.13)$$

with

$$S_{major} = \frac{(S_{\phi\phi} + S_{\eta\eta}) + \sqrt{(S_{\phi\phi} - S_{\eta\eta})^2 + 4S_{\phi\eta}^2}}{2} \quad (5.14)$$

$$S_{minor} = \frac{(S_{\phi\phi} + S_{\eta\eta}) - \sqrt{(S_{\phi\phi} - S_{\eta\eta})^2 + 4S_{\phi\eta}^2}}{2} \quad (5.15)$$

Major and minor axes of the energy deposit from an OP photon are shown in Figure 5.11. The major axis represents the major axis of the ellipse which describe the shape of the energy deposit in the ECAL and the eigenvalue  $S_{major}$  is the standard deviation of the two dimensional energy distribution calculated along the major axis. This variable has been used to discriminate energy deposits from photons and neutral pions (see Appendix A).

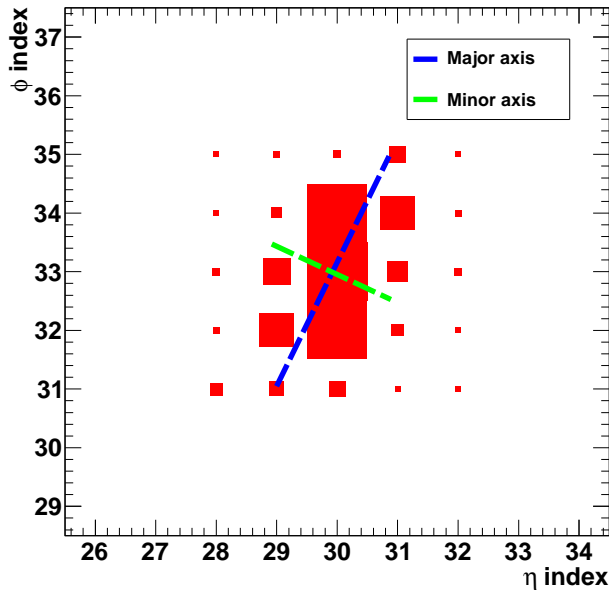


**Figure 5.11.** Example of major and minor axes of the energy deposit from an OP photon.

Figure 5.12 shows the distributions of  $S_{major}$  for pointing and OP photons, defined as GMSB photons from neutralinos with flight path larger than 60 cm. As expected, large  $S_{major}$  values are seen for OP photons with respect to clusters from

pointing photons. To be noted that the distributions in Figure 5.12 refer only to unconverted photons. The case of converted photons (which represent a major background for this analysis) will be considered in Section 5.3.

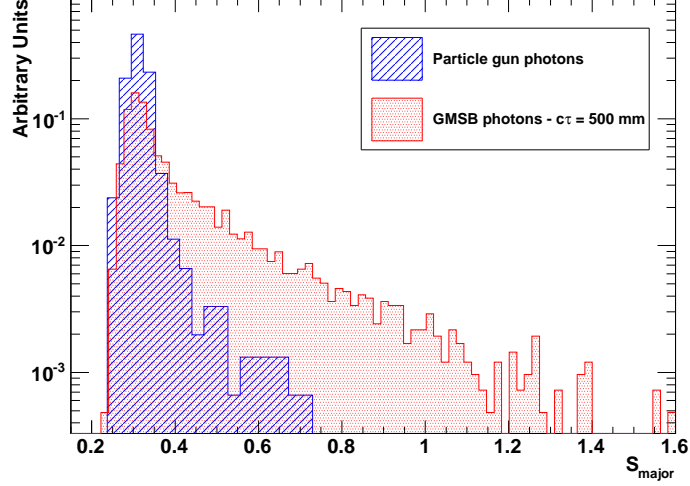


**Figure 5.12.** Distribution of  $S_{major}$  for pointing photons (in blue) and from GMSB neutralino decay, with  $c\tau = 500$  mm and decay path larger than 60 cm. Only unconverted photons are considered.

The other eigenvalue  $S_{minor}$  represents the energy spread along the orthogonal direction with respect to  $S_{major}$ . The importance of this variable is that it has the same distribution for all types of electromagnetic deposits. As an example, Figure 5.13 shows the distribution of  $S_{minor}$  for pointing and off-pointing photons, including also  $\gamma \rightarrow e^-e^+$  conversions. The distributions are very similar and, for this reason,  $S_{minor}$  can be used to identify electromagnetic deposit in the ECAL (unconverted, converted, pointing and off-pointing photon,  $\pi^0 \rightarrow \gamma\gamma$  decays) with respect to hadronic energy deposits from charged particles or jets, whose  $S_{minor}$  distribution is very different from the electromagnetic case.

As already stated,  $S_{major}$  is strongly related to the angle between photon direction and the axis of the ECAL crystal. Therefore, the measurement of  $S_{major}$  can be used to obtain an estimate for the angle  $\delta$ . Figure 5.14 shows the correlation between  $S_{major}$  and  $\sin(\delta)$ . The profile of the scatter plot (red points) is fitted with a parabolic function, to obtain the following parametrization for  $\sin(\delta)$ :

$$\sin(\delta) = \sqrt{\frac{S_{major} - 0.310}{1.763}} \quad (5.16)$$

To reduce the uncertainties due to the fit, the determination of  $\delta$  is performed only for clusters with  $S_{major} < 1.2$ . The uncertainty in the determination of  $\sin(\delta)$  using Equation 5.16 is shown in Figure 5.15, as a function of  $\sin(\delta)$ .

In this work,  $S_{major}$  in combination with  $T_{REC}$  will be used to select OP photons from the decay of long-lived particles. Figure 5.16 shows the distribution for pointing and GMSB photons in the  $S_{major} - T_{REC}$  plane. Pointing photons are seen to populate regions at lower values of  $S_{major}$  and  $T_{REC}$ , whilst OP photons populate areas at larger values.

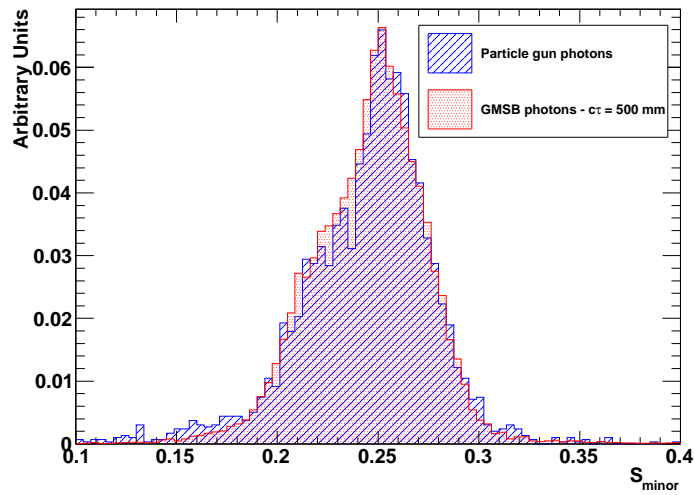


**Figure 5.13.** The  $S_{minor}$  distribution for pointing photons and from GMSB neutralino decay with  $c\tau = 500$  mm. Photon conversions are also considered. Distributions are normalized to unity.

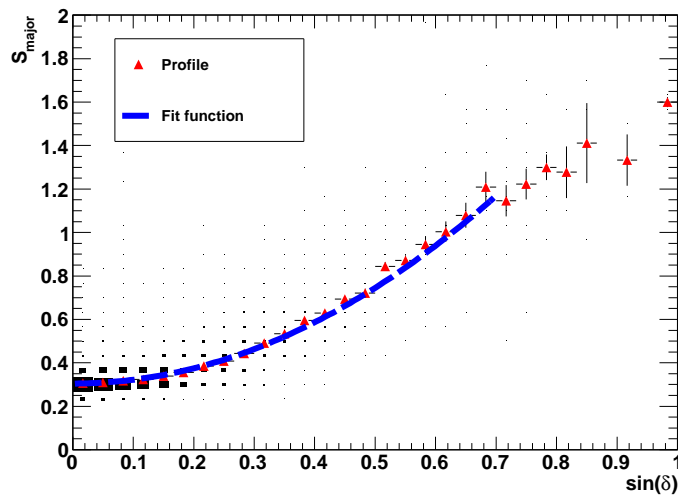


**Figure 5.14.** Scatter plot  $S_{major}$  versus  $\sin(\delta)$ . Histogram profile is superimposed and fitted with a parabolic function.

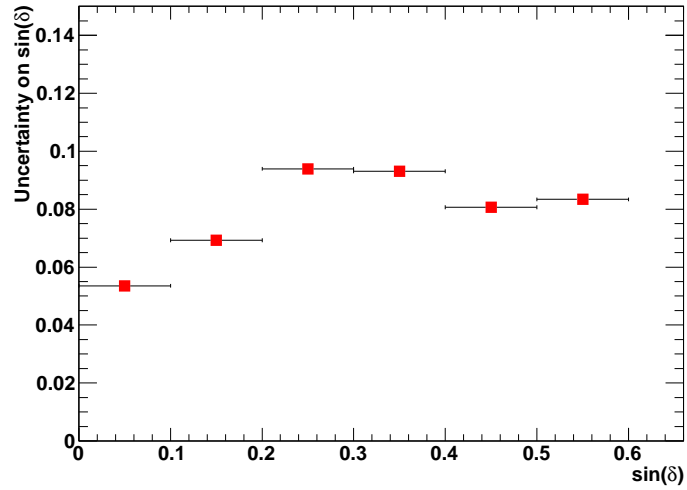


**Figure 5.15.** Uncertainty in the determination of the angle of incidence as a function of  $\sin(\delta)$ .

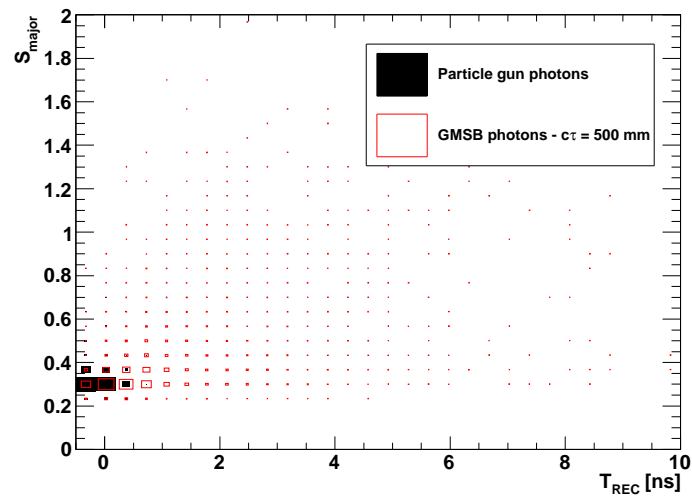


**Figure 5.16.** The  $S_{major}$  versus  $T_{REC}$  distribution for pointing and GMSB photons.

Hence, the following selection criteria are used to identify OP photons:

1. ECAL time requirement:  $T_{REC} > 0.8$  ns;
2. Major axis requirement:  $S_{major} > 0.31$ .

As already shown in Figure 5.6, almost all the in-time photons are rejected by requiring  $T_{REC} > 0.8$  ns. The additional requirement on  $S_{major}$  is quite loose to keep the efficiency at a reasonable value and, at the same time, to allow for the reconstruction of the angle of incidence  $\delta$  using the expression Equation 5.16.

### 5.3 Rejection of photon conversions

Photon conversions represent a major background in the GMSB analysis as they also are found to produce large values of  $S_{major}$  similar to OP photons, regardless of the angle of incidence on the ECAL surface. This is due to the fact that the electron-positron pair is curved along  $\phi$  direction due to the CMS magnetic field, and the energy of the incoming photon will be therefore shared between a large number of crystals, resulting in a large  $S_{major}$  value. Figure 5.17 shows the distribution of  $S_{major}$  for unconverted and converted pointing photons, demonstrating that conversions can mimic an OP photon signature because of large values of  $S_{major}$ .

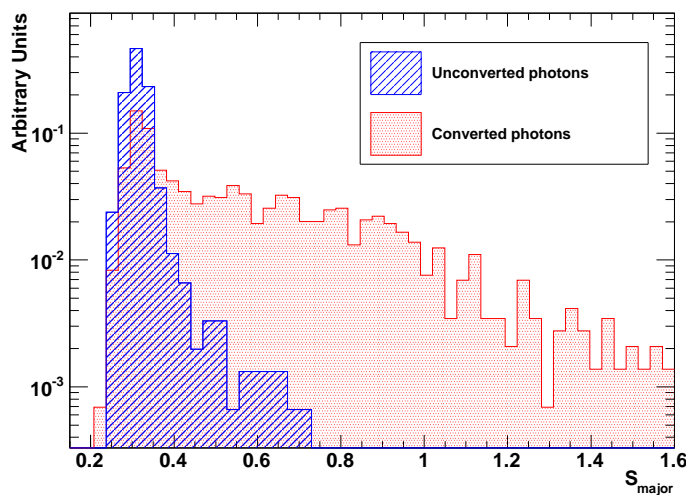


**Figure 5.17.** The  $S_{major}$  distribution for unconverted and converted pointing photons. Distributions are normalized to unity.

A common method for the identification of photon conversions relies on the use of  $\sigma_{\phi\phi}$  (Equation 5.10) as a discriminating variable. In fact,  $\sigma_{\phi\phi}$  indicates the spread of cluster energy along  $\phi$  direction, which is expected to be very large for converted photons. Figure 5.18 shows the distribution of  $\sigma_{\phi\phi}$  for unconverted and converted pointing photons.

Despite the rejection power,  $\sigma_{\phi\phi}$  cannot be used due to its strong relation to  $S_{major}$  (Equation 5.14) which is needed for the determination of  $\delta$ . Therefore an alternative variable uncorrelated with  $S_{major}$  is used to reject  $\gamma$  conversions: the

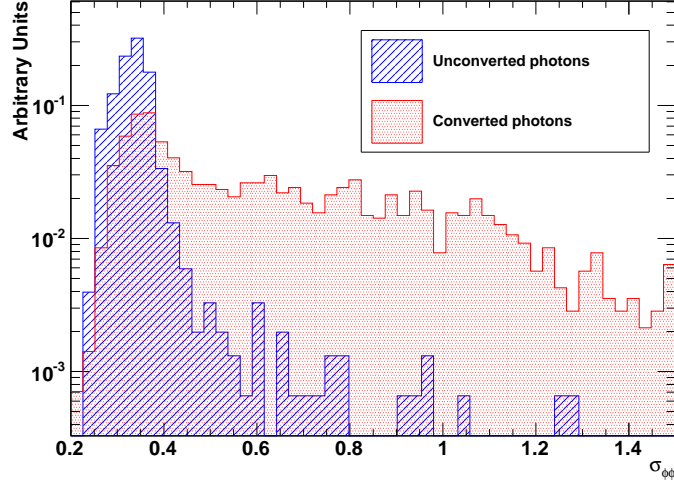


**Figure 5.18.** The  $\sigma_{\phi\phi}$  distribution for unconverted and converted pointing photons. Distributions are normalized to unity.

angle  $\alpha$ , defined as the angle between  $\phi$  ECAL direction and the major axis of the cluster. A graphical view of the energy deposit in the ECAL from a converted photon with the respective  $\alpha$  angle is shown in Figure 5.19. The value of  $\alpha$  can be calculated using the following expression:

$$\tan(\alpha) = \frac{(\sigma_{\eta\eta} - \sigma_{\phi\phi}) + \sqrt{(\sigma_{\eta\eta} - \sigma_{\phi\phi})^2 + 4\sigma_{\eta\phi}^2}}{2\sigma_{\eta\phi}} \quad (5.17)$$

The electron-positron pair produced from photon conversion is reconstructed as two bumps in the ECAL displaced along  $\phi$  direction, as confirmed by Figure 5.19. This results in a very small angle  $\alpha$ . The distribution of  $\alpha$  is expected to be a narrow peak at zero for converted photons, while, for unconverted photons, the distribution should be almost flat. Figure 5.20 shows the distribution of  $\alpha$  for clusters from a) converted and b) unconverted pointing photons.

It can be seen that  $\alpha$  confirms the expectations for the case of converted photons, but the distribution for unconverted photons shows an unexpected enhancement for small  $\alpha$  rather than being flat. This is due to the effect of the magnetic field on the electromagnetic shower, where the electrons produced during the development of the shower are curved along the  $\phi$  direction, causing an asymmetry between  $\sigma_{\eta\eta}$  and  $\sigma_{\phi\phi}$  even for unconverted photons. The symmetry is restored when the magnetic field is switched off. Figure 5.21 shows the distributions in the  $\sigma_{\phi\phi}$  versus  $\sigma_{\eta\eta}$  plane for unconverted photons with the a) magnetic field switched on and b) magnetic field switched off.

The amount of asymmetry in the shape of the unconverted photon clusters due to the effect of the magnetic field, can be quantified by considering the ratio  $C$  between the mean value of  $\sigma_{\eta\eta}$  and  $\sigma_{\phi\phi}$ . This quantity, which is expected to be very close to unity in absence of the magnetic field, assumes values lower than one when the magnetic field is switched on. The measured value for  $C$ , obtained from the sample of pointing photons without the magnetic field, is:

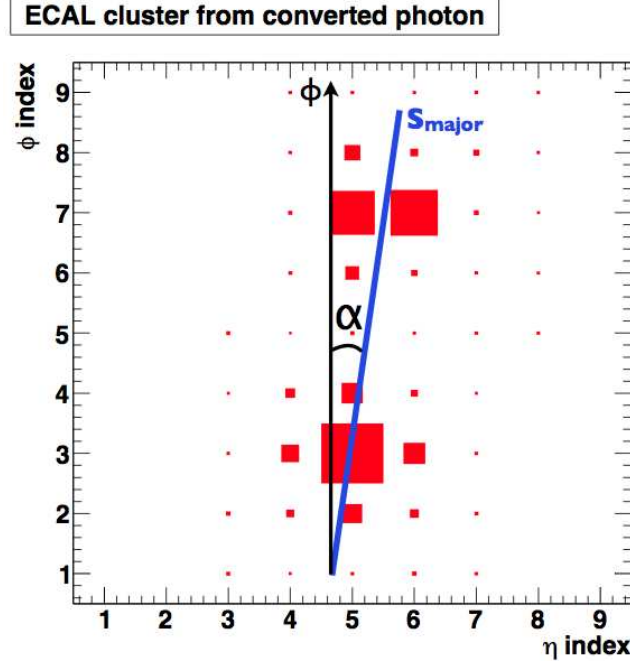


Figure 5.19. Energy deposit from a converted photon with the respective  $\alpha$  angle.

$$C^2 = \frac{\langle \sigma_{\eta\eta} \rangle}{\langle \sigma_{\phi\phi} \rangle} = 0.838 \quad (5.18)$$

To restore the symmetry, it is sufficient to define the following covariance matrix:

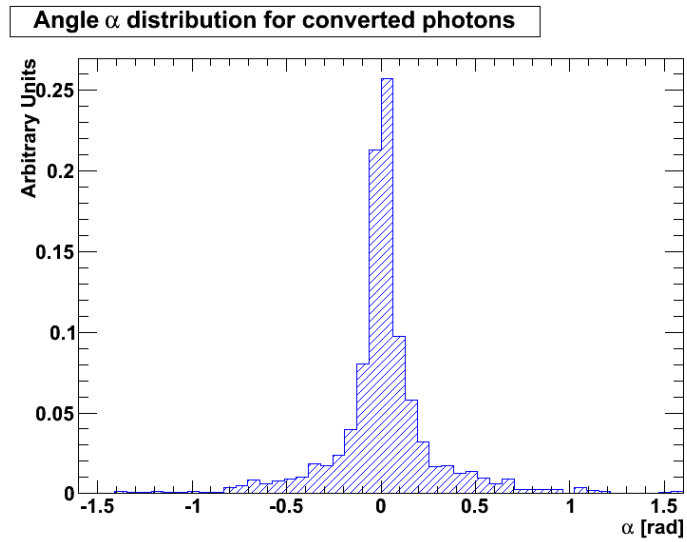
$$\text{COV}_{\eta\phi}^* = \begin{pmatrix} \sigma_{\eta\eta} & C \cdot \sigma_{\eta\phi} \\ C \cdot \sigma_{\phi\eta} & C^2 \cdot \sigma_{\phi\phi} \end{pmatrix} \quad (5.19)$$

Using the new covariance matrix, a modified  $\alpha$  angle, corrected for the effect of the magnetic field, is computed. Figure 5.22 shows a comparison between the modified  $\alpha$  for unconverted and converted photons. It can be seen that  $\alpha$  becomes very sensitive to the identification of photon conversions after the correction. It should be noted that the distribution of  $\alpha$  is expected to be very similar for both pointing and off-pointing scenarios. The residual peaks around  $\alpha = \pm\pi/4$  can be explained if one considers an alternative definition of  $S_{major}$ :

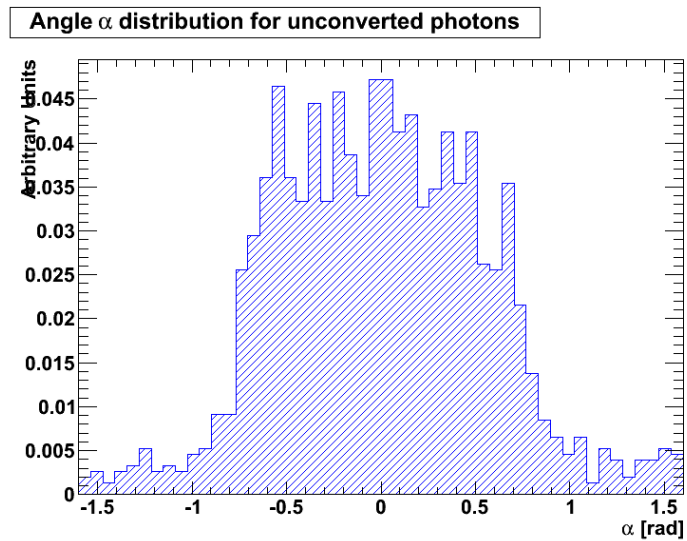
$$S_{major} = \frac{\sum_{i=1}^N w_i \times (d_i^{MIN})^2}{\sum_{i=1}^N w_i} \quad (5.20)$$

where  $d_i^{MIN}$  is the distance between the center of  $i$ -th crystal and the minor axis. Due to the finite granularity of the ECAL, crystals along the diagonals have larger values of  $d_i^{MIN}$  and therefore also a large impact in Equation 5.20. This geometrical effect is illustrated in Figure 5.23. As a consequence, the diagonals of a cluster represent the preferred directions for the major axis, justifying the presence of the  $\pm\pi/4$  residual peaks in the  $\alpha$  distribution for unconverted photons.

Since the majority of converted photons are within a narrow peak around  $\alpha = 0$ , the following selection criteria on  $\alpha$  is applied to reject photon conversions:



(a)



(b)

**Figure 5.20.** The distribution of  $\alpha$  for clusters from: a) converted and b) unconverted pointing photons. Distributions are normalized to unity.

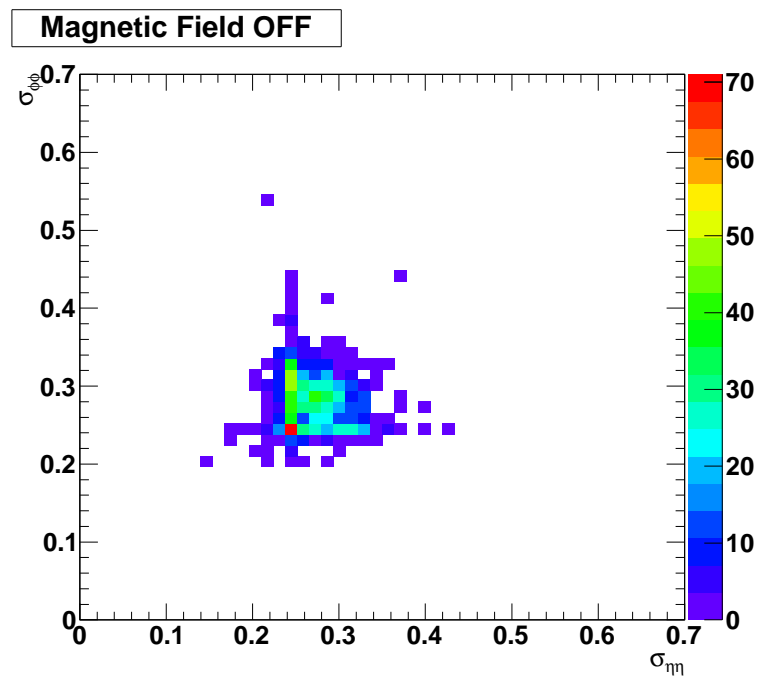
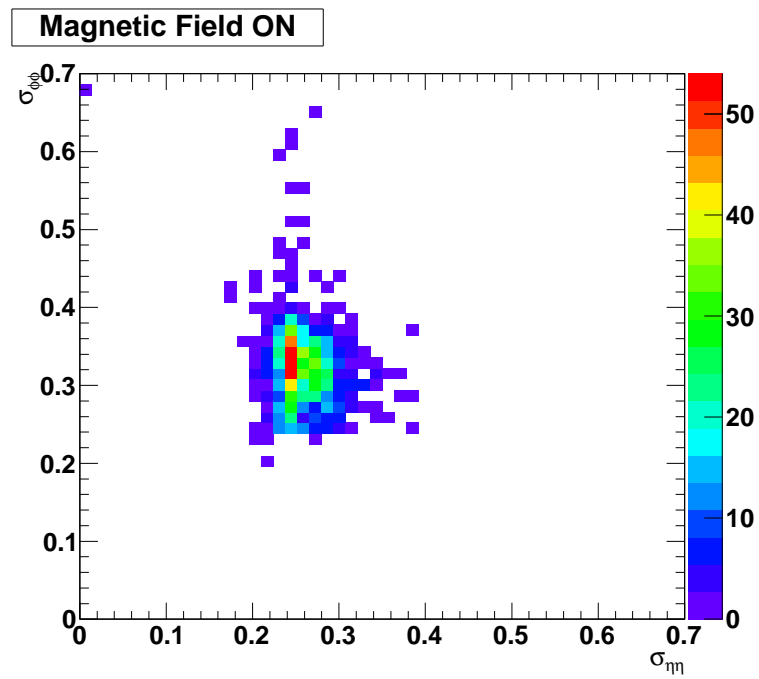


**Figure 5.21.** The distribution for unconverted photons with a) the magnetic field switched on and b) magnetic field switched off.

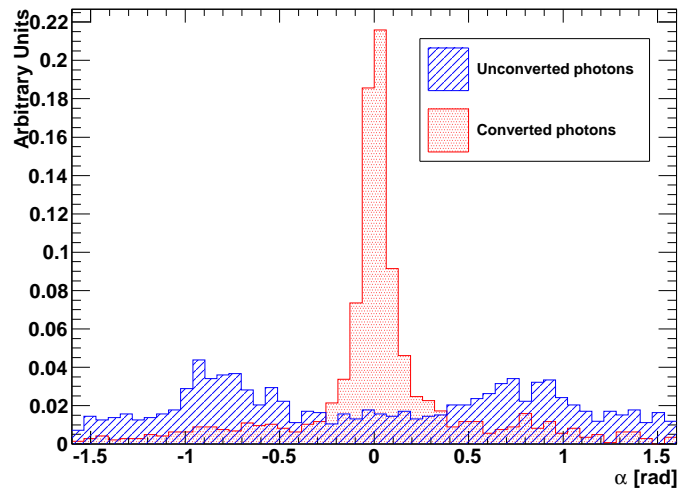


**Figure 5.22.** The distribution of  $\alpha$  for unconverted and converted pointing photons after the correction for the effect of the magnetic field. Distributions are normalized to unity.

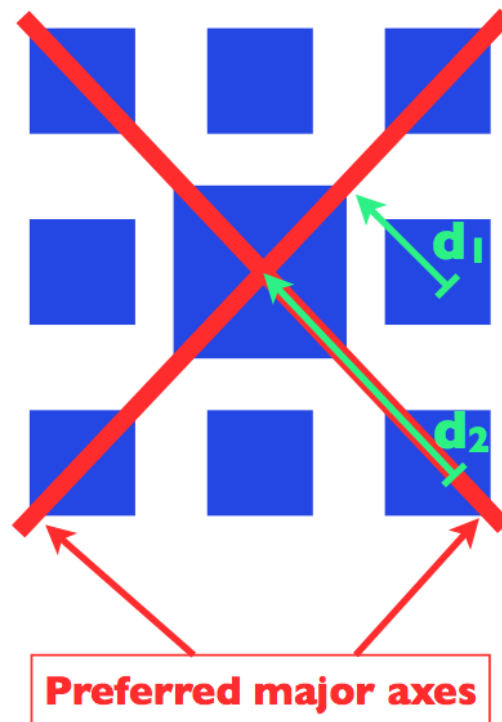


**Figure 5.23.** Preferred directions for the major axis. Crystals along the diagonals have larger  $d^{MIN}$  values than the other crystals.

- Unconverted photons:  $|\alpha| > 0.3$ ;
- Converted photons:  $|\alpha| < 0.3$ .

## 5.4 Algorithm for lifetime reconstruction

Once a clean sample of OP photons is identified, the next step consist in the determination of the lifetime of the parent particle. In this section an algorithm to extract the flight path of long-lived particles decaying into photons is presented, exploiting the excellent time determination and the fine lateral granularity of the ECAL. The algorithm consists of two steps:

1. The momentum vector of the OP photon is reconstructed using both the ECAL energy measurement and the cluster shape variables introduced in Section 5.2.2;
2. The spatial coordinates of the decay vertex of the long-lived particle are subsequently determined, using both the ECAL time measurement and the direction of the photon.

### 5.4.1 Reconstruction of photon momentum vector

The momentum of an OP photon can be reconstructed using:

- The magnitude of the momentum, given by the energy of the reconstructed cluster;
- The angle of incidence  $\delta$  between the axis of the ECAL crystal and the photon direction calculated from Equation 5.16;
- The angle  $\alpha$  between the major axis of the cluster and the ECAL  $\phi$  direction, calculated from Equation 5.17.

The momentum vector of the OP photon can be written as a sum of two components:

$$\vec{P}^\gamma = \vec{P}_{//}^\gamma + \vec{P}_T^\gamma \quad (5.21)$$

where  $\vec{P}_{//}^\gamma$  is the projection of photon momentum on the ECAL surface and  $\vec{P}_T^\gamma$  is the component along the crystal axis. The magnitude of each component is given by:

$$\begin{aligned} P_{//}^\gamma &= E_{CLU} \cdot \sin(\delta) \\ P_T^\gamma &= E_{CLU} \cdot \cos(\delta) \end{aligned} \quad (5.22)$$

The angle  $\alpha$  can be used to further decompose  $\vec{P}_{//}^\gamma$  in two components, along the  $\eta$  and  $\phi$  direction on the ECAL surface:

$$\begin{aligned}
P_{\eta}^{\gamma} &= E_{CLU} \cdot \sin(\delta) \cdot \sin(\alpha) \\
P_{\phi}^{\gamma} &= E_{CLU} \cdot \sin(\delta) \cdot \cos(\alpha)
\end{aligned}
\tag{5.23}$$

To summarize, the momentum vector of an OP photon can be reconstructed as:

$$\vec{P}^{\gamma} = \left( \vec{P}_{\eta}^{\gamma}, \vec{P}_{\phi}^{\gamma}, \vec{P}_T^{\gamma} \right)
\tag{5.24}$$

Figure 5.24 shows a scatter plot for the true value of  $\alpha$  angle versus the reconstructed value using Equation 5.17. Only unconverted photons with  $T_{REC} > 0.8$  ns and  $S_{major} > 0.31$  are considered in this plot. Despite the strong correlation, an

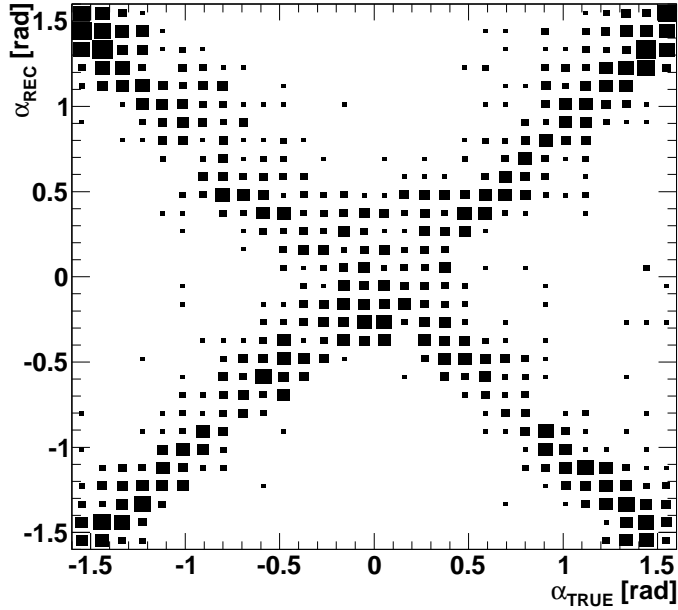


Figure 5.24. A scatter plot  $\alpha_{REC}$  versus  $\alpha_{TRUE}$ .

unresolved issue is still present since a distinctive “X-shape” can be noticed. This behavior can be explained by the fact that  $S_{major}$  only identifies the direction of the momentum projection on the ECAL surface, and not its verse. Figure 5.25 shows  $\alpha_{REC}$  versus  $\alpha_{TRUE}$  where the ambiguity on the verse has been eliminated using Monte Carlo information on the photon direction. The uncertainty on the determination of  $\alpha$  angle is shown in Figure 5.26.

The ambiguity on  $\alpha$  determination is still not solved and therefore needs more dedicated studies. Nevertheless, the ambiguity produces a bias on the reconstruction of photon momentum only, while it will not affect the calculation of the flight path of the long-lived particle. In fact, whilst a wrong determination of  $\alpha$  will affect the determination of the photon momentum, the decay length of the long-lived particle can be calculated with good accuracy using only the angle of incidence  $\delta$  of the OP photon. The algorithm used for the flight path calculation will be presented in the next section.

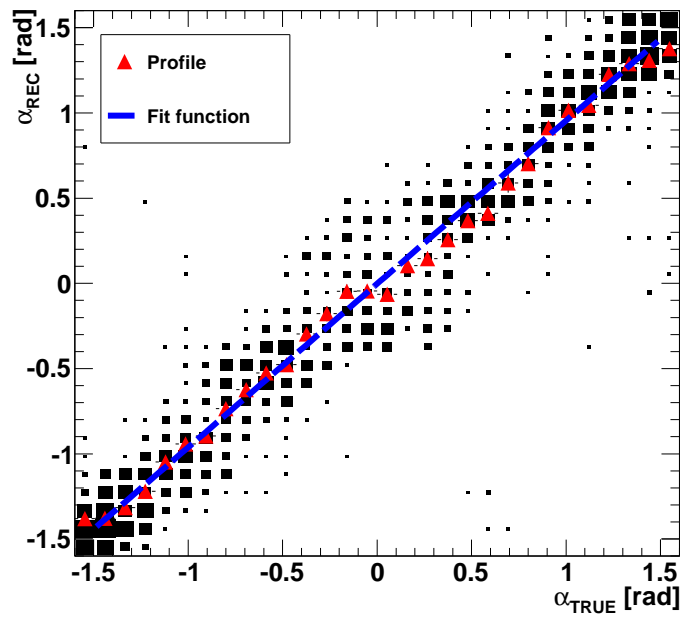


Figure 5.25. A scatter plot  $\alpha_{REC}$  versus  $\alpha_{TRUE}$ . The correct verse of the major axis is chosen from Monte Carlo truth information. The histogram profile is superimposed and fitted with a linear function.

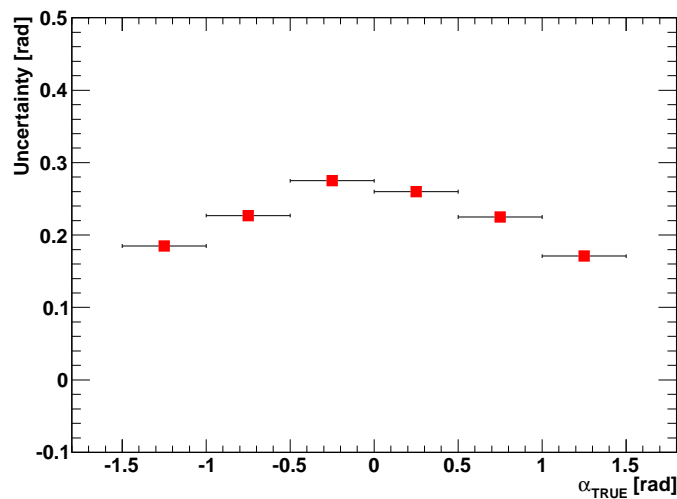
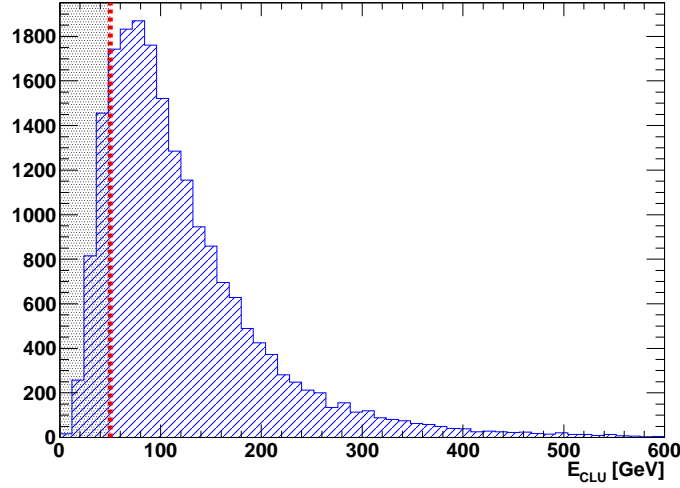


Figure 5.26. The uncertainty on the determination of  $\alpha$  as a function of  $\alpha_{TRUE}$ .

### 5.4.2 Flight path calculation

Once the direction of the OP photon has been determined, the decay vertex, and the flight path for the long-lived particle can be calculated. Since photons from neutralino decay have large energies, a preliminary selection on the ECAL reconstructed energy is applied. In the following, only clusters with  $E_{CLU} > 50$  GeV are considered: this choice allows for the rejection of the majority of background events with large cross section, such as QCD. The reconstructed energy spectrum for the decay photons for  $\Lambda = 100$  TeV<sup>1</sup> is shown in Figure 5.27.



**Figure 5.27.** The reconstructed energy spectrum for photons from  $\chi_1^0$  decay with  $\Lambda = 100$  TeV. Only photons with  $E_{CLU} > 50$  GeV will be considered.

Focusing on GMSB events, the reconstructed ECAL time can be related to the sum of the neutralino and photon flight path as follows:

$$T_{REC} = \frac{D_{\tilde{\chi}_1^0}}{\beta_{\tilde{\chi}_1^0} \cdot c} + \frac{D_\gamma}{c} \quad (5.25)$$

where  $D_{\tilde{\chi}_1^0}$  and  $D_\gamma$  refer to the flight path of the neutralino and photon respectively,  $\beta_{\tilde{\chi}_1^0}$  refers to the speed of the neutralino, and  $c$  is the speed of the light. A schematic view of the neutralino and photon flight paths is shown in Figure 5.28

Following the notation introduced in Figure 5.28, the decay vertex of the neutralino can be expressed as:

$$\begin{aligned} x_{\chi_1^0} &= x_\gamma - \hat{x}_\gamma \cdot t \\ y_{\chi_1^0} &= y_\gamma - \hat{y}_\gamma \cdot t \\ z_{\chi_1^0} &= z_\gamma - \hat{z}_\gamma \cdot t \end{aligned} \quad (5.26)$$

where  $(x_\gamma, y_\gamma, z_\gamma)$  are the coordinates of the impact point of the photon on the ECAL surface,  $(\hat{x}_\gamma, \hat{y}_\gamma, \hat{z}_\gamma)$  is the vector representing the photon direction and  $t$  is the parameter that coincides with the flight path of the photon. Additionally, the

<sup>1</sup>The energy spectrum of the photon strongly depends on the mass of neutralino which is established by the choice of the GMSB parameter  $\Lambda$ .

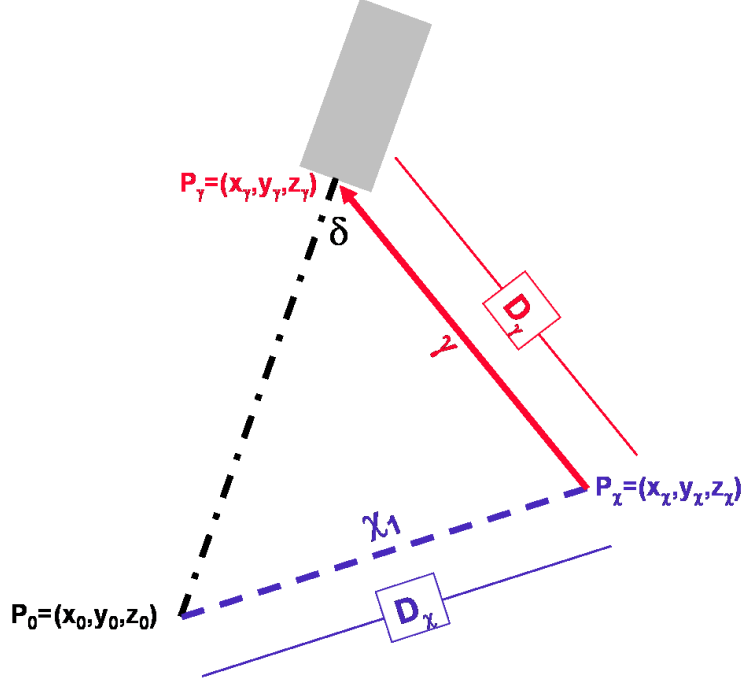


Figure 5.28. A schematic view of the neutralino and photon flight paths.

neutralino flight path can be written as a function of parameter  $t$  according to the following expression:

$$D_{\tilde{\chi}_1^0} = \overline{P_0 P_{\tilde{\chi}_1^0}} = \sqrt{((x_0 - x_\gamma + \hat{x}_\gamma \cdot t)^2 + (y_0 - y_\gamma + \hat{y}_\gamma \cdot t)^2 + (z_0 - z_\gamma + \hat{z}_\gamma \cdot t)^2)} \quad (5.27)$$

Combining Equation 5.25 and Equation 5.27, and setting  $D_\gamma = t$ , a second-order equation for  $t$  can be established as follows:

$$T_{REC} = \frac{t}{c} + \frac{\sqrt{(x_0 - x_\gamma + \hat{x}_\gamma \cdot t)^2 + (y_0 - y_\gamma + \hat{y}_\gamma \cdot t)^2 + (z_0 - z_\gamma + \hat{z}_\gamma \cdot t)^2}}{\beta_{\tilde{\chi}_1^0} \cdot c} \quad (5.28)$$

From Equation 5.28 it can be noticed that the speed of the neutralino  $\beta_{\tilde{\chi}_1^0}$  is the only unknown variable. The speed of the neutralino cannot be determined directly; however the correlation with the energy of the  $\tilde{\chi}_1^0$  decay photon can be exploited to obtain an estimate of  $\beta_{\tilde{\chi}_1^0}$ .

A relationship between the speed of the neutralino and the photon energy can be then established by fitting for the profile of  $\beta_{\tilde{\chi}_1^0}$  versus  $E_{CLU}$  distribution, as shown in Figure 5.29.

The function used for the fit is expressed as:

$$\begin{aligned} \beta_{\tilde{\chi}_1^0} &= \frac{1}{c} \cdot (\sum_{i=0}^2 A_i \cdot (E_{CLU})^i) & 50 < E_{CLU} < 70 \text{ GeV} \\ \beta_{\tilde{\chi}_1^0} &= \frac{1}{c} \cdot (\sum_{i=0}^4 B_i \cdot (E_{CLU})^i) & E_{CLU} \geq 70 \text{ GeV} \end{aligned} \quad (5.29)$$

The fit parameters  $A_i$  and  $B_i$  are listed in Table 5.1 and Table 5.2 respectively. It should be noted that the correlation between  $\beta_{\tilde{\chi}_1^0}$  and  $E_{CLU}$  critically depends on

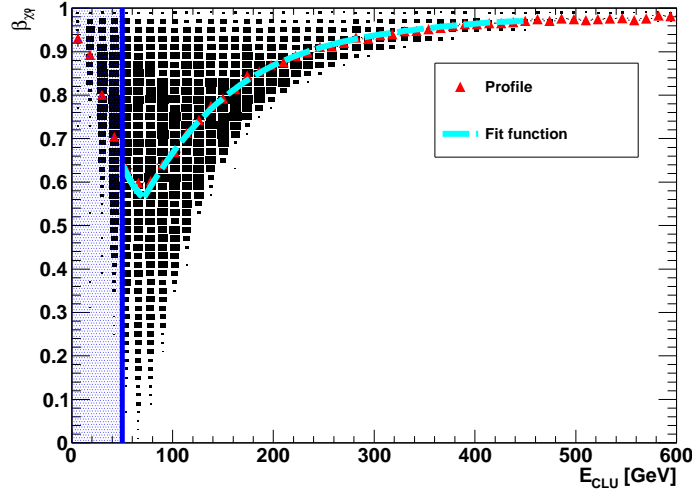


**Figure 5.29.** A scatter plot  $\beta_{\chi_1^0}$  versus  $E_{CLU}$ . The histogram profile is superimposed and fitted with a polynomial function.

the GMSB model parameters and in particular on the neutralino mass (which is set by  $\Lambda$ ).

$A_0$	$A_1$	$A_2$
$3.14 \cdot 10^1$	$-3.40 \cdot 10^{-1}$	$1.91 \cdot 10^{-3}$

**Table 5.1.** The fit parameters for  $50 < E_{CLU} < 70$  GeV.

$B_0$	$B_1$	$B_2$	$B_3$	$B_4$
$5.02 \cdot 10^0$	$2.17 \cdot 10^{-1}$	$-7.98 \cdot 10^{-4}$	$1.39 \cdot 10^{-6}$	$-9.36 \cdot 10^{-10}$

**Table 5.2.** The fit parameters for  $E_{CLU} > 70$  GeV.

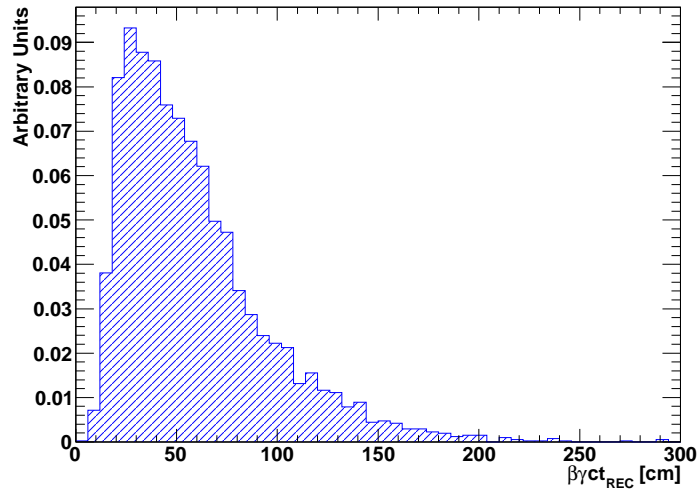
The parameter  $t$  is then extracted by taking the largest of the two solutions in Equation 5.28 and inputting this in Equation 5.27 to obtain the flight path  $\beta\gamma ct_{REC}$  of the neutralino. Figure 5.30 shows the distribution of  $\beta\gamma ct_{REC}$  for  $\tilde{\chi}_1^0$  with  $c\tau = 500$  mm.

The largest solution is considered since it provides a better resolution on the determination of  $\beta\gamma ct_{REC}$  (17.5 cm against 19.3 cm). The distributions of  $(\beta\gamma ct_{REC} - \beta\gamma ct_{TRUE})$  using both the largest and the smallest solution of Equation 5.28 are shown in Figure 5.31.

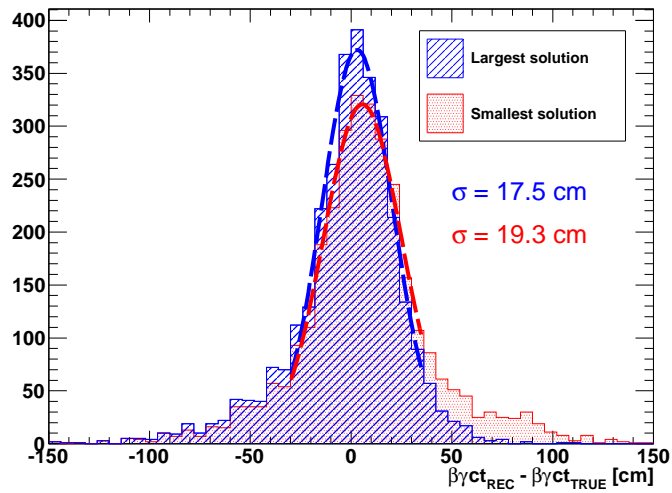
The selection used for the reconstructed photons is summarized in Table 5.3.

Figure 5.32 shows a scatter plot of the reconstructed value of neutralino flight path as a function of the true value obtained from Monte Carlo information. The histogram profile is fitted and shows a linear correlation.

The distribution of the reconstructed flight path for different GMSB samples at increasing values of neutralino lifetime is shown in Figures 5.33, 5.34, 5.35 and 5.36. It can be noticed that as the lifetime increases, the distribution of  $\beta\gamma ct_{REC}$



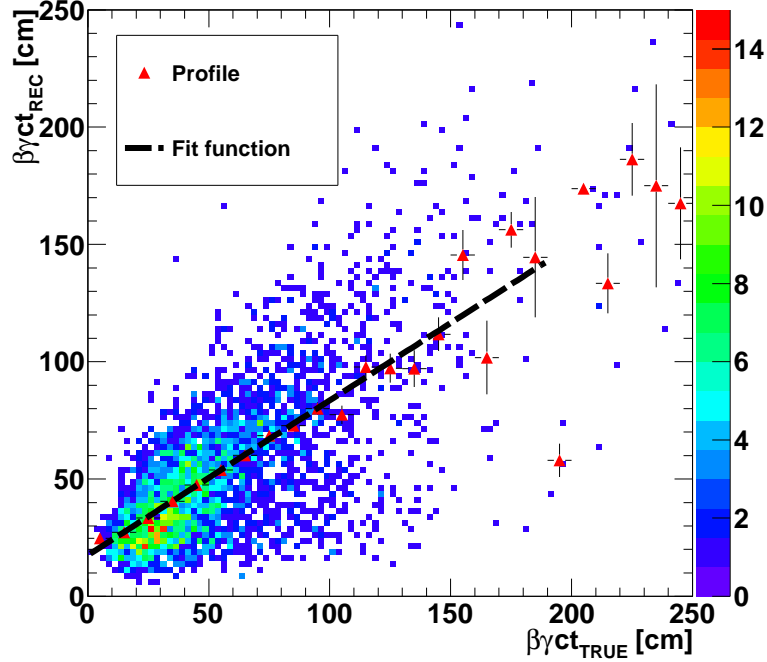
**Figure 5.30.** The distribution of the reconstructed flight path  $\beta\gamma ct_{REC}$  of neutralinos with  $c\tau = 500$  mm.



**Figure 5.31.** The resolution on the determination of  $\beta\gamma ct_{REC}$  using both the largest and the smallest solution of Equation 5.28.

$\gamma$ selection	
$T_{\text{REC}}$	$> 0.8$ ns
$S_{\text{major}}$	$> 0.31$
$ \alpha_{\text{REC}} $	$> 0.3$
$E_{\text{CLU}}$	$> 50$ GeV

Table 5.3. The selection for reconstructed photons.

Figure 5.32. A scatter plot of  $\beta\gamma ct_{\text{REC}}$  versus  $\beta\gamma ct_{\text{TRUE}}$ . Histogram profile is superimposed and fitted with a linear function.

start to flatten out due to the finite size of the ECAL. When the neutralino lifetime is comparable with the maximum length of the ECAL, an increasing number of neutralinos will decay outside the bounds of the ECAL producing an undetectable photons with no appreciable variations in the  $\beta\gamma ct_{\text{REC}}$  distribution. Therefore, the distribution of the reconstructed flight path will have an upper limit which is dependent on the size of the ECAL.

Figure 5.37 shows the average value of the reconstructed flight path distribution,  $\langle\beta\gamma ct_{\text{REC}}\rangle$  as a function of the  $C_{\text{grav}}$  parameter, which sets the neutralino lifetime  $c\tau$ . After a rapid increase of  $\langle\beta\gamma ct_{\text{REC}}\rangle$  at small values of  $C_{\text{grav}}$ , the distribution is shown to plateau when the neutralino lifetime is comparable with the size of the ECAL. The  $C_{\text{grav}}$  parameter (and therefore the neutralino lifetime) can be determined from the measurement of  $\langle\beta\gamma ct_{\text{REC}}\rangle$ , using the following function:

$$f(c\tau) = C_0 - \frac{C_1}{(c\tau)^{C_2}} \quad (5.30)$$

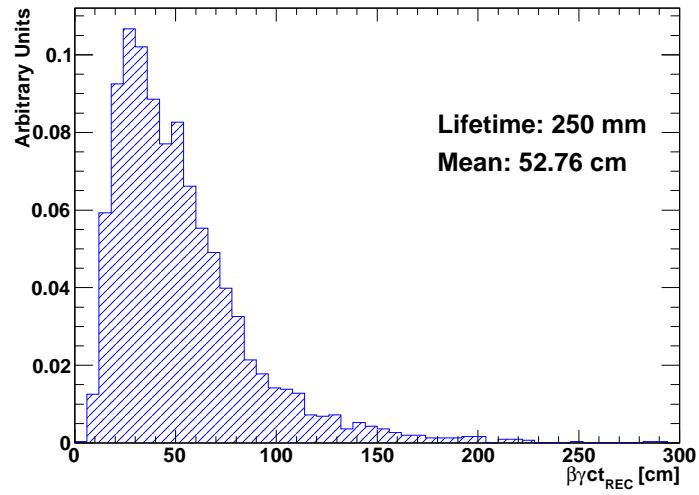


Figure 5.33. The  $\beta\gamma ct_{REC}$  distribution for  $ct = 250$  mm.

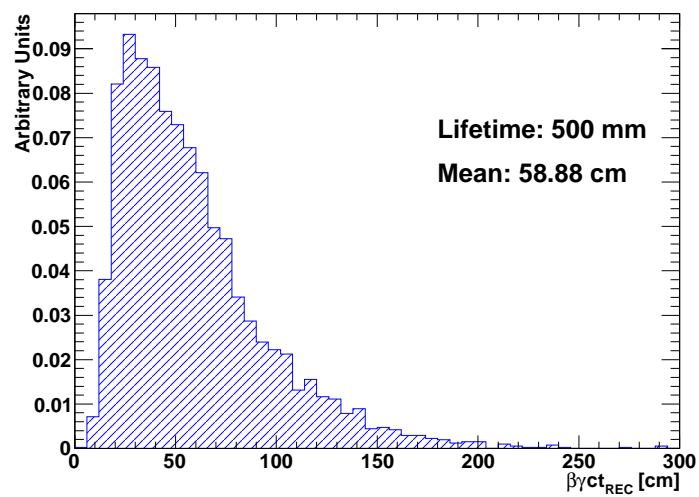


Figure 5.34. The  $\beta\gamma ct_{REC}$  distribution for  $ct = 500$  mm.

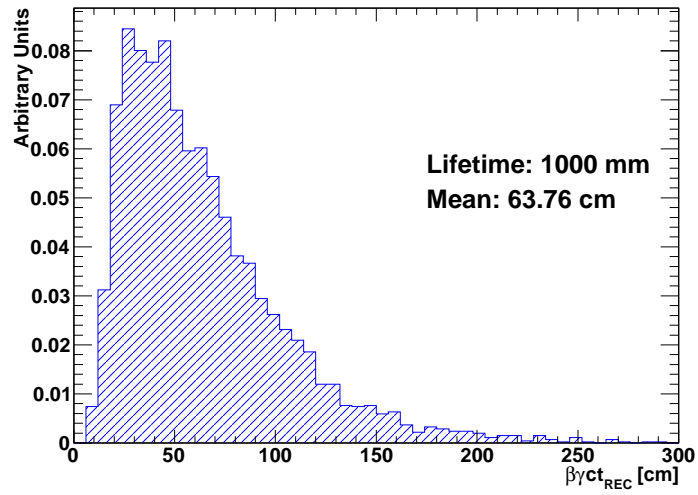


Figure 5.35. The  $\beta\gamma ct_{REC}$  distribution for  $ct = 1000$  mm.

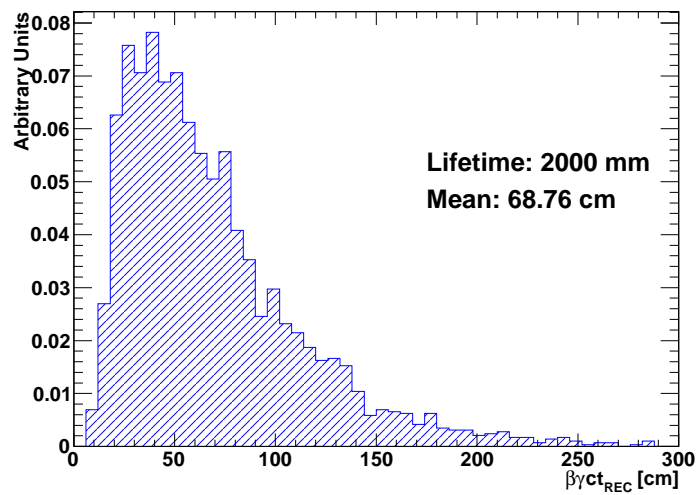
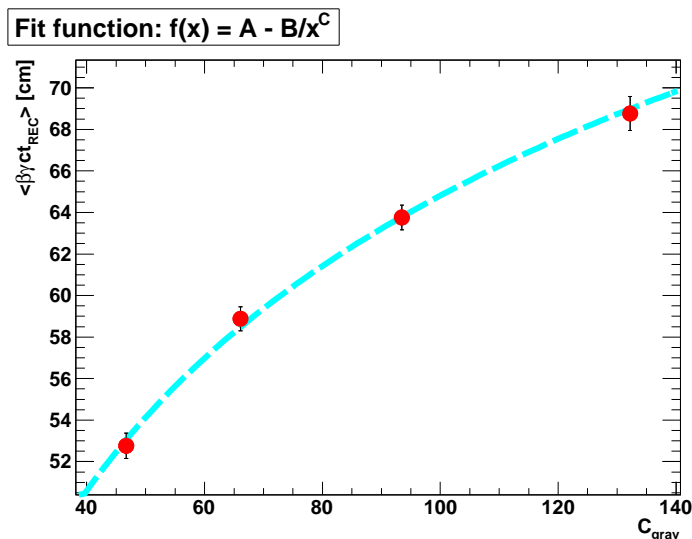


Figure 5.36. The  $\beta\gamma ct_{REC}$  distribution for  $ct = 2000$  mm.



**Figure 5.37.** The  $\langle \beta \gamma ct_{REC} \rangle$  distribution as a function of  $C_{grav}$  parameter. The fit function of Equation 5.30 is superimposed.

where  $C_0$  represents the asymptotic value for  $\langle \beta \gamma ct_{REC} \rangle$  for large values of neutralino lifetime. The parameter values extracted from the fit are listed in Table 5.4.

$C_0$	$C_1$	$C_2$
$3.078 \cdot 10^{+2}$	$3.234 \cdot 10^{+2}$	$6.205 \cdot 10^{-2}$

**Table 5.4.** The fit parameters for Equation 5.30.

The efficiency of the OP selection used in this analysis (and shown in Table 5.3) is strongly dependent on the neutralino lifetime. Figure 5.38 shows the efficiency of the OP photon selection as a function of the  $C_{grav}$  parameter, where for small values of  $C_{grav}$  (i.e. small neutralino lifetimes) is very low due to the fact that most of the photons originate from the interaction point and are therefore rejected. Then, an increase in the efficiency is encountered until a maximum is reached at around  $C_{grav} = 93.5$ . For large values of  $C_{grav}$ , corresponding to large neutralino lifetimes, the efficiency decreases since most of the neutralinos will decay outside the ECAL. Therefore, a combination of both  $\langle \beta \gamma ct_{REC} \rangle$  and selection efficiency measurement can be used in order to obtain a precise determination of the  $C_{grav}$  parameter.

Figure 5.39 shows the dependence of the efficiency selection from  $C_{grav}$  only for true OP photons, i.e. for photons from those neutralinos which have a true decay path length between 40 and 100 cm and  $\beta_{\tilde{\chi}_1^0} < 0.67$ . The true value of neutralino decay path length and the speed  $\beta_{\tilde{\chi}_1^0}$  are obtained from Monte Carlo information. As expected, when only true long-lived and relatively slow neutralinos are considered, the efficiency of the OP selection is not completely dependent on the value of  $C_{grav}$ .

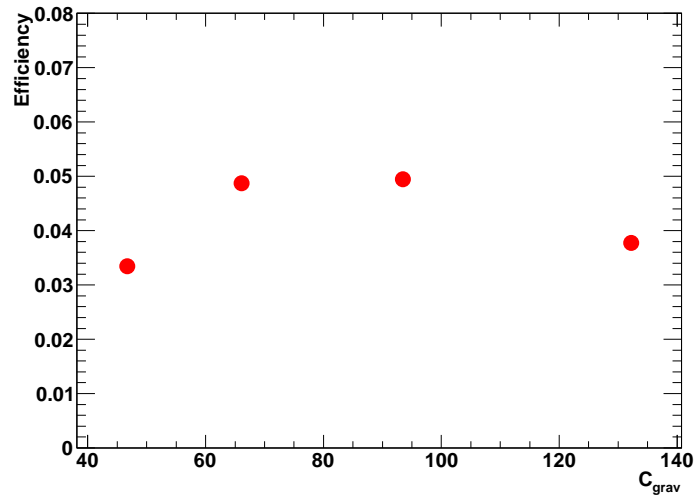


Figure 5.38. The efficiency of OP photon selection as a function of  $C_{grav}$  parameter.

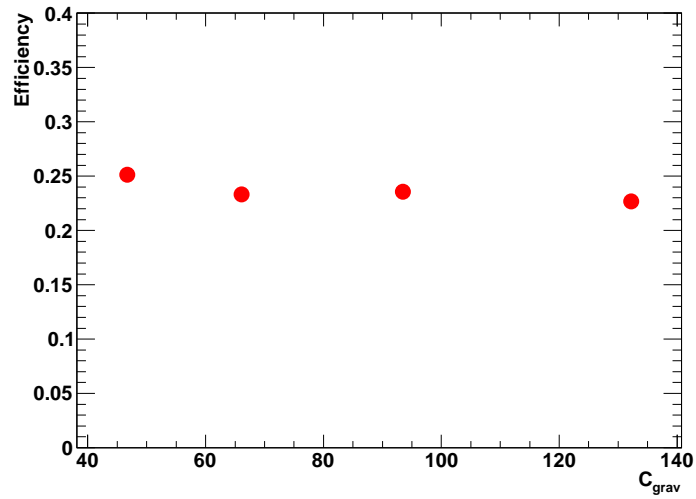


Figure 5.39. The efficiency of OP photon selection as a function of  $C_{grav}$  parameter, where only neutralinos with a true flight path between than 40 and 100 cm and  $\beta_{\chi_1^0} < 0.67$  are considered.

## Chapter 6

# Identification of SUSY events with photons

This chapter is devoted to the description of the experimental strategy to identify physics phenomena beyond the SM with large missing transverse energy and high  $P_T$  photons in the final state. Although a model-independent approach is followed, the study is focused on GMSB  $\tilde{\chi}_1^0 \rightarrow \tilde{G}\gamma$  events. Section 6.1 describes the experimental signature for new physics phenomena with high  $P_T$  photons in the final state. The main backgrounds are discussed in Section 6.2. Finally, the observables used for GMSB event selection are introduced in Section 6.3.

### 6.1 Signature of new physics with photons

In general, new physics phenomena are predicted to have very distinctive experimental signatures, allowing for a good rejection of SM backgrounds and high discovery potential with the early LHC data. In particular, SUSY models with high  $P_T$  photons in the final state are commonly considered as benchmarks for the discovery of physics beyond the SM. A sketch of a typical SUSY process with photons in the transverse plane is shown in Figure 6.1.

The most important features of this kind of events are:

1. High  $P_T$  photons from the decay of unstable SUSY particles, resulting in large electromagnetic energy deposits in the ECAL. The photons usually appear to be isolated, i.e. very low hadronic/electromagnetic activity can be detected near the photon energy deposit;
2. Large energy imbalance in the transverse plane, due to the LSPs produced at the end of the SUSY chains. These massive, stable and weakly-interactive particles usually escape detection, resulting in a net missing transverse momentum (the black, solid arrow in Figure 6.1);
3. Many quarks produced in the decay chains, which form high  $P_T$  jets detected as large energy deposits in the HCAL. Focusing on the GMSB process shown in Figure 3.4, the typical number of quarks produced in the decay chain is four, resulting in at least four high  $P_T$  jets in the final state.

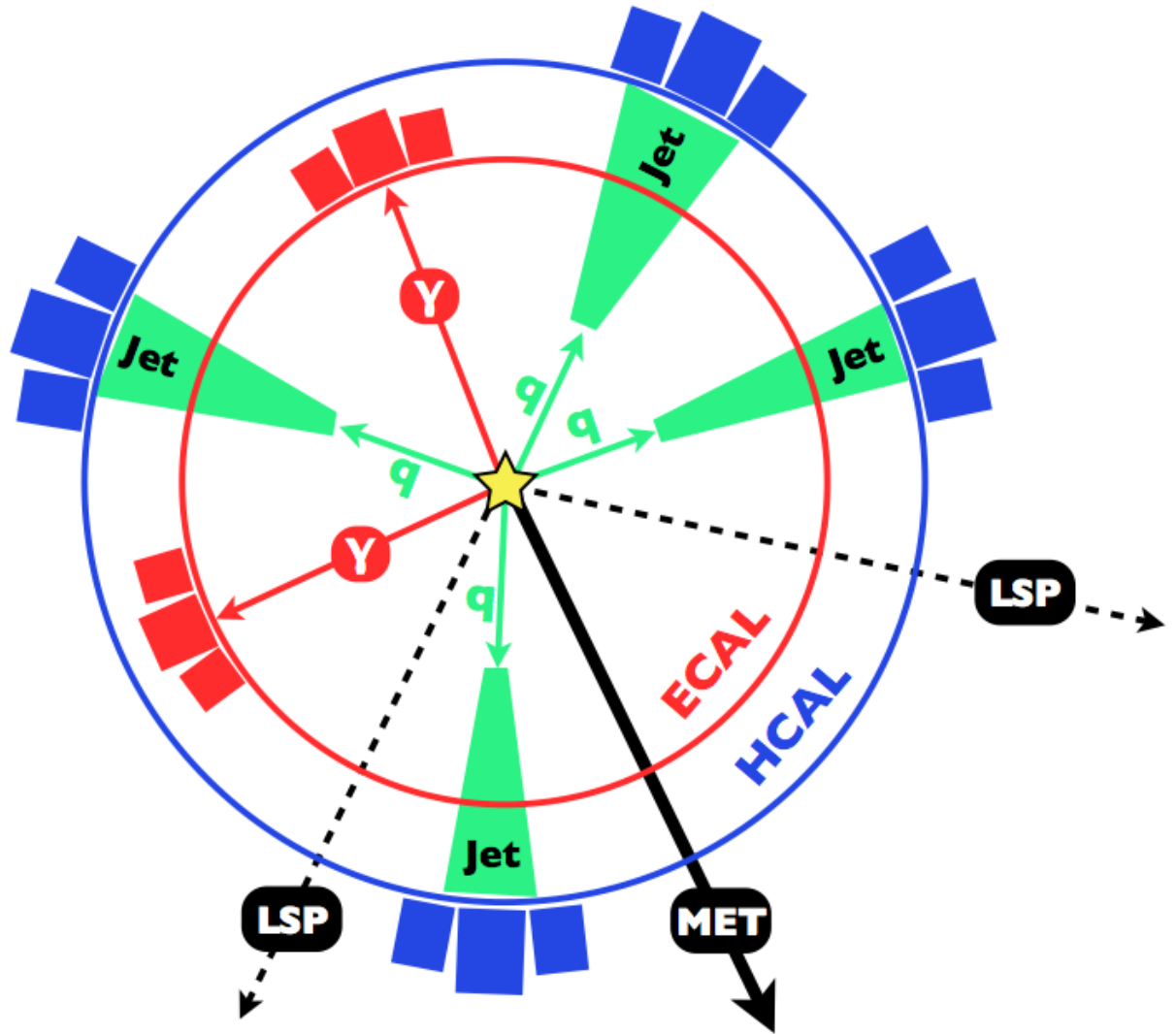


**Figure 6.1.** A SUSY process in the transverse plane, inside an HEP detector. The yellow star indicates the interaction point.

The final state  $\tilde{\chi}_1^0 \rightarrow \tilde{G}\gamma$  will be considered as the benchmark channel for this study.

## 6.2 Sources of background

In this section the most important backgrounds for the GMSB  $\tilde{\chi}_1^0 \rightarrow \tilde{G}\gamma$  final state are discussed. Irreducible SM backgrounds, i.e. events with real missing transverse energy and high  $P_T$  photons in the final state, are negligible. Furthermore there are no other SUSY processes that can mimic the experimental signature of  $\tilde{\chi}_1^0 \rightarrow \tilde{G}\gamma$  decay. The main backgrounds are instead reducible and arise from SM processes with misidentified photons and/or mismeasured missing transverse energy. Another source of background is represented by the emission of bremsstrahlung photons produced from the interaction of charged particles with the layers of the tracker. In the following, the backgrounds are divided in two categories according to the nature of the event:

- **In-time background:** this category includes some SM processes with large cross section with respect to the GMSB neutralino production, where the measured ECAL time of the photon candidate cluster is comparable with the time of a pointing photon from the interaction vertex of CMS;
- **Off-time background:** this category includes events not coming from the LHC proton - proton collisions. Since the reconstructed time is usually very large for these events, they represent an important background in the case of non-zero neutralino lifetime.

### 6.2.1 In-time backgrounds

#### QCD events

QCD events represent the background with the largest total cross section for this analysis. The main characteristic of QCD events is the high multiplicity of hadronic jets, produced by the fragmentation of light quarks and gluons. The processes leading to the formation of jets are the following:

- $q^i q^j \rightarrow q^i q^j$ ;  $q^i \bar{q}^i \rightarrow q^j \bar{q}^j$ ;  $q^i \bar{q}^i \rightarrow gg$
- $q^i g \rightarrow q^i g$ ;  $gg \rightarrow q^i \bar{q}^i$ ;  $gg \rightarrow gg$
- semi-hard interactions between the partons constituting the incoming protons

where  $q, g$  represent the generic light quark and the gluon respectively and the indexes  $i, j$  are the different flavors of the quarks. All these interactions are two body processes described at the tree-level by a cross section proportional to the square of the strong coupling constant,  $\alpha_s^2$ .

QCD events can mimic the signature of  $\tilde{\chi}_1^0 \rightarrow \tilde{G}\gamma$  decay due to the presence of both fake reconstructed photons and fake missing transverse energy. In fact, a  $\pi^0$  produced during the jet fragmentation, can be misinterpreted as a high  $P_T$  photon due to the  $\pi^0 \rightarrow \gamma\gamma$  decay. Since the majority of  $\pi^0$ s are detected inside hadronic jets, strict requirements on both calorimeter and tracker isolation can be

used to drastically reduce the QCD background. In addition, those  $\pi^0$ s which pass the isolation criteria, i.e.  $\pi^0$ s which escape from the jet cone and are therefore reconstructed as isolated energy deposits in the ECAL, can be distinguished from isolated photons by applying some photon ID requirements based on the cluster shape, as discussed in Appendix A.

Furthermore, although QCD events have no intrinsic missing transverse energy because of the suppression of neutrino production, a large amount of missing transverse energy can be found mostly because of mis-reconstructed energy in the calorimeters or energy lost in the detector cracks.

QCD events generated at center of mass energy  $\sqrt{s} = 7$  TeV and in a wide  $\hat{P}_T$  range are used for this analysis, where  $\hat{P}_T$  is the transverse momentum of one of the two partons in the rest frame of the hard process. The event sample size, the cross section  $\sigma$  at the leading order and the equivalent integrated luminosity for each  $\hat{P}_T$  bin are listed in Table 6.1.

### Photon plus Jet events

QCD events with a direct photon production are commonly referred as “ $\gamma$ +Jet” events. Direct photon production at the LHC is described by the following processes:

- $q^i \bar{q}^j \rightarrow g\gamma$ ;
- $gg \rightarrow g\gamma$ ;
- $q^i g \rightarrow q^i \gamma$ .

The  $\gamma$ +Jet events represent an important background source for this analysis because of the presence of one real isolated prompt photon in the final state. In addition, fake missing transverse energy is also expected, due to the same effects discussed for the QCD events.

Although the presence of a real, high  $P_T$ , isolated photon can mimic the signature of the signal, the event topology is very different between  $\gamma$ +Jet and GMSB events. In fact,  $\gamma$ +Jet events are characterized by a lower jet multiplicity than the signal. A requirement on the minimum number of jet above a threshold in  $P_T$  can therefore reject a large fraction of this background.

Monte Carlo samples generated at center of mass energy  $\sqrt{s} = 7$  TeV and in a wide  $\hat{P}_T$  range are used for this analysis. The event sample size for each  $\hat{P}_T$  bin, the cross section  $\sigma$  at the leading order and the equivalent integrated luminosity are listed in Table 6.1.

### $t\bar{t}$ events

Given the large cross section at the LHC, the production of  $t\bar{t}$  pairs is an important source of reducible backgrounds for this analysis. The main  $t\bar{t}$  production processes are:

- $gg \rightarrow t\bar{t}$
- $q^i \bar{q}^i \rightarrow t\bar{t}$

The top quark decay nearly 100% of the times into a W boson plus a b quark. Most of the fake photons come from mis-identified electrons (where track reconstruction has failed) produced in the leptonic decay of W bosons:

$$W \rightarrow e + \nu \quad (6.1)$$

Also isolated  $\pi^0$ s, produced during the hadronization of light quarks from hadronic W decays, give a small contribution to the fake photon rate. In addition, large missing transverse energy is expected due to high energy neutrinos produced in leptonic W decays. Leptonic and semi-leptonic decays of B hadrons, produced in the hadronization of b quarks, give a small contribution to the fake photon rate and to the missing transverse energy of the event, because of the softer  $P_T$  spectrum of the decay products.

The majority of  $t\bar{t}$  is easily rejected by requiring a tight tracking isolation for the energy deposit in the ECAL. In fact, because of its electric charge, the electron from W decay is usually detected by the tracking system and it can be therefore distinguished from a neutral photon.

The event sample size, the cross section  $\sigma$  at the leading order and the equivalent integrated luminosity are listed in Table 6.1.

In-time backgrounds			
Dataset	$N_{gen}$	$\sigma$ [fb]	$\mathcal{L}_{int}^{eq}$ [fb] $^{-1}$
QCD samples			
qcd_50_80	518465	6.371E+09	8.138E-05
qcd_80_120	2713621	7.861E+08	3.452E-03
qcd_120_170	263188	1.154E+08	2.281E-03
qcd_170_300	1677297	2.434E+07	6.891E-02
qcd_300_500	2941995	1.206E+06	2.439E-00
qcd_500_INF	1455265	5.981E+04	2.433E+01
Photon + Jet samples			
pj_50_80	109730	2.723E+06	4.030E-02
pj_80_120	110827	4.462E+05	2.484E-01
pj_120_170	122281	8.443E+04	1.448E+00
pj_170_300	125128	2.255E+04	5.549E+00
pj_300_500	107606	1.545E+03	6.965E+01
pj_500_INF	106895	9.230E+01	1.158E+03
$t\bar{t}$ sample			
ttbar	632010	9.430E+04	6.702E+00

**Table 6.1.** The number of generated events  $N_{gen}$ , the cross section  $\sigma$  at the leading order and the equivalent integrated luminosity  $\mathcal{L}_{int}^{eq}$  for the in-time background samples.

### 6.2.2 Off-time backgrounds

#### Cosmic rays

Cosmic rays represent the major source of off-time background for the GMSB analysis. Cosmic rays are particles originating from outer space that hit on the Earth's atmosphere. The majority of these particles (about 90%) are protons, while the remaining are electrons, helium nuclei and heavier elements.

When the cosmic rays approach the Earth they begin to collide with the nuclei of atmospheric gases. These collisions result in the production of a particle shower mainly composed by pions and kaons which decay into muons. Because muons do not interact strongly with the atmosphere, and because of the relativistic effect of time dilatation in the Earth's reference frame many of these muons are able to reach the Earth surface and even penetrate underground for significant depths.

Cosmic background muons which reach the CMS detector are seen to interact with the detector material, and in the process will release high energy bremsstrahlung radiation. Since these particles are not generated at the interaction point, the ECAL energy deposits exhibit a reconstructed time very different than the reconstructed time of pointing photons. For this reason, bremsstrahlung radiation from cosmic muons mimic the experimental signature of off-pointing photons from long-lived  $\tilde{\chi}_1^0$  decay.

The cosmic sample used for this study consists of about 7M events simulated with the 3.8 T CMS magnetic field.

#### Beam halo

Beam halo refers to a cloud of particles which do not emanate from the proton - proton collisions. This halo consists of muons, mesons and baryons coming from beam losses around the beam core or from collisions of the beam protons with the residual gas in the beam pipe. The beam halo particles are therefore expected to accompany the beam collision events. They typically impact the detector at large pseudorapidity, i.e. parallel with the direction of the proton beams. The particles that form the beam halo are emanating from the proton beam and are extremely energetic. For this reason, the immediate effect of such events when they overlap with otherwise normal collision events is to produce large missing transverse energy.

In addition, the muonic component of the beam halo can emit bremsstrahlung radiation which produces energy deposits in the ECAL with large reconstructed time.

The beam halo sample used for this study consists of about 6M events.

## 6.3 GMSB event selection

The selection strategy is based on three main ingredients:

1. Photon identification;
2. Reconstruction of the missing transverse energy (MET);
3. Jet reconstruction.

A detailed description of the photon identification and jet/MET reconstruction techniques adopted by CMS is provided. In addition, the distribution of each selection variable for GMSB signal and the different source of background is presented. Since the variables are in general correlated, each of them is shown considering a reduced event sample, obtained after the application of a loose selection on the other variables except the one under study. The loose selection is summarized in Table 6.2, where each of the variables will be discussed in the following sections. The GMSB sample with  $c\tau = 500$  mm is used as signal and only the ECAL barrel region ( $|\eta| < 1.4$ ) is considered. Finally, all distributions are normalized to unity.

The commissioning of the selection variables with  $1.2 \text{ pb}^{-1}$  collision data at  $\sqrt{s} = 7$  TeV will be also presented. The dataset used for this comparison is */EG/Run2010A-PromptReco-v4/RECO* and the trigger used for the selection is *HLT\_Photon10\_L1R OR HLT\_Photon15\_L1R*. Comparison plots between data and Monte Carlo are produced selecting  $\gamma$ +Jet events. Both MC and data are required to have at least one photon candidate satisfying the selection criteria shown in Table 6.3.

MET	$> 15$ GeV
$N_{jet}$	$> 1$
$ \eta $	$< 1.4$
$P_T(\gamma)$	$> 15$ GeV
$S_{minor}$	$< 0.5$
HCAL Iso	$\left\{ \begin{array}{l} \sum \text{HCAL}/E(\gamma) < 0.3 \\ \sum \text{HCAL} < 6.5 \text{ GeV} \end{array} \right.$
ECAL Iso	$\left\{ \begin{array}{l} \sum \text{ECAL}/E(\gamma) < 0.3 \\ \sum \text{ECAL} < 5.5 \text{ GeV} \end{array} \right.$
TRK Iso	$\left\{ \begin{array}{l} \sum P_T/P_T(\gamma) < 0.4 \\ N_{tracks} < 5 \end{array} \right.$

**Table 6.2.** Loose selection criteria.

$ \eta $	$< 1.4$
$P_T(\gamma)$	$> 25$ GeV
$S_{minor}$	$< 0.5$
HCAL Iso	$\left\{ \begin{array}{l} \sum \text{HCAL}/E(\gamma) < 0.1 \\ \sum \text{HCAL} < 4 \text{ GeV} \end{array} \right.$
ECAL Iso	$\left\{ \begin{array}{l} \sum \text{ECAL}/E(\gamma) < 0.1 \\ \sum \text{ECAL} < 4 \text{ GeV} \end{array} \right.$
TRK Iso	$\left\{ \begin{array}{l} \sum P_T/P_T(\gamma) < 0.2 \\ N_{tracks} < 5 \end{array} \right.$

**Table 6.3.** Photon selection criteria for data-MC comparison plots.

### 6.3.1 Photon identification

Photon reconstruction in CMS starts with the identification of energy deposits in the ECAL according to dedicated supercluster algorithms, as described in Section 4.4. Energy, momentum, cluster shape and isolation variables are then calculated and associated with the photon candidate.

A good variable to distinguish between GMSB signal and background is the  $P_T$  of the photon candidate. In fact, photons from the decay of a massive particle such as the neutralino are expected to have a very tight  $P_T$  spectrum compared to photons from SM backgrounds. Figure 6.2 shows the distribution of  $P_T$  for GMSB signal and for SM backgrounds.

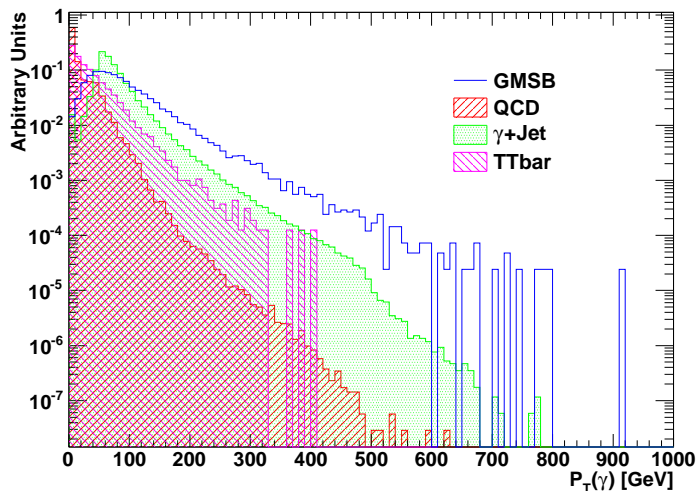


**Figure 6.2.** The distribution of  $P_T$  for GMSB signal and for different sources of SM background, after loose selection criteria of Table 6.2. All the distributions are normalized to unity.

In addition, cluster shape requirements and isolation criteria are also applied to achieve large background rejection.

#### Cluster shape

A large fraction of background events are removed by applying some requirements on the shape of the clusters. The minor axis  $S_{minor}$  has almost the same distribution for every kind of electromagnetic deposits and therefore it can be used to identify electromagnetic particles in the ECAL. Figure 6.3 shows the distribution of  $S_{minor}$  for GMSB signal and for SM backgrounds. As expected, GMSB events populate the region at lower values of  $S_{minor}$ , whilst background (with the exception of  $\gamma$ +Jet, due to the presence of a real, isolated photon) populates areas at larger values.

As discussed in Section 5.2, the major axis  $S_{major}$  plays a fundamental role in the selection of OP photons. For this reason, no requirement on  $S_{major}$  is applied in order to allow a possible measurement of the neutralino lifetime. The distribution of  $S_{major}$  for GMSB signal and SM backgrounds is shown in Figure 6.4.

Figure 6.5 shows the distribution of  $S_{minor}$  and  $S_{major}$  in data and simulation, confirming that the ECAL response is well reproduced by the simulation.

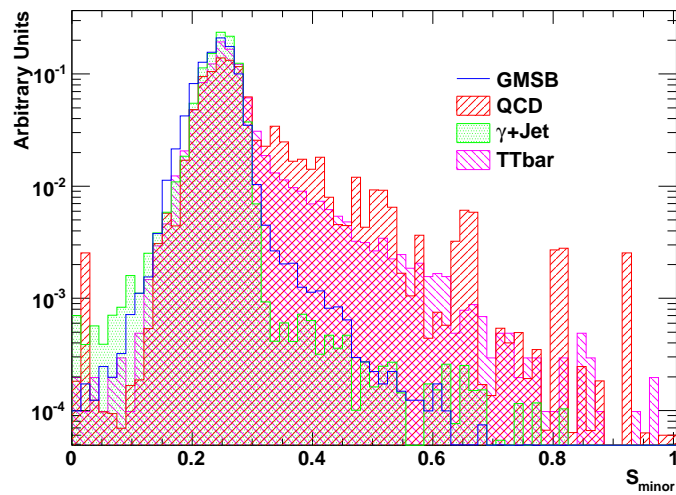


**Figure 6.3.** The distribution of  $S_{minor}$  for GMSB signal and for different sources of SM background, after loose selection criteria of Table 6.2. All the distributions are normalized to unity.

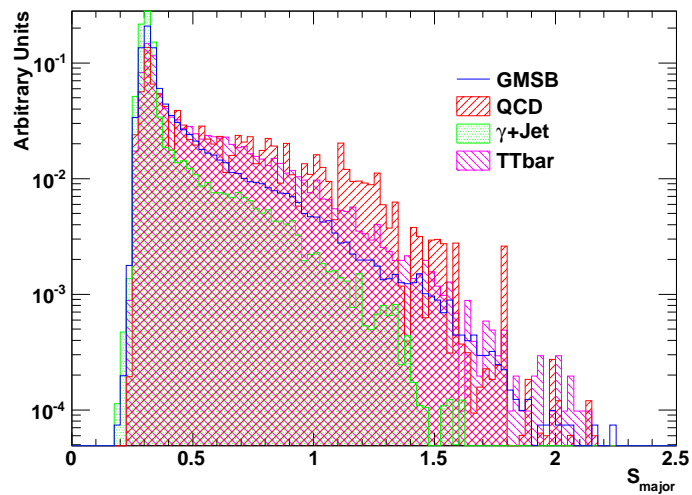
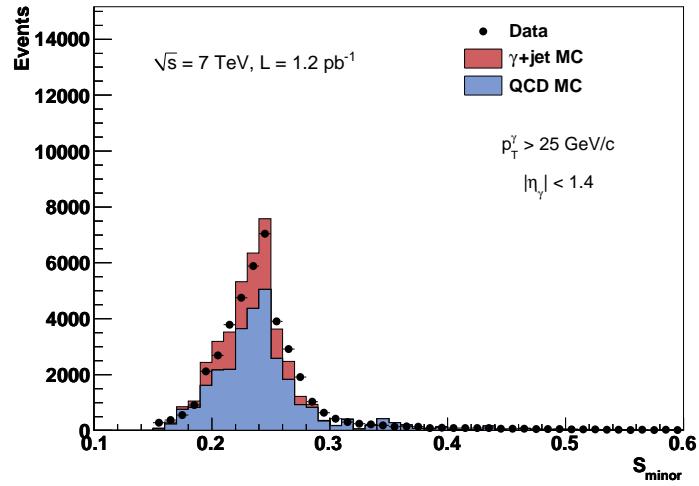
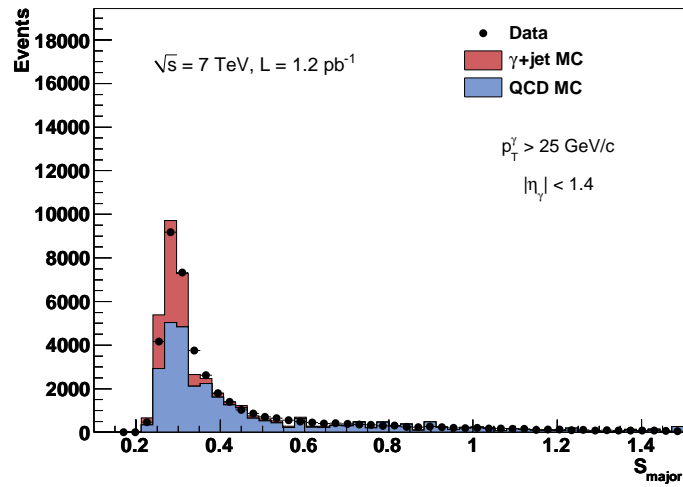


**Figure 6.4.** The distribution of  $S_{major}$  for GMSB signal and for different sources of SM background, after loose selection criteria of Table 6.2. All the distributions are normalized to unity.



(a)



(b)

**Figure 6.5.** Distribution of a)  $S_{minor}$  and b)  $S_{major}$  for data and simulation, after photon selection criteria of Table 6.3. Monte Carlo distribution is normalized to the number of events in data.

### Isolation

In this analysis, three requirements on photon isolation are applied:

- **HCAL isolation:** sum of the HCAL reconstructed energy within a  $\Delta R = 0.4$  cone behind the photon candidate and normalized to the photon energy, with

$$\Delta R = \sqrt{(\eta_{SC} - \eta)^2 + (\phi_{SC} - \phi)^2} \quad (6.2)$$

where  $\eta_{SC}$  and  $\phi_{SC}$  are the coordinates of the supercluster position on the ECAL surface;

- **ECAL isolation:** sum of the ECAL reconstructed energy not belonging to the photon cluster within a  $\Delta R = 0.4$  cone around the photon candidate and normalized to the photon energy;
- **Tracking isolation:** sum of the  $P_T$  and number of the tracks in a  $\Delta R = 0.35$  cone from the photon direction. Sum of  $P_T$  is normalized to the momentum of the photon candidate.

In addition, the relative HCAL and ECAL isolation cuts are limited by absolute thresholds in order to prevent energy cuts which are tighter than the noise level of the calorimeters. In fact, cutting tighter than the average noise level does not bring significant improvement in the signal over background ratio, but rapidly decreases signal efficiency. Figures 6.6, 6.7 and 6.8 show respectively the distributions of HCAL, ECAL and tracking isolation variables for GMSB signal and SM backgrounds.

Isolation requirements are very efficient in rejecting QCD and  $t\bar{t}$  backgrounds. In particular,  $t\bar{t}$  events are strongly suppressed by tracking isolation. In fact, the misidentified electron produced by the W boson decay is expected to be also detected as a charged particle in the tracker, leading to the prominent peak at 1 in the  $\sum P_T(\text{tracks})/P_T(\gamma)$  distribution shown in Figure 6.8a).

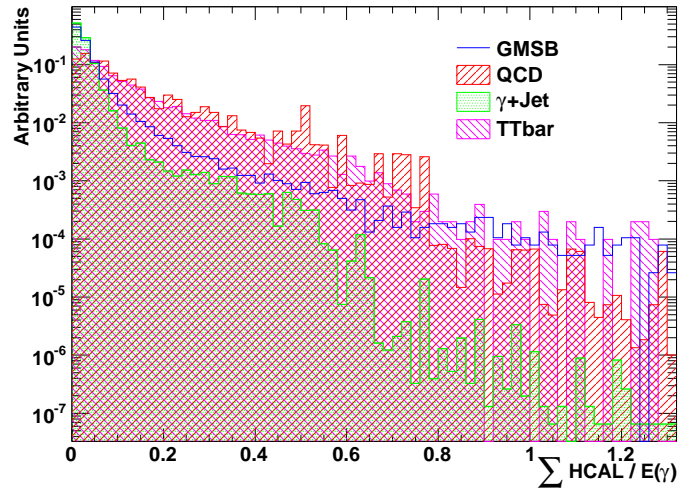
On the other hand,  $\gamma$ +Jet events cannot be rejected by any isolation cut, due to the presence of a real, isolated photon in the final state. It can be noted that photons from GMSB events are less isolated than the photons from  $\gamma$ +Jet events. In fact, because of the presence of many hadronic jets in the final state, the probability for a GMSB photon to come inside the jet cone is not negligible.

Figures 6.9, 6.10 and 6.11 show, respectively, the distribution of HCAL, ECAL and tracking isolation variables for data and simulation. The distributions exhibit a good agreement for both HCAL and ECAL isolation, whilst some disagreements still exist for tracking isolation variables.

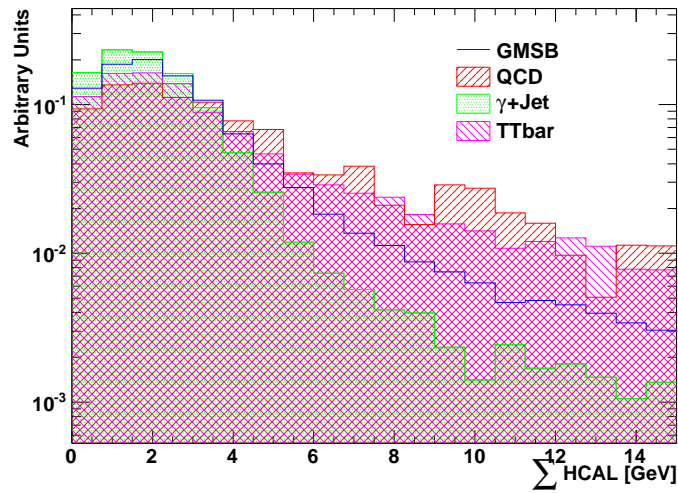
#### 6.3.2 MET reconstruction

In a particle collider the projection of the total momentum vector of the particles in the initial state on the plane transverse to the beam axis is almost zero. For this reason an overall energy balance in the transverse plane is expected for every collision.

The net momentum of outgoing particles in the transverse plane is commonly referred as *missing transverse energy* (MET). In SM processes, a small MET is predicted, mainly caused by detector effects and by non-detectable neutrinos produced

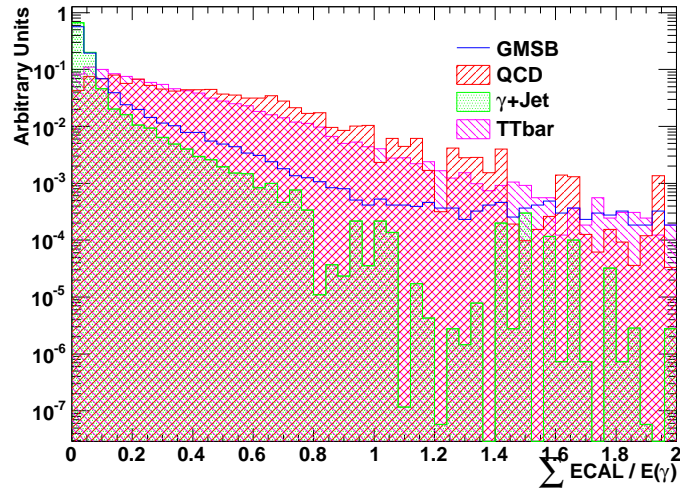


(a)

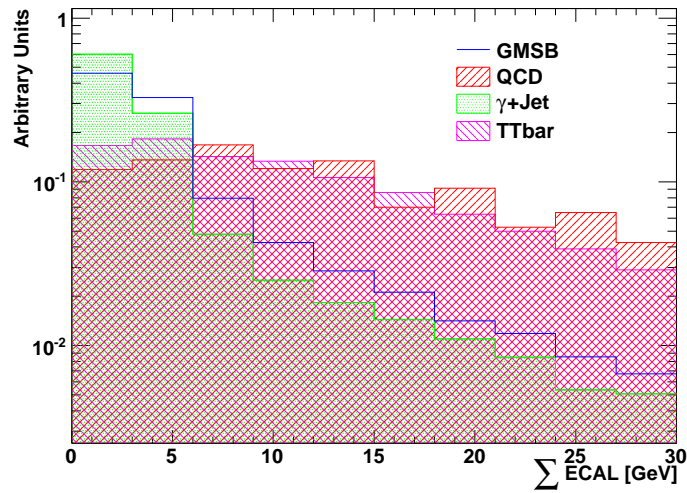


(b)

**Figure 6.6.** Distribution of a)  $\sum \text{HCAL}/E(\gamma)$  and b)  $\sum \text{HCAL}$  for GMSB signal and for different sources of SM background, after loose selection criteria of Table 6.2. All the distributions are normalized to unity.

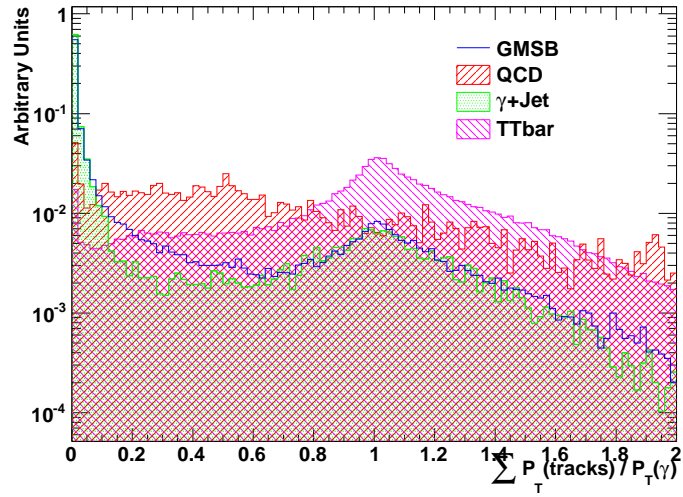


(a)

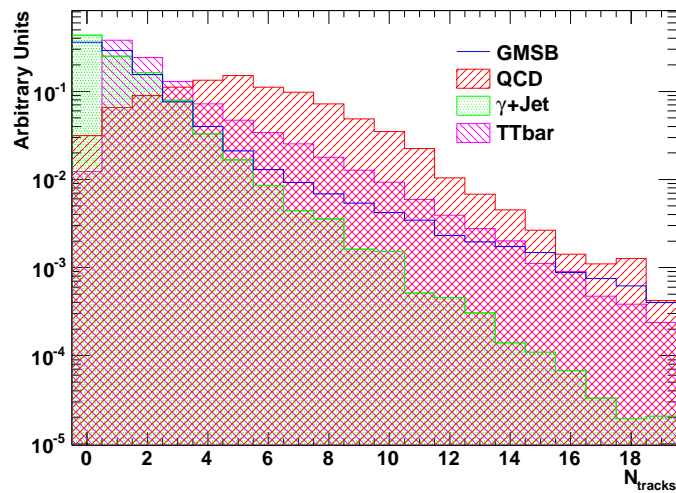


(b)

**Figure 6.7.** Distribution of a)  $\sum \text{ECAL}/E(\gamma)$  and b)  $\sum \text{ECAL}$  for GMSB signal and for different sources of SM background, after loose selection criteria of Table 6.2. All the distributions are normalized to unity.

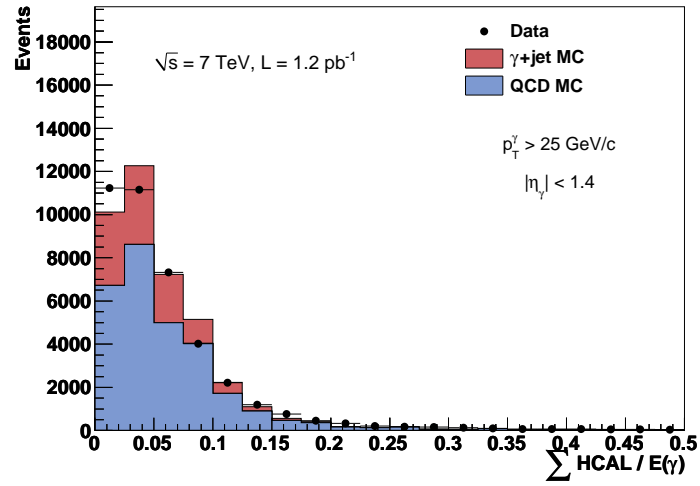


(a)

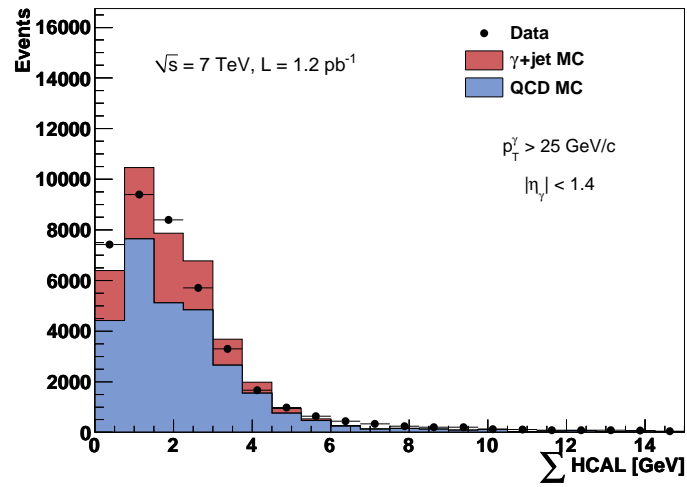


(b)

**Figure 6.8.** Distribution of a)  $\sum P_T(\text{tracks}) / P_T(\gamma)$  and b)  $N_{\text{tracks}}$  for GMSB signal and for different sources of SM background, after loose selection criteria of Table 6.2. All the distributions are normalized to unity.

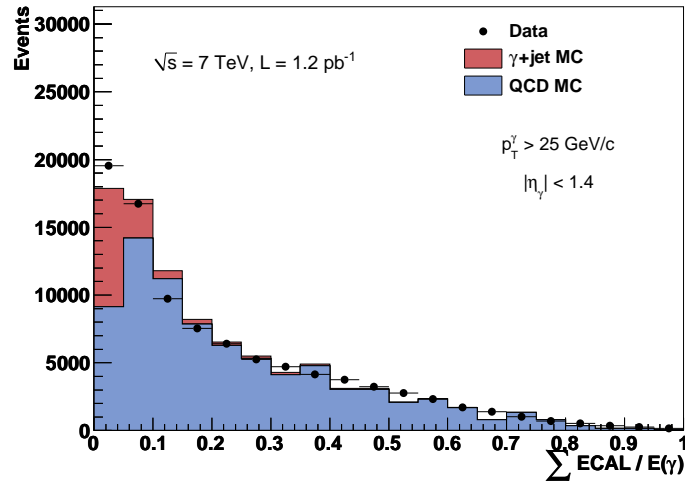


(a)

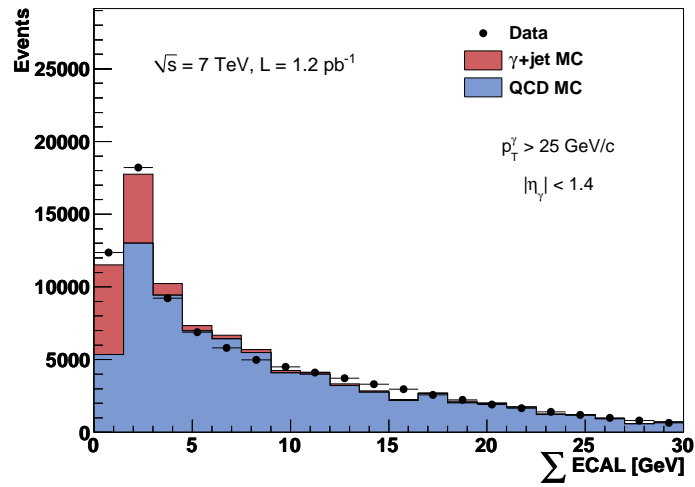


(b)

**Figure 6.9.** Distribution of a)  $\sum \text{HCAL}/E(\gamma)$  and b)  $\sum \text{HCAL}$  for data and simulation, after photon selection criteria of Table 6.3. Monte Carlo distribution is normalized to the number of events in data.

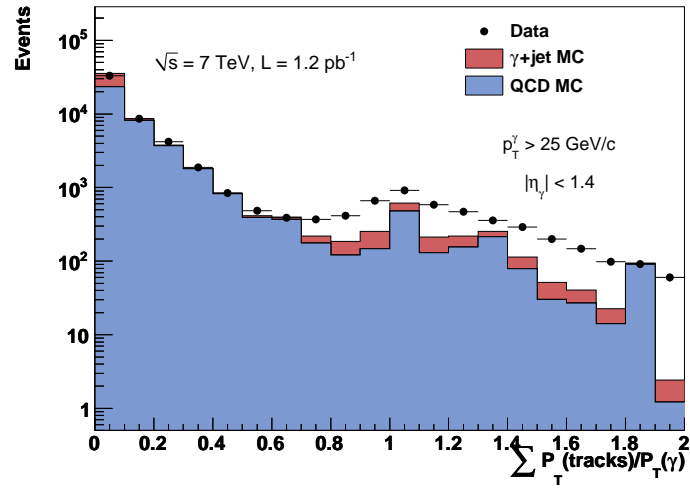


(a)

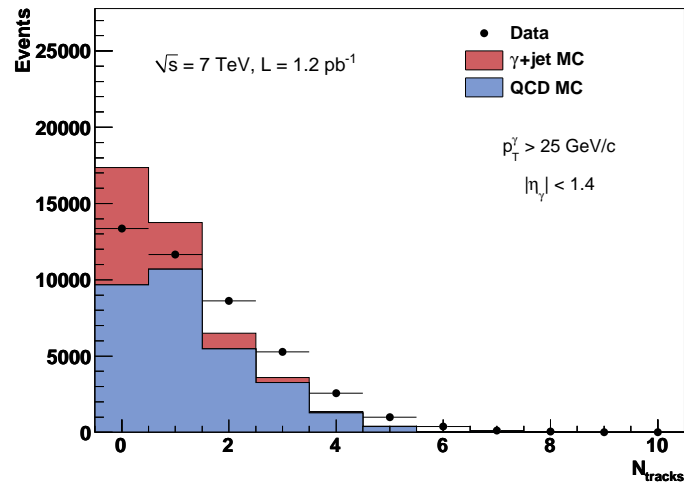


(b)

**Figure 6.10.** Distribution of a)  $\sum \text{ECAL}/E(\gamma)$  and b)  $\sum \text{ECAL}$  for data and simulation, after photon selection criteria of Table 6.3. Monte Carlo distribution is normalized to the number of events in data.



(a)



(b)

**Figure 6.11.** Distribution of a)  $\sum P_T(\text{tracks})/P_T(\gamma)$  and b)  $N_{\text{tracks}}$  for data and simulation, after photon selection criteria of Table 6.3. Monte Carlo distribution is normalized to the number of events in data.

in some electroweak processes. On the contrary, the expected MET in SUSY events is very large as a consequence of two high  $P_T$  LSP particles escaping detection.

Large MET is therefore one of the most distinctive signature of new physics processes. The preliminary step for MET calculation is the event reconstruction, which allows for the identification of (almost) all the particles in the final state of the event. The Particle Flow (PF) algorithm [74] ensures the best performance for event reconstruction and it will be therefore considered for this study. The PF event reconstruction combines the information from all CMS subdetectors to identify and individually reconstruct all the particles produced in proton - proton collisions, namely charged and neutral hadrons, photons, electrons and muons. The PF algorithm is composed of the following steps:

1. all the charged tracks linked to a single ECAL cluster are considered as electrons;
2. tracks compatible with photon conversions are found;
3. for each remaining track linked only to an ECAL cluster a muon or a charged hadron is created, whether compatible hits in muon chamber are found or not;
4. for each HCAL cluster, all linked tracks and all ECAL clusters linked to the tracks are considered in order to create charged hadrons. Any imbalance between the total energy measured by the calorimeters and the sum of the momenta measured by the tracking system is interpreted as a neutral hadron and/or a photon;
5. for all remaining ECAL (HCAL) clusters not linked to tracks, a photon (neutral hadron) is created.

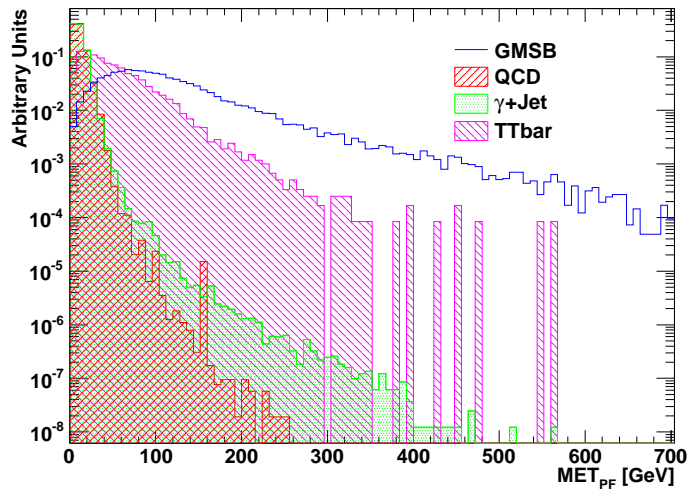
Once the event reconstruction is terminated, a list of PF candidates is available. These candidates are then used to calculate the MET vector (the black, solid arrow in Figure 6.1) as the opposite of the transverse momentum sum of all the particle candidates identified in the PF reconstruction step. The module of this vector represent the missing transverse energy of the event and it is defined as:

$$\text{MET}_{PF} = \sqrt{\left(E_x^{miss}\right)^2 + \left(E_y^{miss}\right)^2} \quad (6.3)$$

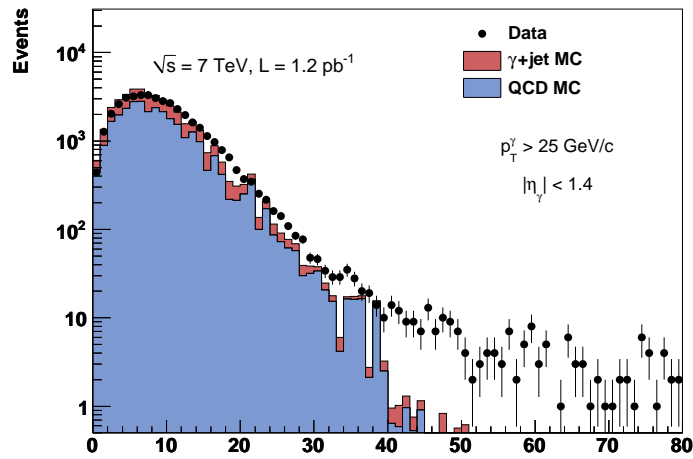
where  $E_x^{miss}$  and  $E_y^{miss}$  indicate the transverse momentum sum of all particles on the x and y axis respectively, and the ‘‘PF’’ subscript indicates that the MET has been calculated using the Particle Flow algorithm for the event reconstruction.

Figure 6.12 shows the distribution of  $\text{MET}_{PF}$  for GMSB signal and SM backgrounds. As expected, the signal has very large MET values compared to the SM backgrounds. As already discussed,  $t\bar{t}$  distribution exhibit a large tail compared to the other SM processes, due to the presence of undetectable neutrinos in the final state.

Figure 6.13 shows the distribution of  $\text{MET}_{PF}$  for data and simulation. The core of the distribution confirms an acceptable agreement. The discrepancies on the tail are due to unsolved problems in the implementation of PF algorithm still present in the version of CMS software used for this study (CMSSW\_3\_5\_6).



**Figure 6.12.** The distribution of  $\text{MET}_{PF}$  for GMSB signal and for different sources of SM background, after loose selection criteria of Table 6.2. All the distributions are normalized to unity.



**Figure 6.13.** The distribution of  $\text{MET}_{PF}$  for data and simulation, after photon selection criteria of Table 6.3. Monte Carlo distribution is normalized to the number of events in data.

### 6.3.3 Jet reconstruction

Because of the QCD confinement, particles carrying a color charge, such as quarks or gluons, cannot exist in free form. For this reason, they fragment into hadrons before being directly detected, becoming jets. A jet can be naively described as a narrow cone of hadrons and other particles produced by the hadronization of a quark or gluon. SUSY events are characterized by an intense hadronic activity caused by the hadronization of many quarks and gluons produced in the decay chains. This results in the reconstruction of several high  $P_T$  jets. On the other hand, the SM processes are usually characterized by a lower jet multiplicity.

As for the MET, jet reconstruction in CMS relies on PF particle candidates, which are clusterized according to dedicated jet algorithm. Multiple algorithms for jet reconstruction are currently available at CMS. In the following, the so-called “anti- $k_T$ ” jet algorithm with  $R = 0.5$  is considered. A detailed description of anti- $k_T$  algorithm can be found in [75].

The number of jets above a  $P_T$  threshold can be used as discriminating variable between GMSB signal and backgrounds. The  $P_T$  threshold allows to reject spurious jet not coming from the fragmentation of prompt quarks.

Figure 6.14 shows the number of reconstructed jets as a function of the  $P_T$  threshold, for GMSB events. For low  $P_T$  thresholds, the number of jets is typically very large due to spurious jet reconstruction. As the threshold increases, the number becomes smaller, allowing for the reconstruction of only true hard jets from high  $P_T$  quarks fragmentation. As already stated, the expected number of high  $P_T$  jets in signal events is four, resulting from the four quarks produced during the GMSB decay chains. For this reason, the choice of 25 GeV as  $P_T$  jet threshold appears to be quite reasonable because of the prominent peak at four in the  $N_{jet}$  distribution.

Figure 6.15 shows the distribution of  $N_{jet}$  with  $P_T > 25$  GeV for GMSB signal and SM backgrounds. Jet multiplicity is seen to have a large background rejection power especially for  $\gamma$ +Jet events, where a small jet multiplicity is expected.

The number of reconstructed jets is expected to be the most discriminating variable also for the off-time background. In fact, non collision events are characterized by a very low jet multiplicity. Figure 6.16 shows the distribution of  $N_{jet}$  with  $P_T > 25$  GeV for GMSB signal and for cosemics/beam halo events. It can be noted that the main sources of off-time backgrounds can be fully rejected by requiring at least three reconstructed jets in the event.

### 6.3.4 Measured time in the ECAL

As already discussed, the time measured with ECAL represents the most important variable to identify GMSB events in the case of long-lived neutralinos. In fact, a macroscopic lifetime would result in ECAL energy deposits from OP photons characterized by a large reconstructed time. Figure 6.17 shows the distribution of  $T_{REC}$  for GMSB signal ( $c\tau \sim 500$  mm) and SM backgrounds. It can be noted that GMSB distribution populates the region at large reconstructed time. As for  $S_{major}$ ,  $T_{REC}$  is planned to be used for a possible determination of neutralino lifetime, according to the strategy described in Chapter 5.

Di-photon candidates from  $\pi^0$  decays in Minimum Bias events are utilized for

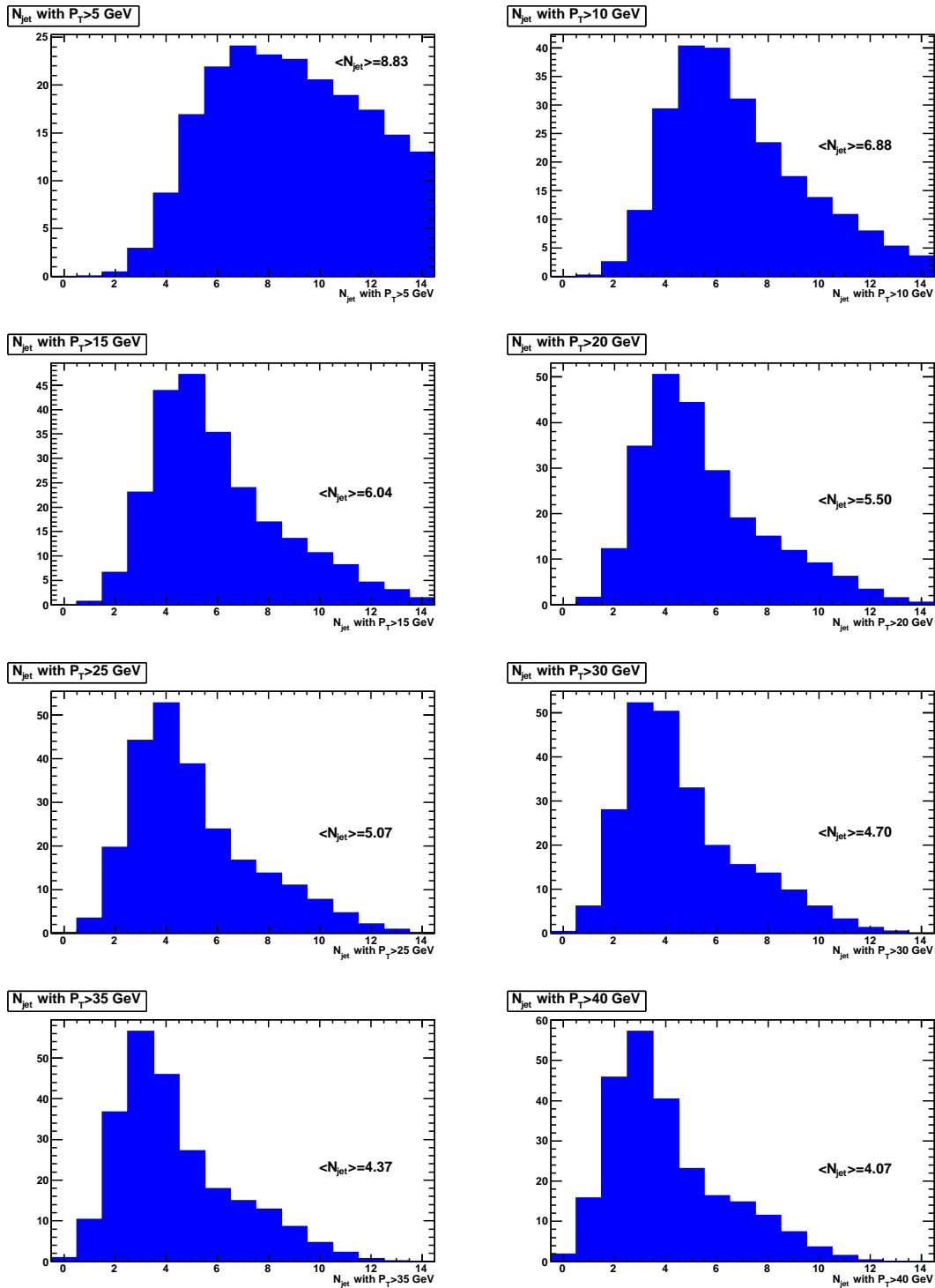
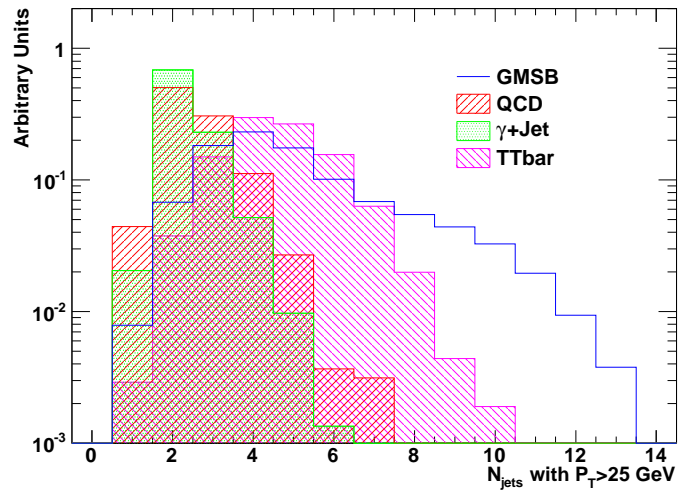
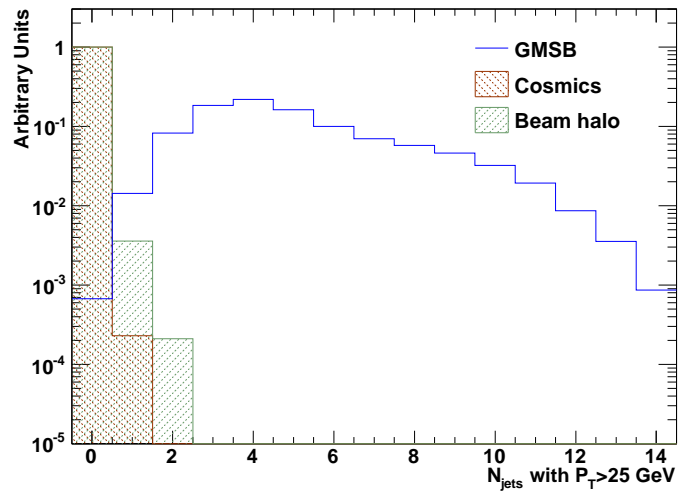


Figure 6.14. Number of reconstructed jets above a certain  $P_T$  threshold, for GMSB events.



**Figure 6.15.** Number of reconstructed jets with  $P_T > 25$  GeV for GMSB signal and for different sources of SM background, after loose selection criteria of Table 6.2. All the distributions are normalized to unity.



**Figure 6.16.** Number of reconstructed jets with  $P_T > 25$  GeV for GMSB signal and for the off-time backgrounds, after loose selection criteria of Table 6.2. All the distributions are normalized to unity.

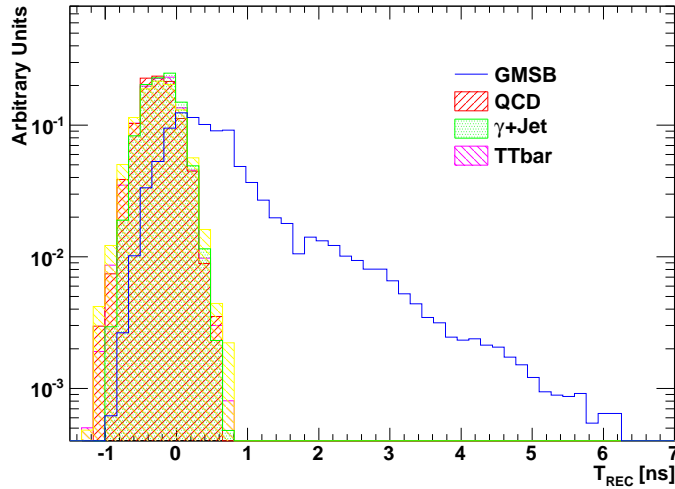


**Figure 6.17.** Measured time with the ECAL for GMSB signal and for different sources of SM background, after loose selection criteria of Table 6.2. All the distributions are normalized to unity.

the commissioning of the ECAL time. The MC sample used in this study consists of about 10M Minimum Bias event. Both MC and data are required to satisfy an optimized online selection of  $\pi^0 \rightarrow \gamma\gamma$  events. This selection is implemented in a HLT stream which is dedicated to the ECAL calibration with  $\pi^0$  [76].

The selection of  $\pi^0 \rightarrow \gamma\gamma$  decays is based on the following requirements:

- Photon candidate
  1. transverse momentum  $P_T > 0.8$  GeV;
  2. cluster shape  $E_{2 \times 2}/E_{CLU} > 0.83^1$ ;
- $\pi^0$  candidate (defined as a pair of photon candidates)
  1. transverse momentum  $P_T > 1.6$  GeV;
  2. the  $P_T$  sum of all clusters (excluding the two forming the  $\pi^0$  candidate) within  $\Delta R < 0.2$  and  $\Delta\eta < 0.05$  from  $\pi^0$  direction is required to be less than 50% of the  $P_T$  of the  $\pi^0$  candidate;
  3. reconstructed invariant mass  $0.06 \text{ GeV} < M_{\pi^0} < 0.22 \text{ GeV}$ .

Figure 6.18 shows the ECAL time resolution  $\sigma(t_1 - t_2)$  as a function of the variable  $A_{eff}/\sigma_n$ , defined in Section 5.2.1, for both data and MC simulation. The resolution is extracted from a fit to the  $(t_1 - t_2)$  distribution, where  $t_1$  and  $t_2$  are the measured time of the most energetic crystal of the two clusters from the photon candidate. Resolution has been fitted to a model described in Equation 5.6. It can be noted that the noise contribution  $N$  in the simulation is overestimated. Time resolution with 7 TeV data is then compared with the results on cosmic ray (Figure 6.19), exhibiting a good agreement.

<sup>1</sup>The variable  $E_{2 \times 2}$  corresponds to the highest energy value chosen between the four possible combinations of  $2 \times 2$  crystal arrays containing the central crystal.

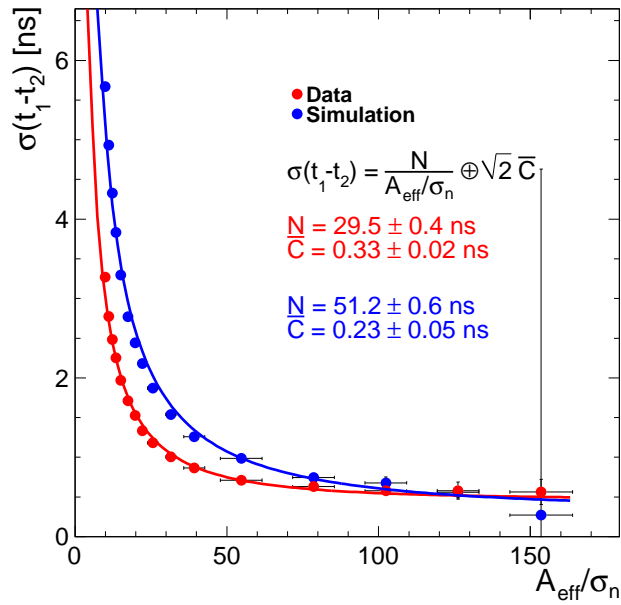


Figure 6.18. Time resolution with 7 TeV data and minimum bias simulation.

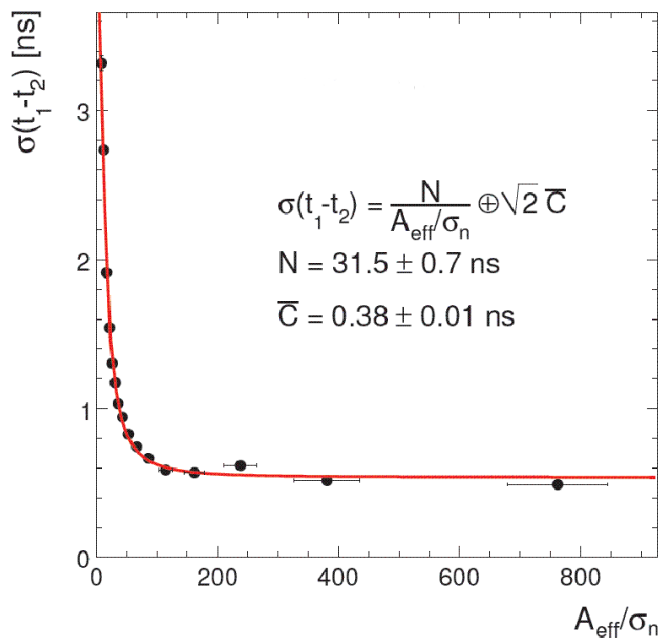
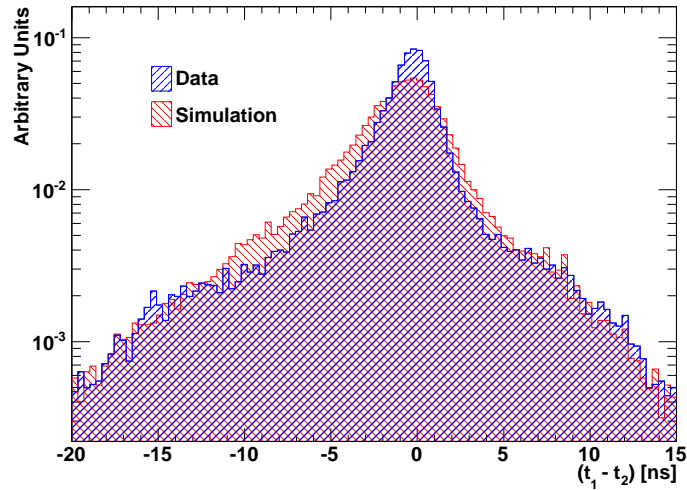


Figure 6.19. Time resolution with cosmic ray events [73].

Due to the importance in the lifetime reconstruction, the tails of the time resolution have to be under control. Figure 6.20 shows  $(t_1 - t_2)$  distribution for 7 TeV data and simulation, pointing out that the simulation reproduces accurately the tails in the distribution of time resolution. In particular, the agreement between data and simulation is confirmed by the percentage of events with  $|t_1 - t_2| > 0.8$  ns: 11% for data and 13% for the simulation.



**Figure 6.20.** Distribution of  $(t_1 - t_2)$  for 7 TeV data and minimum bias simulation.



# Chapter 7

## Analysis results

This section is devoted to the description of the event selection and the analysis strategy. Section 7.1 describes the event selection. Section 7.2 illustrates the exclusion limits on the GMSB model, obtained with a unbinned maximum likelihood fit. Finally, Section 7.3 is devoted to the discussion of the main systematics that affect the analysis.

### 7.1 Event selection

The selection of  $\tilde{\chi}_1^0 \rightarrow \tilde{G}\gamma$  starts with the identification of isolated photon candidates with large transverse momentum. Tight requirements on HCAL, ECAL and tracking isolation are applied to the photon candidate in order to obtain large rejection factor for most of the SM backgrounds. In addition, the minor axis  $S_{minor}$  is used to identify energy deposits in the ECAL produced by isolated photons and to reduce fake  $\gamma$ s from mis-identification of jets. Finally, only the region of the ECAL barrel is taken into consideration in this study. Photon identification requirements (in the following referred as *PhotonID*) are listed in Table 7.1 [77].

PhotonID	
$ \eta $	$< 1.4$
$S_{minor}$	$< 0.3$
HCAL Iso	$\left\{ \begin{array}{l} \sum \text{HCAL}/E(\gamma) < 0.053 \\ \sum \text{HCAL} < 2.4 \text{ GeV} \end{array} \right.$
ECAL Iso	$\left\{ \begin{array}{l} \sum \text{ECAL}/E(\gamma) < 0.05 \\ \sum \text{ECAL} < 1.7 \text{ GeV} \end{array} \right.$
TRK Iso	$\left\{ \begin{array}{l} \sum P_T/P_T(\gamma) < 0.1 \\ N_{tracks} < 3 \end{array} \right.$

**Table 7.1.** PhotonID selection criteria.

The last two variables used for the event selection are  $P_T(\gamma)$  and  $N_{jets}$ , which are respectively the  $P_T$  of the photon candidate and the number of reconstructed jets with  $P_T > 25$  GeV.

### 7.1.1 Unbinned maximum likelihood fit

The missing transverse energy is the best variable to discriminate signal from SM background. In addition, for large regions of the GMSB parameter space where the neutralino could have a non negligible lifetime, the measured time with the ECAL ( $T_{REC}$ ) becomes a key ingredient to identify delayed energy deposits in the electromagnetic calorimeter. For these reasons, MET and  $T_{REC}$  distributions have been chosen to determine the exclusion limits with a maximum likelihood fit.

The missing transverse energy and  $T_{REC}$  are assumed to be uncorrelated. This assumption is verified by computing MET for different  $T_{REC}$  bins (corresponding to increasing values of neutralino lifetime), as illustrated in Figure 7.1. It can be

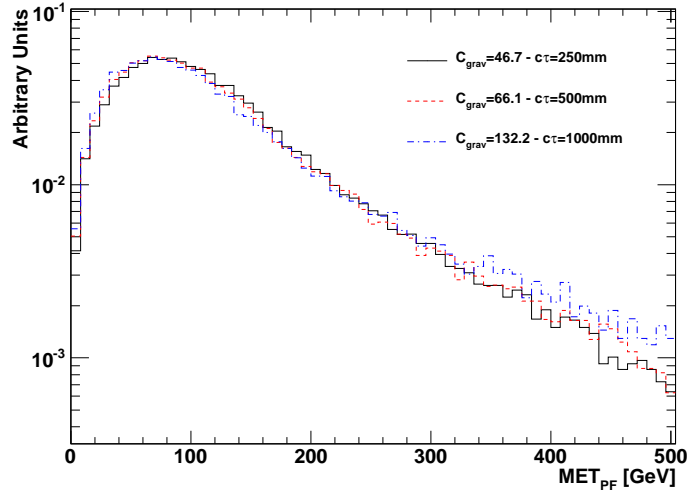


**Figure 7.1.** Distribution of MET for different values of neutralino lifetime.

noted that the shape of MET distribution does not change appreciably for larger lifetimes, confirming a very weak correlation between MET and  $T_{REC}$ . Under the assumption of no correlation, the probability density function (p.d.f.) distribution for GMSB signal  $F_{sig}(MET, T_{REC})$  can be factorized:

$$F_{sig}(MET, T_{REC}) = f_{sig}^M(MET) \times f_{sig}^T(T_{REC}) \quad (7.1)$$

where  $f_{sig}^M$  and  $f_{sig}^T$  are respectively the p.d.f. for MET and  $T_{REC}$ . The total p.d.f. can be then expressed as a sum of four components, one for the signal and three for QCD, PJ and  $t\bar{t}$  backgrounds:

$$F_{TOTAL}(MET, T_{REC}) = N_{sig} \cdot F_{sig} + N_{QCD} \cdot F_{QCD} + N_{PJ} \cdot F_{PJ} + N_{t\bar{t}} \cdot F_{t\bar{t}} \quad (7.2)$$

where  $F_{GMSB}$  is defined in Equation 7.1 and  $F_{QCD}$ ,  $F_{PJ}$ ,  $F_{t\bar{t}}$  are the probability density functions for each of the background sample, while  $N_{GMSB}$ ,  $N_{QCD}$ ,  $N_{PJ}$  and  $N_{t\bar{t}}$  are respectively the yield of signal, QCD, Photon+Jet and  $t\bar{t}$  components which are left as free parameters in the fit.

The main purpose of the analysis is to set the exclusion limit for GMSB for different values of  $\Lambda$  and  $C_{grav}$  parameters, i.e. for different values of neutralino mass and lifetime. For this reason, the expected 95% confidence level signal cross

section limit ( $\sigma^{95\%}$ ) for various point in parameter space will be calculated. The upper limits on the cross section are computed using a Bayesian method with a flat signal prior [71]

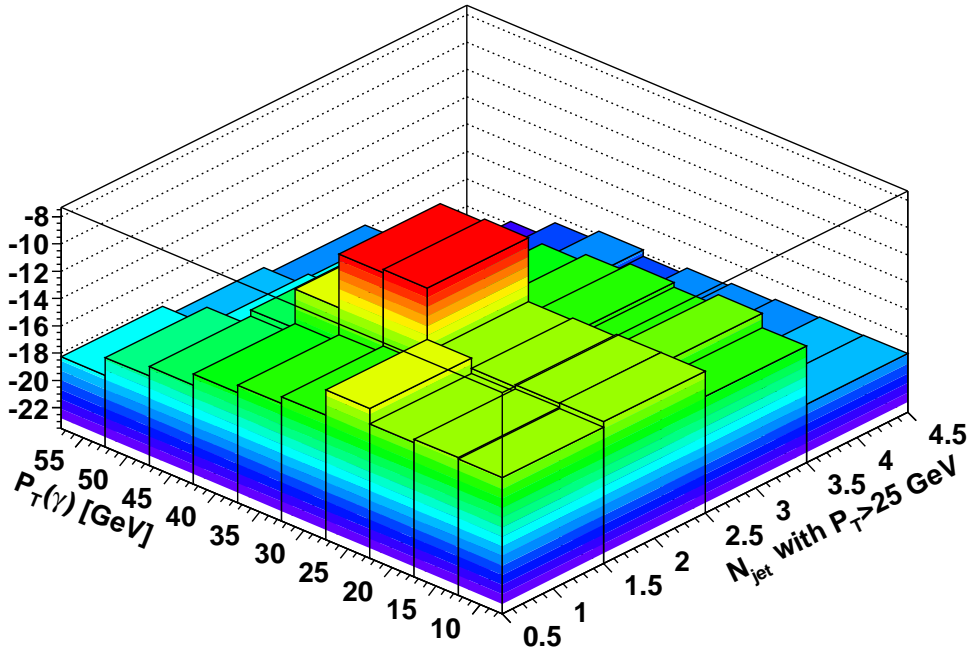
### 7.1.2 Optimization of selection criteria

The optimization of selection criteria aims at finding the  $P_T(\gamma)$  and  $N_{jet}$  thresholds to obtain the best expected limit for the analysis. The optimization is performed as follows:

- a grid of the possible thresholds for  $P_T(\gamma)$  and  $N_{jet}$  is defined;
- for each  $(P_T(\gamma), N_{jet})$  combination, a fit to the background distribution of MET and  $T_{REC}$  is performed and  $\sigma^{95\%}$  is computed;
- the  $(P_T(\gamma), N_{jet})$  combination which gives the best sensitivity is chosen.

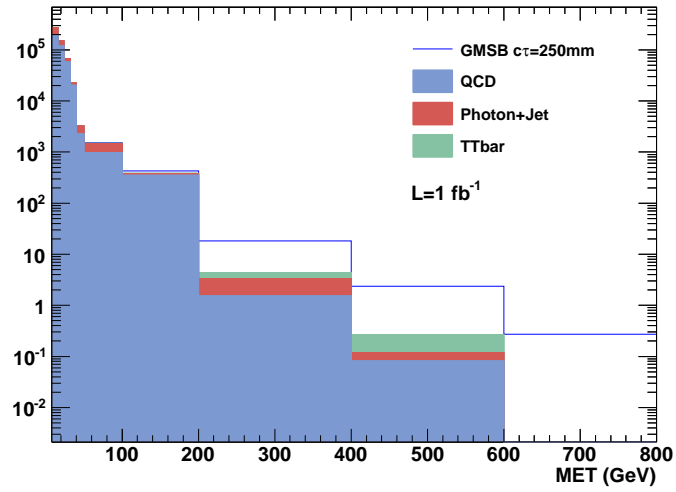
Due to the limited size of the MC samples, binned distributions from MC events are used as p.d.f. in the likelihood fit.

Figure 7.2 shows the value of  $-\sigma^{95\%}$  for all the combinations considered in the optimization. The final selection criteria for best upper limit are summarized in Table 7.2.



**Figure 7.2.** The inverse of 95% cross section upper limit  $-\sigma^{95\%}$  for different pairs of cuts in the  $P_T(\gamma)$  vs  $N_{jet}$  plane.

Figures 7.3 and 7.4 show respectively the distribution of MET and  $T_{REC}$  for signal and SM backgrounds after the final selection, normalized to  $1 \text{ fb}^{-1}$  of integrated luminosity.



**Figure 7.3.** Distribution of MET for GMSB signal and SM backgrounds, normalized at  $1 \text{ fb}^{-1}$  of integrated luminosity.

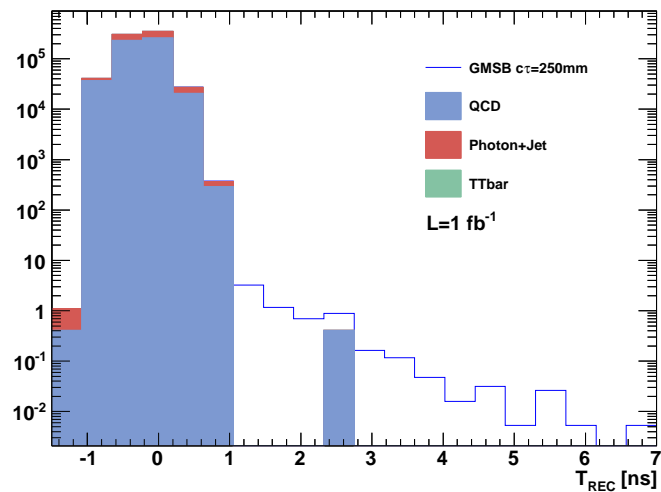


**Figure 7.4.** Distribution of  $T_{REC}$  for GMSB signal and SM backgrounds, normalized at  $1 \text{ fb}^{-1}$  of integrated luminosity.

Optimized event selection
At least one photon candidate which passes PhotonID
$P_T(\gamma) > 30 \text{ GeV}$
$N_{jet} > 2$

**Table 7.2.** Optimized selection criteria for the best upper limit.

The efficiencies of full selection with  $1 \text{ fb}^{-1}$  of integrated luminosity for GMSB signal with  $\Lambda = 100 \text{ TeV}$  and  $C_{grav} = 46.7$  and for SM backgrounds are reported in Table 7.3. Other sources of background other than SM, e.g. cosmics and beam halo, are not reported since they are completely rejected by requiring more than two jets with  $P_T > 25 \text{ GeV}$  (as discussed in Section 6.3.3).

	GMSB	QCD	$\gamma$ +Jet	tt	All bkg
$ \eta  < 1.4$	97.3%	59.7%	60.87%	91.7%	59.7%
$S_{minor} < 0.3$	96.7%	36.9%	81.59%	63.0%	36.9%
HCAL Iso	86.4%	24.9%	84.4%	38.6%	25.0%
ECAL Iso	74.6%	2.5%	66.1%	22.8%	2.7%
TRK Iso	85.4%	34.4%	90.1%	4.4%	39.0%
$P_T(\gamma) > 30 \text{ GeV}$	94.5%	22.9%	98.2%	43.2%	37.4%
$N_{jet} > 2$	92.6%	53.2%	21.3%	97.9%	37.1%
$\epsilon_{TOT}$	45.2%	5.7E-03%	5.2%	9.5E-02%	8.1E-03%

**Table 7.3.** Selection efficiency for different requirements of event selection, for GMSB signal with  $\Lambda = 100 \text{ TeV}$  and  $C_{grav} = 46.7$  and the SM backgrounds. The efficiencies are shown after the application of the selection requirements in cascade, starting from the top to the bottom of each column.

## 7.2 Exclusion limits

In order to investigate the exclusion potential with the early LHC data, a short-term scenario of  $200 \text{ pb}^{-1}$  of integrated luminosity is considered. Figures 7.5, 7.6, 7.7 and 7.8 show the GMSB cross section limits as a function of the neutralino mass, for different values of  $C_{grav}$  parameter. The  $c\tau = 0$  scenario corresponds to  $C_{grav} = 1$ .

The resulting exclusion region in the  $M_{\tilde{\chi}_1^0} - C_{grav}$  plane is shown in Figure 7.9. Neutralino masses below  $200 \text{ GeV}/c^2$  are excluded for all values of neutralino lifetime. This limit is well beyond the current limit of  $149 \text{ GeV}/c^2$  [72] set by the CDF experiment at Tevatron and shown in Figure 7.10. However, these limits do not include yet the systematic uncertainties, which will lower the actual limit.

## 7.3 Systematic uncertainties

There are several sources of systematic uncertainty that affect the measured upper limit. The most important source of systematic uncertainty for this analysis, especially for early discoveries where the number of observed events is small, is the

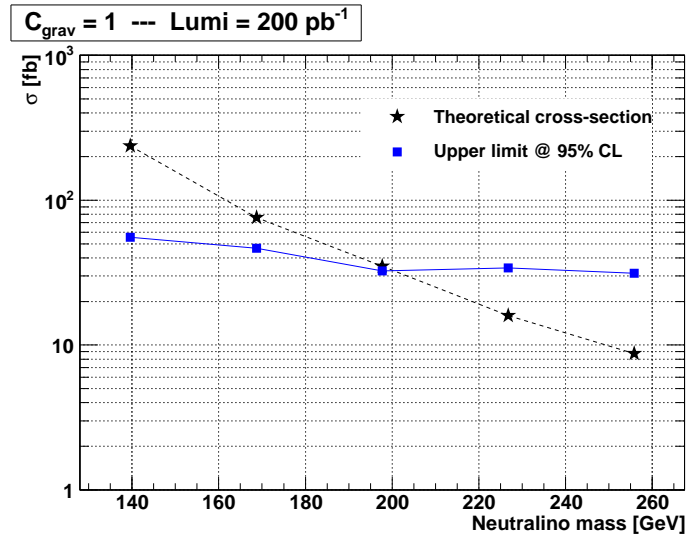


**Figure 7.5.** The expected upper limit at 95% CL as a function of  $\tilde{\chi}_1^0$  mass, for  $C_{grav} = 1$ . Black stars represent the production cross section.

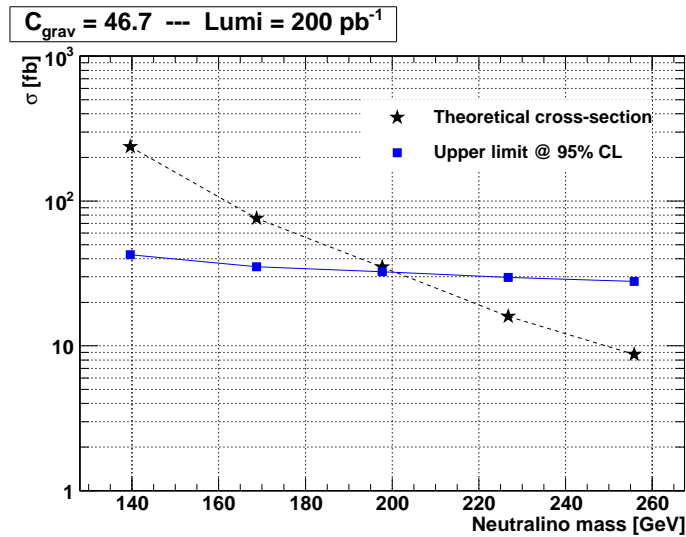


**Figure 7.6.** The expected upper limit at 95% CL as a function of  $\tilde{\chi}_1^0$  mass, for  $C_{grav} = 46.7$ . Black stars represent the production cross section.

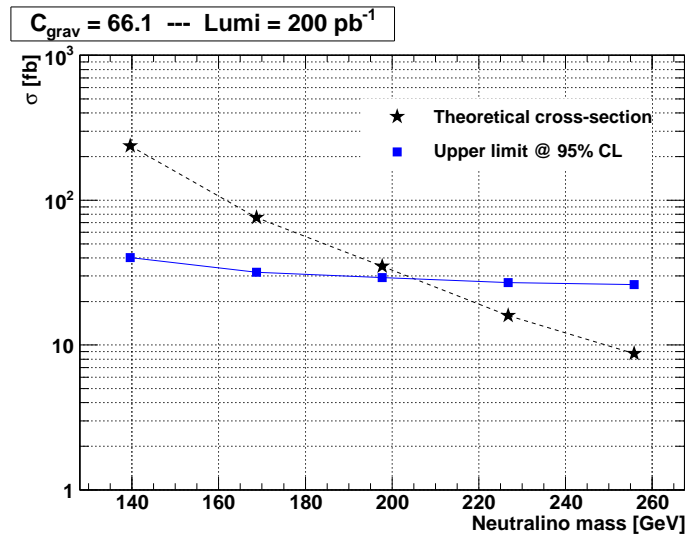


**Figure 7.7.** The expected upper limit at 95% CL as a function of  $\tilde{\chi}_1^0$  mass, for  $C_{grav} = 66.1$ . Black stars represent the production cross section.

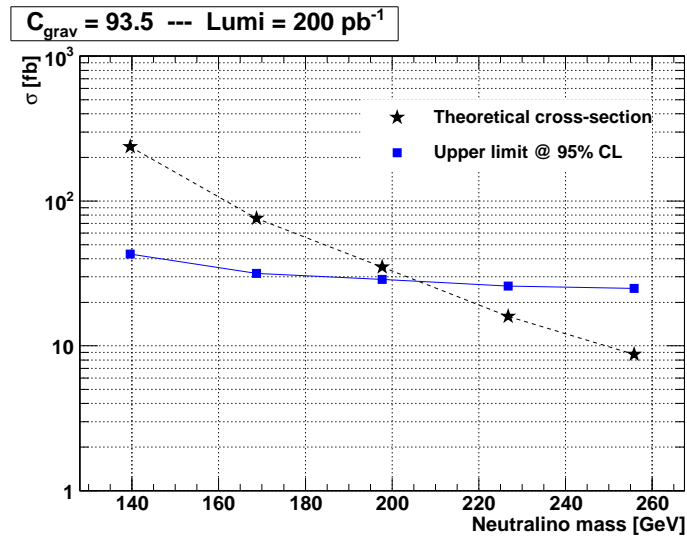


**Figure 7.8.** The expected upper limit at 95% CL as a function of  $\tilde{\chi}_1^0$  mass, for  $C_{grav} = 93.5$ . Black stars represent the production cross section.

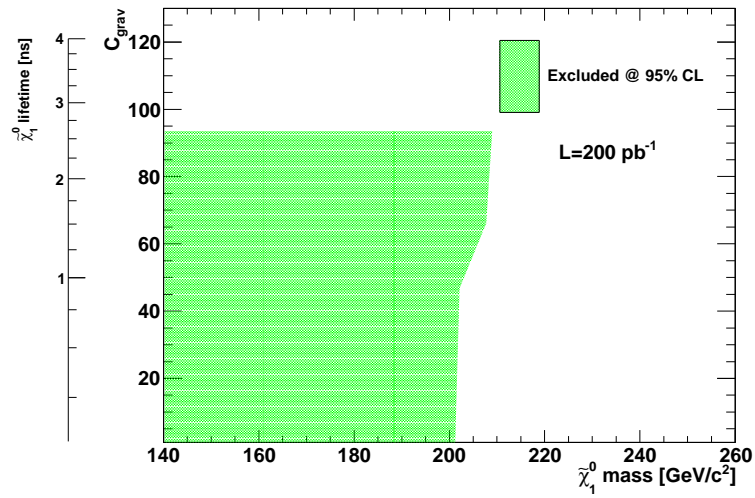


Figure 7.9. The expected exclusion region in the  $M_{\tilde{\chi}_1^0} - C_{grav}$  plane.

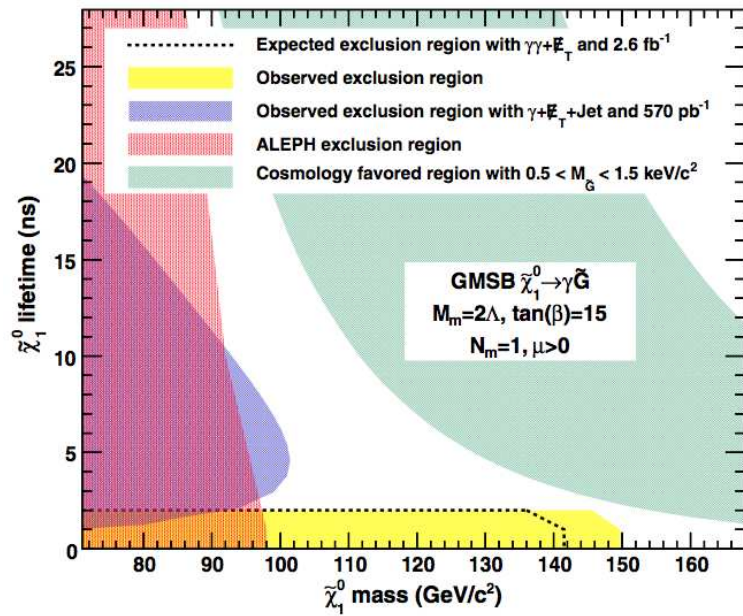
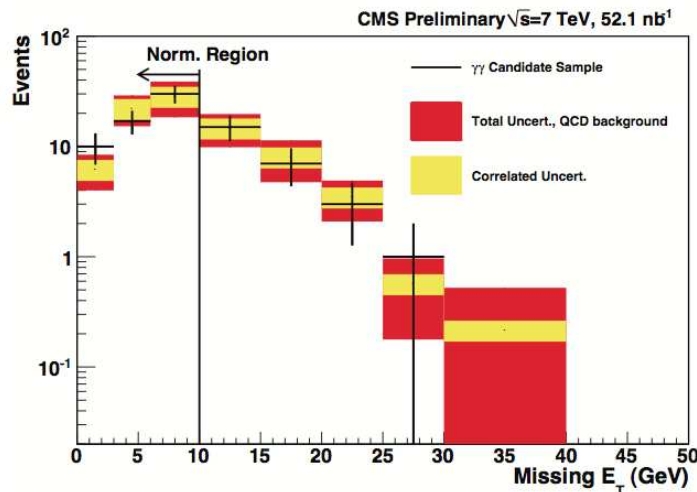


Figure 7.10. The exclusion region as a function of  $\tilde{\chi}_1^0$  lifetime and mass, set by CDF Collaboration.

tail in the resolution of the missing transverse energy and the time measured in the ECAL. In fact, the missing transverse energy and the ECAL time are used to extract the signal yields and therefore tails in background distribution can fake the presence of signal events. For this reason, any uncertainty related to MET and  $T_{REC}$  measurement is directly propagated to the final results of the analysis.

### 7.3.1 Missing transverse energy

The most important source of background for the GMSB analysis is represented by processes with no true MET, such as QCD and Photon+Jet events. Data-driven strategies can be therefore used to predict the MET distribution in the background samples. For new physics analyses, such as the searches for supersymmetric processes, the best control samples are those that reproduces the hadronic activity in the candidate sample while having no significant real MET. A recent study [78] demonstrates that a sample composed of two mis-identified photon signals due to jets (referred as “fake-fake” sample) provides an accurate representation of the MET distribution due to QCD events. Figure 7.11 shows the MET distribution for di-photon events with estimated background from fake-fake events, confirming that data-driven methods allows for very accurate MET representation.



**Figure 7.11.** Distribution of MET for di-photon candidates with estimated background from fake-fake events. Red band represents the total uncertainty on the background estimates.

Further improvements on MET measurement comes from jet energy calibration. The energy response of the CMS calorimeter to a particle level jet is smaller than unity and varies as a function of jet  $P_T$ . The purpose of the absolute jet energy correction is to remove this variation and make the response equal to unity at all  $P_T$  values. The absolute jet energy correction from data has been determined by using Photon+Jet events and the uncertainty on jet resolution is currently established to be 10% [79].

Another source of systematic uncertainty on MET determination is the existence of high-energy fake signals in the calorimeters originated by energy deposited by heavily ionizing particles in the avalanche photodiode. These fake signals can also

cause the PF reconstruction algorithm to reconstruct fake neutral particles. This ultimately leads to significant fake missing transverse energy. Substantial progress has been achieved in removing such noise and specific rejection criteria have been adopted for both ECAL and HCAL [80].

### 7.3.2 ECAL time measurement

The systematic uncertainties on the ECAL time measurement involve both the resolution and the tail of the distribution. As for the MET, control samples on data can be identified to estimate the uncertainties on the ECAL time measurement. As discussed in Section 6.3.4, di-photon candidates from  $\pi^0$  decays in Minimum Bias events are used as control sample for studies on time resolution and tails.

Tails of time distribution are affected by the anomalous signal in the ECAL due to ionization in the avalanche photodiode. In fact, the reconstructed time for these signals is biased due to their different pulse shape. The resulting time distribution has a much wider spread around the correct time measurement, as shown in Figure 7.12

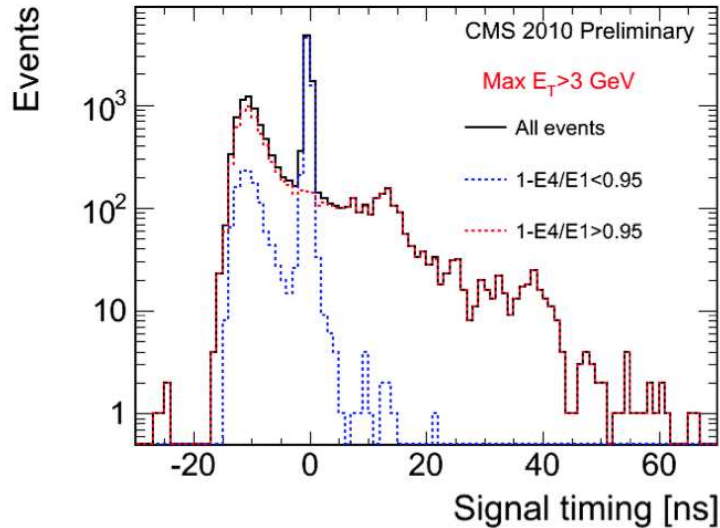


**Figure 7.12.** Signal timing distribution using  $\sqrt{s} = 7$  TeV data. Red line represents the contribution from anomalous signals.

In conclusion, mis-measurements of missing transverse energy and ECAL time can be sources of large systematic uncertainties. In particular, the tails in the distribution of background events are dangerous since they can fake the presence of signal events.

### 7.3.3 Luminosity uncertainties

The uncertainty on the luminosity  $\mathcal{L}$  is linearly propagated to an uncertainty on the measurement of the cross section  $\sigma$  since

$$\sigma \propto \frac{1}{\mathcal{L}} \quad (7.3)$$

The design goal for the precision of the absolute luminosity measurement at CMS is 5%, which is expected to be achieved after  $1 \text{ fb}^{-1}$  of collected data. For integrated luminosities of less than  $1 \text{ fb}^{-1}$ , the systematic error on the luminosity normalization is estimated to be 11% [81].

### 7.3.4 Theoretical uncertainties

The sources of theoretical uncertainties on signal and background can be summarized as [82]:

- the effect of neglecting higher order corrections to the coupling constants in the matrix element calculation of the physics process;
- the experimental precision of the SM parameters, which appear in the matrix element calculation;
- the parton showering, which describes the QCD radiation of outgoing partons from the hard processes;
- the fragmentation model, which describes the hadronization using phenomenological models tuned with experimental data;
- the description of the underlying event, which includes all the remnant activity from the same p - p interaction, the Initial State Radiation (ISR) and the pile-up;
- the description of the Parton Density Functions used to model the proton structure in the p - p collision;
- the definition of  $Q^2$  energy scale of the interaction.

Recent studies performed by CDF [83] experiment at Tevatron indicate that the main systematic uncertainties on the GMSB signal come from the Parton Distribution Functions (7.6%), the Initial/Final State Radiation (3.9%) and the  $Q^2$  energy scale of the interaction (2.6%).



## Chapter 8

# Conclusions

Theoretical models with long-lived particles decaying into photons have been largely studied as candidates of new physics beyond the TeV energy scale. The relatively high production cross section and the striking experimental signature allow for early discoveries with first data collected by the experiments at the proton-proton Large Hadron Collider (LHC), at CERN laboratories in Geneva.

The detector of Compact Muon Solenoid (CMS) experiment provides a unique tool to probe new energy scale phenomena. In particular, the excellent performance of the electromagnetic calorimeter (ECAL) allows for very precise measurement of high energy photons.

Although a model-independent approach is followed, this thesis is focused on Supersymmetry theories with Gauge Mediated Supersymmetry Breaking (GMSB), where the neutralino  $\tilde{\chi}_1^0$  is the Next To Lightest Supersymmetric Particle (NLSP) decaying into a photon and a gravitino  $\tilde{G}$ . In this model,  $\tilde{G}$  plays the role of Lightest Supersymmetric Particle (LSP) and behaves as a massive neutrino, since it is stable, neutral and weakly interacting.

An algorithm for the determination of the flight path of long-lived particles decaying into photons is presented. The algorithm is based on two main ingredients: the determination of the  $\gamma$  direction from the shape of the energy deposit in ECAL and the measurement of its arrival time on the ECAL surface. For this studies, GMSB samples at different values of neutralino lifetime are used. It is demonstrated that the algorithm allows for flight path reconstruction with a resolution less than 18 cm.

Subsequently, a study of the  $\tilde{\chi}_1^0 \rightarrow \tilde{G} + \gamma$  channel is presented. Event selection based on the requirement of at least one isolated photon with high  $P_T$  and more than two hadronic jets in the final state, allows for a significant reduction of the most important sources of background from common Standard Model processes. Since the missing transverse energy and the reconstructed ECAL time are the most discriminating variables between signal and background, they have been combined in a 2D maximum likelihood fit to determine the 95% upper limit on the GMSB cross section. Event samples at different values of  $\Lambda$  and  $C_{grav}$  parameters have been used to probe a limited region in the GMSB parameter space. For  $\tilde{\chi}_1^0$  lifetimes up to  $\sim 3$  ns the expected exclusion limit on neutralino mass is  $> 200$  GeV/ $c^2$  with  $200$  pb $^{-1}$  at  $\sqrt{s} = 7$  TeV, well above the current world's best limit set by the CDF experiment at Tevatron.

The expected limits do not include the effect of the systematic uncertainties, that has been discussed in the last part of the thesis. However, the preliminary results obtained in this thesis are very encouraging and it can be expected that the Tevatron limits will be improved even including the effect of the systematic uncertainty.

# Appendix A

## Identification of photons and $\pi^0$ in the ECAL

Neutral pion decay  $\pi^0 \rightarrow \gamma\gamma$  represents an important source of background for all the analyses with high energy photon in the final state, such as the search for the Higgs boson in the  $\gamma\gamma$  decay channel. In fact, when the  $\pi^0$  decay photons reach the ECAL surface in two points that are too close to each other, they are detected as a single energy deposit and the  $\pi^0$  is misinterpreted as a photon of the same energy. For this reason, the importance of productive algorithms to distinguish between photons and neutral pions is very crucial for many of the primary goals of the CMS physics program.

In this appendix, an optimized  $\gamma - \pi^0$  discrimination algorithm for the ECAL barrel region is presented [84]. The algorithm exploits the differences on the shape of  $\gamma$  and  $\pi^0$  deposits which can be described by the so-called “cluster shape variables” (see Section 5.2.2). Together with the principal axes of the cluster, a new set of variables will be used in order to improve the discrimination power.

The appendix is organized as follows:

- Section A.1 describes the datasets and the analysis procedure used in this study;
- Section A.2 introduces the principal axes and the moments of the energy deposits in the ECAL;
- Section A.3 illustrates other cluster shape variables and describes the  $\gamma - \pi^0$  discrimination algorithm.

### A.1 Datasets and analysis procedure

The event samples used in this study are 150K single photons and 150K single neutral pions generated using the CMS Particle Gun. The particles have energies flatly distributed between 30 GeV and 70 GeV, are generated within the ECAL barrel ( $|\eta| < 1.479$ ) and are reconstructed with a  $9 \times 9$  array of crystals around the most energetic seed of the event. Only the crystals inside this matrix are considered to calculate cluster shape variables.

### A.1.1 Distance between the decay photons

Figure A.1 shows a schematic view of a  $\pi^0 \rightarrow \gamma\gamma$  decay, emphasizing the distance  $\delta$  between the impact points of the decay photons on the ECAL surface.

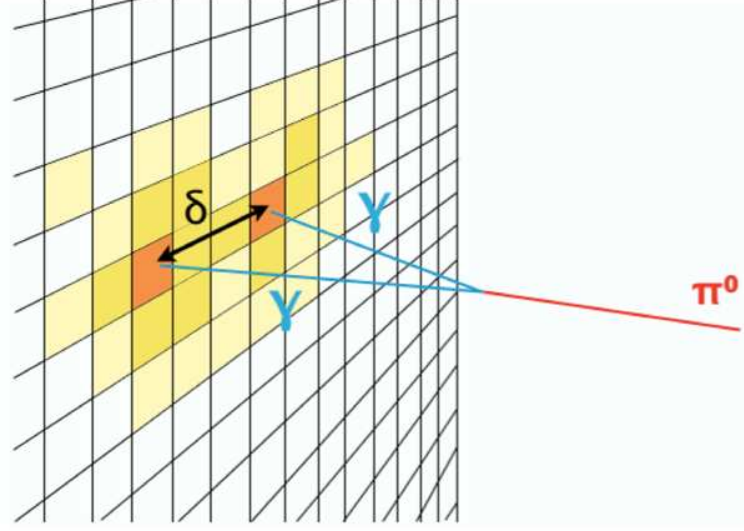


**Figure A.1.** A schematic view of a  $\pi^0 \rightarrow \gamma\gamma$  decay. The distance between the impact points of the decay photons on the ECAL surface is referred as  $\delta$ .

As illustrated in Figures A.2, A.3 and A.4, which show different topologies for  $\pi^0$  energy deposits corresponding to different values of  $\delta$ , this variable sensibly affects the shape of a  $\pi^0$  cluster. Three different cases are presented:

1.  $\delta = 6 \text{ cm}$ :  $\delta$  is several times the size of an ECAL crystal (2.2 cm) so the decay photons are well separated. The  $\pi^0$  can be easily recognized by calculating its invariant mass (Figure A.2);
2.  $\delta = 2 \text{ cm}$ :  $\delta$  is comparable with the crystal size and the decay photons are reconstructed as two overlapping clusters. In this case, the invariant mass cannot be calculated with high accuracy but the  $\pi^0$  can be still recognized exploiting the elliptical shape of the energy deposit (Figure A.3);
3.  $\delta = 0.5 \text{ cm}$ :  $\delta$  is lower than the crystal size and the impact point of both the decay photons lies in the same crystal. There is a strong overlap between the clusters and the  $\pi^0$  is totally indistinguishable from a single photon (Figure A.4).

An approximate expression for  $\delta$  is:

$$\delta \sim 2 \cdot L(\eta_{\pi^0}) \cdot \tan \left[ \frac{\alpha(E_1, E_2)}{2} \right] \quad (\text{A.1})$$

where  $L$  represents the distance between the  $\pi^0$  decay vertex and the point on the ECAL surface corresponding to the pion pseudorapidity  $\eta_{\pi^0}$ ,  $\alpha$  is the angle between the directions of the decay photons and  $E_1, E_2$  are the energies of the decay photons.

Starting from Equation A.1, an estimate of  $\delta$  based only on reconstructed variables can be obtained. For instance, the distance  $L$  can be calculated using the

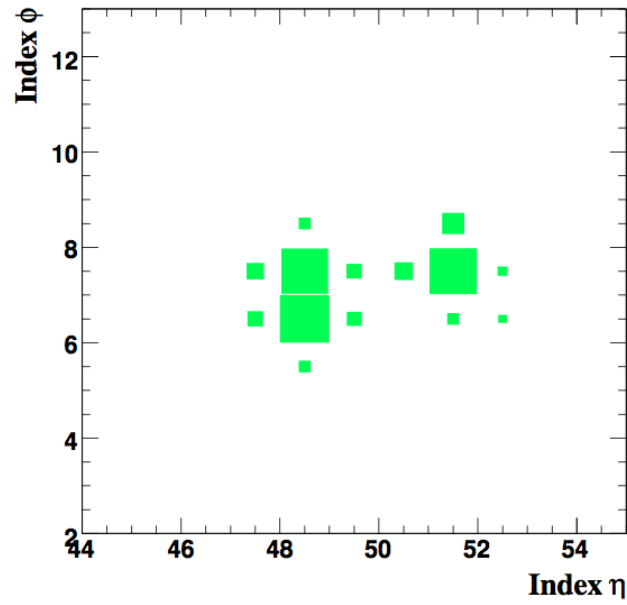


Figure A.2. Energy deposit in the ECAL from a neutral pion with  $\delta = 6$  cm.

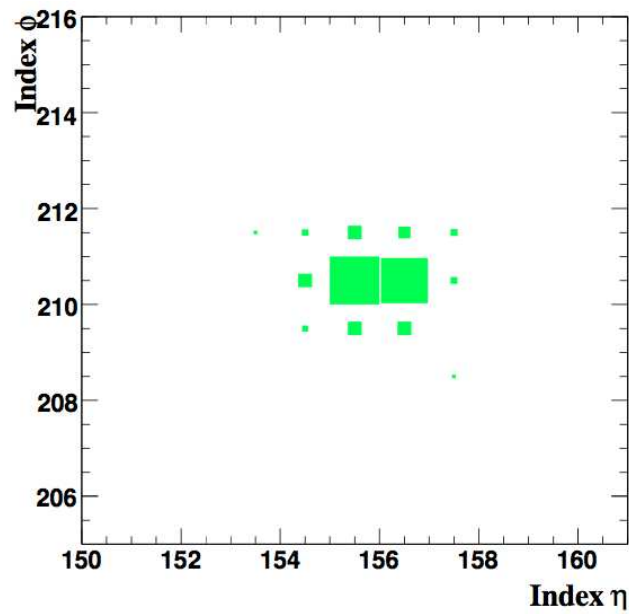
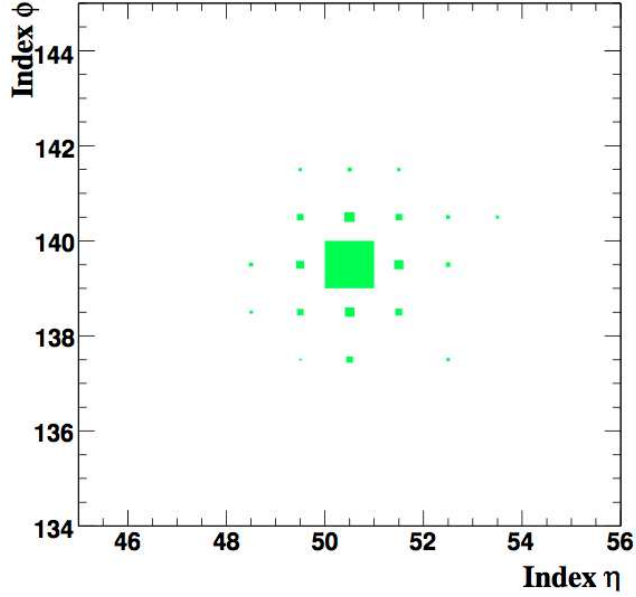


Figure A.3. Energy deposit in the ECAL from a neutral pion with  $\delta = 2$  cm.



**Figure A.4.** Energy deposit in the ECAL from a neutral pion with  $\delta = 0.5$  cm.

pseudorapidity of the reconstructed cluster  $\eta_{RECO}$ , according to the following expression:

$$L(\eta_{RECO}) = \frac{L(0)}{\sin(\theta_{RECO})} \quad (\text{A.2})$$

where  $L(0) = 1.29$  meters, i.e. the ECAL radius, and  $\theta_{RECO}$  represents the polar angle associated to  $\eta_{RECO}$ .

The angle  $\alpha$  can be obtained from the general expression for the decay angle:

$$\sin^2\left(\frac{\alpha}{2}\right) = \frac{M_{\pi^0}^2}{4E_1E_2} \quad (\text{A.3})$$

However,  $\alpha$  cannot be calculated with high accuracy. In fact, the energies  $E_1$  and  $E_2$  are determined with large uncertainties due to the difficulties in distinguishing between two overlapping energy deposits. To avoid this problem, the minimum decay angle  $\alpha_{MIN}$  will be considered. It is the decay angle which corresponds to the case where both the decay photons bring half of the pion energy. The expression for  $\alpha_{MIN}$  is:

$$\sin^2\left(\frac{\alpha_{MIN}}{2}\right) = \left(\frac{M_{\pi^0}}{E_{RECO}}\right)^2 \quad (\text{A.4})$$

obtained by replacing  $E_1 = E_2 = \frac{E_{RECO}}{2}$  in Equation A.3, where  $E_{RECO}$  represents the reconstructed energy of the pion cluster. The minimum decay angle is well determined since it depends only on the total energy of the pion that, unlike  $E_1$  and  $E_2$ , is always reconstructed with high precision. Figure A.5 shows the scatter plot  $\alpha_{MIN}$  versus the true decay angle  $\alpha$ , obtained from Monte Carlo information. It can be noticed that the plot exhibits a linear correlation, which ensures that the use of  $\alpha_{MIN}$  instead of  $\alpha$  can be considered as a reasonable assumption.

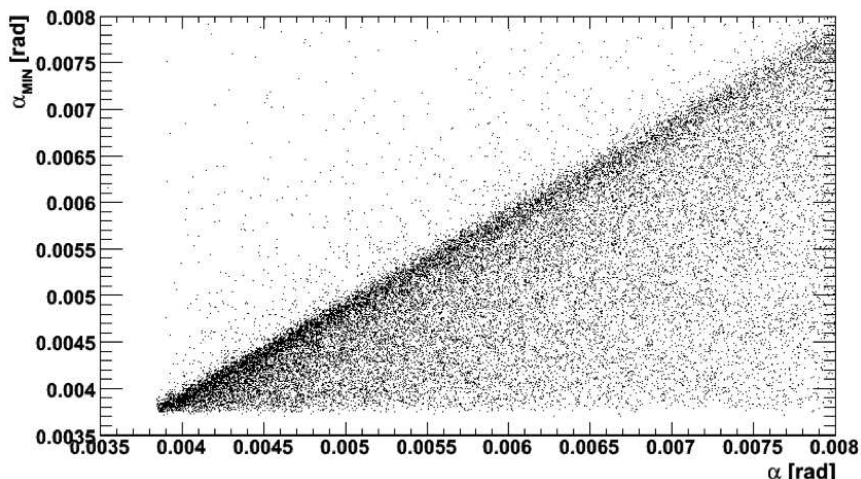


Figure A.5. The scatter plot  $\alpha_{MIN}$  versus  $\alpha$ .

In the following, for each  $9 \times 9$  reconstructed matrix from a single photon or pion, an estimate of  $\delta$  (in the hypothesis of a  $\pi^0$ ) is calculated by replacing  $L(\eta_{\pi^0})$  and  $\alpha(E_1, E_2)$  with the reconstructed variables defined in Equation A.2 and Equation A.3:

$$\delta_{EST}(\eta_{RECO}, E_{RECO}) = 2 \cdot L(\eta_{RECO}) \cdot \tan\left(\frac{\alpha_{MIN}(E_{RECO})}{2}\right) \quad (\text{A.5})$$

The shape of a  $\pi^0$  cluster is very sensitive to variations of  $\delta_{EST}$ . The cluster shape variables that will be introduced in Section A.2 and Section A.3 to describe the geometrical properties of the electromagnetic deposit in the ECAL, also depend on  $\delta_{EST}$ . Therefore, in order to maximize the  $\gamma - \pi^0$  discriminating power, the event samples used in this study will be split into three different  $\delta_{EST}$  categories:

1. Low separation:  $0.5 \text{ cm} < \delta_{EST} < 0.8 \text{ cm}$ ;
2. Intermediate separation:  $0.8 \text{ cm} < \delta_{EST} < 1.0 \text{ cm}$ ;
3. High separation:  $1.0 \text{ cm} < \delta_{EST} < 1.2 \text{ cm}$ .

Figure A.6 shows the correlation between the reconstructed energy of the neutral pion and the estimated separation, showing the three  $\delta_{EST}$  regions that will be considered in this study. It can be noticed that these regions correspond to a large fraction of the photon energies expected for interesting physics processes, such as Higgs decay in the di-photon channel.

## A.2 Moments of the ECAL cluster

As discussed in Section 5.2.2, the definition of the covariance matrix is the starting point for the calculation of the cluster shape variables. In particular, the eigenvalues  $S_{major}$  and  $S_{minor}$  of the covariance matrix represent the standard deviation of the energy deposit calculated along the major and the minor axis respectively.

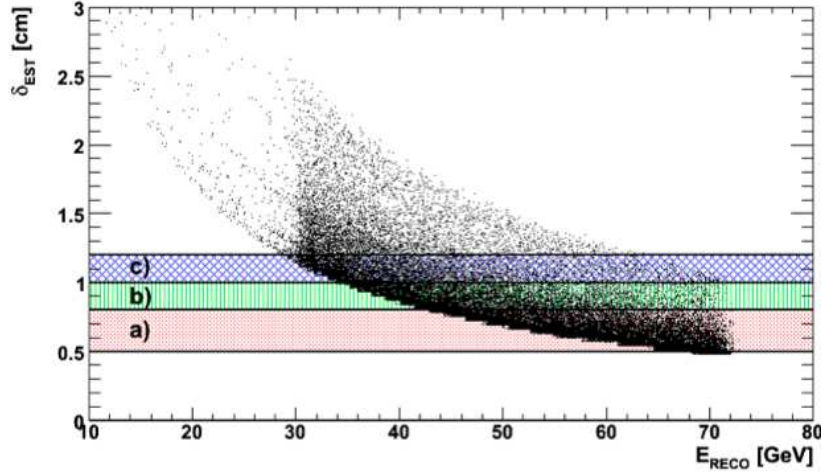


**Figure A.6.** The scatter plot  $\delta_{EST}$  versus the reconstructed pion energy. The regions that will be considered in this study are indicated as: a)  $0.5 \text{ cm} < \delta_{EST} < 0.8 \text{ cm}$ ; b)  $0.8 \text{ cm} < \delta_{EST} < 1.0 \text{ cm}$ ; c)  $1.0 \text{ cm} < \delta_{EST} < 1.2 \text{ cm}$ .

Once the principal axes of the cluster have been identified, the moments of the energy distribution can be defined. The generic moments of order  $n$  are defined as:

$$M_{MAJ(MIN)}^n = \frac{\sum_{i=1}^N w_i \times \left(d_i^{MIN(MAJ)}\right)^n}{\sum_{i=1}^N w_i} \quad (\text{A.6})$$

where  $d_i^{MAJ}$  ( $d_i^{MIN}$ ) represents the distance between the center of the  $i$ -th crystal in the cluster and the major (minor) axis, expressed in terms of  $\eta, \phi$  indexes. In the following, only the second-order moments will be considered, since they have the highest  $\gamma - \pi^0$  discriminating power. Moments with  $n > 2$  are strongly correlated with the second-order moments and therefore they are quite useless. It can be noticed that the second-order moments coincides with the eigenvalues of the covariance matrix. In particular:

$$M_{MAJ}^2 = S_{major} \quad (\text{A.7})$$

$$M_{MIN}^2 = S_{minor} \quad (\text{A.8})$$

Figure A.7 shows a cluster from a  $\pi^0$  with  $\delta = 6 \text{ cm}$ . Solid and dotted lines represent the major and the minor axis respectively.

Figure A.8 shows the distribution of the average value of  $M_{MAJ}^2$  for photons and neutral pions, as a function of the estimated separation  $\delta_{EST}$ . For pions, larger values of  $M_{MAJ}^2$  are encountered as  $\delta_{EST}$  increases, because of the strong dependence of the spread of the energy deposit along the major axis direction on the value of  $\delta_{EST}$ . For photons, instead,  $M_{MAJ}^2$  is quite independent on  $\delta_{EST}$ . In fact, the estimated separation  $\delta_{EST}$ , which is calculated in the hypothesis of a  $\pi^0$ , has not a physical meaning in the case of photons: the shape of a  $\gamma$  cluster is always round and symmetrical, corresponding to a characteristic value of  $M_{MAJ}^2$ . For the reasons listed above,  $M_{MAJ}^2$  is a very powerful variable to distinguish between photons and neutral pions.

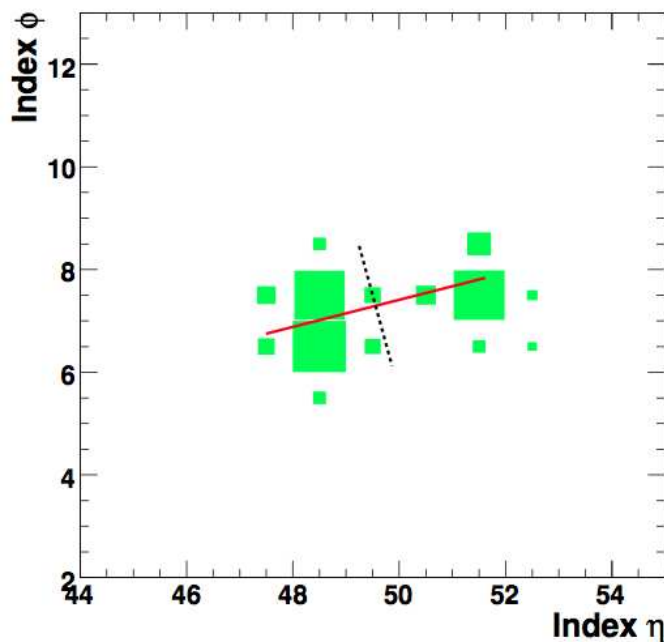


**Figure A.7.** The energy deposit for a  $\pi^0$ . The major (solid line) and minor (dotted line) are superimposed.

On the other hand, the spread of energy deposit along the minor axis has the same distribution for every kind of electromagnetic deposit. As shown in Figure A.9 the average values of  $M_{MIN}^2$  for photons and neutral pions are very similar and they are not dependent on  $\delta_{EST}$ . In other words,  $M_{MIN}^2$  is strongly connected to the electromagnetic nature of a reconstructed cluster in the ECAL. For this reason,  $M_{MIN}^2$  has no  $\gamma - \pi^0$  discriminating power and cannot be used in this study. However, it can have other applications of interest: for instance,  $M_{MIN}^2$  plays an important role in the rejection of the hadronic clusters from reconstructed jets.

The  $\gamma - \pi^0$  discriminating power of  $M_{MAJ}^2$  can be appreciated in Figure A.10, where the distribution of  $M_{MAJ}^2$  for photons and neutral pions with  $0.8 \text{ cm} < \delta_{EST} < 1.0 \text{ cm}$  is shown. The  $\gamma$ -efficiency versus  $\pi^0$ -rejection curve for  $M_{MAJ}^2$  is shown in Figure A.11. Efficiency and rejection values are calculated by selecting only those events that satisfy the requirement  $M_{MAJ}^2 < M_{CUT}$  and varying the value of  $M_{CUT}$ . The excellent  $\gamma - \pi^0$  discriminating power, even in the case of very small values of  $\delta_{EST}$ , can be appreciated. In fact, for an efficiency in  $\gamma$ -identification of 80%, the pion rejection is about 60%.

### A.3 Improved discrimination

In this section, an improved  $\gamma - \pi^0$  discriminating algorithm is investigated, combining  $M_{MAJ}^2$  with other variables. Two additional cluster shape variables will be therefore considered: the lateral moment and the pseudo-Zernike moments.

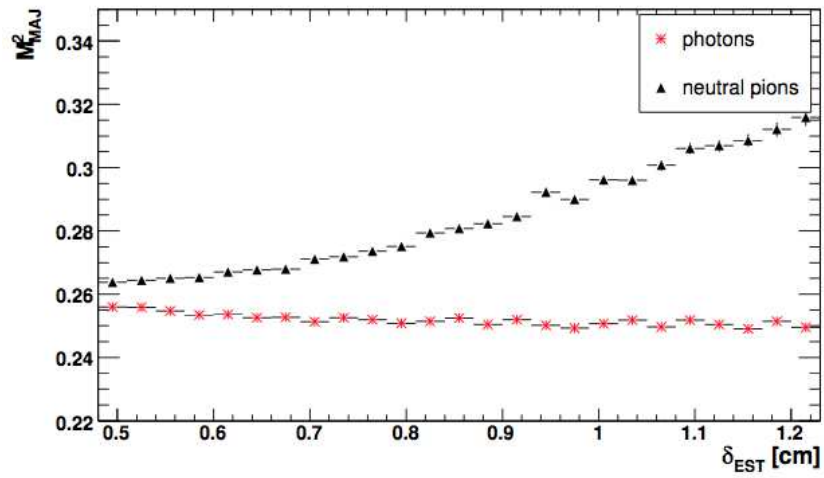


**Figure A.8.** The distribution of the average value of  $M^2_{MAJ}$  for photons and neutral pions, as a function of  $\delta_{EST}$ .

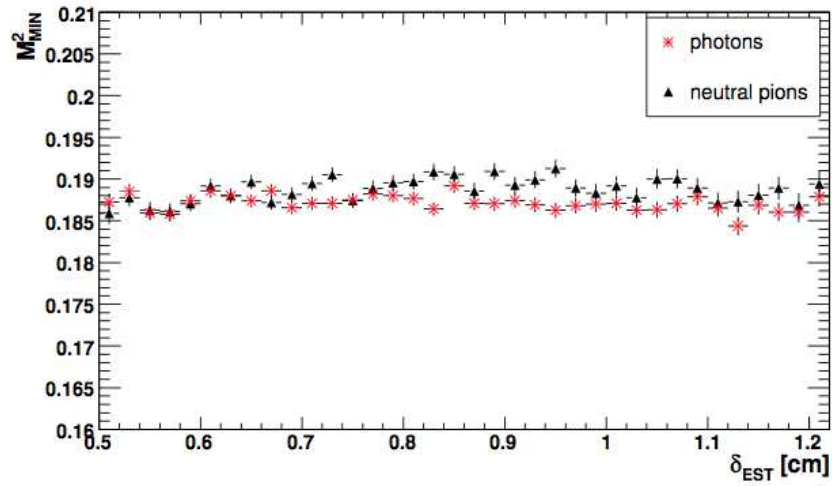


**Figure A.9.** The distribution of the average value of  $M^2_{MIN}$  for photons and neutral pions, as a function of  $\delta_{EST}$ .

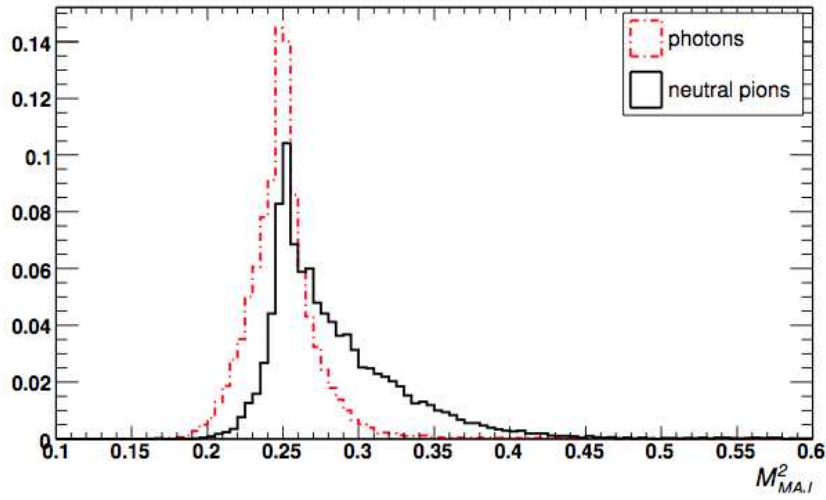


**Figure A.10.** The distribution of  $M_{MAJ}^2$  for photons and neutral pions with  $0.8 \text{ cm} < \delta_{EST} < 1.0 \text{ cm}$ .

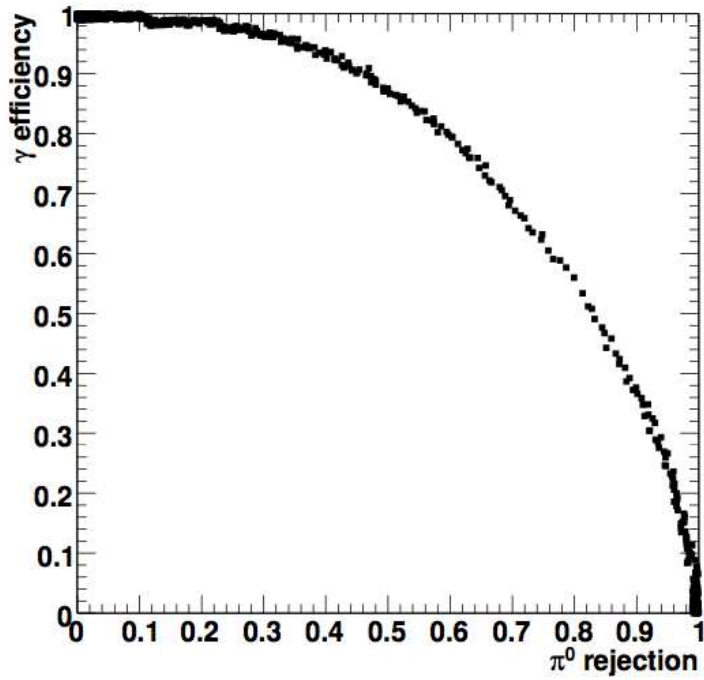


**Figure A.11.** The  $\gamma$ -efficiency versus  $\pi^0$ -rejection curve for  $M_{MAJ}^2$ . Only particles with  $0.8 \text{ cm} < \delta_{EST} < 1.0 \text{ cm}$  are considered.

### A.3.1 Lateral moment

The lateral moment LAT was firstly introduced by the Argus collaboration to distinguish between electrons and hadrons [85]. The variable LAT is defined as:

$$\text{LAT} = \frac{\sigma_r^2}{\sigma_r^2 + E_1^{cry} + E_2^{cry}} \quad (\text{A.9})$$

where  $E_1^{cry}$  and  $E_2^{cry}$  are the energies of the two most energetic crystals of the cluster, and  $\sigma_r^2$  has the following expression:

$$\sigma_r^2 = \sum_{i=3}^N \frac{E_i^{cry} \times (\vec{r}_i - \vec{r})^2}{r_M^2} \quad (\text{A.10})$$

where  $\vec{r}_i$  is the radius of the  $i$ -th crystal,  $\vec{r}$  is the radius of the cluster centroid and  $r_M$  is the Molière radius of the ECAL (2.2 cm). The two most energetic crystals are not included in the sum of Equation A.10. Figure A.12 shows the distribution of LAT for photons and neutral pions with  $0.8 \text{ cm} < \delta_{EST} < 1.0 \text{ cm}$ . As expected, the lateral moment for pion clusters is larger than the lateral moment for photon clusters.

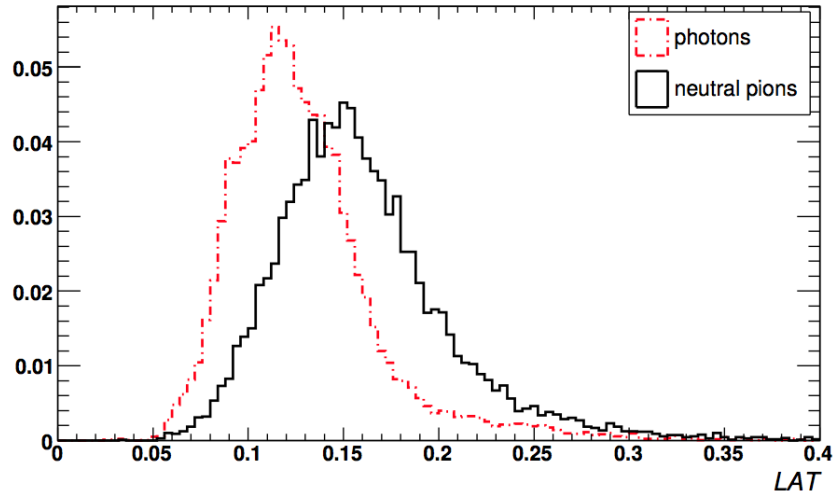


**Figure A.12.** The distribution of LAT for photons and neutral pion with  $0.8 \text{ cm} < \delta_{EST} < 1.0 \text{ cm}$ .

### A.3.2 Pseudo-Zernike moments

Another cluster shape variable can be extracted from the pseudo-Zernike moments, which are a set of polynomials that constitutes an orthonormal basis on the unitary circle. These moments were used by Zeus collaboration to identify electromagnetic particles [86], exploiting the characteristics of an electromagnetic shower inside the electromagnetic calorimeter. The generic pseudo-Zernike moment  $A_{nm}$  is defined as:

$$A_{nm} = \frac{n+1}{\pi} \sum_{i=1}^N \frac{E_i^{cry}}{E_{RECO}} \times V_{nm}^*(\rho_i, \phi_i) \quad (\text{A.11})$$

where  $n$  and  $m$  are two integer indexes. The complex polynomial  $V_{nm}^*(\rho_i, \phi_i)$ , expressed in polar coordinates, is defined as:

$$V_{nm}^*(\rho_i, \phi_i) = \sum_{s=0}^{\frac{n-m}{2}} \frac{(-1)^s (m-s)!}{s! \left(\frac{n+m}{2} - s\right)! \left(\frac{n-m}{2} - s\right)!} \rho_i^{m-2s} \cdot \exp^{-im\phi_i} \quad (\text{A.12})$$

The cluster shape variable PZM used in this study is:

$$\text{PZM} = \sqrt{[\text{Re}(A_{20})]^2 + [\text{Im}(A_{20})]^2} \quad (\text{A.13})$$

i.e. the norm of the  $A_{20}$  moment. The distribution of PZM for photons and neutral pions with  $0.8 \text{ cm} < \delta_{EST} < 1.0 \text{ cm}$  is shown in Figure A.13.

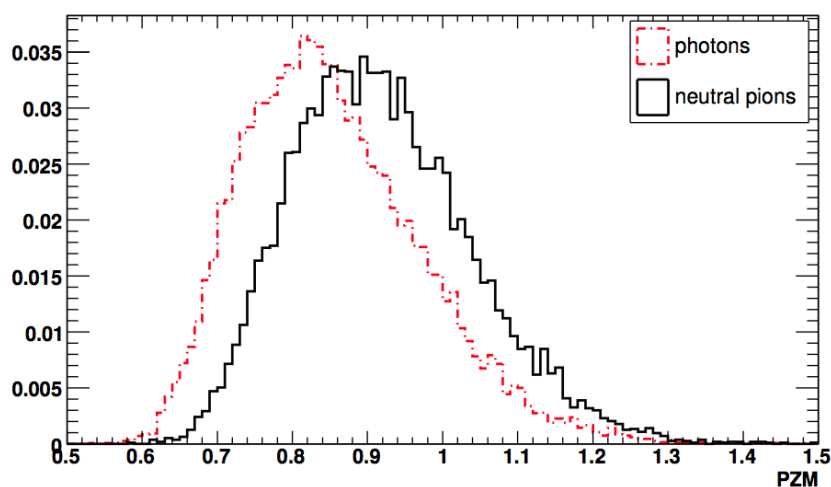


**Figure A.13.** The distribution of PZM for photons and neutral pion with  $0.8 \text{ cm} < \delta_{EST} < 1.0 \text{ cm}$ .

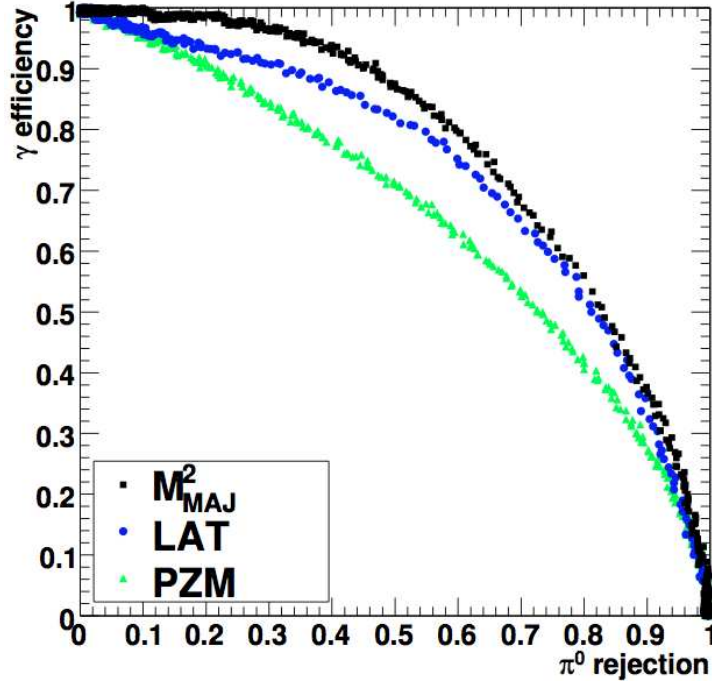
### A.3.3 Combination of different discriminants

Figure A.14 shows the  $\gamma$ -efficiency versus  $\pi^0$ -rejection curve for  $M_{MAJ}^2$ , LAT and PZM. It can be seen that  $M_{MAJ}^2$  provides the best discriminating power for any value of photon efficiency. In this section, a simple algorithm to improve the discriminating power of  $M_{MAJ}^2$  combining it with other cluster shape variables, is presented.

The linear discriminant method of Fisher will be used. This method is used to maximize the separation between two samples, commonly referred as signal and background. The cluster shape variables can be combined to form a Fisher linear discriminant  $Y$ , defined as:

$$Y = \sum_i a_i \cdot x_i \quad (\text{A.14})$$

where  $x_i$  represents the generic  $i$ -th input variable and  $a_i$  is the respective Fisher coefficient, obtained using the training samples of Particle Gun photons and neutral pions described in Section A.1. A detailed description of the Fisher linear discriminant method can be found in [87].



**Figure A.14.** The  $\gamma$ -efficiency versus  $\pi^0$ -rejection curve for  $M_{MAJ}^2$ , LAT and PZM. Only particles with  $0.8 \text{ cm} < \delta_{EST} < 1.0 \text{ cm}$  are considered.

Firstly,  $M_{MAJ}^2$  is combined with the other variables in a Fisher discriminant to obtain the combination which provides the best separation power. Figure A.15 demonstrates that any possible combination is worse than  $M_{MAJ}^2$  alone. This happens because the Fisher method does not work well when the distribution of the input variables is very different from the gaussian shape. This is the case of  $M_{MAJ}^2$ , whose distribution for  $\gamma$  and  $\pi^0$  is shown in Figure A.10.

The next step consists in using  $M_{MAJ}^2$  considered as a stand-alone variable, and combining LAT and PZM in a Fisher discriminant  $Y^*$ . The distribution of  $Y^*$  for photons and neutral pions is shown in Figure A.16. Finally, the selection based only on  $M_{MAJ}^2$  is compared with a new selection criteria, based on both  $M_{MAJ}^2$  and  $Y^*$ . Efficiency and rejection values are calculated by selecting only those events that satisfy the following requirements

- $M_{MAJ}^2 < M_{CUT}$ ;
- $Y^* > Y_{CUT}^*$ .

The values of  $M_{CUT}$  and  $Y_{CUT}^*$  are varied to maximize the pion rejection for any fixed value of photon efficiency. Figure A.17 shows the  $\gamma$ -efficiency versus  $\pi^0$ -rejection curves for  $M_{CUT}$  and for the optimized selection on both  $M_{CUT}$  and  $Y^*$ .

The  $\gamma - \pi^0$  selection procedure can be repeated for different bins of  $\delta_{EST}$ . Figure A.18 and Figure A.19 show the  $\gamma$ -efficiency versus  $\pi^0$ -rejection curves for  $M_{CUT}$  and for the optimized selection criteria on both  $M_{CUT}$  and  $Y^*$ , for  $0.5 \text{ cm} < \delta_{EST} < 0.8 \text{ cm}$  and  $1.0 \text{ cm} < \delta_{EST} < 1.2 \text{ cm}$  respectively. It can be noticed that as  $\delta_{EST}$  increases, i.e. large separation between the decay photons of the pion, the

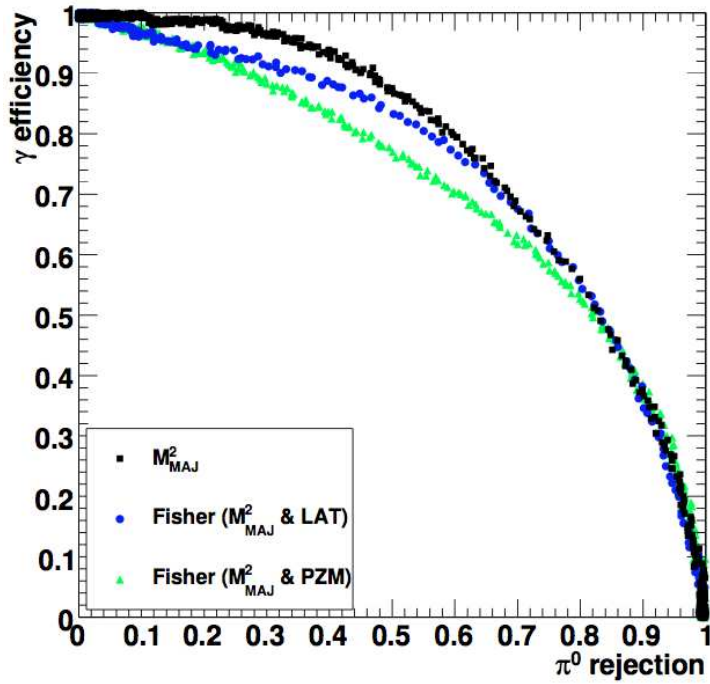


**Figure A.15.** The  $\gamma$ -efficiency versus  $\pi^0$ -rejection curve for  $M^2_{MAJ}$  and for the Fisher discriminants containing  $M^2_{MAJ}$ . Only particles with  $0.8 \text{ cm} < \delta_{EST} < 1.0 \text{ cm}$  are considered.

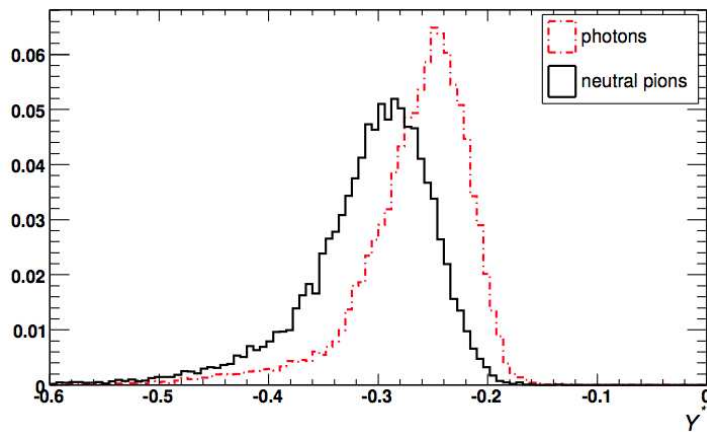


**Figure A.16.** The distribution of  $Y^*$  for photons and neutral pion with  $0.8 \text{ cm} < \delta_{EST} < 1.0 \text{ cm}$ .

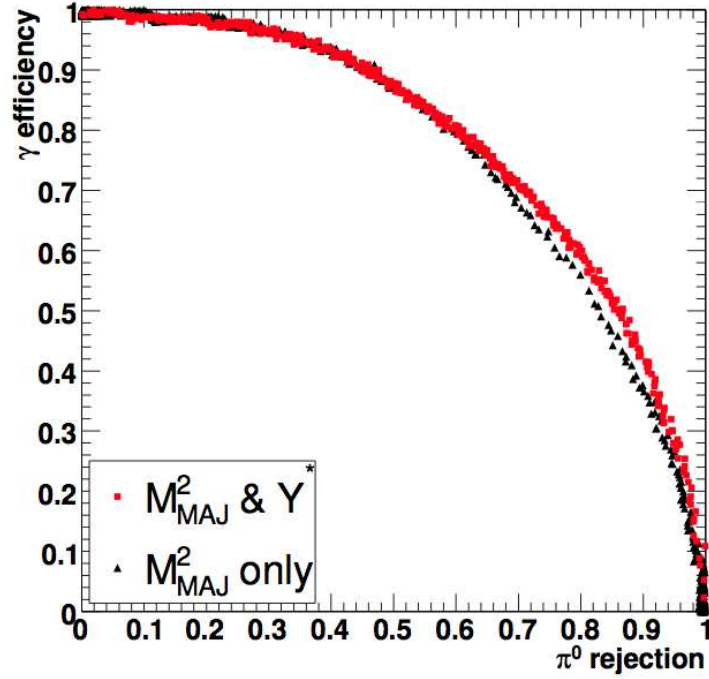


**Figure A.17.** The  $\gamma$ -efficiency versus  $\pi^0$ -rejection curve for  $M_{MAJ}^2$  and for the optimized selection on both  $M_{MAJ}^2$  and  $Y^*$ . Only particles with  $0.8 \text{ cm} < \delta_{EST} < 1.0 \text{ cm}$  are considered.

discriminating power of  $M_{MAJ}^2$  dominates and the selection based only on  $M_{MAJ}^2$  is equivalent to the optimized one. On the contrary, the  $M_{MAJ}^2 - Y^*$  selection is very productive in case of large overlap of the energy deposits of the decay photons.

Finally, Figure A.20 shows a comparison between  $M_{MAJ}^2$  selection and the optimized one, including all the three categories on  $\delta_{EST}$  previously considered. An equal number of particles has been considered in each category. In addition, the selection has been optimized separately for each category. It can be seen that the optimized selection provides an improved separation power in the region of high  $\pi^0$  rejection values. For low values of  $\pi^0$  rejection, instead, the two selections are almost equivalent.

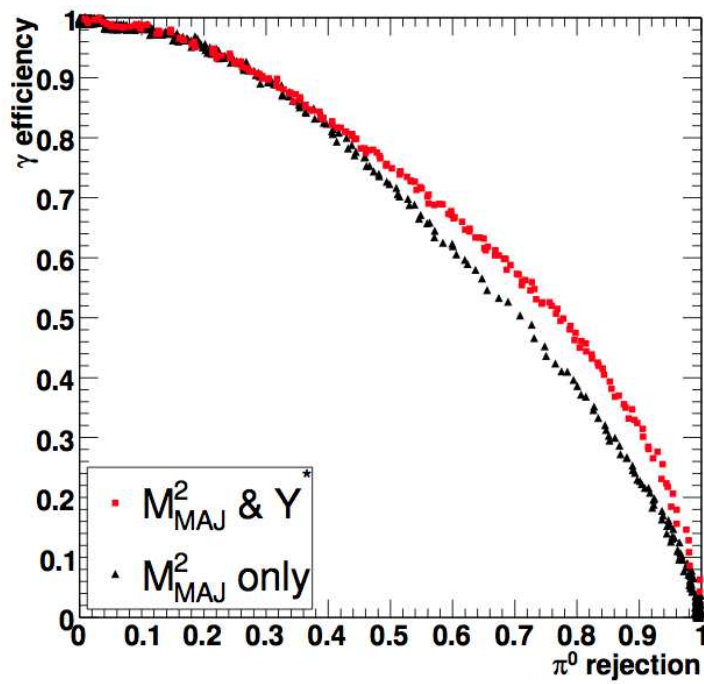


**Figure A.18.** The  $\gamma$ -efficiency versus  $\pi^0$ -rejection curve for  $M_{MAJ}^2$  and for the optimized selection on both  $M_{MAJ}^2$  and  $Y^*$ . Only particles with  $0.5 \text{ cm} < \delta_{EST} < 0.8 \text{ cm}$  are considered.

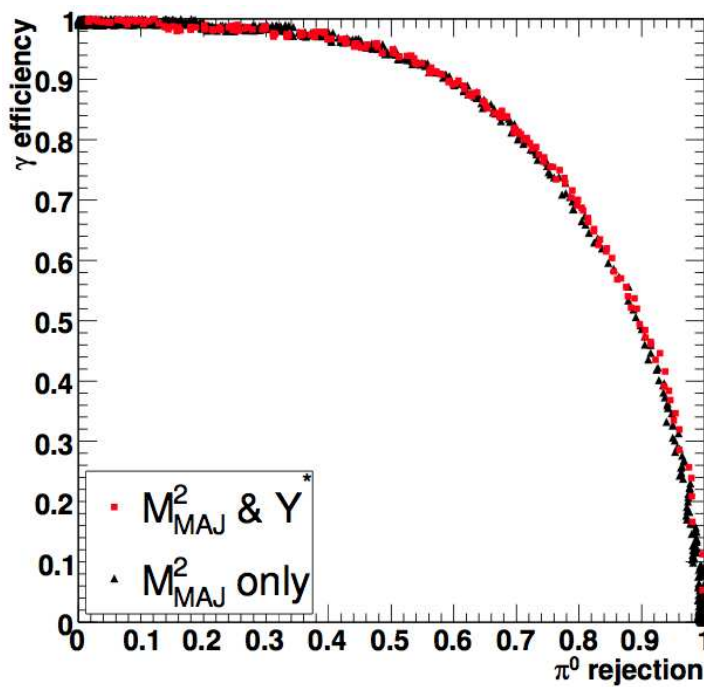


**Figure A.19.** The  $\gamma$ -efficiency versus  $\pi^0$ -rejection curve for  $M_{MAJ}^2$  and for the optimized selection on both  $M_{MAJ}^2$  and  $Y^*$ . Only particles with  $1.0 \text{ cm} < \delta_{EST} < 1.2 \text{ cm}$  are considered.

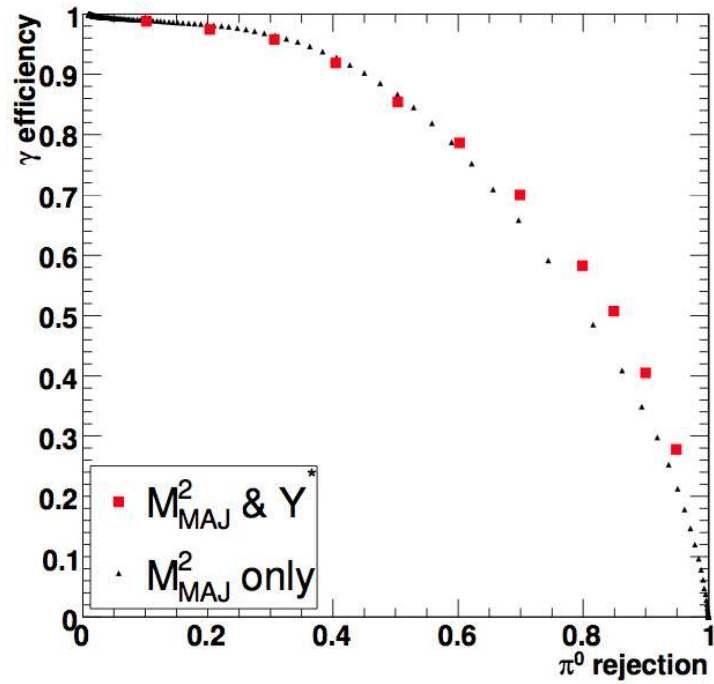


**Figure A.20.** The  $\gamma$ -efficiency versus  $\pi^0$ -rejection curve for  $M^2_{MAJ}$  and for the optimized selection on both  $M^2_{MAJ}$  and  $Y^*$ , including all the three categories of  $\delta_{EST}$  previously considered.

# Appendix B

## Improvements on $\pi^0$ reconstruction

Neutral pion decay  $\pi^0 \rightarrow \gamma\gamma$  is used to achieve a fast and precise calibration of the ECAL barrel. A calibration  $\pi^0$  technique has been recently studied using simulated data [76]. This method allows for a calibration precision of 0.5% with the first 5-10 pb<sup>-1</sup> of data.

In this appendix, possible improvements on  $\pi^0 \rightarrow \gamma\gamma$  calibration are presented. Firstly, the biases which affect  $\pi^0$  reconstruction are investigated and a simple correction is proposed. In the second part of the section, a method to improve the reconstruction of high energy  $\pi^0$ , based on the fit to the energy deposit released in the ECAL, is presented. This is a very important issue since it allows to extend the calibration up to energies of about 15 GeV.

The appendix is organized as follows:

- Section B.1 presents the dataset used for this study and illustrates the the photon reconstruction method;
- Section B.2 describes the effect of the variation of the lateral energy containment of the ECAL crystals;
- Section B.3 is devoted to the description of the improved  $\pi^0$  reconstruction algorithm.

### B.1 Dataset and photon reconstruction

The dataset used for this study consists of about 9M of QCD events with  $\hat{P} > 15$  GeV, at a center of mass energy  $\sqrt{s} = 10$  TeV. The sample has been generated assuming the ideal detector calibration and alignment conditions. Event digitization (assuming the low luminosity scenario of  $\mathcal{L} = 2 \cdot 10^{30} \text{ cm}^{-2}\text{s}^{-1}$ ) and the HLT reconstruction has been performed using CMSSW\_2\_1\_9 software release.

To obtain an event rate suitable for a fast crystal-by-crystal intercalibration, an optimized  $\pi^0$  selection method has been developed. The objects created by L1 trigger are used as seeds for the regional ECAL unpacking sequence. At the end of the sequence, a collection of the most interesting ECAL crystals is created. The collection is then used as input for the HLT filter dedicated to  $\pi^0$  calibration. To

be considered as a valid  $\pi^0$  candidate, each event has to satisfy all the requirements imposed by the HLT selection.

A simple  $3 \times 3$  array clustering algorithm is used for the online selection. Starting from an ordered list of seeds, defined as crystals with energy above 0.5 GeV, a  $3 \times 3$  array is considered. The crystals already used in the previous steps will not be used again. The clustering procedure ends when all the seeds are used.

In order to minimize the size of the stored data, a threshold on the minimum crystal energy can be set. The default value for the energy threshold is  $E_{CRY} > 0$  GeV. Figure B.1 shows the ratio between the reconstructed ( $E_{REC}$ ) and the true ( $E_{true}$ ) energy of the most energetic photon from the  $\pi^0$  decay, as a function of  $E_{REC}$ , with and without the HLT energy threshold. Considering only crystals with positive energy is equivalent to cut the negative tail of crystal noise distribution. This introduces a bias in the reconstruction of the photon energy, as shown by red points in Figure B.1. In order to avoid this effect, the energy threshold will be relaxed and the crystals with negative energy will be also considered.

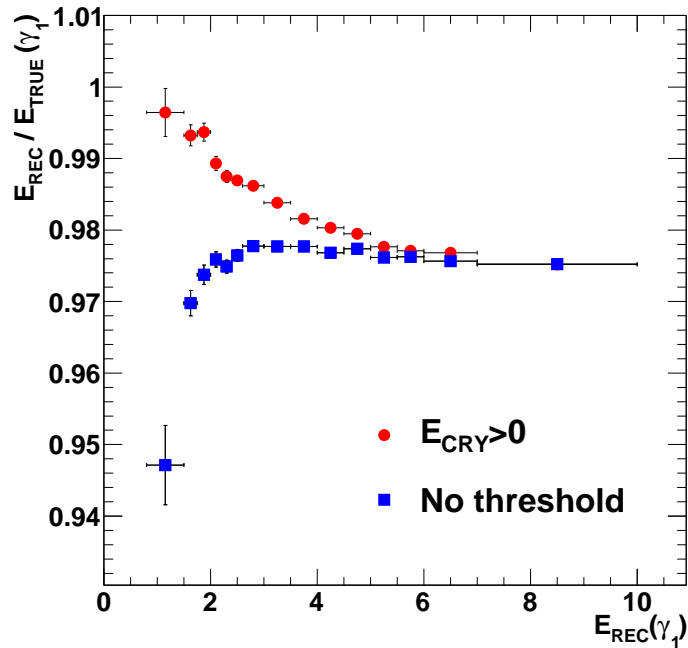


**Figure B.1.** The energy containment of a  $3 \times 3$  matrix as a function of the reconstructed energy for the most energetic photon, with and without HLT threshold  $E_{CRY} > 0$  GeV.

## B.2 Variation of the lateral containment

The basic idea of calibration with  $\pi^0$  is that different  $\eta$ -rings of the ECAL have to be calibrated at the same time. For this reason, the reconstructed  $\pi^0$  mass should be not dependent on the pseudorapidity. Figure B.2 shows the gaussian peak of the  $\pi^0$  mass as a function of the absolute value of the  $\eta$  coordinate. Only the region of the ECAL barrel has been considered.

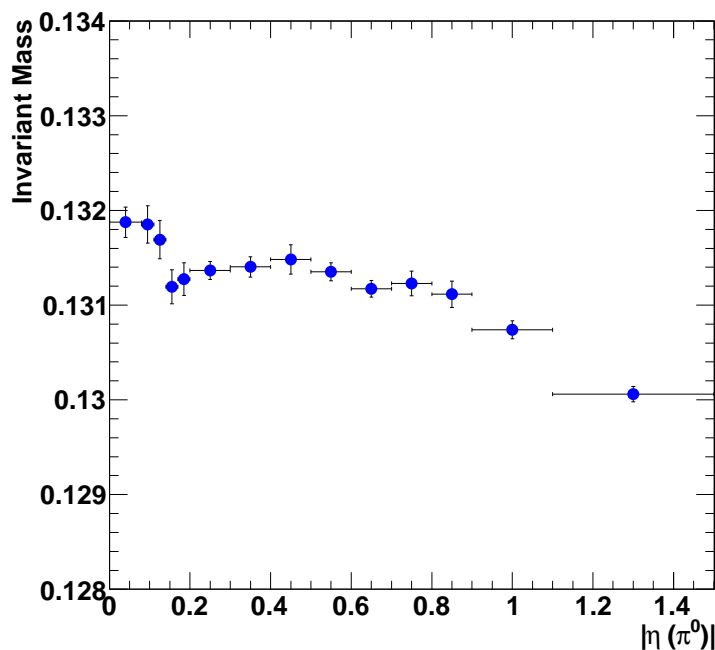


**Figure B.2.** The reconstructed  $\pi^0$  mass as a function of the absolute value of  $\eta$ .

The reconstructed mass of  $\pi^0$  exhibits a variation of about 1.5% between the center and the edges of the barrel. The  $\eta$ -dependence of  $\pi^0$  mass is mainly due to the variation of the lateral shower containment of the ECAL crystals, as a function of the energy and pseudorapidity. The fraction of the photon shower energy deposited in a crystal array of fixed size depends on the pseudorapidity. This effect is caused by the particular ECAL geometry. In order to obtain a quasi-projective calorimeter, the ECAL crystals have to be staggered as shown in Figure B.3a). This particular configuration produces an empty space between each crystal and its  $\eta$ -neighbour: part of the electromagnetic shower can therefore escape from detection. In absence of staggering the shower is entirely contained into the crystals and no energy losses occur.

Since the staggering increases with the  $\eta$  coordinate, the containment variation has to be studied as a function of the pseudorapidity. Furthermore, the energy containment varies also as a function of the energy itself, introducing a deviation from the linearity.

Recent studies on the energy containment in the ECAL barrel have been performed using the full simulation of electron showers in the Test Beam condition [88]. Figure B.4 shows the fraction of the electron energy contained by a  $3 \times 3$  array as a function of the true electron energy, for different  $\eta$ . The fit function is:

$$R(E, \eta) = P_0 \cdot e^{-P_1 \cdot E} \quad (\text{B.1})$$

where  $P_0$  and  $P_1$  are two parameters that depend on the pseudorapidity.

Equation B.1 can be used to correct the energy of a  $3 \times 3$  array. According to the  $\eta$  coordinate of the seed crystal, 17 different values for  $P_0$  and  $P_1$  (one for each

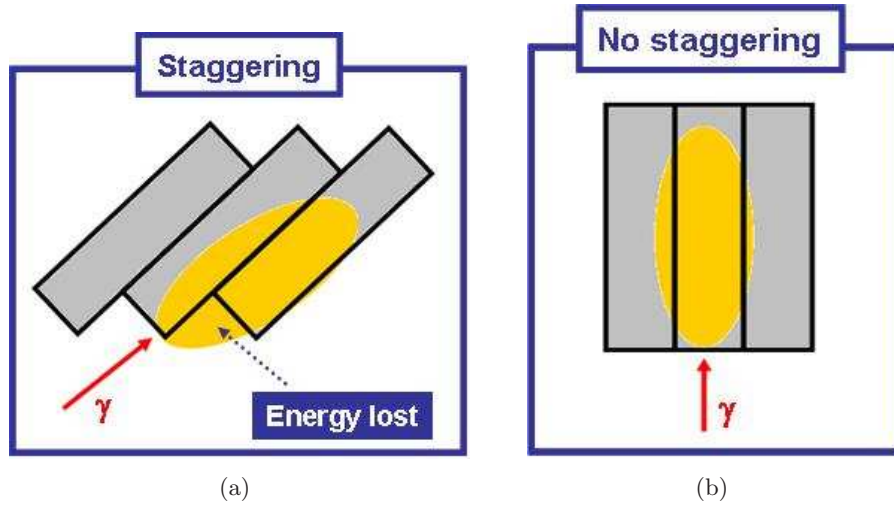


**Figure B.3.** The quasi-projective ECAL geometry and crystal staggering. Part of  $\gamma$  shower is lost inside the gap between adjacent crystals a). In absence of staggering, the entire shower is contained inside the crystals b).

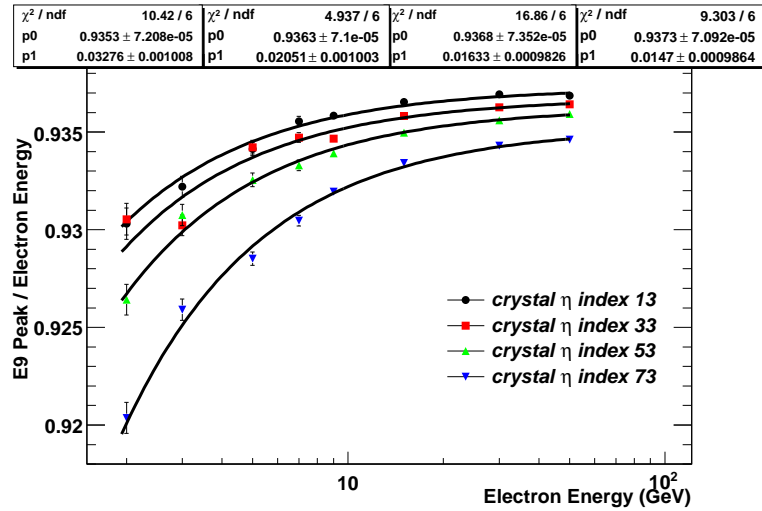


**Figure B.4.** The energy containment of  $3 \times 3$  arrays for full simulated electrons in Test Beam condition, fitted using eq. B.1 [88]. Different  $\eta$  values are considered.

trigger tower constituting an half of the barrel) have been determined and used in Equation B.1. The corrected energy can be expressed as:

$$E_{3\times 3}^{CORR} = \frac{K}{R(E, \eta)} \cdot E_{3\times 3} \quad (\text{B.2})$$

where  $E_{3\times 3}$  represents the energy of the  $3\times 3$  array and  $K$  is a factor used to assign the correct energy normalization. In the following  $K = 0.961$  will be used.

The effect of the containment correction on photon reconstruction is shown in Figures B.5a) and B.5b), which show the dependence of the energy fraction of the most energetic  $\pi^0$  decay photon in the  $3\times 3$  array as a function of the reconstructed energy, before and after the containment correction respectively. The different modules constituting the ECAL barrel have been considered. It can be noticed that the correction obtained from Test Beam electrons work quite well even in a more complex environment such as QCD events from proton - proton collisions. Figure B.6 shows the dependence of reconstructed  $\pi^0$  mass before and after the correction for the energy containment. The overall effect of the correction is to make the mass distribution flatter, reducing the mass variation within the barrel. These correction are therefore expected to provide large improvements on the ECAL calibration with neutral pions.

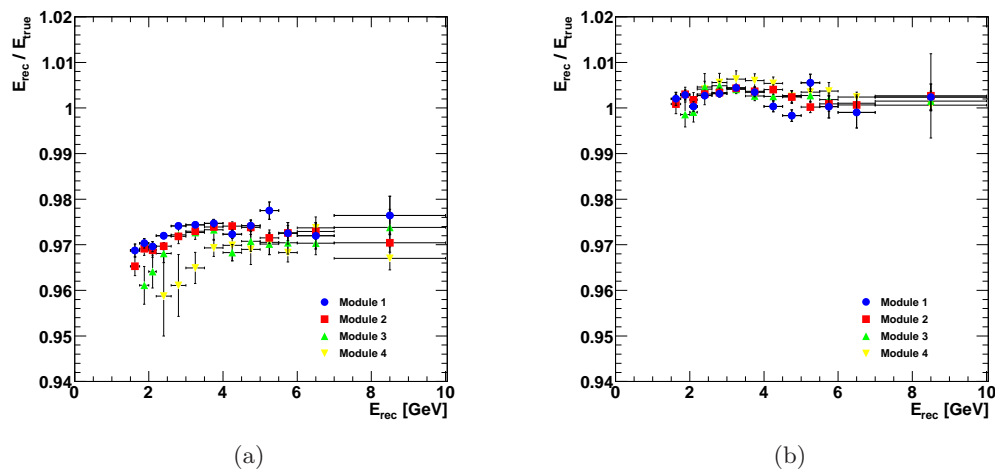


**Figure B.5.** The energy containment of  $3\times 3$  arrays for the most energetic decay photon before a) and after b) the energy containment correction. The different modules constituting the ECAL barrel have been considered.

### B.3 Improved $\pi^0$ reconstruction algorithm

As discussed in Section A.1, the decay angle of a  $\pi^0$  is anti-correlated with its energy: high  $\pi^0$  energy results in a small distance between the impact points of the decay photons on the ECAL surface, producing a large overlap between the electromagnetic showers. For energies above 10 GeV, some crystals of the  $3\times 3$  array are shared between both the decay photons. Figure B.7 shows how the reconstruction algorithm works in the case of overlapping clusters.

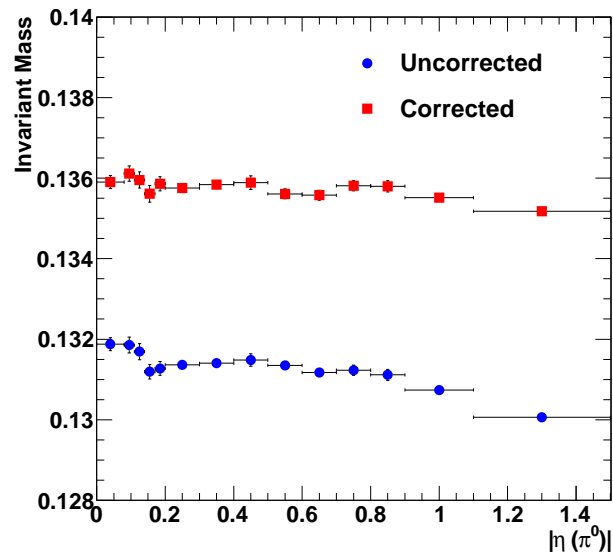


**Figure B.6.** The reconstructed  $\pi^0$  mass as a function of the absolute value of  $\eta$ , before (blue points) and after (red points) the energy containment correction.

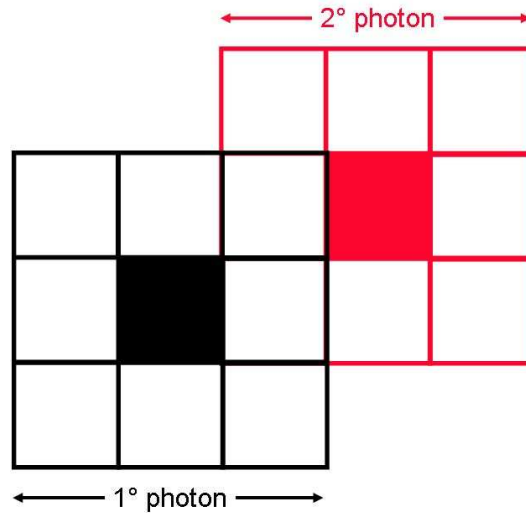


**Figure B.7.** The 3×3 clustering algorithm. When some crystals are shared between two clusters, they are assigned to the most energetic one.

When some crystals are shared between two or more clusters, they are assigned to the most energetic one. For this reason, the less energetic photon can be reconstructed as a matrix with less than 9 crystals, introducing a considerable bias in the determination of both the energy and position. To reduce this bias, an alternative reconstruction technique based on a fit to the  $\pi^0$  energy deposit has been studied, that aims at improving  $\pi^0$  calibration performance in an energy range which is strongly affected by the effect of the overlap. Each  $\pi^0$  is considered as a two-dimensional histogram in the  $\eta - \phi$  plane, as shown in Figure B.8. Each bin corresponds to an ECAL barrel crystal and the bin content represents the amount of the photon shower released inside the crystal.

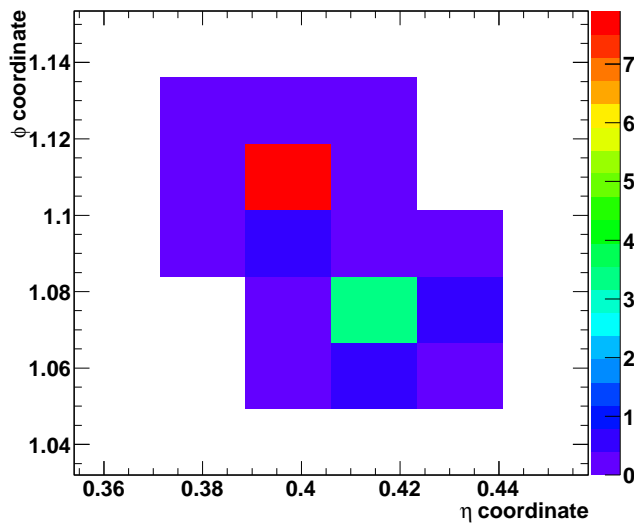


**Figure B.8.** The energy deposit of a  $\pi^0$  in the ECAL barrel. Each bin represents a crystal. The bin content corresponds to crystal energy.

### B.3.1 Parametrization of photon shower shape

To fit the energy deposit of a  $\pi^0$ , a parametrization of the photon shower shape in the ECAL is needed. For this purpose, a sample of about 100K single photons is generated with the CMS Particle Gun. The photon energy is uniformly distributed between 2 - 30 GeV. Only a limited region of the ECAL barrel has been considered ( $0.12 < \eta < 0.28$ ). Particles are reconstructed using a  $11 \times 11$  array around the most energetic crystal of the event. The use of a large crystal array allows for the study of the tails of the energy distribution.

Assuming  $\eta$  and  $\phi$  as not correlated, a factorized function can be considered:

$$f_{\gamma}(\eta, \phi) = f_{\gamma}(\eta) \cdot f_{\gamma}(\phi) \quad (\text{B.3})$$

where  $f_{\gamma}$  factors are calculated from the cumulative functions of the photon energy distribution  $F(\eta)$  and  $F(\phi)$ . Cumulative functions are extracted using the following procedure:

1. A  $11 \times 11$  array is used for photon reconstruction;

2. For each value of  $\eta$ , an energy integration along  $\phi$  is considered;
3. All the photons are processed at the same time, extracting an average cumulative function  $F(\eta)$ ;
4. The procedure is then repeated, exchanging  $\eta$  and  $\phi$ .

Figure B.9 shows the cumulative functions as a function of  $(\eta - \eta_{true})$  and  $(\phi - \phi_{true})$ .

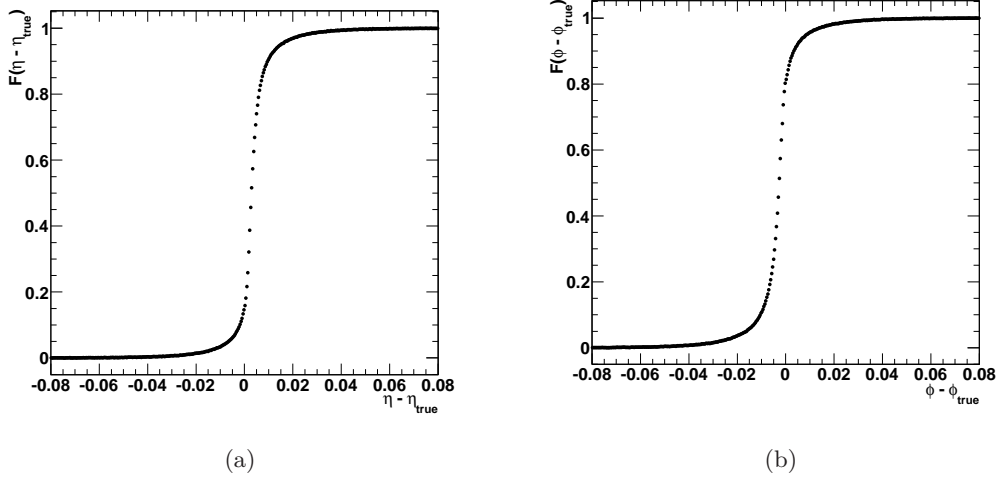


**Figure B.9.** The cumulative functions of a photon shower as a function of  $\eta - \eta_{true}$  a) and  $\phi - \phi_{true}$  b).

The two factors in Equation B.3 are obtained by fitting the derivate of the cumulative functions shown in Figure B.9. The fit function is the sum of three gaussians:

$$f_{\gamma}(x) = (1 - F_{tail} - F_{outl}) \cdot e^{-\frac{1}{2} \left( \frac{x - x_{true} - \Delta x_{core}}{\sigma_{core}} \right)^2} + F_{tail} \cdot e^{-\frac{1}{2} \left( \frac{x - x_{true} - \Delta x_{tail}}{\sigma_{tail}} \right)^2} + F_{outl} \cdot e^{-\frac{1}{2} \left( \frac{x - x_{true} - \Delta x_{outl}}{\sigma_{outl}} \right)^2} \quad (\text{B.4})$$

where  $F_{tail}$  and  $F_{outl}$  represent the fraction of the second and third gaussian respectively. Functions  $f_{\gamma}(\eta - \eta_{true})$  and  $f_{\gamma}(\phi - \phi_{true})$  are shown in Figure B.10a) and B.10b). Fit functions are superimposed and the values of parameters are summarized in Table B.1 and B.2.

It can be noticed that the maximum of the photon shower is slightly shifted with respect to the impact point the photon  $(\eta_{true}, \phi_{true})$ . This is a consequence of the quasi-projective geometry of the ECAL barrel: the axis of each crystal forms a  $3\checkmark$  angle with the direction of a photon from the interaction vertex, as shown in Figure B.11. This configuration has been chosen in order to ensure a better hermeticity of the detector. The use of a fit to the energy deposit has therefore the advantage of an improved determination of the cluster position.

Another consequence is that both  $f_{\gamma}(\eta - \eta_{true})$  and  $f_{\gamma}(\phi - \phi_{true})$  are not perfectly symmetric with respect to the maximum of the shower. Due to the  $3\checkmark$  angle, all the particles from the interaction point are slightly off-pointing. For a photon, therefore, this means that the shower shape will be quite elliptical, instead of perfectly round.

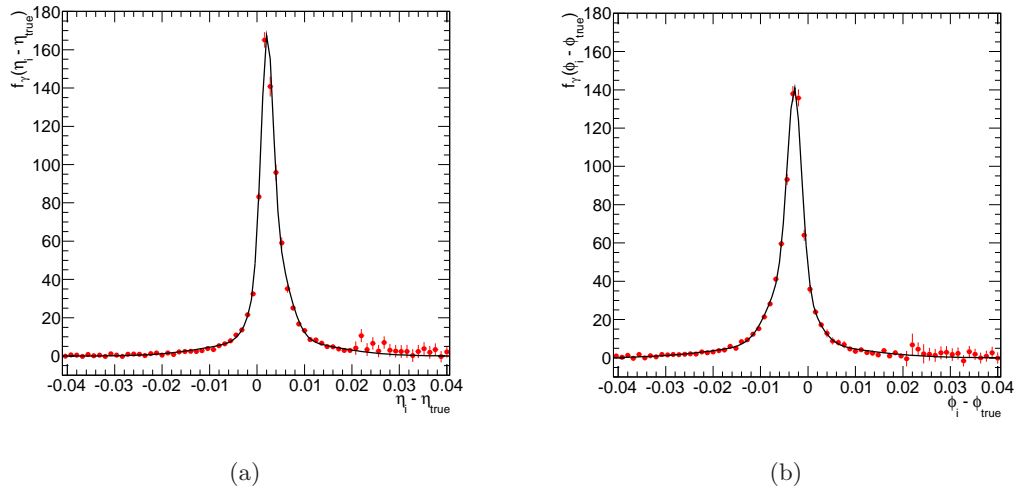


**Figure B.10.** The parametrization of photon shower as a function of  $\eta - \eta_{true}$  a) and  $\phi - \phi_{true}$  b). Equation B.4 is used for fitting.

$\sigma_{core}$	$\sigma_{tail}$	$\sigma_{outl}$	$\Delta\eta_{core}$	$\Delta\eta_{tail}$	$F_{tail}$	$F_{outl}$
0.00111	0.00316	0.01139	0.0021	0.0033	0.387	0.256

**Table B.1.** Fit parameters for  $\eta$  profile.

$\sigma_{core}$	$\sigma_{tail}$	$\sigma_{outl}$	$\Delta\phi_{core}$	$\Delta\phi_{tail}$	$F_{tail}$	$F_{outl}$
0.00137	0.00399	0.01373	-0.0028	-0.0038	0.387	0.256

**Table B.2.** Fit parameters for  $\phi$  profile.

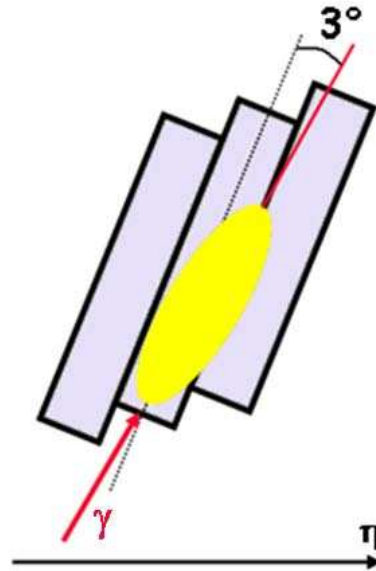


**Figure B.11.** The quasi-projective geometry of the ECAL barrel.

To preserve the symmetry of the ECAL barrel, the tilt of the crystal axis changed sign passing from  $\eta > 0$  to  $\eta < 0$ . This means that the cumulative functions are symmetric with respect to  $\eta = 0$ , as shown in Figure B.12.

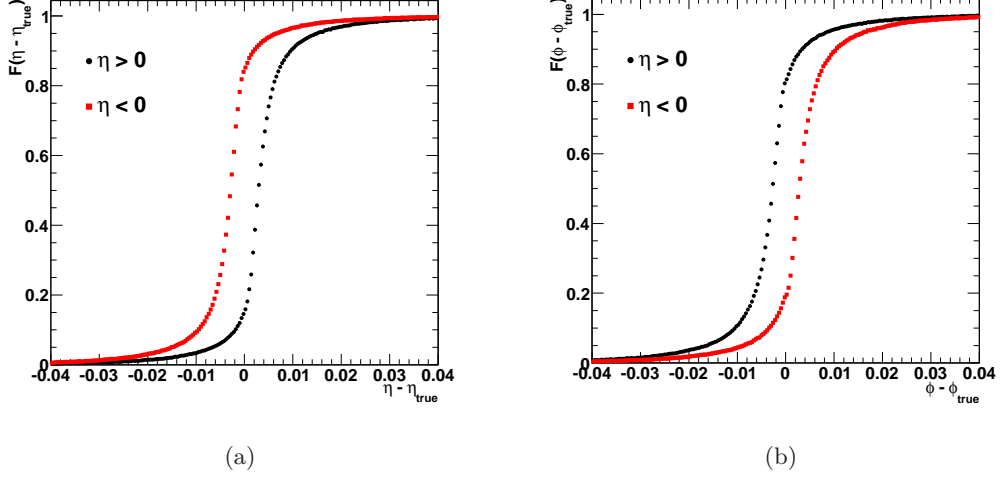


Figure B.12. The cumulative functions for  $\eta > 0$  and  $\eta < 0$ .

### B.3.2 Improved $\pi^0$ reconstruction

Once the parametrization of the photon shower has been determined, the fit function for  $\pi^0$  reconstruction can be defined as:

$$f_{\pi}(\eta, \phi) = (1 - F_2) \cdot f_{\gamma_1}(\eta, \phi) + F_2 \cdot f_{\gamma_2}(\eta, \phi) \quad (\text{B.5})$$

where  $f_{\gamma_1}$  and  $f_{\gamma_2}$  are defined in B.4 and  $F_2$  represents the fraction of  $\pi^0$  energy carried out by the less energetic photon. Five parameters are left floating:

1. Pseudorapidity of the most energetic photon  $\eta_{true1}$ ;
2. Azimuthal angle of the most energetic photon  $\phi_{true1}$ ;
3. Pseudorapidity of the less energetic photon  $\eta_{true2}$ ;
4. Azimuthal angle of the less energetic photon  $\phi_{true2}$ ;
5. Fraction of  $\pi^0$  energy carried out by the less energetic photon  $F_2$ .

Since the variation of the fit function within the size of a bin could be very large, a modified  $\chi^2$  function is defined:

$$\chi^2 = \sum_{i=1}^{N_{bin}} \frac{\left(E_i - \int_{bin_i} f_{\pi} d\eta d\phi\right)^2}{\sigma_i^2} \quad (\text{B.6})$$

where the integral of the p.d.f. function inside the bin is considered instead of its value calculated at the bin centre. The value of  $\sigma_i$  is assumed to be constant and equal to 40 MeV.

The fit technique is tested using  $\pi^0$  with large overlap between the decay photons. These are the most interesting particles for calibration since they have high energies. In the following, only  $\pi^0$ s with a photon separation  $\Delta R < 0.04$ , i.e. about 2.5 ECAL crystals, are considered. Figure B.13 shows the correlation between  $\pi^0$  energy and photon separation. Events with  $\Delta R < 0.04$  are emphasized. Figures B.14a) and B.14b) show  $\eta$  and  $\phi$  profile of a  $\pi^0$  cluster respectively. Fit results superimposed. It can be noticed that the fit technique reproduces with high accuracy the energy deposit of  $\pi^0$  in the ECAL barrel.

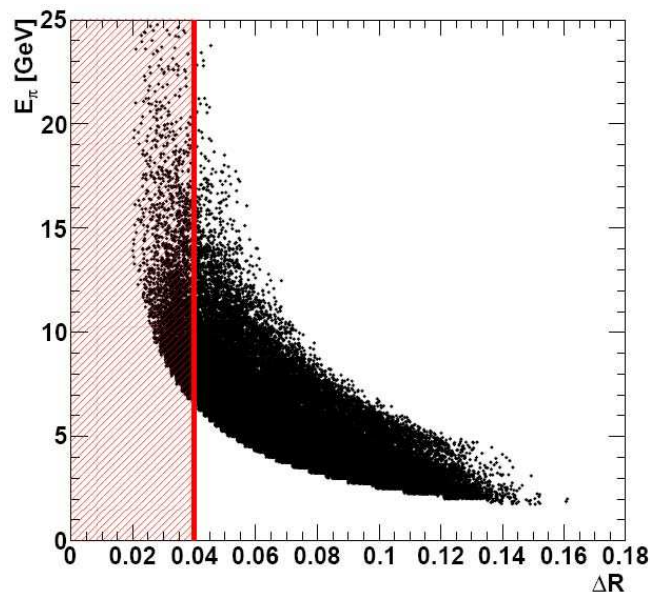


**Figure B.13.** The energy of  $\pi^0$  as a function of the photon separation. The region  $\Delta R < 0.04$  is emphasized.

Figures B.15 and B.16 show the resolution on the determination of  $\Delta R$  and  $E_2$ , for the standard reconstruction and the fit technique respectively. As expected, the fit technique ensures large improvements, especially in the determination of the energy fraction assigned to each of the two decay photons. Figure B.17 shows a comparison between the standard mass reconstruction and the results of the fit technique. The position of the gaussian peak, the standard deviation of the mass resolution are listed in Table B.3. The mass reconstruction sensibly benefits from fit technique, as demonstrated by the improvement on the mass resolution (7.3% versus 8%).

In conclusion, the algorithm based on the fit of the  $\pi^0$  energy deposit in the ECAL represents a very powerful tool to improve  $\pi^0$  calibration performance, especially in the high energy region.

	Peak [MeV]	RMS [MeV]	Resolution %
Standard reco	136.7	11.1	8%
Fit technique	134.7	9.86	7.3%

**Table B.3.** Peak position, standard deviation and mass resolution for standard reconstruction and fit technique. Only  $\pi^0$  with  $\Delta R < 0.04$  are considered.

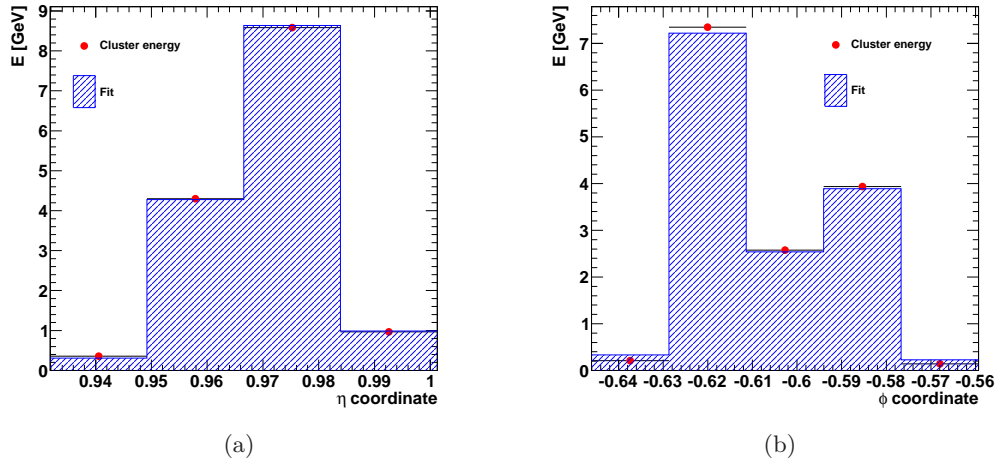


**Figure B.14.** Energy profiles of a  $\pi^0$  with overlapping photons. Fit results are superimposed.

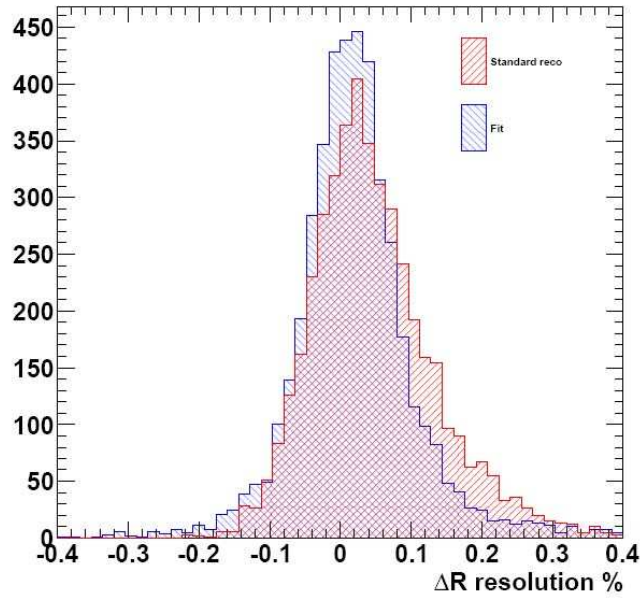


**Figure B.15.** Resolution on  $\Delta R$  for standard reconstruction and fit technique. Only  $\pi^0$  with  $\Delta R < 0.04$  are considered.

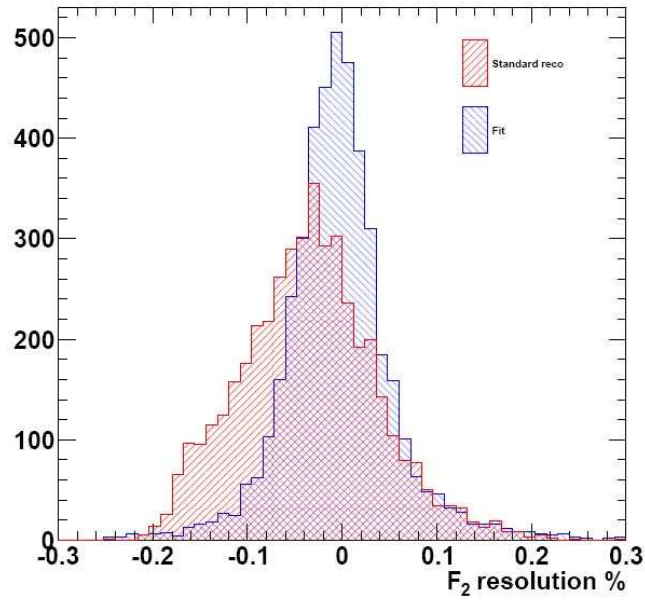


**Figure B.16.** Resolution on  $F_2$  for standard reconstruction and fit technique. Only  $\pi^0$  with  $\Delta R < 0.04$  are considered.

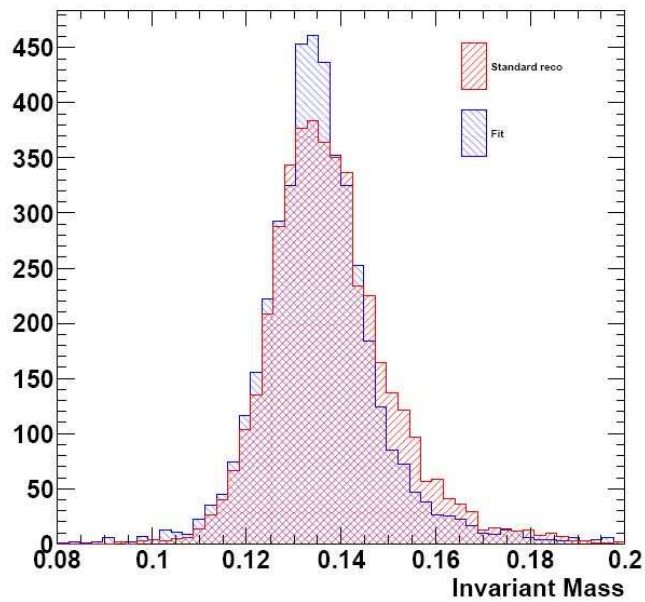


**Figure B.17.** Invariant mass for standard reconstruction and fit technique. Only  $\pi^0$  with  $\Delta R < 0.04$  are considered.



# Bibliography

- [1] S. Weinberg et al., Conceptual foundations of the unified theory of weak and electromagnetic interactions, *Rev. Mod. Phys.*, 52, 515 (1980).
- [2] S. Weinberg, A Model of Leptons, *Phys. Rev. Lett.*, 19, 1264 (1967).
- [3] P. W. Higgs, Broken symmetries, massless particles and gauge fields *Phys. Lett.*, 12(2), 132 (1964).
- [4] The LEP Electroweak Working Group, <http://lepewwg.web.cern.ch/LEPEWWG/>.
- [5] The TEVNPH Working Group, Combined CDF and D0 Upper Limits on Standard Model Higgs-Boson Production with up to  $6.7 \text{ fb}^{-1}$  of data, *hep-ex/1007.4587*.
- [6] G. G. Ross, Grand Unified Theories, *Reading, Usa: Benjamin/cummings* 497 (1984).
- [7] M. Kaku, Introduction to Superstring and M-Theory, *Springer-Verlag* (2nd edition ed.).
- [8] M. E. Peskin, Beyond the Standard Model, *hep-ph/9705479*, *SLAC-PUB-7479*.
- [9] Y. Fukuda et al., *Phys. Lett. B* 436, 33 (1998); *Phys. Rev. Lett.* 81, 1562 (1998).
- [10] R. Davis, *Prog. Part. Nucl Phys.* 32, 13 (1994)
- [11] C. Athanassopoulos et al., *Phys. Rev. Lett.* 75, 2650 (1995)
- [12] J. Bennett, M. Donahue, N. Schneider, and M. Voit, The Cosmic Perspective, *Addison Wesley Pub Co* (2003).
- [13] S. Ambrosanio et al., *Phys. Rev. D* 54, 5395 (1996).
- [14] J. L. Feng et al., *Phys.Rev.Lett.* 91, 011302 (2003).
- [15] M. J. Strassler and K. M. Zurek, *Phys. Lett. B* 651, 374 (2007), *hep-ph/0604261*.
- [16] T. Appelquist, H.C. Cheng and B.A. Dobrescu, *Phys. Rev. D* 64 (2001), *hep-ph/0012100*.
- [17] C. Friberg, E. Norrbin and T. Sjostrand, *Phys. Lett. B* 403 (1997), *hep-ph/9704214*.

- [18] K. Kohri and Y. Santoso, Cosmological scenario of stop NLSP with gravitino LSP and the cosmic lithium problem, *arXiv:0811.1119v1*.
- [19] J. L. Diaz-Cruz et al., On the feasibility of a stop NLSP in gravitino dark matter scenarios, *hep-ph/0701229v1*.
- [20] N. Arkani-Hamed and S. Dimopoulos, *JHEP* 06 073 (2005), *hep-th/0405159*.
- [21] G. F. Giudice and R. Rattazzi, Theories with Gauge-Mediated Supersymmetry Breaking, *hep-ph/9801271*.
- [22] S. P. Martin, A supersymmetry primer, *hep-ph/9709352*.
- [23] S. Coleman and J. Mandula, *Phys. Rev.* 159, 1251 (1967).
- [24] U. Amaldi, W. de Boer and H. Fürstenau, *PBL* 260, 447 (1991).
- [25] R. J. Scherrer and M. S. Turner, *Phys. Rev. D* 33, 1585 (1986).
- [26] D. I. Kazakov, Beyond the Standard Model, *hep-ph/0411064v1*.
- [27] P. Fayet, *Nucl. Phys. B* 90, 104 (1975).
- [28] R. K. Kaul and P. Majumdar, *Nucl. Phys. B* 199, 36 (1982).
- [29] S. Dawson, *Nucl. Phys. B* 261, 297 (1985).
- [30] L. Hall, J. Lykken and S. Weinberg, *Phys. Rev. D* 27, 2359 (1983).
- [31] H. P. Nilles, *Phys. Lett. B* 115, 193 (1982).
- [32] M. Dine and A. E. Nelson, *Phys. Rev. D* 48, 1277 (1993).
- [33] H. P. Nilles, *Phys. Rept.* 110, 1 (1984).
- [34] C. H. Chen and J. F. Gunion, *Phys. Rev. D* 58, 075005 (1998).
- [35] L. Randall and R. Sundrum, *Nucl. Phys. B* 557, 79 (1999).
- [36] D. E. Kaplan, G. D. Kribs and M. Schmaltz, *Phys. Rev. D* 62, 035010 (2000).
- [37] S. L. Dubovsky, D. S., Gorbunov and S. V. Troitsky, Gauge mechanism of mediation of supersymmetry breaking, *Phys. Usp.* 42, 623 (1999).
- [38] S. Deser and B. Zumino, *Phys. Rev. Lett.* 38, 1433 (1977).
- [39] D. V. Volkov and V. A. Soroka, *JETP Lett.* 18, 312 (1973).
- [40] S. P. Martin, Low scale and gauge mediated supersymmetry breaking at the Fermilab Tevatron Run II, *hep-ph/0008070*.
- [41] S. Schael et al., *Eur. Phys. J. C* 47, 547 (2006).
- [42] B. C. Allanach et al, The Snowmass points and Slopes: Benchmarks for SUSY Searches, *hep-ph/0202233*.
- [43] P. Bryant and L. Evans, LHC Machine, *JINST*, S08001:3 (2008).

- [44] A. Achilli et al., Total cross-section and rapidity gap survival probability at the LHC through an eikonal with soft gluon resummation, *IISC- CHEP-09-07*.
- [45] CMS Collaboration, The Compact Muon Solenoid Technical Proposal *CERN/LHCC 94-38*, *LHCC/P1* (1994).
- [46] CMS Collaboration, The Magnet Project: Technical Design Report, *CERN/LHCC 97-10*.
- [47] CMS Collaboration, The Tracker Project: Technical Design Report, *CERN/LHCC 98-10*.
- [48] CMS Collaboration, The Hadron Calorimeter Project: Technical Design Report, *CERN/LHCC 97-31*.
- [49] CMS Collaboration, The Muon Project: Technical Design Report, *CERN/LHCC 97-32*.
- [50] CMS Collaboration. The TriDAS Project Technical Design Report, Vol. 1. *CERN/LHCC 2000-38*.
- [51] CMS Collaboration. The TriDAS Project Technical Design Report, Vol. 2. *CERN/LHCC 2002-026*.
- [52] The CMS Offline SW Guide, <https://twiki.cern.ch/twiki/bin/view/CMS/SWGuide>.
- [53] The GEANT4 Collaboration, GEANT4: A simulation toolkit. *Nucl. Instrum. Meth.*, 250:250D303 (2003).
- [54] CMS Collaboration. CMS Physics Performance, Vol. 2, *CERN/LHCC 2006-021*.
- [55] CMS Collaboration, The Electromagnetic Calorimeter Project: Technical Design Report, *CERN/LHCC 97-33*.
- [56] P. Lecoq et al., *CMS-TN/94-308*.
- [57] R. Rusack, Avalanche Photodiodes for the CMS Lead Tungstate Calorimeter, presentation at CALOR2002, Caltech, 25-30 May 2002.
- [58] Yu. Blinnikov et al., *Nucl. Instrum. Meth. A* 504, 228 (2003).
- [59] C. Biino et al., The CMS ECAL Very Front end Electronics: production and tests, Proceedings of the 10th Workshop on Electronics for LHC and future Experiments, Boston USA.
- [60] W. Lusterhann, Low Voltage Supply System for the Very Front End Readout Electronics of the CMS Electromagnetic Calorimeter, Proceedings of the 9th Workshop on Electronics for the LHC Experiments, Amsterdam.
- [61] S. Chatrchyan et al., The CMS experiment at the CERN LHC, *JINST* 3, S08004 (2008).
- [62] P. Adzic et al., Energy resolution of the barrel of the CMS Electromagnetic Calorimeter, *JINST* 2, P04004 (2007).

- [63] P. Adzic et al., Results of the first performance tests of the CMS electromagnetic calorimeter, *Eur. Phys. C*, 44:1D10 (2006).
- [64] R. Paramatti, Calibration of the CMS Electromagnetic Calorimeter at LHC startup, *CR-2010/139*.
- [65] E. Meschi et al., Electron Reconstruction in the CMS Electromagnetic Calorimeter, *CMS Note 2001/034*.
- [66] T. C. Awes et al., A Simple Method of Shower Localization and Identification in Laterally Segmented Calorimeters, *Nucl. Instrum. and Methods A* 311.
- [67] H. Baer et al., ISAJET, <http://www.hep.fsu.edu/isajet/>.
- [68] P. Skands et al., SUSY Les Houches Accord: Interfacing SUSY Spectrum Calculators, Decay Packages, and Event Generators, *hep-ph/0311123v4*.
- [69] <http://home.thep.lu.se/torbjorn/Pythia.html>.
- [70] <http://geant4.cern.ch>.
- [71] F. James, Statistical Methods in Experimental Physics, *World Scientific*, Singapore (2006).
- [72] D0 Collaboration, Search for Supersymmetry with Gauge-Mediated Breaking in Diphoton Events at D0, *hep-ex/0408146v1*.
- [73] CMS collaboration, Time reconstruction and performance of the CMS electromagnetic calorimeter, *JINST* 5, T03011 (2010).
- [74] CMS Collaboration, Particle-Flow Event Reconstruction in CMS and Performance with Jets, Taus and  $E_{miss}^T$ , *CMS PAS PFT-09/001*.
- [75] M. Cacciari, G. P. Salam and G. Soyez, The anti-kt jet clustering algorithm, *JHEP* 0804 (2008) 063.
- [76] M. Gataullin et al.,  $\pi^0(\eta)$  Calibration Trigger Performance and Inter-Calibration of the CMS Barrel Electromagnetic Calorimeter with 7 TeV Data, *CMS AN-2010/216*.
- [77] F. Pandolfi et al., Jet Response and Resolution Measurement with Photon+Jet Events, *CMS AN-2010/076*.
- [78] A. Askew et al., Understanding missing transverse energy in di-photon events for SUSY searches with 7 TeV data, *CMS AN-2010/168*.
- [79] CMS Collaboration, Jet Performance in pp Collisions at  $\sqrt{s}=7$  TeV, *CMS PAS JME-10-003*.
- [80] CMS Collaboration, ECAL Anomalous Signals in 7 TeV Data, *CMS DPS-2010/008*.
- [81] N. Adam et al., Measurement of CMS Luminosity in the 2010 Run, *CMS AN-2010/175*.

- [82] CMS Collaboration, CMS Physics Technical Design Report Volume II: Physics Performance - Theoretical uncertainties. *CERN/LHCC 2006- 021*, pag 1490.
- [83] D.Acosta et al., Search for Anomalous Production of Diphoton Events with Missing Transverse Energy at CDF and Limits on Gauge Mediated Supersymmetry Breaking Models, *Phys. Rev. Lett.* 94, 041803 (2005).
- [84] D. Franci, S. Rahatlou and D. del Re, Studies for photons and neutral pions identification in the ECAL barrel region, *CMS AN-2008/075*.
- [85] Argus Collaboration, *Nucl. Instrum. Meth. A* 237, 464 (1985).
- [86] R. Sinkus and T. Voss, *Nucl. Instrum. Meth. A* 389, 160 (1997).
- [87] R. A. Fisher, The use of multiple measures in taxonomic problems, *Ann. Eugenics*, vol. 7, 179 (1936).
- [88] R. Paramatti and C. Rovelli, Shower containment studies in ECAL barrel, *CMS DN-2009/004*.